



HAL
open science

3D Structured coherent light state emitted by a self imaging laser cavity based on semiconductor VECSEL technology.

Nathan Vigne

► **To cite this version:**

Nathan Vigne. 3D Structured coherent light state emitted by a self imaging laser cavity based on semiconductor VECSEL technology.. Electronics. Université de Montpellier, 2022. English. NNT : 2022UMONS077 . tel-04161405

HAL Id: tel-04161405

<https://theses.hal.science/tel-04161405v1>

Submitted on 13 Jul 2023

HAL is a multi-disciplinary open access archive for the deposit and dissemination of scientific research documents, whether they are published or not. The documents may come from teaching and research institutions in France or abroad, or from public or private research centers.

L'archive ouverte pluridisciplinaire **HAL**, est destinée au dépôt et à la diffusion de documents scientifiques de niveau recherche, publiés ou non, émanant des établissements d'enseignement et de recherche français ou étrangers, des laboratoires publics ou privés.

THÈSE POUR OBTENIR LE GRADE DE DOCTEUR DE L'UNIVERSITÉ DE MONTPELLIER

En Électronique

École doctorale Information Structure Systèmes

Unité de recherche Insitut d'Électronique et des Systèmes

3D STRUCTURED COHERENT LIGHT STATE EMITTED BY A SELF IMAGING LASER CAVITY BASED ON SEMICONDUCTOR VECSEL TECHNOLOGY

Présentée par Nathan VIGNE
Le 15 décembre 2022

Sous la direction de Arnaud GARNACHE

Devant le jury composé de

Massimo GIUDICI, Professeur, INPHYNI Univ Nice-Sophia Antipolis

Mircea GUINA, Professeur, ORC Tampere University (Finland)

Arnaud MUSSOT, Professeur, PhLAM CNRS Univ de Lille

Isabelle SAGNES, DR CNRS, C2N (Plaiseau)

Baptiste CHOMET, Docteur, ENS (Paris)

Étienne BRASSELET, DR CNRS, LOMA (Talence)

Stephane BLIN, MC, IES Univ de Montpellier

Arnaud GARNACHE, DR CNRS, IES (Montpellier)

Président du jury

Rapporteur

Rapporteur

Examinateur

Examinateur

Examinateur

Examinateur

Directeur de thèse



UNIVERSITÉ
DE MONTPELLIER

Résumé

Ce projet de thèse aspire à développer un système laser capable de générer, intra-cavité, des états de lumière structuré en 3D. Le système est composé d'une cavité optique auto-imageante et d'un milieu actif fondé sur des micro-lasers à cavité externe et émission verticale (VECSEL). La cavité auto-imageante offre la possibilité d'avoir un grand rapport d'aspect spatial. La taille transverse du spot laser étant petite devant la surface de possible existence. De plus, pour la génération de structures localisées temporellement, cette cavité présente un grand rapport d'aspect temporel. La cavité pouvant être très longue tout en gardant une grande étendue spatiale.

L'existence de structure localisée temporellement (SLT) et individuellement adressable grâce à l'ajout d'un absorbant saturable rapide a déjà été démontré dans un système fondé sur technologie. En outre, des structures localisées spatialement (SLS) dans des microcavités VCSEL monolithiques ou dans un système auto-imageante fondé sur des colorants ont été démontrés. Nous proposons dans ce manuscrit de démontrer les capacités d'un système auto-imageante combiné à un composant VECSEL, à supporter les deux types de localisations. Ce type de structure, localisés spatio-temporellement (Balle de lumière) contrôlable et adressable à la manière de « bit », sont intéressantes pour le traitement tout optique de l'information. Ce travail intervient dans le cadre de l'ANR BLASON en collaboration entre les laboratoires de l'IES et l'INPHYNI.

Le premier élément important du système est le milieu actif non-linéaire (gain et absorbant) fondé sur des nanostructures à semi-conducteurs III-V développées au C2N RENATECH. La génération de structures localisées émergeant grâce à l'existence d'une bistabilité optique, nécessite une grande modulation des pertes saturables. Un large gain optique est essentiel. Pour l'existence de STL, une large bande passante spectrale est nécessaire. Dans le design, un compromis est alors fait pour limiter l'effet de filtrage spatial et spectral de la micro-cavité et favoriser le couplage du champ électromagnétique avec la cavité externe. Un absorbant saturable (SESAM) a aussi été simulé et fabriqué pour s'adapter correctement aux

paramètres gain. Ce concept a d'abord été pensé pour la structuration spatiale du champ (temps de réponse long de la matière) afin de simplifier la dynamique temporelle à un régime continu. Des mesures de réflectivité non-linéaire et les longueurs de diffusion des porteurs dans le SESAM nous ont aussi permis d'identifier une limitation sur les SLS.

Dans un second temps, une étude de la cavité optique externe de forte ouverture numérique a été réalisée. Pour répondre au besoin d'un système étendu transversalement et longitudinalement, le choix d'une cavité auto-imageante est évident. Nous avons mis en évidence l'importance des effets perçus comme perturbatifs, comme la lentille thermique ou les aberrations optiques. Dans des configurations en 4-f la lentille thermique devient le facteur principal de la stabilité sur l'axe optique du système alors que les aberrations lèvent la dégénérescence entre les modes dits à composante sphérique (sur l'axe) et conique (Bessel-Gauss).

Malgré ces limitations, le système actuel est capable d'émettre sur différents types d'états de photon transverses. À l'aide de métasurface absorbante intégrée sur le semi-conducteur, la génération de fonctions d'onde arbitraires, structurées en champ proche a été démontrée. Le multiplexage de plusieurs émetteurs ou modes laser dans une seule cavité optique a aussi été montré. Enfin, en combinant les métasurfaces et le SESAM, une localisation spatiale a été démontrée, contrôlée par les inhomogénéités et une injection non résonante. À l'aide de l'équation de Schrödinger non-linéaire avec bi-laplacien une analyse de la dynamique spatiale a permis d'expliquer ces états localisés de la lumière, leur dynamique spatiale, et *in fine* la difficulté d'observation des SLS.

Abstract

This thesis project aims to develop a laser system capable of intra-cavity generation of 3D structured light states. It is composed of a self-imaging optical cavity and an active medium based on micro-lasers with surface emission and external cavity (VECSEL). The self-imaging cavity offers the possibility of having a large transverse aspect ratio. The laser spot size being small in front of the transverse area of the system. Moreover, for the generation of temporally localized structures, this cavity can support a large temporal aspect ratio. Indeed, the cavity can be very long without degradation over the spatial extent.

The existence of individually addressable temporally localized structure (TLS) thanks to the addition of a fast saturable absorber has already been demonstrated in a system based on the same technology. Additionally, spatially localized structures (SLS) in monolithic VCSEL microcavities or dye-based self-imaging system have been shown. We propose in this manuscript to demonstrate the capabilities of a self-imaging system combined with a VECSEL device, to support both types of localization. A spatially and temporally localized structure (light bullet) capable of being controlled and addressed in the manner of “bits” is interesting for all-optical information processing. This work was done in collaboration between the IES and INPHYNI laboratories within the framework of the ANR BLASON.

The first element of the system is the non-linear active medium (gain and absorber) based on III-V semiconductor nanostructures developed at C2N REN-ATECH. The generation of localized structures is possible thanks to an optical bistability and requires a large modulation of saturable losses. A large optical gain is then essential. For the existence of TLS, a large spectral bandwidth is required. For the design, a compromise is made to limit spatial and spectral filtering effects of the micro-cavity, and favor coupling of the electromagnetic field with the external cavity. A saturable absorber (SESAM) is also simulated and manufactured to match the gain parameters. To first focus on the spatial structuring of the field, complex or unstable temporal dynamics is avoided (long response time of matter) and a continuous regime is targeted. Nonlinear reflectivity and carrier diffusion

length measurements of the SESAM allow us to identify limitations on SLS.

In a second step, a study of a high numerical aperture external optical cavity is carried out. To meet the need for a transversely and longitudinally extended system, the choice of a self-imaging cavity is obvious. We have highlighted the importance of perturbative effects, like thermal lensing or optical aberrations. In 4-f configurations thermal lens becomes the main force for stability on the optical axis while optical aberrations lift the degeneracy between the so-called spherical (on the axis) and conical (Bessel-Gauss) component.

Despite these limitations, the current system can emit on different types of transverse photon states. Using an absorbing metasurface integrated on the semiconductor device, the generation of arbitrary, near-field structured wave functions is demonstrated. Multiplexing of several emitters or laser modes in a single optical cavity is also shown. Finally, by combining the metasurface and the SESAM, spatial localization was demonstrated, controlled by the inhomogeneities and non-resonant injection. Using the non-linear and bi-Laplacian Schrödinger equation, an analysis of the spatial dynamics allows us to explain these localized states of light, their spatial dynamics, and ultimately the difficulty of observing SLS.

Acknowledgment

The work written in this manuscript was done at the “Institut d’électronique et des Systèmes” in Montpellier, where I was welcomed by its former director Alain Foucaran and its current one, Philippe Combette to whom I am grateful.

First, I want to express my sincere gratitude to my advisor Dr. Arnaud Garnache for his support and patience throughout my Ph.D. research and study. I greatly appreciate his guidance and scientific knowledge.

I would like to thank my reviewers, Professor Mircea Guina from the Optoelectronics Research Center of Tampere university in Finland, and Professor Arnaud Mussot from the “Laboratoire de Physique des Laser, Atomes et Mollécules” of Lille university in France, for the interest they have shown to my work.

I thank Professor Massimo Giudici from “Institut de Physique de Nice” of the Nice university for presiding my committee. I also want to thank him and his colleges at INPHYNI, Adrian Bartolo, Mathias Marconi, Guillaume Huyet, for their warm welcomes during our multiples workshops together.

I also thank Professor Isabelle Sagnes from the “Centre de nanosciences et de nanotechnologies” of Paris-Saclay university for participating in my thesis committees. I am also grateful to her and her team, Gregoire Beaudoin, Konstantinos Pantzas, for the great semiconductor structures that were used in this work.

I am also thankful to my thesis examiners, Professor Étienne Brasselet from “Laboratoire Ondes et Matière d’Aquitaine” of Bordeaux university, Associate Professor Stephane Blin from “Institut d’électronique et des Systèmes” of Montpellier university, and Ph.D. Baptiste Chomet of “Ecole Normale Supérieure de Paris”.

I want to thank all the members of the PhoTéra team for their warm welcome during my time at the Institute.

Lastly, I would like to thank my family and friends, and especially my flatmates, for their unconditional support.

Contents

General introduction	1
I From conventional laser to non-conventional light structuration in lasers	5
Chapter 1 Motivation and basic principles of a laser and light structuration	7
1.1 What is structured light?	7
1.1.1 Transverse structuration	8
1.1.2 Longitudinal structuration	9
1.1.3 Localized structure	12
1.1.3.1 Spatially localized structure	13
1.1.3.2 Temporally localized structure	15
1.1.4 Motivation	16
1.2 EM-wave propagation	16
1.2.1 Traveling wave model	17
1.2.2 Fourier optics	19
1.3 Optical cavity structuration	20
1.3.1 Quantum mechanic analogy	21
1.4 Light amplification	23
1.5 Technologies overview	25
1.5.1 Solid state medium	25
1.5.2 Gas medium	25
1.5.3 Dye medium	26
1.5.4 Semiconductor medium	26
1.6 3D Light structuration inside a laser cavity	28
1.6.1 Longitudinal band engineering	28
1.6.2 Transversal band engineering	29
1.6.3 Spatial structuration with self-imaging cavity	30

II	Gain and Absorber technologies and design	33
Chapter 2	VECSEL technology: building blocks	35
2.1	Semiconductor design requirement	35
2.2	Bragg mirror	36
2.3	Quantum wells active area	38
2.3.1	Quantum Well	39
2.3.2	Absorption and Gain in QW	40
2.3.3	Carrier lifetime	44
2.3.4	Gain dichroism	46
2.4	Non-resonant optical pumping in barrier	46
2.4.1	Carrier generation	47
2.4.2	Thermal properties	48
2.5	Conclusion	51
Chapter 3	Design of semiconductors structures: GAIN & SESAM	53
3.1	Modal Gain	53
3.1.1	QWs placement	55
3.1.2	Micro-cavity factor	56
3.1.2.1	Fourier Spatial filtering	57
3.1.2.2	Resonant Design	59
3.1.2.3	Anti-resonant Design	60
3.2	High Gain Design	61
3.2.1	Active zone layout	62
3.2.2	Growth process	64
3.2.2.1	Large-scale inhomogeneity	65
3.2.2.2	Small-scale inhomogeneity	66
3.2.3	First order characterization	67
3.2.3.1	Output power	67
3.2.3.2	Lasing wavelength tunability	69
3.3	SESAM Design	70
3.3.1	SESAM interest	71
3.3.2	Very-slow lifetime design	72
3.3.2.1	Saturable absorption measurement	73
3.3.2.2	Diffusion length measurement	75
3.4	Air-semiconductor interface functionalization	79
3.4.1	Amplitude mask	80
3.4.2	Phase mask	82
3.4.3	Technological steps	82
3.5	Perspective: MIXSEL (Two in one)	84
3.5.1	Conclusion	86

III Design of a spatially modeless optical cavity 89

Chapter 4 Optical resonator design for 3D light structuration 91

4.1 Introduction 91

4.1.1 Different types of laser cavities 91

4.1.2 Design guidelines for transverse structuration 93

4.2 Concept of stable optical cavity 96

4.2.1 Longitudinal modes 97

4.2.2 Transverse eigenstates 98

4.2.2.1 Gaussian propagation 99

4.2.2.2 Higher order modes : Spherical wave cavity 101

4.2.2.2.1 Higher order modes : LG & HG 101

4.2.2.3 Conical wave cavity: Bessel-Gauss Beam 102

4.2.2.4 Transverse modes frequency spacing 104

4.2.3 Polarisation modes 106

4.2.4 Cavity stability 107

4.2.4.1 ABCD matrix formalism 107

4.2.4.2 Diffractive cavity: Plano-Concave example 109

4.3 Conclusion 111

Chapter 5 Spatially modeless cavity: Self-imaging optical system 113

5.1 Self-imaging interest 114

5.1.1 Extended transverse broad area 115

5.1.2 Extended longitudinal area 115

5.1.3 Active component placement 116

5.2 System stability 116

5.2.1 Thermal lensing: local anharmonic potential 117

5.2.2 Longitudinal misalignment: non-local parabolic phase dif-
fraction tuning 118

5.2.3 Transverse degeneracy tolerances 120

5.3 Aberrations effects on self-imaging system 123

5.3.1 Spherical aberration 124

5.3.1.1 Seidel coefficient 127

5.3.1.2 Off-axis incident beam 127

5.3.2 Stability analysis with spherical aberration 129

5.3.2.1 Spherical aberration limits 133

5.3.3 Numerical aperture 135

5.3.3.1 Strehl ratio 136

5.3.3.2 Aperture limits for On-axis beam 136

5.4 Conclusion 137

IV	Experimental results and analysis	141
Chapter 6	Analysis tools: Multi-harmonic Schrödinger Non-linear like equation	143
6.1	Derivation of multi-harmonic Schrödinger like non-linear equation	144
6.1.1	Simplified system and hypothesis	145
6.1.2	Master equation	146
6.2	Physical interpretation of the operators	149
6.2.1	Non-local operator	149
6.2.1.1	Diffraction coefficient	149
6.2.1.2	Fourth order diffraction coefficient	150
6.2.1.3	Combined diffraction effects	151
6.2.2	Local operators	152
6.2.2.1	Complex potential	152
6.2.2.2	Complex reaction	153
6.3	Eigenvalue problem : Bi-Harmonic Helmholtz like equation	155
6.4	Conclusion	156
6.4.1	Passive Eigenfunctions	159
6.4.2	Non-linear localization	160
Chapter 7	Non-linear self-imaging laser cavity modes topology	163
7.1	Experimental set-up	163
7.1.1	Instrumentation	164
7.1.2	Pumping profiles	165
7.2	Study of the spatial morphology in a 4-f self-imaging laser	167
7.2.1	On-axis spherical wave emission.	167
7.2.1.1	Without chromium mask: Thermal lens based potential stabilization.	167
7.2.1.2	With chromium mask: Guided mode stabilisation.	172
7.2.2	Off-axis, conical-wave behaviour	173
7.2.3	Summary of the different emission behaviour	176
7.3	Arbitrary wavefunction	179
7.3.1	Chromium mask "A"	179
7.3.2	Chromium defects	181
7.3.3	Degenerated conical wave	181
Chapter 8	Non-linear light structuration in the spatial domain	185
8.1	Non-linear travelling wave	186
8.1.1	Dynamically instable NL travelling wave	186
8.1.1.1	Without mask, magnification: 2	186
8.1.1.2	Chromium mask 30 μm , magnification: 2	187

8.1.2	Stable NL travelling wave	190
8.1.2.1	Chromium mask 30 μm , magnification: 0.75	190
8.1.2.2	Chromium mask 15 μm , magnification: 2	195
8.1.3	Experimental limits	196
8.1.3.1	Quantum particle analogy	200
8.2	Laser multiplexing	203
8.2.1	Two lasers in one	203
8.2.1.1	Large separation : Independent system	204
8.2.1.2	Small separation: coupled system	204
8.2.2	Multiplexed NL localized structure	205
	Conclusion and perspective	209
	Bibliographie	215

General introduction

Since Einstein predicted the phenomenon of stimulated emission in the early 20th century, and after the first demonstration of a MASER (Microwave Amplification by Stimulated Emission of Radiation), the field of Lasers (Light Amplification by Stimulated Emission of Radiation) took off in the latter half of the 20th century. Laser systems are devices that generate a coherent electromagnetic wave ranging from the ultraviolet to the infra-red. They are based on two main components. A coherent field can be built up using the active medium for light amplification and the optical cavity for optical feedback.

Using these principles, a wide range of laser devices were developed from various gain mediums, ranging from solid-state crystal (Ruby crystal was used for the first laser demonstration.), Gas medium (He-Ne laser, CO₂ laser, ...) to more recently, semiconductor devices (laser diode, disk laser). Traditionally, laser sources are developed to emit a single light state such as single transverse mode (Gaussian profile), single frequency and a linear polarization state. However, more structured light emission is generating interest for some of their unique properties.

For example, lasers with temporal structuration such as pulsed laser are used in a myriad of applications ranging from optical spectroscopy [Mandon 2009, Villares 2014] to material processing [Bliedtner 2016, Booth 2004]. Spatially structured lasers such as Vortex laser [Seghilani 2016], carrying orbital angular momentum are used in optical tweezers [Jeffries 2007, Tian 2021], or as spatial multiplexing in optical telecommunications [Wang 2016, Wang 2011]. Non-linear localized state, also called localized structure in time and in space, holds interest for all optical information processing. They are light states where chromatic dispersion effect and non-linearity are balanced, leading to invariant propagation. Inside a laser system, they appear as addressable light peaks or holes.

The combination of spatial and temporal structuration is still a recent field: this thesis project aims to develop a laser system capable of intra-cavity generation of 3D structured light states in space, time, and polarization. Direct generation inside a laser cavity poses its own challenges, and we will address them. This

work took place at the *Institut d'Électronique et des Systèmes* (IES) together with the *Institut de Physique de Nice* (INPHYNI), the *Centre de Nanosciences et de Nanotechnologies* (C2N), and the *Universitat de les Illes Balears* (UIB) within the framework of the ANR BLASON. The manuscript is split into four main parts, each addressing one aspect of intra-cavity 3D structured coherent light generation.

First Part

The first part will serve to more precisely define the basics principles of light structuration in a laser system and contains a single chapter. We will define what is coherent 3D structured light. Review some existing systems achieving structuration on either the longitudinal or transverse dimension. We will also introduce some basics laser principle to define the targeted system specifications.

Second Part

The second part will focus on the semiconductor technology based active medium. More specifically, the Vertical external Cavity Surface Emission (VeCSEL) gain mirror design. It's separated into two chapters.

The first chapter consists of a general overview of the VeCSEL technology building blocks, from an integrated high reflectivity Bragg mirror to the design of mutiple quantum well (MQW) gain active region. Keeping in mind the need for a flat phase potential, we also focus on how to reduce parasitic phase effects such as thermal lensing and electronic lensing. We also cover the QW properties in the absorption regime for the design of a semiconductor saturable absorber mirror (SESAM).

The second chapter focuses on the two main designs (high gain structure and SESAM) used in this work. We will present the design choices in accordance with our targeted specifications. We will also present the first order characterization of the gain structure performances, as well as a complete characterization of the SESAM saturable absorption and carrier diffusion properties.

Third Part

The third part will focus on the optical cavity, and it's design for degenerated or modeless transverse emission. It is separated into two chapters.

The first chapter will describe the general concept of a stable optical cavity and its various transverse mode basis. We will also use this chapter to improve cavity specification for intra-cavity 3D light structuration.

The second chapter will go more, in depth, into the analysis of a self-imaging system used inside an optical cavity. The self-imaging cavity allows us to reach a transverse degenerated system. However, we will see that in this condition, high order wavefront distortion (4th order and higher) induced by the optical elements aberrations becomes the main limiting factor to achieve complete degeneracy.

Fourth Part

The concluding part will deal with experimental results obtained with the laser system, combining a semiconductor gain mirror, a self-imaging cavity and saturable losses. It is separated into three chapters.

In the first chapter, we will introduce a Maxwell-Bloch based theoretical model to support physical analysis of the system behavior. The model was inspired by the non-linear Schrödinger equation developed for time domain analysis of passive mode-locking systems. Additional local and non-local operators (high-order diffraction, anharmonic potential) and a matter equation for gain and losses saturation were added. With this model, we will observe the impact of local and non-local phase/amplitude perturbations on the 3D structured light emission.

The second chapter will serve as a description of modes topology observed in our laser system, without inserting the SESAM, and its non-linearity. We will classify three different regimes: the on-axis mode basis akin to Hermite-Gaussian or Laguerre-Gaussian modes, the off-axis mode basis akin to Bessel-Gauss and on axis guided Bessel modes, and the degenerated region where arbitrary wavefunction can be emitted.

The last chapter will focus on the non-linear system in the degenerated region with the saturable absorption mirror inserted. In this condition, we saw non-linear localization, and non-linear multiplexing, thanks to an absorbing meta-surface, creating sharp boundary condition or step like metallic waveguiding.

We analyze such behaviors with our physical model, and conclude on slow light behavior with quantum reflection of light particle as an analogy to quantum mechanics. We then conclude and discuss the next step to reach and control LB generation. We also show perspective applications such as 3D structured multiple frequency combs generations, or the multiplexing of Vortex modes.

Part I

From conventional laser to
non-conventional light structuration
in lasers

Motivation and basic principles of a laser and light structuration

1.1 What is structured light?

Laser emission is built up through physical processes such as stimulated emission in the gain medium and interferometry inside the laser resonator. The interplay between the optical cavity and the active medium will structure the light in its three observable (Degrees of freedom, see figure 1.1). In the paraxial approximation they are: the transverse axis (\vec{k}), the propagating/temporal axis ($Z(t)$) and the polarization axis (\vec{E}).

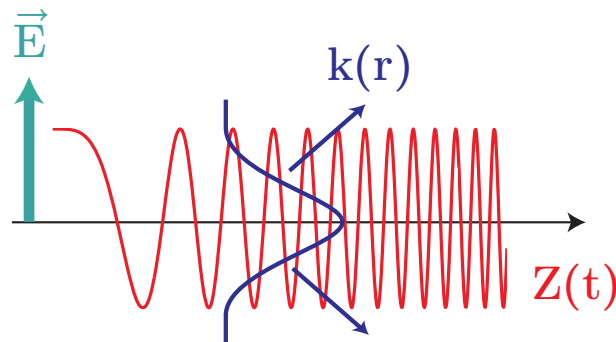


Figure 1.1: The three-light axis: Transverse (k), longitudinal (Z), and polarization (E)

In this context, structured light can be classified depending on the degree of complexity. A 3D coherent structuration refers to a \vec{k} and $Z(t)$ (spatio-temporal) complex light state. While intra-cavity means it takes place inside the laser system

during the laser emission build up and not outside through phase/amplitude shaping optical element.

1.1.1 Transverse structuration

Transversal structuration is related to the spatial aspect of the laser emission. Inside a laser system, this is closely related to the design of the optical cavity. Indeed, waveguided systems like laser diodes or fiber laser will not exhibit the same challenges for transversal structuration than free space optical cavities. We can classify those systems in three main categories, from the least to the most complex transversal structure.

- Fundamental TEM_{00} mode emission as in single transverse mode laser. Those systems are quite common and can find several applications. The usually good beam quality can be interesting for low divergence system such as LIDAR. The single transverse state can also help to limit temporal instability for continuous single frequency emission.
- Higher order discrete transverse mode emission from the optical cavity mode family. We find in such system, the “Vortex” laser [Seghilani 2016] using the Laguerre-Gauss transverse mode basis or diffraction-free laser beam using Bessel-Gauss mode basis [Uehara 1989].
- Transversally degenerate optical system. In this case, the mode separation is blurred, and any shape can be decomposed onto a linear combination of any mode basis. Self-imaging optical cavities are inherently diffraction free and a high number of simultaneous transverse modes operation is possible.

Figure 1.2 shows two examples of the use of a degenerate optical cavity for laser light structuration. The panels a) b) c) are from Knitter et al. [Knitter 2016] where the 4-f degenerate external system is used to provide coherent feedback onto the gain medium (semiconductor surface emission laser). The gain plane is imaged onto itself after one round-trip, allowing for any arbitrary eigenfunction to exist. They managed to control the number of transverse modes lasing using a pin-hole in the Fourier plane of the optical system (between the two lenses). This effectively reduced the spatial coherence of the laser. Panel a) shows the image of the gain surface and speckle image to measure coherence without any pinhole for high multimode operation (estimated at 1030 modes). Panel b) shows the same for a pin-hole of 80 μm diameter for a couple of transverse mode operation. They gained an order of magnitude on the speckle imaging contrast between the two, reaching the human eye limit of the speckle-perception. Using this controllable coherence, they managed to improve the quality of flow imaging by combining speckle with

speckles free imaging technics [Cao 2019]. However, they point out that the number of simultaneous transverse mode operation was lower than predicted. Due in part to perturbative effects of the optical system, such as lens aberrations or thermal lensing.

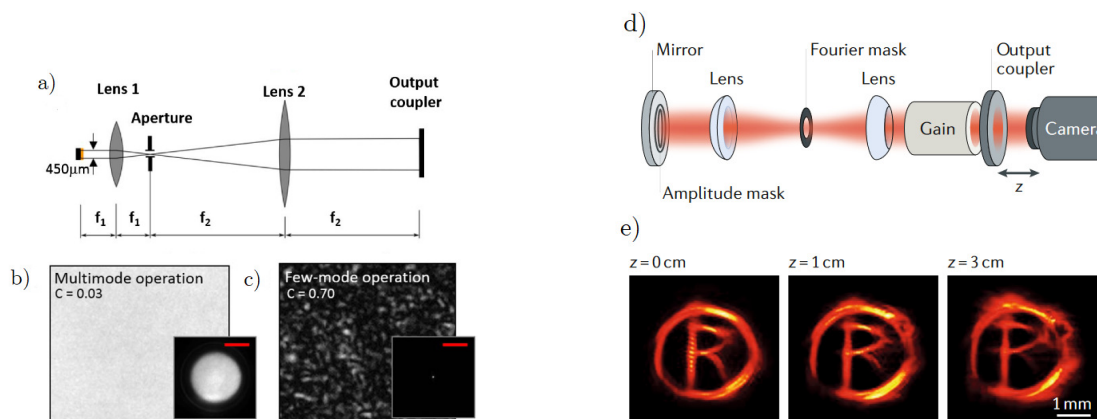


Figure 1.2: a), b), c) Spatial coherence switching for degenerate multimode VECSEL [Knitter 2016]. a) Self-imaging cavity set-up with a controllable diaphragm. b) Generated speckle and transverse profile for low coherence/high number of modes. c) Generated speckle and transverse profile for low coherence/low number of modes. d) and e) Modified degenerate cavity laser for invariant laser beam propagation [Chriki 2018]. d) Experimental set-up with amplitude mask and Nd:YAG gain medium. e) Generated laser profile at different position extra-cavity.

The panel d) and e) of figure 1.2 display the experiment of Chriki et al. [Chriki 2018] where they set out to use the same type of degenerate optical cavity for propagation invariant shaped laser beam generation. In their case, the gain was provided by a 11 cm long Nd:YAG rod. Using an amplitude filtering mask on the end-mirror to shape an arbitrary field and on the system Fourier plane to filter spatial frequency, they managed to decompose the near field shape onto a Bessel-Gauss mode basis to generate a propagation invariant beam over 37 mm. The use of a long ND:YAG rod compared to a delta-like semiconductor gain region, limits their achievable resolution through NA limitation.

1.1.2 Longitudinal structuration

The longitudinal structuration is related to the temporal aspect. In this manuscript and most of the literature, the longitudinal direction is always taken as the field propagation direction and is thus related to the temporal evolution seen

in space. Different temporal behavior can be thought of longitudinal structuration and classified into two main categories with increasing complex structure:

- The continuous wave regime, where no coherent structuration of the temporal envelope exists. The laser emits a field with a constant amplitude with a narrow spectral width. Usually, in this regime, single frequency operation is desired for many types of application from Optical metrology to high-resolution spectroscopy or optical telecommunication. Despite its apparent simplicity, creating a continuous wave single frequency laser system is not always easy to implement. A lot of care is needed to select a single longitudinal light state such as dispersion control [Chomet 2019] or an intra-cavity frequency selection element such as a Fabry-Perot etalon [Collins 1963] or a diffraction grating in DFB laser [Kogelnik 1972]. Some gas lasers such as He-Ne take advantage of the narrow gain bandwidth with a reasonably size cavity to select a single light state [Baird 1965], the same way semiconductor vertical cavity surface laser emission works [Koyama 1989].
- The pulsed regime, where the laser emits a series of pulses. Temporal dynamics of laser emission have long been studied, and the multimode instability of laser emission understood through several factors. The amplified spontaneous emission induced modes hopping in wave-guided laser [Pedaci 2005], spatial hole burning effect in standing wave cavity [Kimura 1971] or spectral hole burning in inhomogeneously broaden gain. To generate a fixed temporal structure, one needs an external force to create a phase relationship between several co-existing longitudinal modes. Those systems are also called mode-locked laser [Haus 2000]. This can be achieved either by an active scheme with an optical modulator synchronized to the cavity repetition rate [Hargrove 1964] or a passive one with a saturable absorber opening a small temporal gain window [Ippen 1972].

Several mechanisms exist to shorten the generated pulse width for passive mode-locking (PML), mainly using soliton mode-locking, where the cavity dispersion is managed to compensate the pulse self-phase modulation. The panels d) and e) of figure 1.3 show an example of a 477 fs pulse width inside a broadband surface emitting semiconductor laser coupled to a saturable semiconductor mirror (SESAM). The micro-cavity anti-resonant design allows for broad gain bandwidth and high saturation fluence of the gain. It also reduces the structure dispersion to a small range of 900 fs^2 to 0 fs^2 around the max gain position. They showed a pulse width reduction from 1.15 ps to 477 fs when tuning the laser emission from 1035 nm to 1045 nm, thus also tuning the wavelength dependent GDD from 1000 fs^2 to 250 fs^2 . The pulse also changed from a Gaussian envelope to a sech-squared one. The

shortening occurs in the region where SPM effect from the SESAM and Gain is balanced with the cavity dispersion. Semiconductor PML laser is a choice for small and integrated system with high repetition rate (small cavity). However, for ultra-short pulses formation ($< 100 \text{ fs}^2$) solid state laser based on Ti:sapphire remains the best option [Keller 2003].

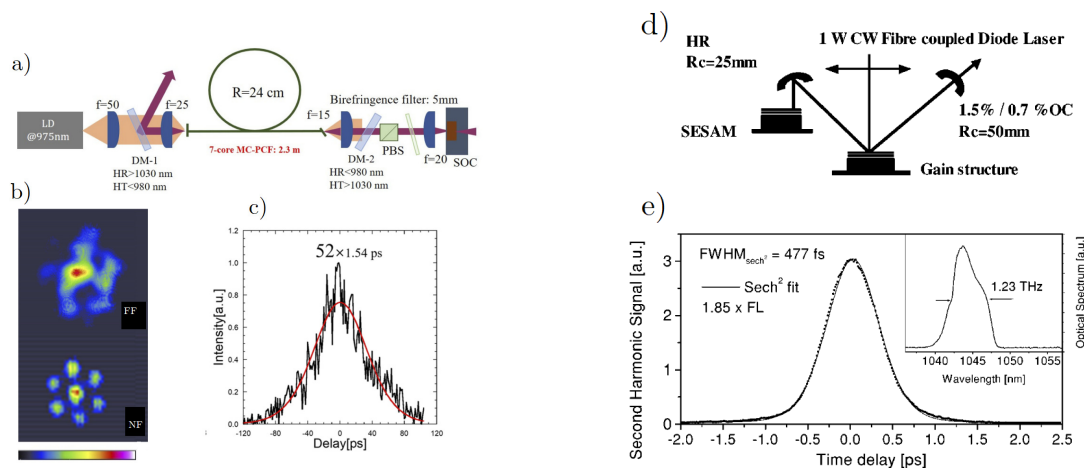


Figure 1.3: a), b), c) Phase-locked and mode-locked multicore photonic crystal fiber laser with a saturable absorber [Kawamura 2021]. a) Cavity setup. LD: laser diode, DM: dichroic mirror, PBS: Polarizing Beam Splitter, SOC: Saturable Output Coupler. b) Far-field profile and near-field profile in mode-locked operation. c) Autocorrelation trace at 24 W excitation. d), e) Sub-500-fs soliton-like pulse in a passively mode-locked broadband surface-emitting laser [Garnache 2002]. d) Experimental setup: OC output coupler; HR high reflector. e) Femtosecond pulse operation with GDD 250 fs^2 : autocorrelation and optical spectrum (inset). The average output power is 100 mW at a repetition rate of 1.21 GHz.

Fiber laser also has several properties making them interesting for PML pulse generation, such as large gain bandwidth and high gain efficiency. However, some performances (high power) are limited by the strong non-linearity. Photonic crystal fiber using photonic band gap guiding instead of optical index gradient can be a good solution thanks to the large effective mode size or dispersion control. They also can be designed for multicore operation, thus combining transverse and longitudinal structuration. The panels a), b) c) of figure 1.3 show a recent development in multicore photonic crystal fiber. They demonstrated a transverse phase-locked and longitudinal mode-locked laser using Yb-doped 7-core MC-PCF and a semiconductor saturable absorber placed in the near-field inside a resonator (panel (a)). Panel b) shows the 7-spot phase locked output of the PML laser and

panel b the 42 ps resulting pulse width. In this configuration, it is possible to increase the average power compares to a single core system.

1.1.3 Localized structure

Localized structure (LS) is a non-linear complex object deserving of its own special category. In the general physical concept, when an extended system (i.e., not ruled by boundary condition) exhibits non-linearity and dissipative forces, a self-organized pattern can evolve from a homogeneous initial condition [Turing 1952]. A localized structure is then defined as the connection from one homogeneous state to a piece of the self-organized pattern state (see figure 1.4). Those systems have been observed spatially, in colloidal suspensions under vibrations [Lioubashevski 1999], ferrofluids [Richter 2005] and in liquid crystals [Ramazza 2003] to cite a few.

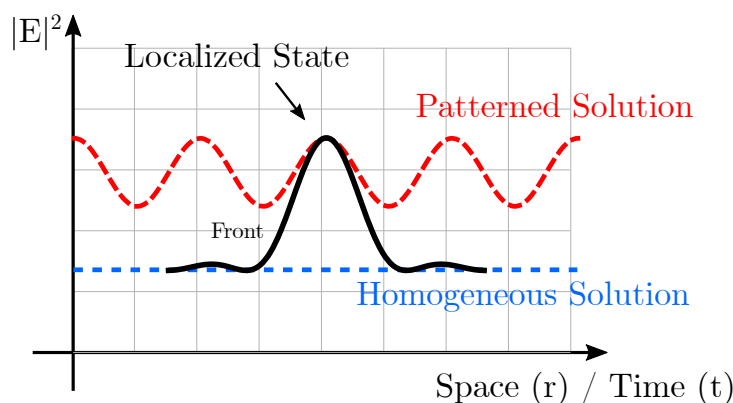


Figure 1.4: Representation of a localized structure as the connection between a homogeneous state and a pattern state in time or space.

In optics, the same process can lead to pattern formation from the interplay of diffraction and non-linearity provided that we are in an extended system (i.e., the correlation range of the LS is small compared to the size of the system). In a passive system, the homogeneous solution can be provided by a coherent driving beam [Grynberg 1988] or coherent feedback [Ackemann 1994], while in an active system the pattern arises from spontaneous emission [Arecchi 1995]. They will appear as independent peaks of intensity. The nature of their formation makes them bi-stable solution from “Off” (only the homogeneous solution) to “On” (intensity peak connection the homogeneous and pattern solution). In addition to their independent nature, the bi-stable behavior makes them interesting for applications such as all-optical information processing, or optical memory buffer [Gibbs 2012] by addressing an array of LS to store information using them as an optical bit. They can exist in both the spatial and temporal area of a laser system.

1.1.3.1 Spatially localized structure

For spatially localized structure (SLS) in an active system, we must have a large transverse aspect ratio to fulfil the extended system condition. The use of a degenerate optical system allows having an optical cavity with a high Fresnel number, meaning a large aperture compared to the optical structure size.

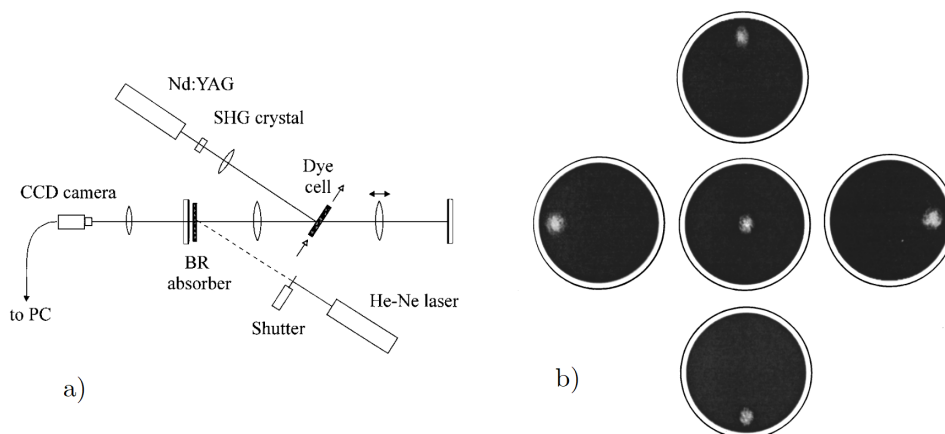


Figure 1.5: a) Self-imaging cavity for SLS generation using dye gain and absorber medium placed at in Fourier conjugate plane. b) Positioning of the SLS initiated by an external beam in different places of the laser cross-section (the region inside the dark circle is 2.7 mm in diameter.) [Taranenko 1997].

Active SLS was demonstrated by Taranenko et al. [Taranenko 1997] using a 4-f self-imaging optical system coupling a dye gain medium and a dye saturable absorber in each other Fourier plane. Figure 1.5 displays the set-up. The use of a slow lifetime saturable absorber tuned to the emission wavelength of the gain created an optical bi-stability. This allowed them to generate a single SLS by locally saturating the saturable absorber using a He-Ne laser. Figure 1.5 also shows the transverse intensity profile onto the saturable absorber of the SLS at different positions. They showed that the SLS could be generated over a large area depending on the position of the injected beam. Their system was limited to only a single SLS at a time due to the gain being placed at the Fourier plane of the SLS emission. Positioning the gain and absorber in the conjugate image plane could solve this issue. However, this placement was chosen to have sufficient gain to generate the SLS, which would not be possible otherwise.

Later, another demonstration of active SLS was made by Genevet et al. [Genevet 2008] inside an 8-f self-imaging cavity (see figure 1.6). By using two broad-area electrically pump vertical cavity surface emission laser (VCSEL), one in the gain and the other in the absorption regime, they managed to have enough

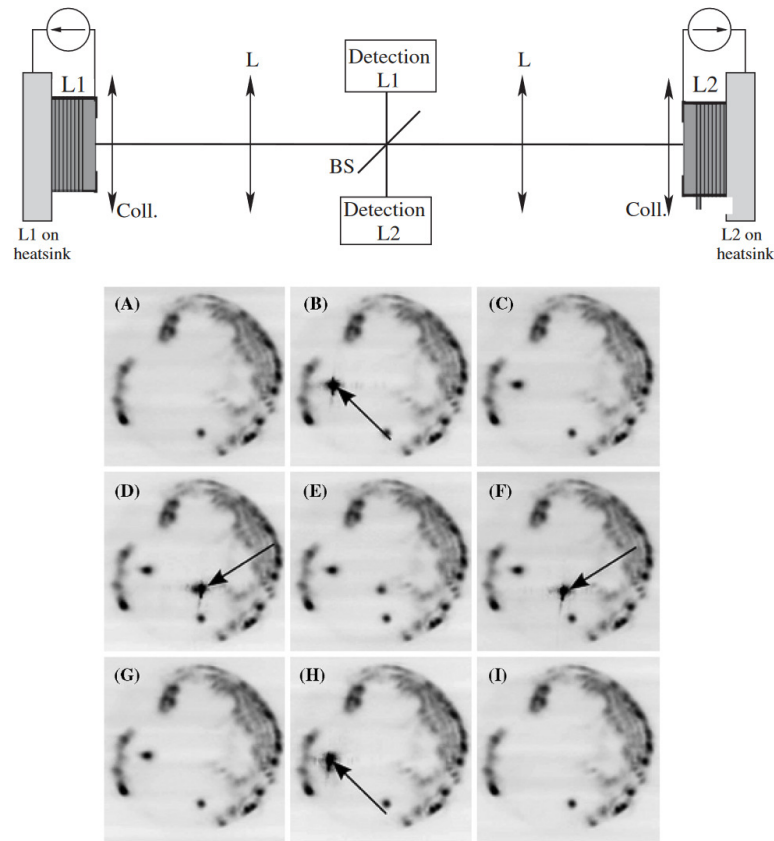


Figure 1.6: (Top) Schematic drawing of the experiment. L1: Laser above the transparency, L2: Laser below the transparency, BS: beam splitter. L1 and L2 were placed in conjugate image plane. (Bottom) Near-field intensity distribution on L1. Dark areas correspond to high intensities. Sequence of successive switching of two independent structures with an incoherent writing beam [Genevet 2008].

optical gain to place them in the conjugate image plane of the optical system. Using this set-up, they demonstrated multiple SLS when the wavelength emission of the one used for Gain was correctly tuned to the absorption resonance of the other. As with Taranenko, individual addressing of the multiple SLS was possible using a laser to locally saturate the absorption. This demonstration using semiconductor technology inside a self-imaging system is important since it opens the way to an eventual 3D structuration (adding temporal pulses). Indeed, semiconductor saturable absorber mirror (SESAM) are commonly used for PML system.

However, both Taranenko and Genevet system in their current state do not possess the ability of temporal structuration. For Taranenko, the saturable absorber lifetime is too slow to be considered for a PML system. For Genevet, the timescale

of the gain medium and saturable absorber were too close to observe stable PML.

1.1.3.2 Temporally localized structure

For PML operation, the saturable absorber opens a net gain window around a pulse. To then achieve an extended system, the time between two consecutive pulses must be large enough so both the gain and absorber recovers fully before the next pulse, leading to a decoupling of the pulses. This can be summarized by saying that for temporally localized structure (TLS) in an active system, the round-trip time must be larger than the matter recovery time.

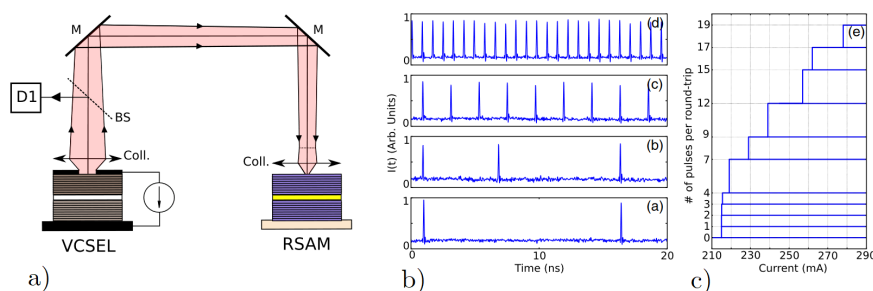


Figure 1.7: (a) Experimental setup. VCSEL and SESAM thermally stabilized. BS: output coupling beam splitters, M: mirrors, Coll: aspheric lenses. b) Different number of pulses for the same parameters of the system, revealing multi-stability. c) Staircase in terms N when changing the current injection of the VCSEL.

Following the SLS experiment by Genevet, Marconi et al. [Marconi 2014] has demonstrated experimentally and theoretically the existence of TLS from a PML scheme in semiconductor laser. Figure 1.7 shows the set-up used for this demonstration. A VCSEL used in the gain regime was coupled through a long external cavity to a VCSEL used in the absorption regime. To ensure a good saturation ratio for PML operation, the cavity was made to focus the full transverse gain emission onto a small point inside the absorber. They then demonstrated multi-stability between several PML solutions with different number of pulses per round-trip. They also showed that those pulses can be individually addressable by an electrical perturbation [Camelin 2017]. In this configuration, however, no complex spatial structuration could be achieved since the optical system exhibited a small Fresnel number.

To address these issues, work to combine the High Fresnel number and long round-trip time is underway in the hope to generate a spatio-temporal localized structure also called “Light bullet” (LB). In a passive system, a first observation of LB was made by Minardi et al. [Minardi 2010] in an array of evanescent coupled single mode fiber. The LB were observed for a few millimeters of propagation

when a high-power femtosecond pulse was injected at the center waveguide. In active system, it has been theoretically shown possible by J. Javaloyes and S. Gurevich [Gurevich 2017, Javaloyes 2016]. Controlling the diffraction in a TLS system evolved from PML could lead to LB addressable by an external optical pulse.

1.1.4 Motivation

This thesis motivation was to design and optimize a laser system capable of complex spatial and temporal structuration. The aim of this laser system is then to combine SLS and TLS into the spatio-temporal Light Bullet. To achieve this goal, we must keep in mind the high Fresnel number condition for a spatially extended system and long cavity condition for a temporally extended system. The optical cavity must not be the driving force behind the transverse light structuration, and some work needs to be done to design and better understand such a system. At the same time, a gain and saturable absorber medium compatible with PML operation must be used.

The work in this thesis was done in collaboration between the IES and INPHYNI laboratories within the framework of the ANR BLASON. Demonstration of a non-linear pattern TLS inside a self-imaging optical cavity was already done by Bartolo [Bartolo González 2022] in the INPHYNI. This thesis will focus more on the active medium and optical system design, as well as the transversal structuration topology.

1.2 EM-wave propagation

To better understand the different processes of structuration inside a laser system, we will first start by describing what is the propagating field. The laser emission is a coherent electromagnetic field. We can write it for a paraxial wave as:

$$\vec{\mathcal{E}}(x, y, z, t) = \Re [U(x, y, z, t).e^{-i\omega_0 t + ik_z z} \cdot \vec{x}] \quad (1.1)$$

Where $U(x, y, z, t)$ represents the complex, slowly varying amplitude of the electric field projected on the polarization axis defined by the unit vector \vec{x} . The term $e^{-i\omega_0 t + ik_z z}$ represents the fast propagation factor in time ($\omega_0 t$) and space ($k_z z$) of the beam. In this case, the wave propagates in the $z > 0$ direction. The description above is true in the semi-classical description of the laser, where the field or photons are described using the Maxwell equations and the light-matter interaction is described with the Bloch equation using quantum properties of the electron-photon interactions. It is justified given the number of photons at play inside a laser cavity ($> 10^{16}$ photon/s) where photon quantum fluctuation can then be neglected.

The field possesses three observable (Degrees of freedom, see figure 1.1) and can be structured along all of them, the transverse axis (\vec{k}), the propagating/temporal axis ($Z(t)$) and the polarization axis (\vec{E}). The transverse profile evolution along propagation represents the spatial structuration. A Gaussian profile is a good description for a simple spatial structuration. The fast temporal evolution describes the oscillating frequency of the EM field, while the slow varying envelopes can be part of the longitudinal structuration. The polarization axis describes the direction of oscillation of the EM wave. All those aspects can be controlled by the main constituents of a laser system, meaning the optical cavity and the active medium, with its linear and non-linear response in space-time.

1.2.1 Traveling wave model

We take an EM field propagating along the z axis, and diffracting transversally in a homogeneous medium. The on-axis z energy-momentum dispersion relation is (light line) $\omega_0 = v_g k_0$ and $v_0 = c/n$. The propagation of such a field can be described by the second order wave equation derived from the Maxwell equations:

$$\nabla^2 E - \frac{1}{v_g^2} \frac{\delta^2 E}{\delta t^2} = 0 \quad (1.2)$$

Where E is the 3D electric field describing the electric field under the Slow Varying Envelope Approximation (SVEA) and the paraxial approximation as in equation 1.1. It is possible to reduce the second order wave equation into a first order one. The SVE approximation means that the time envelope of the EM field varies slowly compared to the field oscillation, thus the time's second order derivative can be ignored. In the same way, the paraxial approximation means that the spatial envelope of the EM field is slowly varying along the propagation direction, thus second order derivative along the propagation direction can be ignored. We end up with the scalar paraxial wave equation for the complex field amplitude:

$$\frac{\delta U}{\delta t} + v_g \frac{\delta U}{\delta z} = i \frac{v_g}{2k_0} \nabla_{\perp}^2 U \quad (1.3)$$

We can add a NL source term in a Maxwell-Bloch equation system (matter polarization vector aligned with light polarization vector, on the right-hand side of wave equation), assuming a slow varying envelope too, and slow matter approximation (compared to coherence time of dipole and optical frequency):

$$P = \epsilon_0 \chi(x, y, z, t) E \quad (1.4)$$

and thus for the complex amplitude:

$$p(x, y, z, t) = \epsilon_0 \chi(x, y, z, t) U(x, y, z, t) \quad (1.5)$$

We must add a physical space-time differential equation (carrier dynamics plus spatial diffusion) to include matter dynamics through $\chi(x, y, z, t)$ (active medium), if slow compared to other physical variables. We can write the travelling wave Maxwell-Bloch equation of motion:

$$\frac{\delta U}{\delta t} + v_g \frac{\delta U}{\delta z} = i \frac{v_g}{2k_0} \nabla_{\perp}^2 U + i \frac{\omega_0}{2n^2} \chi(x, y, z, t) U \quad (1.6)$$

where $U = U(x, y, z, t)$ is the SVE amplitude of the field, $\nabla_{\perp}^2 = \frac{\delta^2}{\delta x^2} + \frac{\delta^2}{\delta y^2}$ is the transverse Laplacian operator and $k_0 = \omega_0/v_g = \sqrt{k_z^2 + k_x^2 + k_y^2}$ is the wavenumber. The left-hand side describes longitudinal propagation of the field and the right-hand side the transverse propagation or diffraction through a homogeneous non-linear medium. To obtain a set of spatio-temporal equations of motion of light and matter for a CW or quasi-CW wave, we can discard the fast time dynamics compared to space dynamics:

$$\frac{\delta U}{\delta t} \ll v_g \frac{\delta U}{\delta z} \quad (1.7)$$

We can define a slow time along z propagation as $T = z/v_g \gg t$, and end up with a NL Schrödinger like equation of motion or Helmholtz like equation without source terms:

$$i \frac{\delta U(x, y, T)}{\delta T} = -\frac{v_g}{2k_0} \nabla_{\perp}^2 U(x, y, T) - \frac{\omega_0}{2n^2} \chi(x, y, z, t) U \quad (1.8)$$

Note that a similar set of equations holds for short temporal dynamics for ultrashort pulse, where $\frac{\delta U}{\delta t} \gg v_g \frac{\delta U}{\delta z}$, like for mode-locking instead of CW wave. This would be schematized by local and/or non-local inhomogeneity in a stacked medium with various complex phase/amplitude transfer function and unitary matrix boundary conditions (no reflection, for example). The same could be done for complex optical systems where a stacked medium with unity boundary condition could represent free space propagation, lens transfer function, high order diffraction or diffusion (Fourier space). Figure 1.8 describes this sort of complex system.

For the inhomogeneous system, we should integrate equation 1.8 over each medium. However, we will see later in the manuscript a way to simplify this complex system if the inhomogeneous propagation effect (gain, losses, filtering, higher order diffraction) is having a small impact on the field for each pass. For this, the Fourier description of the field will be of use.

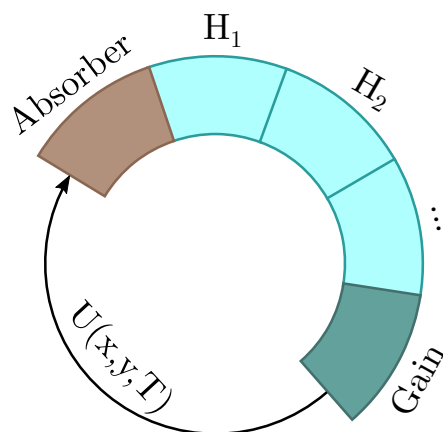


Figure 1.8: Simplified schematic for a travelling wave model optical cavity with non-homogeneous medium

1.2.2 Fourier optics

From the previous equation 1.3, separating the time and space dependencies of the field, $U(x, y, z, t)$ we arrived at the spatial Helmholtz equation. One natural solution to this system is a plane wave:

$$U(x, y, z) = U_0 e^{i(\beta_x x + \beta_y y)} \cdot e^{\pm iz \sqrt{k_0^2 - k_x^2 - k_y^2}}. \quad (1.9)$$

Where $\beta_{x,y} = k_0 \sin(\theta_{x,y})$ represent the projection of the wavevector along its transverse components due to an angle with the z-axis direction. Any field in $z = 0$ can then be described as a superposition of weighted plane waves of different propagating directions [Goodman 2005].

$$U(x, y, 0) = \iint_{-\infty}^{+\infty} \tilde{U}(f_x, f_y; 0) e^{i2\pi(f_x x + f_y y)} df_x df_y \quad (1.10)$$

This equation is simply the 2D inverse Fourier transform, where $\tilde{U}(f_x, f_y; 0)$ describes the complex amplitude of the plane wave component or the angular spectrum of field $U(x, y, 0)$ [Clemmow 1966]. The variables $f_{x,y} = \beta_{x,y}/2\pi$ are the spatial frequencies related to the direction cosine of the individual plane waves. It essentially corresponds to the EM field in the Fraunhofer region, sometime referred to as Far-field [Born 2000].

To compute the field at a position, z one can simply multiply the angular spectrum of the field at $z = 0$ by a complex transfer function $H(f_x, f_y)$ before applying the inverse Fourier transform.

$$U(x, y, z) = TF^{-1} \left[\tilde{U}(f_x, f_y; 0) \cdot H(f_x, f_y) \right] \quad (1.11)$$

For free space propagation:

$$H(f_x, f_y) = e^{\pm ik_0 z \sqrt{1 - (\lambda f_x)^2 - (\lambda f_y)^2}} \quad (1.12)$$

Provided that $\sqrt{(\lambda f_x)^2 + (\lambda f_y)^2} < 1$. Simplifying the transfer function along the Fresnel approximation which is equivalent to the paraxial one [Grella 1982] we find:

$$H(f_x, f_y) = e^{\pm ik_0 z} e^{i\pi \lambda z (f_x^2 + f_y^2)} \quad (1.13)$$

Which is the exact transfer function of the Fresnel diffraction integral [Born 2000]. The constant phase term expresses the accumulated phase during propagation by all plane waves. The parabolic term expresses the phase shift of the different plane wave from the on-propagating axis one due to the angled emission. In the spatial frequency space under paraxial approximation, EM field propagation or diffraction is equivalent to a parabolic phase term with constant amplitude. Any optical system, including aperture, optical components, and aberrations, can be described by its transfer function in Fourier space as the way it affects the plane wave distribution. And any EM field can be described as an amplitude and phase function in Fourier space. In the field of optical imaging, scalar diffraction theory combined with Fourier optics are an important part of the understanding of propagating and imaging EM field [Gu 2000]. It also allows expressing non-local effects such as diffraction as simply as a phase potential in the far-field region.

This vision allows us later in the manuscript to simplify the general form of the structure travelling wave mode in figure 1.8 to an equation describing the transverse field variation for each round-trip while considering higher order non-local diffraction effect.

1.3 Optical cavity structuration

In a laser system, the first method we have to create a transverse and longitudinal field structuration is through the optical cavity. An optical cavity being defined with two end mirrors reflecting the EM wave, we will have a superposition of a propagative wave ε^+ and a contra-propagative wave ε^- . This superposition discretizes the available light state through wave interferences in the longitudinal/propagation space. Similarly, it will define a transverse mode basis (transverse profile of the EM field) though boundary condition of the system. This is the first way to structure the light, and it is important to understand its behavior.

1.3.1 Quantum mechanic analogy

A simple analogy with quantum mechanic theory can be made to express the dispersion of an optical system. In one dimension (the propagation direction z), for a simple linear cavity composed of two infinitely large mirrors separated by a distance L_c and 100% reflection a field propagating in the $z > 0$ and $z < 0$ will form a standing wave pattern following a sinusoidal wavefunction for one dimension:

$$U(z, t) = A(t) \sin\left(n \frac{\pi}{L_c} z\right) \quad (1.14)$$

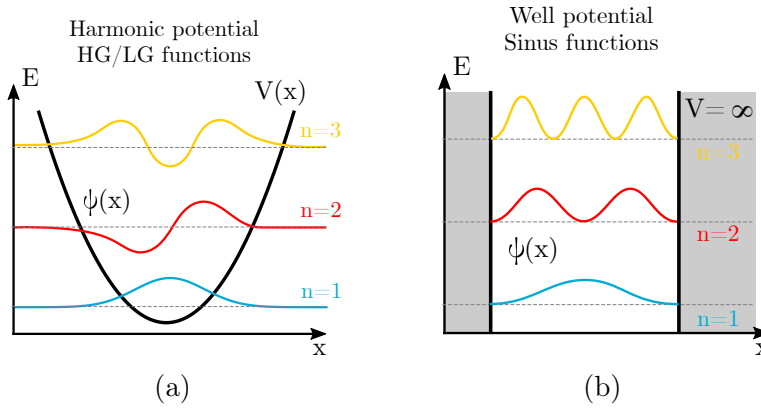


Figure 1.9: Schematic comparison between a parabolic potential with HG/LG wavefunction and an infinite potential well with sinusoidal wavefunction.

In this case, the possible longitudinal wavevector has been discretized such that $k_z = n \frac{\pi}{L_c}$ with the dispersion relation $\omega_n = k_z c = n \frac{\pi}{L_c} c$. Only EM field with photon energy $E_n = \hbar \omega_n = n \pi \frac{\hbar c}{L_c}$ can exist in this system. In quantum mechanics, this problem is similar to the particle of mass m in a box. In 1D, the particle is trapped inside an infinitely high potential well of width a . Solving the 1D time-independent Schrödinger equation gives a discrete energy levels as $E_n = \frac{n^2 \hbar^2}{8ma^2}$.

In both cases, the computed wavefunction is the same and is of the sinus mode family (see eq 1.14). Figure 1.9b shows the equivalent representation of the discrete wavefunction for both the linear cavity and the potential well. In the case of a parabolic potential, in quantum mechanics we found the discrete Hermite-Gaussian (HG) or Laguerre-Gaussian (LG) wavefunction family which also corresponds to the transverse mode profile of a diffractive spherical cavity. A potential well in quantum mechanics corresponds in optics to the sinusoidal longitudinal modes, while a parabolic potential in quantum mechanics corresponds to the transverse mode wavefunction of a diffractive spherical cavity in the paraxial approximation. Generalizing in three dimensions, we have the Schrödinger equation:

$$-i\hbar\frac{\delta}{\delta t}\psi(\vec{r}, t) = -\frac{\hbar^2}{2m}\nabla^2\psi(\vec{r}, t) + V(\vec{r}, t)\psi(\vec{r}, t) = E\psi(\vec{r}, t) \quad (1.15)$$

where \vec{r} is the 3D spatial coordinate and $\psi(\vec{r}, t)$ the wavefunction describes a quantum particle. The total energy of the particle is then a function of the Hamiltonian operator $H = -\frac{\hbar^2}{2m}\nabla^2 + V(\vec{r}, t)$ describing the kinetic and potential energy. Here V describes a step like potential where the boundary conditions are $V = \textit{infinity}$ for $x \leq 0$, $x \geq a$ and zero elsewhere. For the EM field in 3D, we can use equation 1.8 with the $T = z/c$ slow time approximation in the linear case (no source terms and no potential) to get an eigenvalue Helmholtz equation:

$$i\frac{\delta U}{\delta T} = H_{op}U = \Omega U \quad (1.16)$$

where the optical cavity Hamiltonian, describing the wave kinetic energy, is defined as:

$$H_{op} = -\frac{v_g}{2k_0}\nabla_{\perp}^2 \quad (1.17)$$

By analogy with the Schrödinger equation, we see a relationship with the optical cavity Hamiltonian, such as $H_{op}\cdot\hbar \equiv H = -\frac{\hbar^2}{2m}\nabla^2$. In this case, the energy represents the wave pulsation. The kinetic energy is analogous to the wave diffraction and the potential energy to the wave-matter interaction. Assuming a transverse plane wave, we find two dispersion relationships for the longitudinal (propagation) direction and the transverse direction in a homogeneous medium:

$$\frac{E_z}{\hbar} = v_g k_z \quad \text{and} \quad \frac{E_{\perp}}{\hbar} = \frac{v_g \beta^2}{2k_0} \quad (1.18)$$

with β being the transverse wavenumber. By analogy with the quantum Hamiltonian, we can define the equivalent particle mass of the transverse wave packet for a harmonic optical cavity as:

$$m_p = \hbar k_0 / v_g \quad (1.19)$$

In an optical cavity, the transverse and longitudinal dispersion relationship will be discretized along a sinusoidal basis for the longitudinal part and an HG/LG basis for the transversal part of a harmonic cavity (i.e., non-local parabolic band structure from diffraction). Our goal will be to design and engineer the local (real space) and non-local (Fourier space) potential to transversally degenerate the system. This is equivalent to having an infinite optical particle mass (flattening the band structure). From this, we hope to generate arbitrary transverse wavefunction of a non-linear spatially localized structure.

1.4 Light amplification

Since the prediction of the stimulated emission process in an excited atom by A. Einstein [Einstein 1917], the field of lasers and light amplification has been born. Thus, any medium consisting of a collection of excitable atoms can become the basis for light generation. Light-matter interaction also plays a critical part in shaping the laser light state. Describing the general concept is a first step to understand its effect. We can express the Non-linear medium polarization as:

$$P = \epsilon_0 (\chi^{(1)}E + \chi^{(2)}E^2 + \chi^{(3)}E^3 + \dots) \quad (1.20)$$

The polarization describes the response from an electric field of the medium that can be linear (first term only) or non-linear (higher-order terms). In the polarization equation the χ^n terms are the electrical susceptibility parameters of the medium which describe its properties.

By describing the medium using the classical electron oscillator model that simply describes the atomic transition of an excited atom, we can write the electric susceptibility [Siegman 1986]:

$$\chi(\omega, \Delta N) = i \frac{\lambda}{2\pi} \frac{\Delta N}{1 + i(2(\omega - \omega_a)/\Delta\omega_a)} \quad (1.21)$$

where ΔN is the population inversion (difference of the number of atoms in the excited state and fundamental state) in atoms/cm³, ω_a is the transition linewidth and σ the transition cross-section in cm²/atoms. This susceptibility is a complex quantity following a Lorentzian resonance shape and is characteristic of many real atomic transitions. The imaginary part is then proportional to the material gain of the medium in cm⁻¹, while the real part is proportional to the refractive index.

$$g(\omega, \Delta N) = -\frac{2\pi}{\lambda} \text{Im}(\chi(\omega, \Delta N)) \quad (1.22)$$

Figure 1.10 shows the shape of the imaginary part of the transition susceptibility for a single resonance frequency, this is called a homogeneous gain. However, in a real system, a small random shift of the transition frequency of each atom leads to an inhomogeneous gain broadening where the total response of the medium is due to the effect of all the smaller individual responses.

Another important parameter being the transition cross-section σ characterizing the strength of the transition and written as [Siegman 1986]:

$$\sigma = \frac{\lambda_a^2}{4\pi} \frac{\gamma_e}{\Delta\omega_a} \quad (1.23)$$

with λ_a the transition wavelength and γ_e the decay rate of the population inversion. A large transition cross-section means a small lifetime of the upper level,

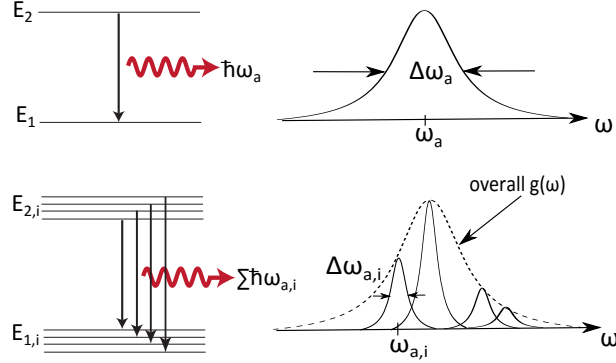


Figure 1.10: Homogeneous (top) and inhomogeneous gain (bottom)

which impedes the population inversion. As the population difference increases with the pumping, the optical response of a homogeneous atomic transition will saturate when the saturation intensity I_s is reached. This saturation intensity is given by:

$$I_s = \frac{hc \gamma_e}{\lambda \sigma} \quad (1.24)$$

To obtain a large gain with a low saturation intensity, one can use a medium with a large transition cross-section. The required population inversion for a given gain is then smaller. On the other hand, with a small cross-section, small saturation intensity can be reached with a long upper level lifetime, but it will require a higher population inversion.

This simple model does not take into account possible non-linearity response that can arise for an intense electric field. These effects can be described by the higher order susceptibility $\chi(n)$. The most common ones being the second $\chi(2)$ and third order $\chi(3)$ ones. Second-order non-linearity is mainly interesting for the harmonic generation or optical parametric amplification. This effect is found only in certain specific crystals with non-centrosymmetric arrangement, such as KDP or quartz. Third-order non-linearity is present in fast gain medium compared to temporal waveform and gives rise to four wave mixing or the optical Kerr effect. The Kerr non-linearity is an intensity dependent refractive index leading to self-phase modulation (SPM) for example.

$$n = n_0 + n_2 I \quad \text{and} \quad n_2 = \frac{3}{4n_0^2 \epsilon_0 c} \chi^{(3)} \quad (1.25)$$

where n_2 is known as the non-linear refractive index. A representative value for the optical Kerr effect in a typical glass (such as might be used in an optical fiber) is $n_2 = 10^{-16} \text{ cm}^2/\text{W}$.

1.5 Technologies overview

A variety of gain medium technologies exist and are used to create a laser system. The choice of a given material over the other is made according to the desired application and properties needed. This can range from the wavelength option, output power capability, manufacturing cost and other considerations.

1.5.1 Solid state medium

This category encompasses mediums where active ions are introduced into an otherwise transparent host matrix at the ion transition wavelength, usually glass or other crystal. The most commonly used dopant are rare-earth ions such as Neodymium (Nd^{3+}), Ytterbium (Yb^{3+}) or Erbium (Er^{3+}) for near infra-red application. The resulting medium can take the form of cylindrical glass rod or cuboid and is even used as the core in optical fiber either for fiber laser or simple optical amplifier.

To generate the required population inversion, only an optical pumping method is used, usually from a laser diode with matched emission to certain pumping transition. Solid state laser exhibit low emission cross-section ($\sim 10^{-20} \text{ cm}^2$) but can compensate by using long interaction distance to reach high effective gain as in the Erbium doped fiber amplifier. They also have a long lifetime from μs to ms making them suitable for Q-switch operation.

1.5.2 Gas medium

Various gases can also be used as gain mediums. Although they have some characteristics in common – low densities, high robustness, heat transport by convection, energy input via an electrical discharge and short (nanosecond) upper-state lifetimes – their properties are extremely diverse in some respects.

The first gas laser was a mixture of helium and neon that offers not only the well-known 632.8-nm transition, but also various other transitions in the green, yellow, orange and infrared regions. Laser operation requires only quite moderate current densities, but is limited to relatively low output powers.

Carbon dioxide molecules are very different, not only because of the long emission wavelength around $10.6 \mu\text{m}$; in CO₂, molecular vibrations play a crucial role for the laser process, which occurs at much higher current densities. Output powers can be many kilowatts, and power efficiencies above 10 percent are possible.

Argon-ion lasers (and, similarly, krypton-ion lasers) are also operated at very high-power densities. Their efficiencies are far lower than those of CO₂ lasers, on the order of 0.1 percent. In earlier times, the low efficiency and limited lifetime of the expensive tubes (a few hundred hours) often had to be accepted, as there

was no alternative; for example, for pumping a Ti:sapphire laser. Nowadays, frequency-doubled diode-pumped lasers are often used instead of argon-ion lasers.

1.5.3 Dye medium

Laser dyes consist of organic molecules, which in most cases are contained in a liquid solution. (Users often make them by dissolving dye powders in some solvents.) The optical transitions of dyes are relatively broad: tens of nanometers or more – roughly comparable to those of ion-doped glasses – resulting in good wavelength tunability. A big difference between dyes and ion-doped glasses, however, is that these transitions in dyes are not forbidden; they exhibit large transition cross-sections, and the upper-state lifetime is correspondingly short (a few nanoseconds). Particularly for pulsed pumping, the gain can easily become rather high, leading to amplified spontaneous emission.

Many laser dyes are available, and together they cover huge wavelength regions, the full visible range and also substantial areas in the ultraviolet and infrared region. A dye laser can be operated with various dyes, ideally, different cuvettes and circulation systems are used for different dyes so that an easy change is possible.

A notorious problem with dyes is their limited lifetime, they degrade during laser operation. Dye circulation systems are usually required, enabling use of a larger volume of dye solution, which may have a lifetime of a few hundred operation hours.

1.5.4 Semiconductor medium

Semiconductors are utterly different from ionic crystals concerning their electronic and optical properties. The relevant electronic wave functions depend on the whole crystal structure and can be influenced strongly by varying chemical compositions, by structures such as very thin layers (quantum wells) and isolated dots of different materials (quantum dots), and by strain resulting from such structures. This opens a massive range of possibilities for engineering semiconductor structures with optimized properties for use as laser gain medium in a wide range of wavelengths.

Wavelengths tuning is possible with semiconductor gain media, often in a range of some tens of nanometers. Varying the material composition can often substantially shift that tuning range so that vast wavelength regions become accessible, although not with a single laser. Using GaAs, InP and GaSb semiconductor material systems, interband heterostructure based semiconductor lasers operating in CW at the ambient temperature can access $0.8\mu\text{m}$, $1.5\mu\text{m}$ and $3.0\mu\text{m}$ wavelength regions respectively. The accessible regions can be extended to $0.4\mu\text{m}$ using GaN-based material systems and to $4.5 - 5\mu\text{m}$ using PbTe and PbSe. Thanks to inter sub-band

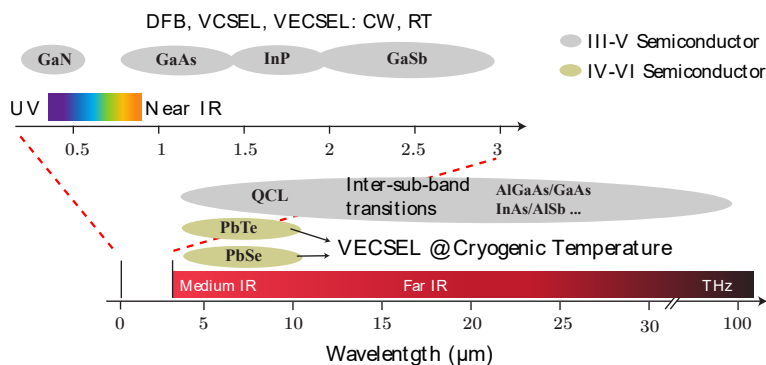


Figure 1.11: Spectral regions accessible by the main semiconductor material-systems used in semiconductor lasers

recombination in cascade lasers, emission wavelengths from $3\mu m$ to THz domain can be achieved.

The optical transitions in semiconductors are very strong, and consequently the carrier lifetime is very short: just a few nanoseconds. This results in a very high gain per unit length, allowing laser operation with a gain medium only a few hundreds of microns long, or even less than $1\mu m$ (in surface-emitting lasers). Table 1.1 resumes some parameters discussed above for different laser media.

Parameters	Ruby	Nd:YAG	Dye	He-Ne	Semiconductor
λ (nm)	694	1064	320 – 1500	633	1000
τ	3 ms	230 μs	2 – 5 ns	150 ns	2 ns
σ (cm^2)	2.5×10^{-20}	2.8×10^{-19}	$\sim 10^{-16}$	30×10^{-14}	$\sim 10^{-15}$
Δa (nm)	0.5	0.5	20 – 30	0.002	~ 50

Table 1.1: Gain medium parameters of various lasers

From the different gain mediums available, the semiconductor is best suited for our targeted application (3D structured light). It can provide a high gain (strong optical transition) with a delta like light matter interaction for a good integration capacity into a complex system for transverse structuration (vertical external cavity semiconductor laser VECSEL). It is also possible to engineer to some extent its properties (modal gain, spectral bandwidth and spatial wavevector spectrum, emission wavelength) as well as design integrated saturable absorber mirror (SESAM) with fast or slow carrier lifetime. Integrated meta-surfaces on the semiconductor device are also possible, allowing a greater control of the spatial amplitude/phase transfer function.

1.6 3D Light structuration inside a laser cavity

To design a system capable of 3D light structuration inside a laser system, we must first generate an electromagnetic wave using an active medium. In our case, semiconductor is a good option thanks to its versatility in design. Secondly, we must confine the EM wave to an optical cavity. To allow for complex structuration the system must exhibit a flat response in both local and non-local potential (flat phase response in the gain, no diffraction) which poses, a real challenge.

1.6.1 Longitudinal band engineering

For the longitudinal structuration, meaning the ability to operate in a pulsed regime such as passive mode-locking or to exhibit temporal localized structure, the requirements are twofold.

First, the system must be able to operate on several longitudinal modes and lock them in phase to generate a pulse train. In a linear optical cavity, the longitudinal wave-function is of the sinus basis, and adding several of them with a fixed phase relationship leads to temporal pulses. For this, the optical gain spectral width must be large enough in front of the cavity mode separation (see figure 1.12).

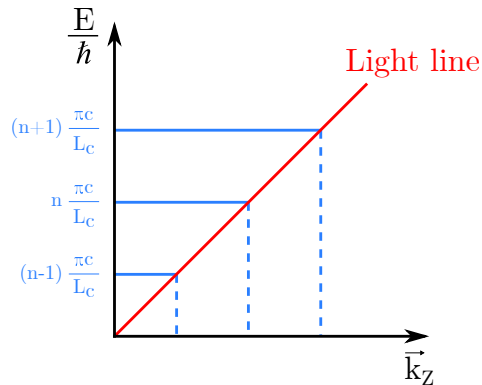


Figure 1.12: Dispersion diagram Pulsation-wavenumber for the longitudinal component in a linear optical cavity.

Secondly, for a PML scheme, a saturable absorber with a faster response time than gain saturation must be added to open a net gain window around the pulse. Dispersion management of the pulse must also be considered to generate ultra-short pulses. For TLS, another condition consists of having an extended longitudinal system, meaning that the round-trip time must be greater than the matter recovery time of the SESAM and Gain. Contrary to the transverse case, there is no need to degenerate the longitudinal system and flatten the band structure of the dispersion diagram.

1.6.2 Transversal band engineering

Transversal structuration is related to the spatial aspect of the EM field emission. It is related to the transverse mode profile of the beam and mostly given by the optical cavity design and boundary conditions. A linear diffractive spherical cavity with rotational symmetry will take the form of a photonic harmonic potential (see figure 1.13a) and generate a Laguerre-Gauss mode basis.

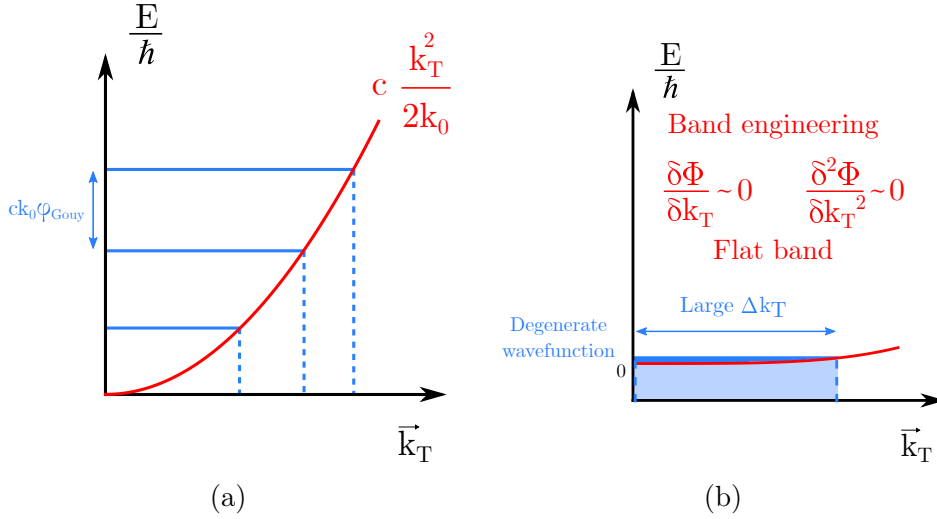


Figure 1.13: Dispersion diagram Pulsation-wavenumber for the transverse component in a linear optical cavity. (a) Free space diffraction relationship. (b) Band engineering for pulsation degeneracy and large wavenumber window.

To operate in the most complex transversal structuration, meaning to have a spatially degenerate emission and/or non-linear spatial localization, we must carefully engineer the optical system. Instead of a harmonic band response, we want to flatten it. This will result in a transversally degenerate system capable of operation along a broad-bandwidth of spatial frequency, thus capable of complex and arbitrary wavefunction. One other way to explain this would be to say that in a transversally degenerate system, any arbitrary wavefunction could be decomposed onto a linear combination of HG or LG modes.

To achieve this, we must design a system with no diffraction (non-local potential) and a flat phase response in real space. To summarize, the non-local and local phase transfer function must be flat, meaning that:

$$\frac{\delta\Phi}{\delta\xi} = 0 \quad \text{and} \quad \frac{\delta^2\Phi}{\delta\xi^2} = 0 \quad (1.26)$$

where ξ is either the local unit x, y (real transverse space) or the non-local

unit β (transverse wave-vector) and Φ the local or non-local phase response of the optical system.

Secondly, to have an extended system for SLS generation, we must have a high Fresnel number (small spatial spot in front of transverse area). This implies that the transverse available bandwidth is large (i.e., large numerical aperture NA) to have a small spatial spot and a good flatness and homogeneity in real space to have a large transverse area.

1.6.3 Spatial structuration with self-imaging cavity

In this work, we want to design and study the behavior of a laser capable of 3D light structuration. This means a system combining the transversal and longitudinal band engineering for PML or TLS and Degenerate wavefunction or SLS. Having a system capable of these two types of localized state is a start for the more complex spatio-temporal localization also called light bullet (LB). To reach this goal, both the optical system and the active medium must be carefully designed. Figure 1.14 shows the complete laser system with a medium that provides gain g and a third-order non-linearity $\chi_g^{(3)}$, another medium with saturable absorption α and non-linearity $\chi_\alpha^{(3)}$, and an optical cavity that couples gain and absorption to create a 3D structured light state.

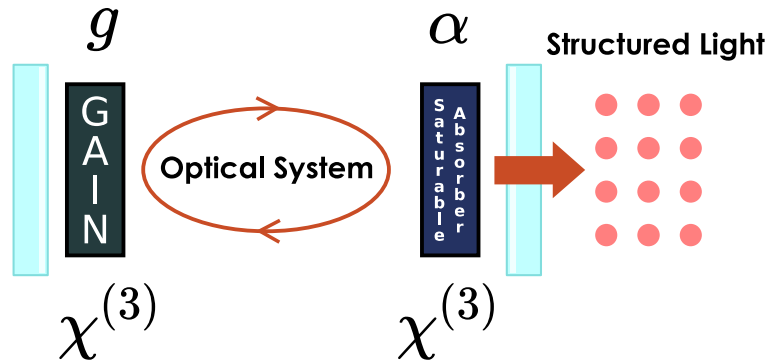


Figure 1.14: Schematic representation of the laser system needed for non-linear light structuration with a gain medium and a saturable absorber medium.

In the end, we chose to use a self-imaging cavity coupled on one plane to a Gain mirror using 1/2-VCSEL and to the second plane with a saturable absorber mirror. Both those active media will be based on III-V semiconductor technology.

First, the optical cavity has to accommodate the extended aspect ratio condition for both the transverse space and longitudinal (time) one. In the transverse plane, the system must be degenerate, meaning that the phase of the transfer function must be flat over a wide range of wavenumber. This implies that $\frac{\delta\varphi(\beta)}{\delta\beta} \sim 0$ and

$\frac{\delta^2 \varphi(\beta)}{\delta \beta^2} \sim 0$ with a large numerical aperture $NA > 0.1$, or in other words, the smallest spot must be small compared to the transverse extent of the system (i.e., large Fresnel number $F = \frac{a^2}{L\lambda} \gg \gg 1$). We also must fulfil the condition $\tau_{RT} \gg \tau_{matter}$, for the extended system in time. To fulfil those two conditions, a self-imaging optical cavity appears to be a good choice.

Secondly, the active medium plays an essential role in a laser to supply the light beam with the necessary coherent photons through the stimulated emission process. Thus, the type of active medium influences the laser beam properties such as the wavelength, the output power, the tunability, the temporal dynamics and more. For 3D Light structuration, both an active medium that provides optical gain and one that provides saturable absorption are needed. For the gain medium, a high gain with high saturation intensity is needed for a large non-linear phase-amplitude coupling and the self-phase modulation effect associated. While for the saturable absorber small saturation intensity with a long lifetime are optimal for self-amplitude modulation in the spatial domain, but short lifetime are required for the pulsed operation. In this optic, we must choose a technology capable of providing both aspect with sufficient control over their properties.

In the rest of this manuscript, we will describe the active medium optical system properties, as well as the different design choices made to reach this goal. In the end, we will analyze the different observed light states.

Part II

Gain and Absorber technologies and design

VECSEL technology: building blocks

The VeCSEL (Vertical External Cavity Surface Emitting Laser) technology uses a 1/2-VCSEL gain structure as a flat mirror in a larger external cavity system. This configuration is interesting for non-linear spatio-temporal light structuration. Indeed, this semiconductor system allows the decoupling of the optical gain and the optical cavity part, for a greater control over the light state compared to guided semiconductor lasers such as edge-emitting lasers. The stack design for surfaces emitting allows for a broad transverse area of operation, while the Semiconductor gain medium allows for large gain bandwidth with a high cross-section. In conjunction, the need for an external cavity permits the use of a complex optical system to combine both the large spatial and temporal aspect ratio needed.

In the rest of this chapter, we will detail the different building blocks of the 1/2-VCSEL gain mirror.

2.1 Semiconductor design requirement

A 1/2-VCSEL is a multilayer semiconductor structure with the primary function of light amplification and a high reflectivity mirror as a part of the optical cavity. It is sometimes referred to as a gain mirror. In semiconductor laser, the gain active zone can be made with a multitude of materials and alloys (binary, ternary, quaternary) that can cover a wide range of wavelengths by bandgap engineering (see figure 2.1). For lasing operation, direct band gap semiconductors are preferred to facilitate radiative transition without momentum transfer.

One important point when designing a semiconductor multilayer structure is to have a good lattice match, meaning a similar atomic separation between the different crystals ($\Delta a/a < 1\%$). If not, the mismatch will cause dislocation in the crystal [Marée 1987]. However, using a strained structure (tensile or compressed)

where the lattice of the deposited layer distorts to fit the lattice substrate can exhibit higher material gain [Piprek 2013], polarization separation [Coldren 2012]. The thickness of the strained layer must not exceed the critical thickness to ensure no crystal dislocation. For thick strained multilayer structure, compensation of strain must be implemented by adding a compensating stress opposing the strained layer. For example, a structure with compressive stress must be compensated with tensile stress and reciprocally.

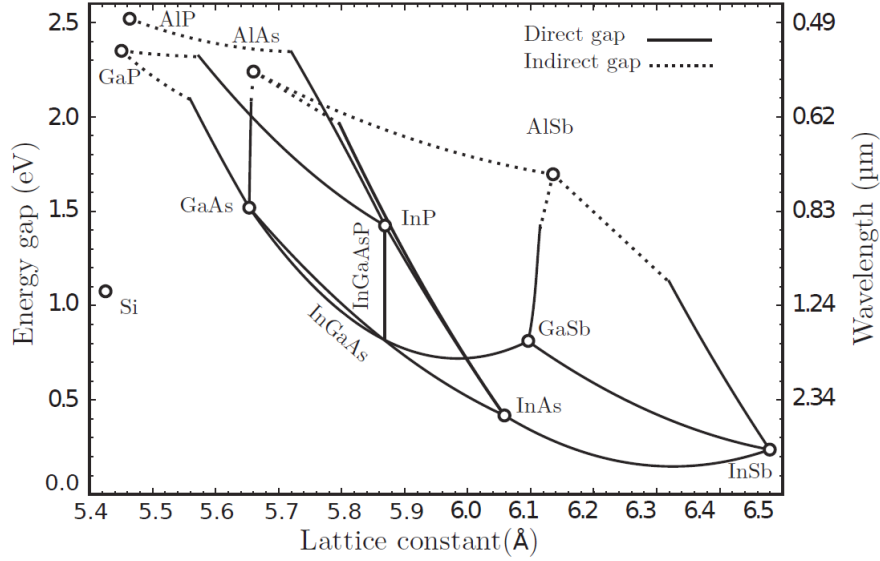


Figure 2.1: Energy gap, Wavelength vs. lattice constant for III-V semiconductor compounds material. Solid line for direct bandgap and dash line for indirect bandgap.

In our case, we use the III-V semiconductor family based on a GaAs substrate and GaAs/InGaAs quantum wells for an emission at $\lambda = 1.064 \mu\text{m}$, while strained compensation is done using GaAsP layers surrounding the QW. The design of the structure (active zone and Bragg mirror) is done at the IES laboratory, while the realization is made at the C2N by Isabelle Sagnes and Gregoire Beaudoin. The growth is carried out by organometallic vapor phase epitaxy (MOCVD) and post-treatment for meta-surface deposition is done through e-beam lithography.

2.2 Bragg mirror

Highly reflecting Bragg mirrors are realized using a stack of alternating layers of different refractive indices. As shown in the figure 2.2, we consider a Bragg

pair as two layers of a low and high refractive index. To optimize the reflective constructive interferences, each layer must have a thickness of, $\lambda_B/4n$ where λ_B is the central wavelength of the mirror. At each interface, the partial reflection introduces a phase shift of π when the wave goes from a medium of a low index towards a medium of a high index and a phase shift of 0 in the opposite case. While the propagation on each layer results in a phase shift of $\pi/2$. In this configuration, we can reach high reflectivity ($R > 99\%$) over a certain bandwidth $\Delta\lambda$ through constructive interferences.

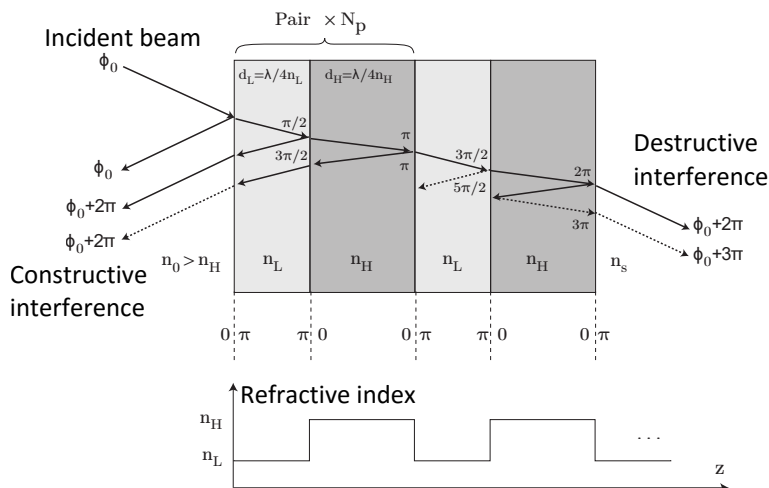


Figure 2.2: Structure of a Bragg mirror, with the refractive indices $n_0 < n_L < n_H$ with $n_L < n_S$; n_0 ambient, n_L medium of low index, n_H medium of high index, n_S medium of the substrate. The phase shift experienced at each first partial reflection is also shown.

It is then possible to write an analytical expression for the reflectivity, the bandwidth and the dielectric losses:

$$R = \left(\frac{1 - \frac{n_s}{n_0} \left(\frac{n_L}{n_H} \right)^{2N_p}}{1 + \frac{n_s}{n_0} \left(\frac{n_L}{n_H} \right)^{2N_p}} \right)^2 \quad (2.1)$$

$$\Delta\lambda = \frac{4\lambda}{\pi} \arcsin \left(\frac{\Delta n}{n_H + n_L} \right) \quad (2.2)$$

$$Loss = 2\alpha_b L_{depth} = 2\alpha_b \frac{\lambda_B}{4\Delta n} \quad (2.3)$$

To achieve a high reflectivity, it is important to have a high refractive index contrast $\Delta n = n_H - n_L$ and a large number of pairs N_p . The choices of material

will fix Δn and, depending on the technological platform, high or low contrast is possible. For the III-V GaAs platform at 1 μm emission, it is possible to use GaAs/AlAs pairs with $\Delta n = 0.53$ while keeping a good lattice match. Having a high contrast index also minimizes the penetration length L_{depth} of the electromagnetic wave inside the Bragg mirror, thus lowering the losses for high reflectivity. On the other hand, the maximum number of pairs is not as much limited by the technology than the ability of the system to evacuate the heat through the Bragg mirror. A large number of pairs will result in large thermal impedance.

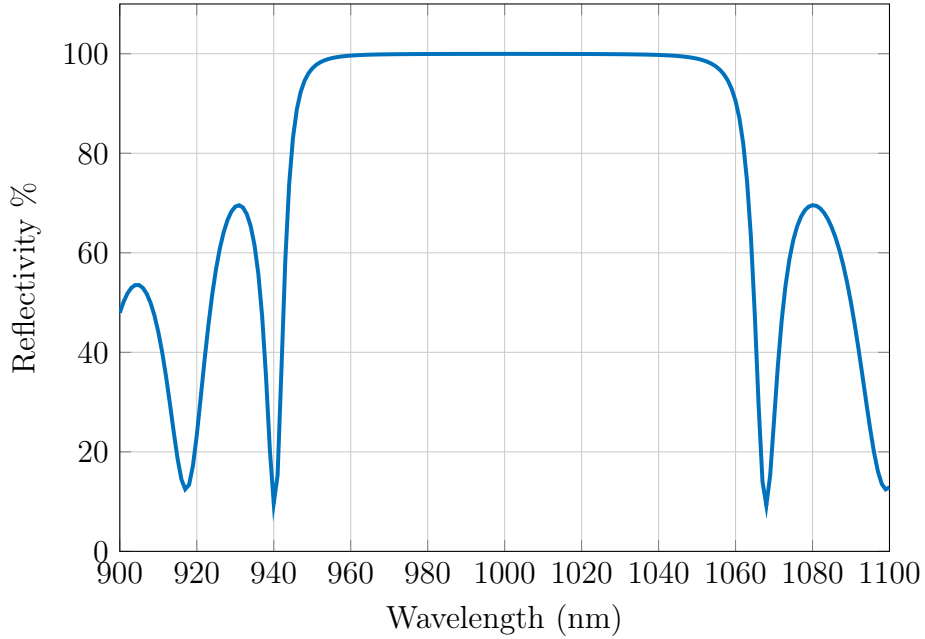


Figure 2.3: Reflectivity spectrum for 25 pair of AlAs/GaAs on a GaAs substrate. The Bragg pair thickness have been optimized for 1 μm wavelength.

As a typical example for a VCSEL emitting at 1 μm with $Np = 25$ AlAs/GaAs Bragg pair ($\Delta n = 0.53$) we have the following reflectivity spectrum (see figure 2.3 with $R_{max} = 99\%$, $\delta\lambda = 110$ nm and $Loss < 0.02\%$). This number of Bragg pairs does not significantly increase the thermal impedance.

2.3 Quantum wells active area

The multi-quantum well active area is the heart of the 1/2-VCSEL semiconductor structure. To have optical gain, we must reach a population inversion between a fundamental and excited energy state. In this case, confining the carrier in a plane (1D confinement: Quantum Well (QW)) allows us to more easily reach a population

inversion than with bulk material. This is linked to the resulting smaller active volume needing less population to reach a same population density. We will now detail the different properties linked with the quantum wells.

2.3.1 Quantum Well

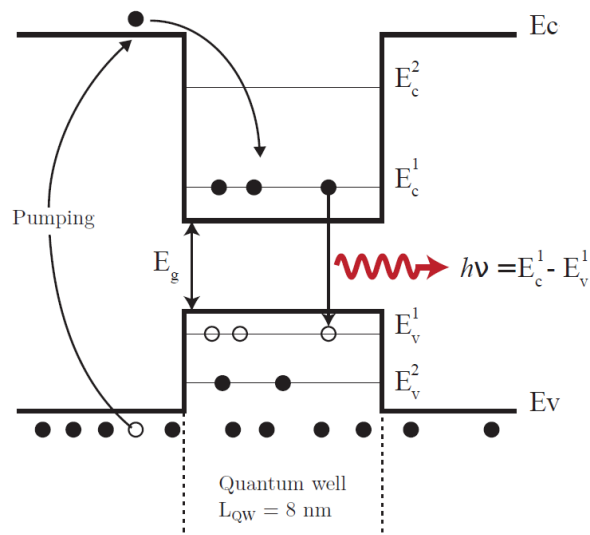


Figure 2.4: Schematic description of an energy diagram of quantum wells pumped in the barriers. Full dots represent electrons. Circles represent holes.

A Quantum Well (QW) is a thin layer of a small energy bandgap (E_g) crystal sandwiched between two higher bandgap materials called “barriers”. Figure 2.4 details the resulting valence and conduction band, with the subband level inside the QW. This heterostructure creates an energy potential, confining holes on the top of the conduction band and electrons on the bottom of the valence band. The resulting energy states in this small layer (8 nm thickness) are then quantized to different subband level. The energy separation from the fundamental subband level in the conduction band (E_c^1) and the valence band (E_v^1) determine the lasing wavelength. We can write in the parabolic band approximation [Zory 1993]:

$$E_c^n - E_v^n = E_g + \left(\frac{1}{2m_r}\right)\left(\frac{n\pi\hbar}{L_{QW}}\right)^2 \quad (2.4)$$

Where E_g is the forbidden gap band energy of the material used, L_{QW} is the thickness of the well, $m_r = (1/m_e + 1/m_h)^{-1}$ is the reduced effective mass related to the effective masses of the electrons of the conduction band (m_e) and the effective mass of the holes of the valence band (m_h). We can see that it is possible

to tune the emission wavelength by playing with the QW thickness and/or the material bandgap. However, the separation between two consecutive levels in the subband must be higher than the thermal energy $k_bT = 26$ meV (at 300 K) to avoid thermal coupling between states, resulting in higher density of states and higher transparency density. It also follows that the energy height of the barrier must be well above the thermal energy for a good carrier confinement and low leakage current (carriers escaping the QW confinement). If these conditions are met, then the leading recombination mechanism becomes the radiative recombination between the fundamental state of the conduction and valence subband.

Depending on the technology choice, some lattices mismatch can exist between the substrate crystal and the QW materials. In this situation, using strained balance QW by adding layers of a material with opposite lattice mismatch to compensate the strained is a valid solution. For InGaAs based QW on GaAs substrate, this solution allows to increase the number of QW and thus gain in the NIR ($\lambda > 1 \mu\text{m}$). Strain QW also exhibits lower threshold and higher differential gain compared to unstrained ones [Coldren 2012].

2.3.2 Absorption and Gain in QW

As seen in § 1.4 the light matter interaction is governed by the complex electrical susceptibility χ from which we can determine the absorption, gain or the refractive index of a medium. For a quantum well laser, S. Balle proposed a simple analytical expression following a parabolic approximation of a single valence and conduction band [Balle 1998]. This leads to the expression:

$$\chi(\omega) = \frac{|M|^2}{\varepsilon_0} \frac{2}{V} \sum_k \frac{f_c(k) - f_v(k)}{h\omega - E_c(k) - E_v(k) + ih\gamma} \quad (2.5)$$

where V is the medium volume, M is the dielectric dipole element between the electronic state, f_c and f_v are the occupation probabilities of the electronic states given by the Fermi-Dirac distribution:

$$f_c = \frac{1}{1 + e^{(E_1 - E_{F_c})/k_bT}} \quad \text{and} \quad f_v = \frac{1}{1 + e^{(E_2 - E_{F_v})/k_bT}} \quad (2.6)$$

where $h\nu = E_1 - E_2$ is the energy of the transition between high and low-energy level and $E_{F_{c,v}}$ is the quasi-Fermi level of the conduction and valence band which strongly depends on the injection level and temperature as follows from the expressions:

$$E_{F_c} = E_c^1 + k_bT \ln \left(e^{\frac{N}{N_c}} - 1 \right) \quad \text{and} \quad E_{F_v} = E_v^1 - k_bT \ln \left(e^{\frac{N}{N_v}} - 1 \right) \quad (2.7)$$

with

$$N_{c,\nu} = \frac{m_{c,\nu}^*}{\pi \hbar^2} k_b T \quad (2.8)$$

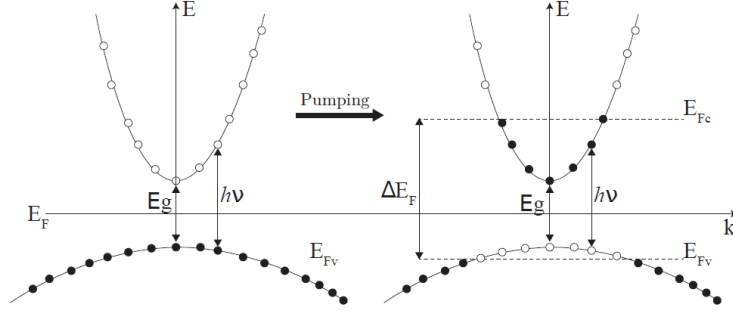


Figure 2.5: Energy diagram of an undoped quantum well, a) thermodynamic equilibrium: the conduction subband is empty, and the valence subband is filled, b) out of equilibrium: the Fermi quasi-level of the electrons (holes) goes up (down) to the conduction subband (valence).

On figure 2.5 we show the first two energy bands of an undoped quantum well with the distribution probabilities of the occupied state. At thermodynamic equilibrium the conduction band is empty, and the quasi-Fermi level for the conduction band (CB) and valence band (VB) are the same. By disrupting this equilibrium through pumping, we can separate the quasi-Fermi levels for electrons and holes. For electrons, the quasi-Fermi level will rise in the CB and reach a state where we have a non-zero probability of finding electrons in the conduction band and holes in the valence band. When the quasi-Fermi level is separated by the energy gap, then transparency is reached, and further increase in separation leads to a population inversion, where more carriers are found on the CB than the VB. Optically, this is equivalent to having gain in an energy band equivalent to [Bernard 1961]:

$$E_g < h\omega < \Delta E_F \quad (2.9)$$

This expression reflects the fact that the material is transparent for photons of energy below the forbidden band and highly absorbing for photons of energy higher than the separation of quasi-Fermi levels. Therefore, the spectral width of the gain will be greater as the separation of the quasi-Fermi levels will be important. In the particular case where the energy difference between the Fermi quasi-levels is equal to the gap energy of the quantum well ($E_g = \Delta E_F$), the material is said

to be transparent to the transition energy: the gain (or absorption) is then zero. Transparency is characterized by a particular carrier density that will be noted N_{tr} .

The optical gain in this medium can be written with the imaginary part of the electrical susceptibility as:

$$g = -\frac{\omega}{c} \text{Im}(\chi(\omega)) \quad (2.10)$$

We note that for cases with no population inversion in the medium, this expression is then representative of the optical absorption. For a real band structure, the analytic calculation of χ is too complex. However, some insight can be gained by considering a simple parabolic band structure of a single QW with only one electron and hole band, and low temperature where the Fermi distribution closely looks like a step function. In the frame of those approximations, S.Balle gave an analytical formula of [Balle 1998]:

$$\chi(\omega, N) = -\chi_0 \left[2 \ln \left(1 - \frac{N/N_{tr}}{u+i} \right) - \ln \left(1 - \frac{b}{u+i} \right) \right] \quad (2.11)$$

with N_{tr} the carrier density at transparency and

$$u = \frac{\omega - \omega_0}{\gamma} + \sigma (N/N_{tr})^{1/3} \quad , \quad \chi_0 = \frac{m^* |M|^2}{W \pi \epsilon \hbar^2} \quad (2.12)$$

where σ defines the band gap shrinkage, $\omega_0 = E_g/\hbar$ is the bandgap pulsation and γ is the width of the considered transition. This expression stands that the maximum gain $g_{max} = \frac{\omega_0}{c} \chi_0$ is only dependent on the material properties, but the center and the width of the gain spectrum is a complex function of N . In figure 2.6 the gain spectrum is displayed for different carrier density N/N_{tr} . For, $N/N_{tr} = 0$ corresponding to the thermodynamic equilibrium, we are in the absorption regime with stronger absorption above the bandgap frequency ω_0 following the Fermi-Dirac distribution. The two other curves are in the gain regime with $N/N_{tr} = 1.1$ and 2. From this, we can see that the gain bandwidth increases with N and exhibits a blue shift (shift towards a smaller wavelength). Even if the transition width of semiconductors is around $\gamma \sim 10^{14} \text{ s}^{-1}$, close to transparency, the gain bandwidth could be very narrow ($\sim \gamma/10$ for $N/N_t = 1.1$) while quite large at stronger excitation ($\sim 2\gamma$ for $N/N_t = 2$).

The linewidth enhancement factor can also be determined by:

$$\alpha_h = \frac{\text{Re}(d\chi/dN)}{\text{Im}(d\chi/dN)} \quad (2.13)$$

This factor introduced by Henry is unique to the semiconductor materials and can explain the mismatch of the laser linewidth from the Schawlow-Townes formula due to the phase-amplitude coupling effect in the semiconductor material

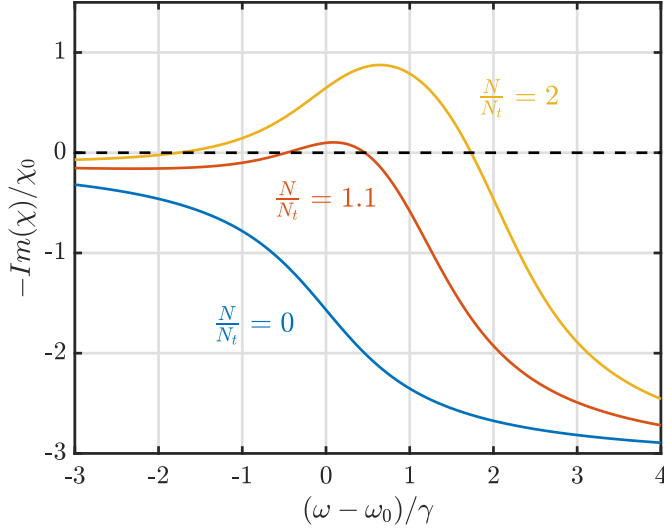


Figure 2.6: Normalized imaginary part of the susceptibility as a function of the normalized frequency deviation $(\omega - \omega_0)/\gamma$ for increasing carrier densities $N/N_{tr} = 0$ (Absorption) and $N/N_{tr} = 1.1, 2$ (Gain).

[Henry 1982, Schawlow 1958]. Indeed, the real part of the electrical susceptibility corresponds to the refractive index (phase variation) while the imaginary part to the gain (amplitude variation), thus the equation 2.13 shows the link between the variation of the refractive index and the gain as the function of carrier variation.

In figure 2.7a we show the variation of the linewidth enhancement factor at the peak gain position from carrier excitation. We see that the phase-amplitude coupling effect gets stronger with higher excitation. In figure 2.7b the linewidth enhancement factor is shown as a function of the normalized frequency deviation for two carrier excitations, $N/N_{tr} = 0$ (blue) and $N/N_{tr} = 2$ (red). We can see that the Henry factor has an opposite sign in the absorption regime ($\alpha < 0$) than the gain regime ($\alpha > 0$). We can also see the increasing trend for the lower energy part of the spectrum. The usual value can range from 2 to 4 depending on the spectral position and carrier excitation [Stohs 2001].

The value of this parameter can play an important role for single frequency laser operation [Chomet 2019] due to its quasi-third order non-linear response arising from the phase-amplitude coupling through the carriers variation. Indeed, since a variation of a refractive index can occur from a variation in gain, this could be interpreted as an intensity induced phase shift, then we have similar characteristics as a third-order Kerr non-linearity. This way, the light beam experiences self-phase modulation during propagation that leads to a self-lensing effect in the transverse plane or four wave mixing from time variation of carrier density.

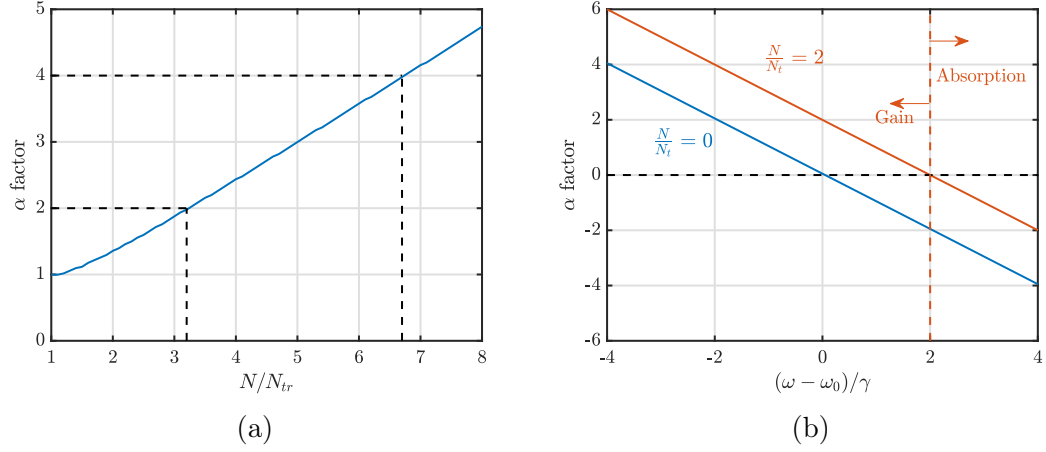


Figure 2.7: a) Linewidth enhancement factor as a function of N/N_{tr} at the maximum of the gain. b) Linewidth enhancement factor as a function of the normalized frequency deviation $(\omega - \omega_0)/\gamma$ for $N/N_{tr} = 0$ (Absorption) and $N/N_{tr} = 2$ (Gain).

2.3.3 Carrier lifetime

The QWs will confine carriers in their potential well for a certain amount of time before the interband recombination occurs. The resulting carriers lifetime $\tau(N)$ is dependent on carrier concentration N and the different radiative and non-radiative recombination processes. This can be approximated by [Coldren 2012]:

$$\frac{1}{\tau(N)} = A + B^*N + CN^2 \quad (2.14)$$

Where A , B^* , C , are respectively the mono-molecular, bi-molecular and Auger coefficient. A and C correspond to non-radiative recombination process. Where A comes from crystal defects and impurities ($A \sim 10^{-7} \text{ s}^{-1}$ for good quality crystal) and C characterize the Auger recombination of three-particle interaction which strongly depends on temperature and wavelength. It appears for large carrier density ($C \sim 3 \times 10^{-30} \text{ cm}^6/\text{s}$ at $\lambda = 1 \mu\text{m}$ for InGaAs QWs).

The radiative recombination is expressed by the bi-molecular coefficient, B^* which is also dependent on the carrier density following [Bourdon 2002, Laurain 2010]:

$$B^* = \frac{2B}{L_{QW}} \frac{N_c^2}{N^2} \left(\frac{N}{N_c} + e^{-N/N_c} - 1 \right) \quad (2.15)$$

where B is the constant bi-molecular coefficient and N_c is the conduction band density of state (see equation 2.8). This form allows us to consider the saturation effect of the spontaneous emission rate for large carrier density due to band filling.

From this, it is possible to define a radiative lifetime:

$$\frac{1}{\tau_r} = B^* N \quad (2.16)$$

And a non-radiative lifetime:

$$\frac{1}{\tau_{nr}} = A + CN^2 \quad (2.17)$$

We can express the internal quantum efficiency η_i , using the previous equation, as the ratio between the number of carriers undergoing radiative recombination versus the number of generated carriers.

$$\eta_i = \frac{\frac{1}{\tau_r}}{\frac{1}{\tau_r} + \frac{1}{\tau_{nr}}} \quad (2.18)$$

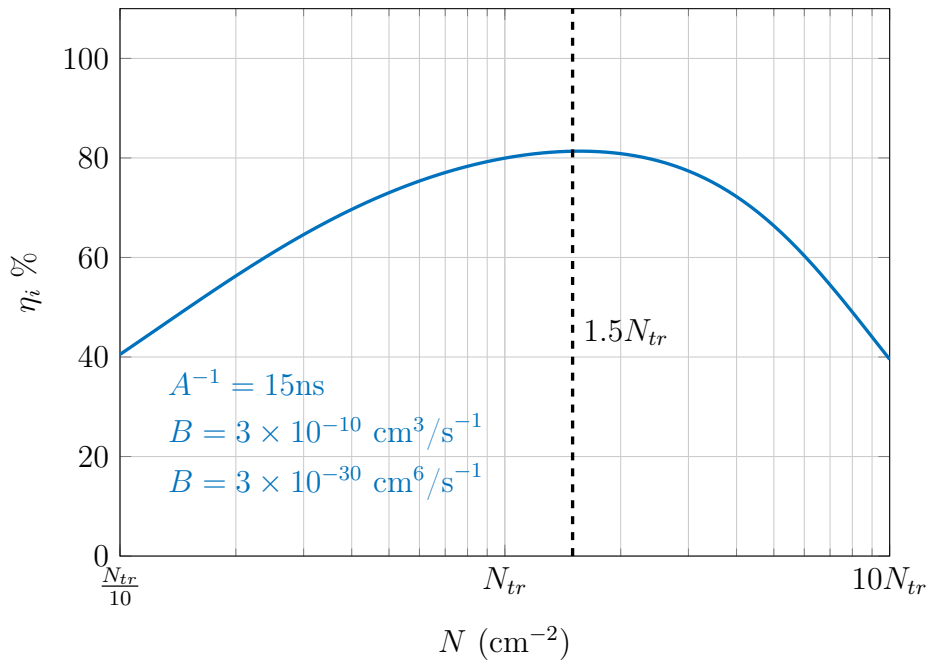


Figure 2.8: Theoretical quantum efficiency function of the carrier density for a typical InGaAs/GaAs QWs.

Figure 2.8 shows the theoretical η_i with the carrier density for the typical A , B^* , C parameters of InGaAs/GaAs QWs at $\lambda = 1 \mu\text{m}$ [Laurain 2010]. We find that the efficiency is maximal (around 80%) slightly above the carrier transparency density. For large excitation density, the quantum efficiency quickly goes down due to Auger recombination effect. The optimal range of operation should not exceed a few time the transparency density to avoid such effects.

Under lasing condition, when the lasing threshold is reached, the quantum efficiency becomes close to 1, since the predominant recombination effects are due to the stimulated emission process.

2.3.4 Gain dichroism

QW surface emitting lasers are known to exhibit an optical gain dependent on polarization angle [Shimizu 1988]. It can be explained by two main effects. First, the anisotropy originates from the breakdown of the rotoinversion symmetry at the interface when the host materials (GaAsP/InGaAs/GaAsP) do not share any common atoms due to growth conditions and chemical segregation. And secondly, the induced birefringence from the axial symmetry breakdown of the crystal at the air-semiconductor interface. As a result of those effects, the gain mirror experiences some gain dichroism along the crystal [110] or $[1\bar{1}0]$ for [100] oriented substrate [Cortez 2000, Krebs 1996, Yu 2011].

Figure 2.9 demonstrates this effect on the 1/2-VCSEL gain. Here we used a $13\lambda/2$ GaAs structure with 6QWs placed at the anti node of the standing wave. A $\lambda/4$ SiN layer has been added to the top surface to suppress the resonant effect of the air semiconductor microcavity. The gain measurement were done using a rotating glass window inside the laser cavity for losses control while measuring the laser threshold for both polarization.

From this, we can extract a gain dichroism of $\Delta G/G \sim 10\%$. The gain being higher along the [110] crystalline axis. A laser based on a 1/2-VCSEL gain mirror without other anisotropy will tend to emit a linear polarization along this axis. One way to suppress or reinforce this dichroism is by introducing thermal strain through an asymmetric optical pump spot. The anisotropic thermally induced strain, can compensate or increase the surface crystal birefringence and thus the gain anisotropy [Seghilani 2015].

2.4 Non-resonant optical pumping in barrier

To achieve a population inversion of the active medium, one must supply the necessary energy into the system. The two most common ways are through an electrical or optical pumping scheme. For our purpose, the optical pumping scheme presents several advantages.

Firstly, the need to dope and post-process the semiconductor to inject the electrically generated carrier puts a lot of strain and complexity on the required broad transverse area of the system. Using an optical pumping scheme negates the need for these processes and allows for a large and uniform pumped area in

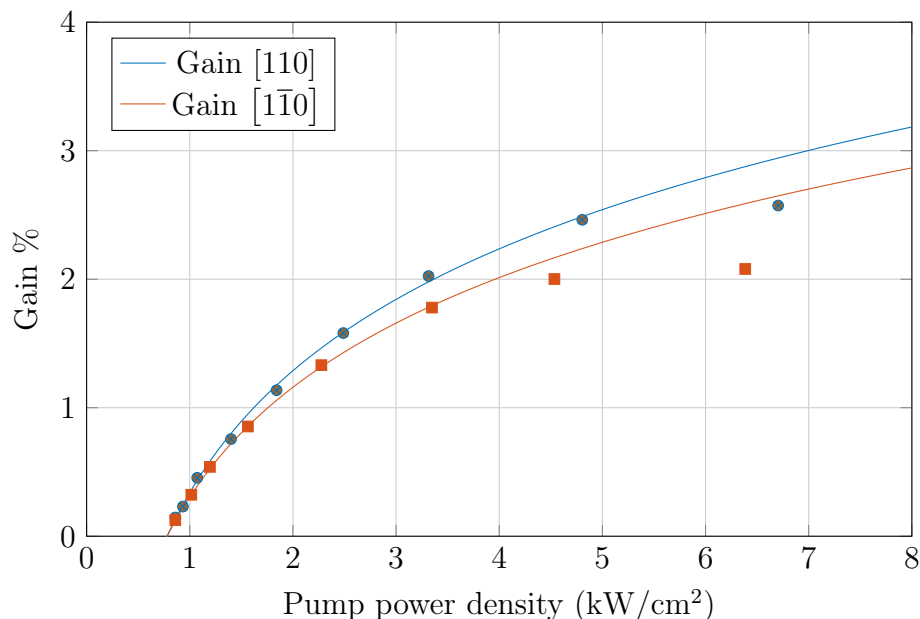


Figure 2.9: Measurement of the modal gain of a VECSEL emitting at 1 μm for two directions of polarization following the crystal axis [110] and [1 $\bar{1}$ 0] [Chomet 2019].

an undoped and homogeneous semiconductor structure. This means that higher optical gain with a longer lifetime can be achieved.

Secondly, the large absorption in the barriers ($> 80\%$ for a single pass) and its broadband nature allow the easy use of a wide range of commercially available laser diodes for pumping.

Lastly, the control of the optical pump beam size and shape, adds a degree of freedom to the transverse structuration of the laser. By using several pumps or by changing the shape of the pump, we can control the lasing transverse modes.

2.4.1 Carrier generation

Figure 2.10 presents a schematic for an optical pumping scheme in the barriers. To avoid surface recombination, a confinement layer with a large bandgap compares to the barrier is added on top of the structure. Then, thanks to the diffusion process, the carriers generated in the structure will end up trapped in the QWs since the lifetime in the barriers is large in front of the capture time ($\tau_{cap} \sim \text{ps} \ll \tau_b \sim \text{ns}$) [Steinkogler 2003]. In this case, population inversion in the QWs is simply achieved by the absorption in the barrier. The resulting lifetime in the QWs can then be written by equation 2.14.

By assuming that all generated carriers end up trapped inside the QWs, we can

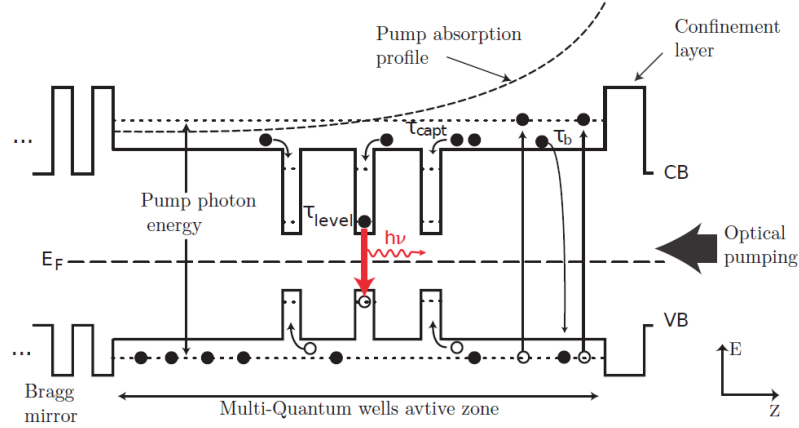


Figure 2.10: Schematic representation of a MQWs active zone for a 1/2-VCSEL optically pumped in the barriers.

express the pump power density I_{pump} needed to generate a carrier density N by:

$$I_{pump} = \frac{N}{\tau(N)} \frac{hc}{\lambda_{pump}} \frac{1}{A_b T_r} N_{QW} \quad (2.19)$$

Where N_{QW} is the number of quantum wells, A_b is the Beer-Lambert pump absorption coefficient inside the barriers and T_r is the pump transmission inside the semiconductor structure. hc/λ_{pump} is the pump photon energy and $\tau(N)$ the QWs lifetimes. With this expression, we can connect a measurable property (I_{pump}) to the important physical parameter ($N/\tau(N)$).

On the other hand, if the pumping action was done at a lower energy level, meaning pumping directly into the QWs, less energy would be lost as phonons from the pump to laser energy conversion. However, the absorption length would also be greatly reduced ($\sim 1\%$ per pass per QWs) and resonant pumping would be needed to increase pumping efficiency.

2.4.2 Thermal properties

For a laser, a certain part of the supplied pump energy is converted into laser light through the spontaneous and stimulated emission process, while the reminder is transformed into heat. The main contribution is from the mismatch in the pump photon energy and the laser photon energy, where the energy difference gets converted into heat. We can summarize the effect with the thermal efficiency $\eta_{th} = 1 - \eta_i \lambda_p / \lambda_l$. It is, therefore, more pronounce when pumping with a high photon energy, such as optical pumping in the barrier. For our GaAs based structure emitting at $1.064 \mu\text{m}$ with a pump at, 808 nm we reach around 40% under the

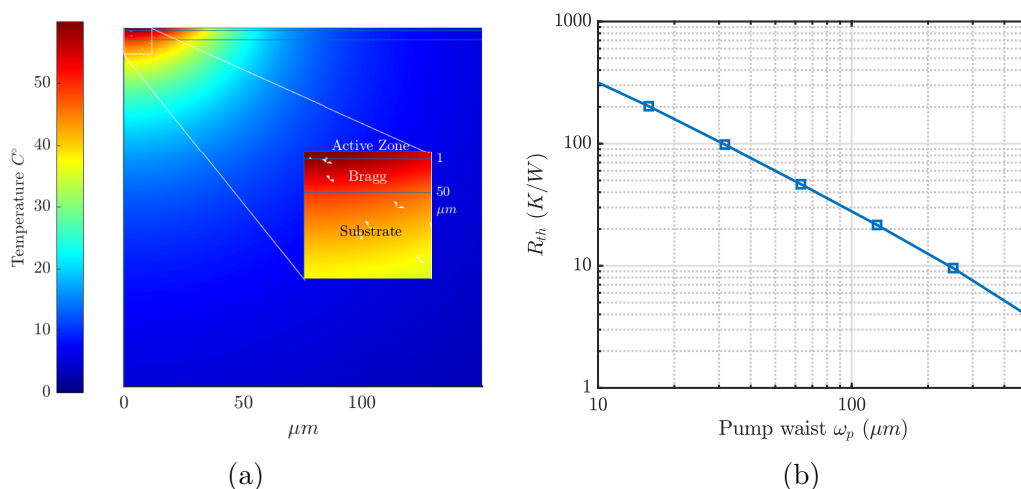


Figure 2.11: (a) Temperature profile inside a 1/2-VECSEL structure with a Gaussian pump of $\omega_p = 50 \mu\text{m}$ (b) Thermal impedance for different waist size.

threshold and 30 % above. This energy difference between the laser and pump is imposed by the bandgap configuration of the QW for good carrier confinement. Pumping directly into the quantum well with 980 nm a pump could be done to lower the thermal efficiency, at the detriment of a good absorption efficiency (80 % in barrier for 1 % in QWs). The resulting heating of the active area is then a function of the pump/laser energy difference and the thermal dissipation from conduction and/or convection effect. This can be summarized with the use of a thermal impedance R_{th} , such that we have:

$$T_{QW} = T_{peltier} + R_{th}P_{inc} \quad (2.20)$$

Where the QW temperature T_{QW} is dependent on the Peltier cooler temperature $T_{peltier}$ and the pumped induce rise in temperature $R_{th}P_{inc}$. Here, the thermal impedance is defined as $R_{th} = \Delta T / \Delta P_{inc}$. To estimate the thermal impedance, which is dependent on the 3D pumped induce thermal profiles and the heat conductivity of the different semiconductor layers, we need to solve the stationary heat equation:

$$\kappa(x, y, z)\nabla^2 T(x, y, z) = Q(x, y, z) \quad (2.21)$$

Where κ is the thermal conductivity in $\text{W m}^{-1} \text{K}^{-1}$ and Q the heat source in W m^{-3} . The heat source is then dependent on the power and pump size, which will impact the resulting thermal impedance. Solving this equation using the finite element method, we can see the thermal behavior of a typical 1/2-VECSEL structure. Figure 2.11a shows the heat distribution on an axisymmetric 2D cut

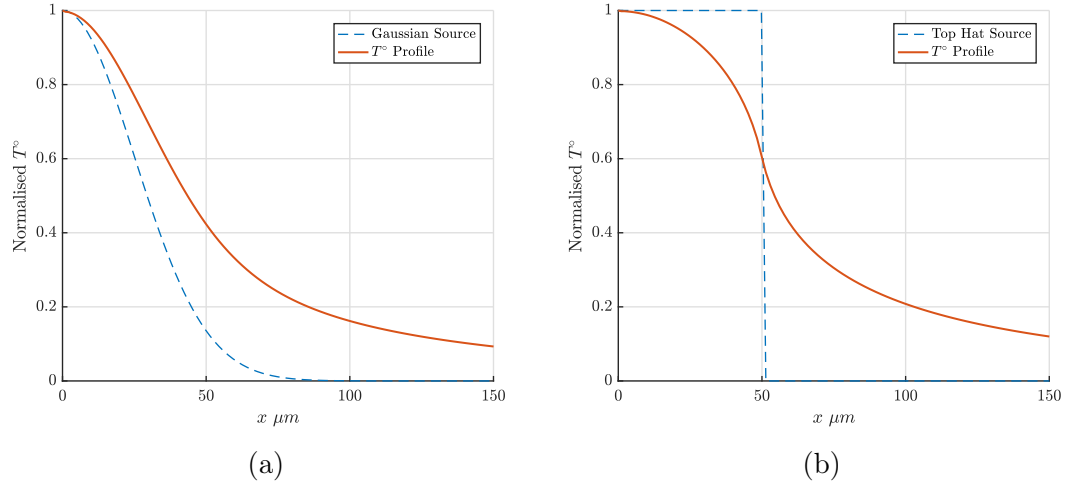


Figure 2.12: Transverse temperature profile for (a) Gaussian source and (b) top hat source.

of the 1/2-VCSEL for a Gaussian pump of $50\mu\text{m}$ of waist. Three layers were used, one for the active region ($7\lambda/2n$ length using the GaAs thermal conductivity $\kappa_{GaAs} = 55\text{ W m}^{-1}\text{ K}^{-1}$), one for the Bragg element (25.5 AlGaAs/GaAs pairs with an effective conductivity of $\kappa_{Bragg} = 34\text{ W m}^{-1}\text{ K}^{-1}$) and the substrate layer ($350\mu\text{m}$ of GaAs). There is almost no longitudinal temperature variation in the active area, since the thermal diffusion length appears a lot larger than λ . We can then use the surface temperature as the QW temperature for calculating the thermal impedance.

In figure 2.11b we calculated the thermal impedance for different waist. A clear inverse proportionality between R_{th} and ω_p is shown. This can be explained by the fact that for a small pump spot, the thermal power is concentrated in a small volume before thermal diffusion spreads the heat, which creates a 3D flux with a high thermal impedance. On the contrary, for large spots, the thermal power is already spread to a large volume with a unidirectional flux thus lower thermal impedance.

The thermal load applied onto the system will have several effects. One effect is the thermal lensing from the induced optical index variation, $\delta n/\delta T \sim 2.7 \times 10^{-4}\text{ K}^{-1}$ leading to a transverse phase variation. The shift of the optical index also induces a spectral variation of the micro-cavity resonance $\delta\lambda/\delta T \sim 0.07\text{ nm K}^{-1}$. Combined with the gain spectral red-shift with temperature, the laser may exhibit roll-over effect (sharp drop of output power) from too much thermal load.

Using the same simulation, we can extract the thermal transverse profile to estimate the thermal lensing. The figure 2.12 displays two examples of the transverse

thermal profile for a Gaussian shaped pump (2.12a) and a top hat shaped pump (2.12b) of the same radius and thermal power. The thermal diffusion leads to a larger temperature profile than the source with a parabolic component at the center. The resulting thermal lensing effect from the parabolic part of the profile will be expanded in section § 5.2.1.

2.5 Conclusion

The surface emission technology combined with the external optical cavity fulfills the requirement for spatial structuration of the light state. Mainly the extended transverse area and its possibility for high gain. In this chapter, we have introduced the different components of a 1/2-VCSEL semiconductor structure and their effects on the overall laser properties. First we looked at the choice of the semiconductor technology for the desired wavelength application and the importance of the strain management.

Then we looked at the different blocks describing the multilayer structure. The first one being the high reflectivity Bragg mirror, where the choice of material can impact the mirror performance. In our case, a high reflectivity ($R > 99\%$) can be achieved with a relatively small number of AlGaAs/GaAs pairs.

Secondly, we went over the different characteristics of a QW which composed the 1/2-VCSEL active area. We saw that large bandwidth are possible and that the phase-amplitude factor in a semiconductor can lead kerr-like non-linear effect. The QW properties also inform us of the optical range of operation we can expect (between N_{tr} to $4 - 5N_{tr}$).

Lastly, we describe the specifications needed for optical pumping. The main perturbative effect of this carrier generation choice is thermal lensing. To understand its origin, we simulated a simple 1/2-VCSEL using the 3D heat equation. This highlighted the importance of good thermal management and pump shape to limit the thermal lensing effect.

In the next chapter, we will take a closer look at the design of the different semiconductor structure used in this manuscript.

Design of semiconductors structures: GAIN & SESAM

We now need to design a gain medium for our laser system that fulfil all the requirements laid out in the previous chapters. Mainly to achieve a high effective gain, to optimize the ratio of saturable to unsaturable losses. To minimize the thermal effect such as thermal lensing while keeping a strong enough phase modulation from the phase-amplitude coupling effects. Minimizing long scale (micro-cavity length variation) and small-scale (QW interfaces inhomogeneity) inhomogeneity from the semiconductor growth as well as having a good crystalline quality, with low defects density, to keep a large homogeneous transverse area.

In parallel, we also have to design a semiconductor saturable absorber (SESAM) to match the maximum available gain and the expected saturation intensity. This will introduce self-amplitude modulation (SAM) in our laser system and help start spatially localized the laser emission.

In the following chapter, we will introduce the design of the gain mirror and the SESAM. We will then characterize their properties, including the modal gain, thermal impedance, carrier diffusion length, saturable absorption, and spatial homogeneity.

3.1 Modal Gain

The effective gain of a laser or modal gain is not only dependent on the material properties of the active medium, but also on the overlap between the laser beam volume and the gain volume. In the 1/2-VCSEL design, this interaction only occurs at the quantum well position. It will be dependent on both the micro-cavity effect and the QWs placement in relation with the electric field standing wave. Making both of them a critical part of the design.

The general form of the modal gain is given by [Coldren 2012]:

$$g_{mod} = \frac{\int_{vol. \text{ actif}} g(x, y, z) n(x, y, z) |\tilde{u}^+(x, y, z) + \tilde{u}^-(x, y, z)|^2 dV}{\int_{vol. \text{ mod}} n(x, y, z) (|\tilde{u}^+(x, y, z)|^2 + |\tilde{u}^-(x, y, z)|^2) dV} \quad (3.1)$$

where $\tilde{u}^+(x, y, z)$ and $\tilde{u}^-(x, y, z)$ are the propagating and contra-propagating complex electromagnetic waves inside the semiconductor. Given the high reflectivity of the Bragg mirror, we can assume they have the same amplitude. By supposing that the electromagnetic mode size is not changing much over the micro-cavity length ($z_r \gg L_{uc}$) we can separate the longitudinal and transverse contribution. Then by integrating along z on the QWs we have:

$$g_{mod} = \frac{n_{sc} g_0 \iint_{x y} T(x, y) |E(x, y)|^2 dx dy \int_{QW} |E_{int}|^2 2 \cos^2(k_0 z) dz}{|E_{ext}|^2 L_c \iint_{x y} |E(x, y)|^2 dx dy} \quad (3.2)$$

where g_0 is the linear gain in cm^{-1} for one QW and $T(x, y)$ is its normalized transverse profile such that $g(x, y) = g_0 T(x, y)$. n_{sc} is the refractive index of the semiconductor and $k_0 = 2\pi n_{sc}/\lambda$ the wavenumber. From the longitudinal dependency of the ratio between the field inside the micro-cavity and outside, we can define the longitudinal confinement factor as [Laurain 2010]:

$$\Gamma_z = \Gamma_{uc} \times \frac{1}{L_c} \int_{QW} 2 \cos^2(k_0 z) dz \quad (3.3)$$

where we find the micro-cavity confinement factor $\Gamma_{\mu c}$ (see § 3.1.2). The other terms reflect the overlap between the QWs and the standing wave pattern. If we assume that the QWs are positioned at the anti-nodes of the standing wave, then the longitudinal confinement factor can be reduced after integration to:

$$\Gamma_z \simeq 2 \Gamma_{uc} N_{QW} \frac{L_{QW}}{L_c} \quad (3.4)$$

where L_{QW} is the QW length, L_c the micro-cavity length and N_{QW} is the number of quantum wells. In the case of a position mismatch δz between the QWs and the standing wave anti-nodes, this parameter will reduce by a factor ($\cos^2(2k\delta_z)$). The other part of equation 3.2 relates to the transverse confinement factor and can be defined as:

$$\Gamma_{x,y} = \frac{\int T(x, y) |E(x, y)|^2 dA}{\int_A |E(x, y)|^2 dA} \quad (3.5)$$

This factor reflects the transverse overlap between the laser transverse mode and the gain distribution. For a TEM_{00} fundamental mode laser emission and Gaussian distribution of the gain, we find that the minimum amount of power needed to cross the threshold is when $\omega_p = \omega_0$ and $\Gamma_{x,y} = 1$.

In the end, we have an expression for the linear modal gain of our system $g_{mod} = \Gamma_{x,y}\Gamma_{uc}g_0$. Thus, by integrating over the round-trip distance inside the micro-cavity ($2L_c$) we have a final expression for the modal gain of the 1/2-VCSEL¹:

$$G_{mod}(N) = 4N_{qw}L_{qw}\Gamma_{uc}\Gamma_{x,y}g(N) \quad (3.6)$$

3.1.1 QWs placement

QWs placement inside the micro-cavity is essential to optimize. As seen from equation 3.3 to ensure an optimal gain extraction we must place the QWs on the anti-nodes of the micro-cavity standing wave pattern. And second, in the case of optical pumping inside the barrier, to achieve a uniform carrier density across all QWs, the longitudinal distribution of the QWs along the different anti-nodes must be optimized. The longitudinal absorption of the pump is given by the Beer Lambert's law:

$$A_b = 1 - e^{-\alpha_p L} \quad (3.7)$$

where A_b is the fraction of the pump absorbed inside the barrier, α_b is the linear absorption coefficient at the pump wavelength, λ_p which is around $1.3 \times 10^6 \text{ m}^{-1}$ at 808 nm for GaAs. L is the length of absorption which is equal to the active area length. It must be long enough to efficiently absorb the pump. For example, 85% of the incident pump power can be absorbed by an $7\lambda/2$ active zone length made of GaAs.

To efficiently distribute the QWs along the active zone. We need to consider the exponential longitudinal carrier density from the pump absorption and the diffusion length in the barrier ($L_d \simeq 150 \text{ nm}$ for GaAs). We can place up to 3 QWs with $\geq 20 \text{ nm}$ spacing on one anti-node and avoid any parasitic coupling effect. All the photo-generated carriers around $\pm L_d$ from the QW ends up contributing to the QW carrier density. We can then choose the optimal distribution of the wells between all the standing wave maxima to reach a uniform excitation. Figure 3.1 shows us an example of an active zone of $7\lambda/2$ and 6 QWs. In this case, the first anti-node has 2 QWs and the rest only one (02111010 distribution pattern). The resulting pump absorption in each QW has good uniformity, thus a good carrier density homogeneity.

¹the approximation of small gain ($e^{g2L_c} \sim 1 + g2L_c$) is made to have our gain percentage.

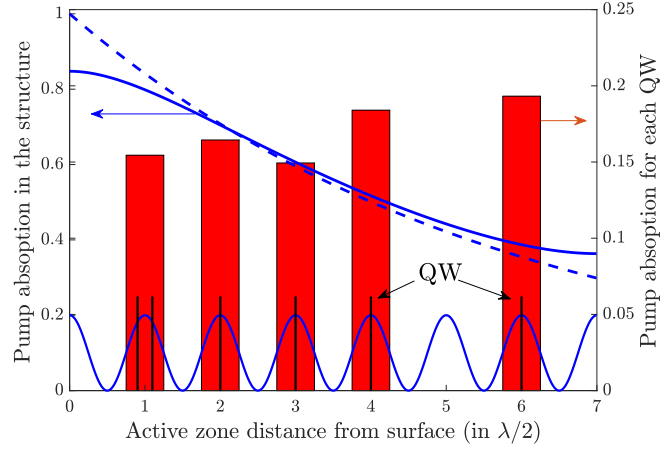


Figure 3.1: Example of optimization of the distribution of 6 quantum wells in an active zone of length $7\lambda/2$ in the case of barrier pumping.

3.1.2 Micro-cavity factor

The 1/2-VCSEL structure is by design a microcavity, with one mirror being the HR Bragg reflector and the other the air-semiconductor interface. This leads to an enhancement of the standing wave pattern inside the structure compared to outside. One way to express this effect is through the micro-cavity confinement factor:

$$\Gamma_{uc} = n_{ns} \frac{|E_{int}|^2}{|E_{ext}|^2} \quad (3.8)$$

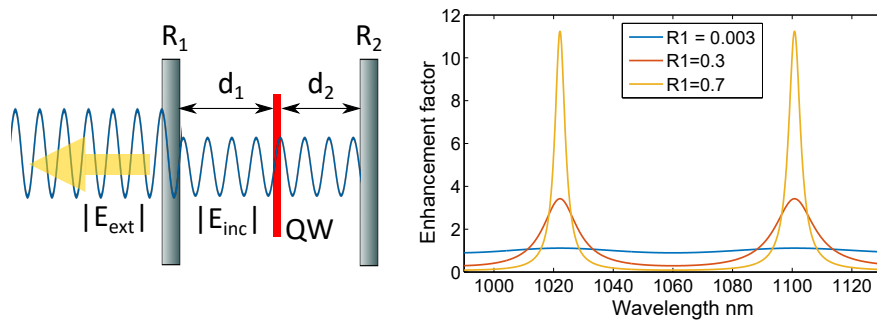


Figure 3.2: (Left) Point emitter within a microcavity formed by highly reflecting and partially transmitting mirrors (Right) Reflectivity of the microcavity with $R_2 = 99.95\%$ and different values of R_1 .

Where n_{sc} is the refractive index of the semiconductor and E_{int} , E_{ext} are respectively the field amplitude inside and outside the structure. All effects related to the field-matter interaction such as the optical gain, thermal lensing, non-linearity and others will be affected by this field enhancement. Following the formalism introduced by Kastler [Kastler 1962] and Benisty et al. [Benisty 1999] of a radiation pattern from a point emitter embedded within an optical micro-cavity (see figure 3.2) we can write:

$$\Gamma_{uc} = \frac{|\sqrt{1-R_1} \exp(-i2\phi)|^2}{|1 - \sqrt{R_1 R_2} \exp(-i2\phi)|^2} = \frac{1 - R_1}{1 + R_1 R_2 - 2\sqrt{R_1 R_2} \cos(2\phi)} \quad (3.9)$$

with

$$\phi = k_0 n (d_1 + d_2) \cos(\theta) \quad (3.10)$$

From this by fixing $R_2 = 1$ (HR Bragg mirror) we can see that it is possible to control the strength of the enhancement by tuning the reflectivity R_1 of the top mirror. This effect is also dependent on the wavelength through the phase term ϕ . If the micro-cavity optical length $n(d_1 + d_2)$ is a multiple of, $\lambda/2$ then the effect is maximum, and we are in a resonant configuration. In the other case, if the optical length is a multiple of $\lambda/4$ the effect is minimal, and we are in an anti-resonant configuration.

3.1.2.1 Fourier Spatial filtering

The phase term is also dependent on the emission angle, implying a filtering of spatial frequency. The Fresnel reflection being polarization-dependent, the filtering should be as well. However, to simplify the calculation, we will for now assume a constant reflectivity with the incident angle. Assuming we are lasing on one resonance at normal incidence, the microcavity will affect both the amplitude and phase of the beam spatial spectrum. Figure 3.3 plots the normalized micro-cavity factor as a function of the numerical aperture in the air $NA = n \sin(\theta)$.

The amplitude filtering is similar to a numerical aperture limit. As with spectral dependence, it has a Lorentzian like shape. Defining the numerical aperture finesse as $F_t = \theta_{1/2}/\pi$ with the angle $\theta_{1/2}$ representing the half width half maximum angle, we can express this function as a parabola. From figure 3.3 we can see the different impacts using the angle dependent reflectivity. We also see that the angle independent reflectivity curve is an average of the two different polarization ones. We also remark that for angles below $\theta_{1/2}$ all curves are similar.

$$\Gamma(\theta) = 1 - \frac{\theta^2}{2\theta_{1/2}^2} \text{ and } \theta_{1/2} = \cos^{-1} \left(1 - \frac{\sin^{-1} \left(\frac{1-R}{2\sqrt{R}} \right)}{k_0 n e} \right) \quad (3.11)$$

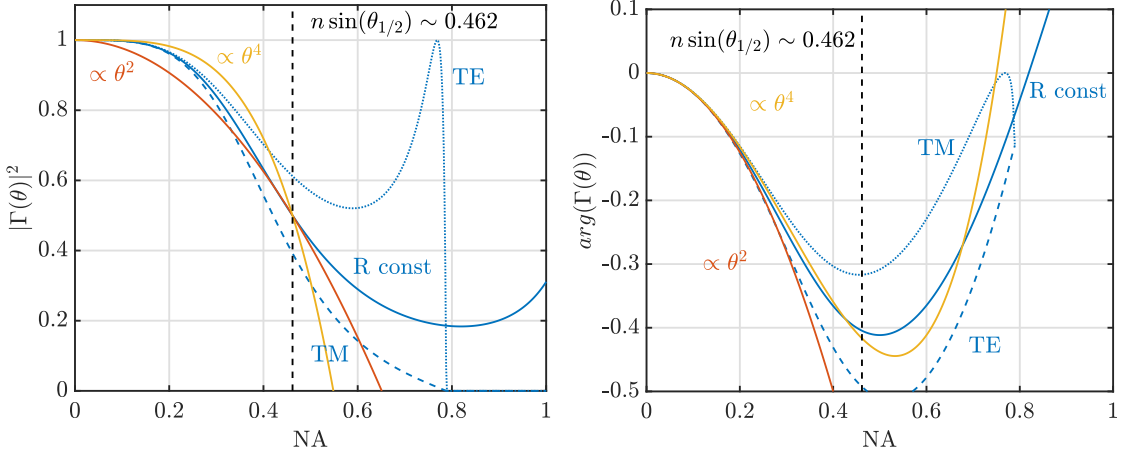


Figure 3.3: (a) Normalized intensity transfer function of the micro cavity versus the transverse wavevector. (b) Normalized phase transfer function of the micro cavity versus the transverse wavevector. Full line for R constant, dashed line for TE polarization and dotted line for TM polarization. Both R constant plots are fitted with a parabolic function and a fourth order one.

From this, we can express the NA limit in the air for a micro-cavity as $NA_{\Gamma_{\mu c}} = n \sin(\theta_{1/2})$. For the parabolic approximation, this corresponds in terms of the spatial spectrum transfer function to a frequency band by:

$$\Delta k \sim \sqrt{\frac{k_0 n}{e} \frac{1 - R_1}{\sqrt{R_1}}} \quad (3.12)$$

Where $e = d_1 + d_2$ is the micro cavity length and R_1 the top mirror reflectivity. For high reflectivity and long cavity length, the band is reducing. In real space, it corresponds to a diffusion term limiting the smallest size achievable. In our case, it must be as high as possible to not limit our system.

The micro-cavity being non-null in length, it will also contribute to the laser cavity diffraction through the effective optical length $L_{eff} = 2\Gamma_{\mu c} n e$. Or if we look at it with the Fresnel approximation in Fourier space, it will be a phase parabola $e^{-i\lambda L_{eff} \nu^2}$.

As seen in figure 3.3, both those effects also contain higher-order terms that will perturb the parabolic expression. For simplicity, we will only look at the fourth order term θ^4 in the phase spectrum that can be related to spherical aberration in the field of imaging optics. In the amplitude spectrum, the fourth order term tends to flatten the response toward a less disturbing top-hat shape, while in the phase spectrum it will perturb the diffraction. The full phase with second and fourth order coefficient can be written for low finesse cavity as:

$$\phi(\theta_{air}) \simeq -\frac{\theta_{air}^2}{1.5\theta_{1/2}^2 n^2} + \frac{\theta_{air}^4}{4\theta_{1/2}^4 n^4} \quad (3.13)$$

3.1.2.2 Resonant Design

For a resonant micro-cavity design, the length of the active area must be a multiple of $\lambda/2$. This gives rise to constructive interference in the active zone, thus an enhancement effect of the field (see figure 3.4). It will result in a higher modal gain, but a more pronounced spectral filtering. The confinement factor $\Gamma_{\mu c}$ is at its maximum at the design wavelength, and its bandwidth is partly dependent on the length of the active zone and the micro-cavity reflectivity. A lengthier active zone and/or higher reflectivity means a smaller bandwidth. One way to increase the semiconductor-air interface reflectivity is to add a Bragg reflector of a few AlGaAs/GaAs pair on the top of the structure (see figure 3.5). With this, it is possible to control the top mirror reflectivity and thus control the strength of the field enhancement effect.

The increased wave-matter interaction in this configuration allows for larger effective gain, thus lower threshold. However, this also increases the disadvantageous effects such as thermal sensitivity, thermal lensing or surfaces losses sensibility. The small bandwidth also means that we need to ensure a good match between the maximum of the gain curve and the micro-cavity resonance. This implies a precise growth process (composition of the wells and thickness of the epitaxial layers) and a good anticipation of the thermal red-shifting effect.

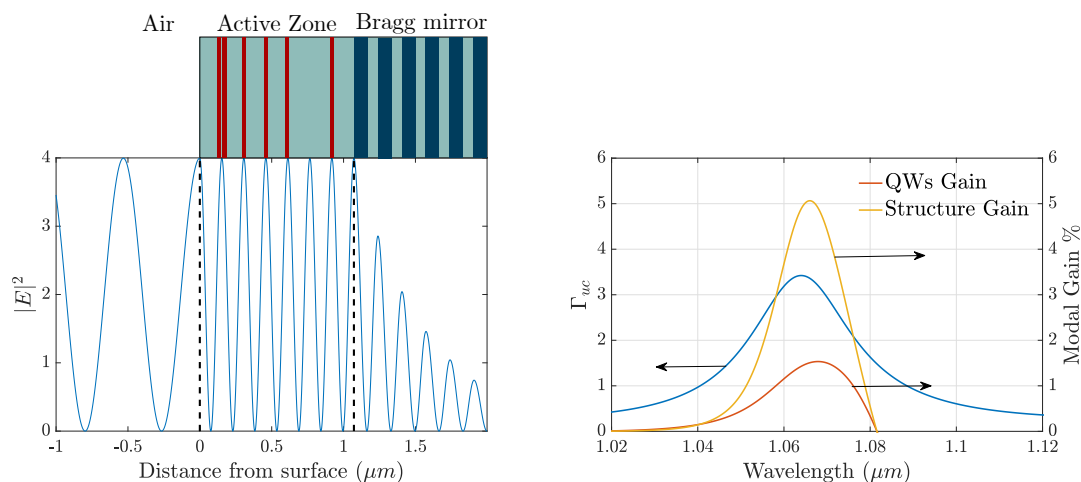


Figure 3.4: (Left) Calculation of the intra-cavity field intensity $|E|^2$ for a simple resonant structure ($7\lambda/2$ length). (Right) Confinement factor $\Gamma_{\mu c}$ and the effective gain of the structure.

This configuration also exhibits a field maximum on the air-semiconductor interface. These properties can be useful when adding a functional layer to the 1/2-VCSEL, such as a phase and/or intensity masks, to increase interaction with the field.

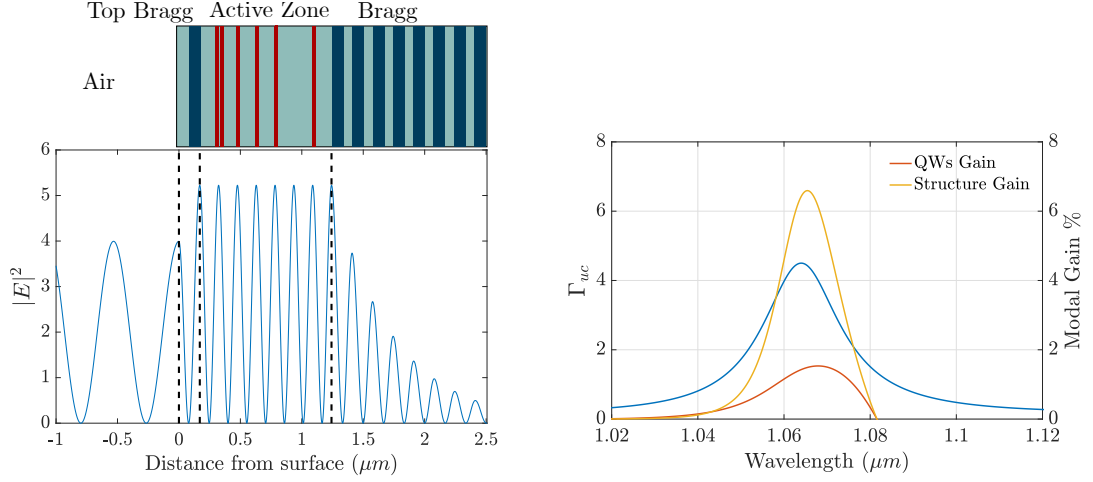


Figure 3.5: (Left) Calculation of the intra-cavity field intensity $|E|^2$ for an enhanced resonant structure ($7\lambda/2$ length and top Bragg mirror). (Right) Confinement factor $\Gamma_{\mu c}$ and the effective gain of the structure.

3.1.2.3 Anti-resonant Design

In the anti-resonant design, the active zone length must be an odd number of $\lambda/4$. In this case, destructive interferences occur inside the micro-cavity and lead to a diminution of the electric field intensity inside the structure compared to outside (see figure 3.6). A node of the standing wave is on the gain chip surface, reducing the effect of surface losses and the interest for phase or intensity integrated masks.

The weak coupling reduces the effective gain thus a higher threshold, but the effective bandwidth becomes equivalent to the QW bandwidth or even larger (higher $\Gamma_{\mu c}$ at the edge of QW bandwidth than it's peak). This can be very valuable for large tunability application or wide bandwidth system (mode-locking) with a high finesse optical system.

In our case, resonant design is preferred for a large effective gain and large non-linearity. However, the need to limit thermal lensing effect and keep a large enough bandwidth for mode-locking means that a simple resonant design with a low enhancement factor is preferred.

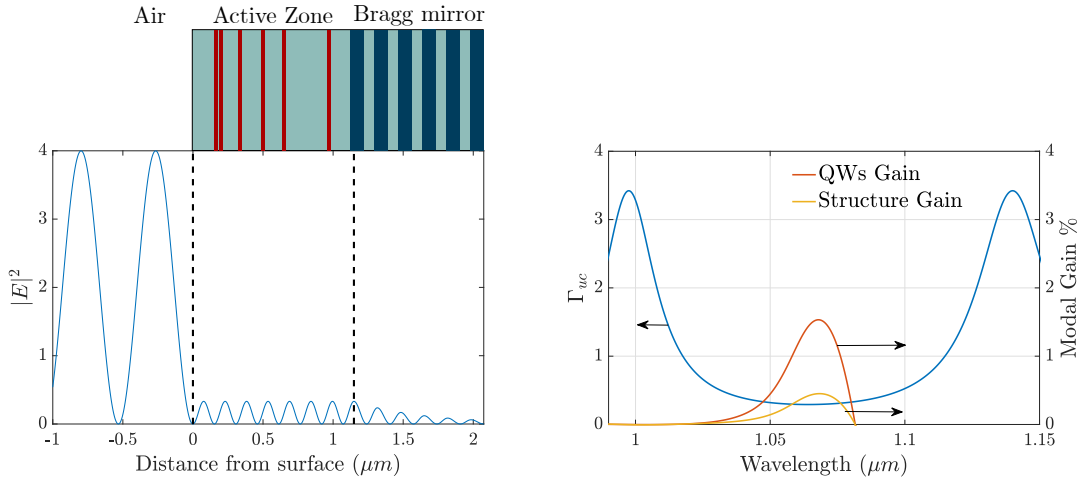


Figure 3.6: (Left) Calculation of the intra-cavity field intensity $|E|^2$ for an anti-resonant structure ($7.5\lambda/2$ length). (Right) Confinement factor $\Gamma_{\mu c}$ and the effective gain of the structure.

3.2 High Gain Design

From the modal gain expression (equation 3.6) we can find the optimum design parameters of our 1/2-VCSEL (number of QWs N_{QW} , micro cavity factor $\Gamma_{\mu c}$). From a phenomenological approach, we can express the max QWs gain as a function of carrier density and incident power density since $I_{inc} \propto N$ and from equation 2.19 we have according to [Coldren 2012]:

$$g(I) = g_0 \times \ln \left(\frac{I}{I_{tr} N_{QW}} \right) \quad (3.14)$$

where I_{tr} is the power density transparency of a single QW and g_0 the material gain in cm^{-1} .

We need a 1/2-VCSEL capable of supporting the losses of the output coupler ($\sim 2\%$), the saturable absorber ($\sim 10\%$), and the cavity elements ($\sim 2\%$). In total, we need a gain section with more than 14% gain. We also want to keep a large bandwidth for mode-locking and temporal localized structure operation. Figure 3.7 shows the plot of equation 3.6 as a function of incident pump power with the assumption of $\Gamma_{x,y} = 1$ for different number of QWs and micro-cavity configuration. We first see that the anti-resonant configuration ($\Gamma_{\mu c} = 0.3$), with a small micro-cavity enhancement factor, is not suitable for large gain despite its large bandwidth. The configuration with $\Gamma_{\mu c} = 11$ easily cross the 15% line with 6 or 12 QWs, however the gain bandwidth starts to be limited $\sim 3 \text{ nm}$. This design also increases dramatically the thermal lensing effect and internal losses due to a

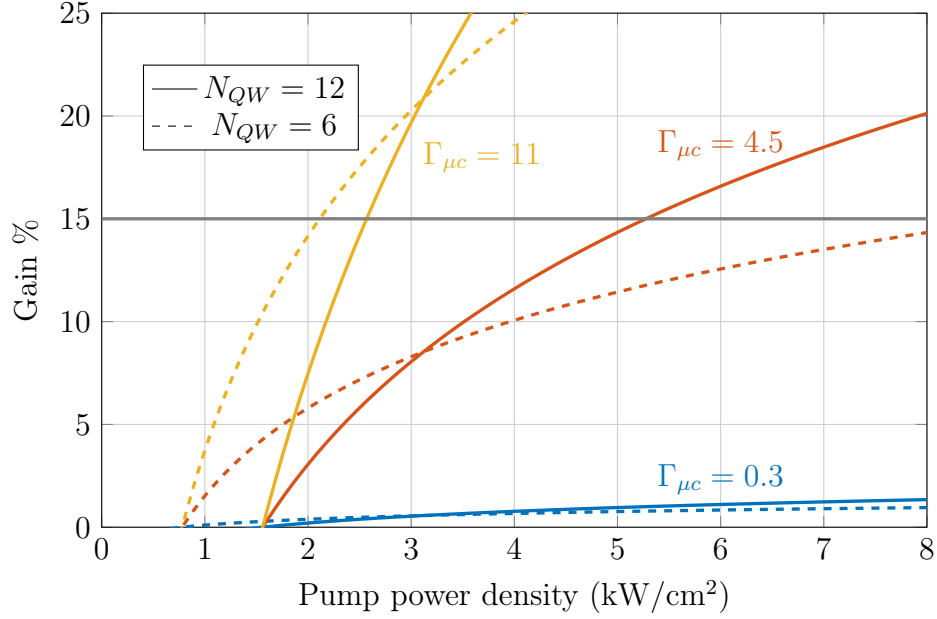


Figure 3.7: Simulated gain for 12 QWs (solid line) and 6 QWs (dashed lines) for different micro-cavity factor. (blue) an anti-resonant configuration $\Gamma_{\mu c} = 0.3$. (red) an enhance resonant configuration with a single top bragg pair $\Gamma_{\mu c} = 4.5$. (gold) an enhance resonant configuration with a four top bragg pair $\Gamma_{\mu c} = 11$.

longer effective length. Finally, for a smaller enhancement factor $\Gamma_{\mu c} = 4.5$ and 12 QWs, we can reach high gain at the detriment of a higher power density. This could be a disadvantage for laser efficiency above the threshold and reaching high output power, but is less of a concern in our case since we aim to work close or below the threshold for non-linear localization.

In the end, we choose the to have 12 QWs with a resonant design and a small micro-cavity factor of $\Gamma_{uc} = 4.5$. To obtain that value, a single Bragg pair is needed.

3.2.1 Active zone layout

The active region length was chosen as $L = 14\lambda/2$ with $\lambda = 1064$ nm as our emission wavelength target. It was chosen to accommodate the 12 QWs and reach a homogeneous excitation across all of them with an optical pumping scheme in the barrier at $\lambda_p = 808$ nm. They have been arranged on the 1064 nm standing wave anti-nodes by group of 2 in a 022202020020000 distribution from top Bragg to bottom Bragg. Strained balance InGaAs/GaAsP quantum wells and GaAs spacer was the chosen semiconductor technology to reach emission wavelength in the near infra-red around $\lambda = 1064$ nm.

To enhance the resonant effect to $\Gamma_{\mu c} = 4.5$ and slightly improve the modal gain to reach, 15% a single pair of a AlAs/AlGaAs were added on top of the active zone to act as a top Bragg mirror. The AlGaAs is chosen for pump energy transparency and thus not degrading the pumping efficiency. This gives us a FWHM resonance of 8.35 nm. Figure 3.8 shows the different layers material and arrangement, as well as the corresponding energy bandgap and refractive index. We can also see in this figure the laser and pump energy relative to the energy gap of the structure.

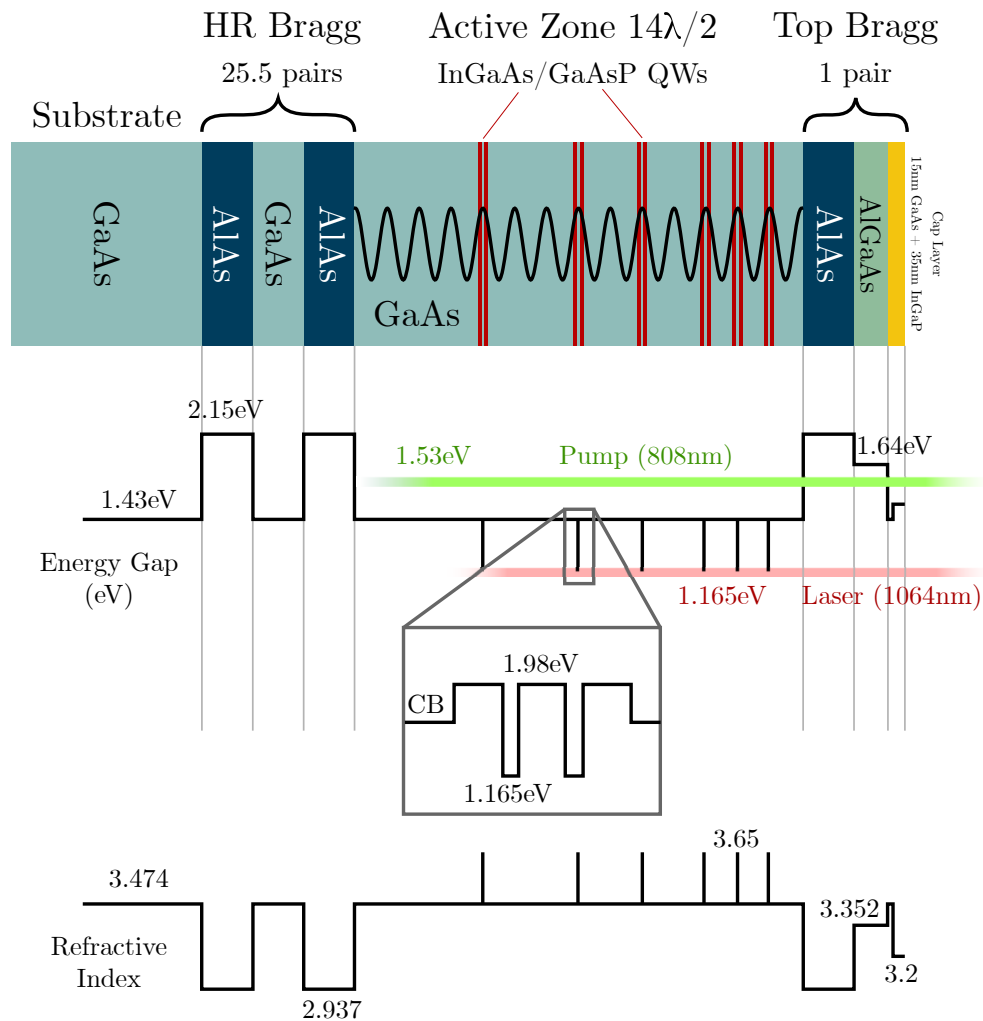


Figure 3.8: Structure design for high gain at 1064 nm. Structure numbered V0450.

Figure 3.9 display the measure reflectivity of the device right after the growth thanks to a Fourier Transform Infrared spectroscopy. The measure of photoluminescence of the QWs is also shown in the same figure. We see the expected active zone resonance at, 1060 nm with a higher order resonance at 1118 nm. The

QWs absorption also provokes a dip in the reflectivity curve at, 1041 nm which corresponds to the QWs absorption spectrum peak. This ~ 20 nm offset of the QWs spectrum is necessary to properly overlap the gain peak and the micro-cavity resonance under excitation because of a red-shift of the gain from the increase in temperature caused by the pumping action (0.3 nm/K).

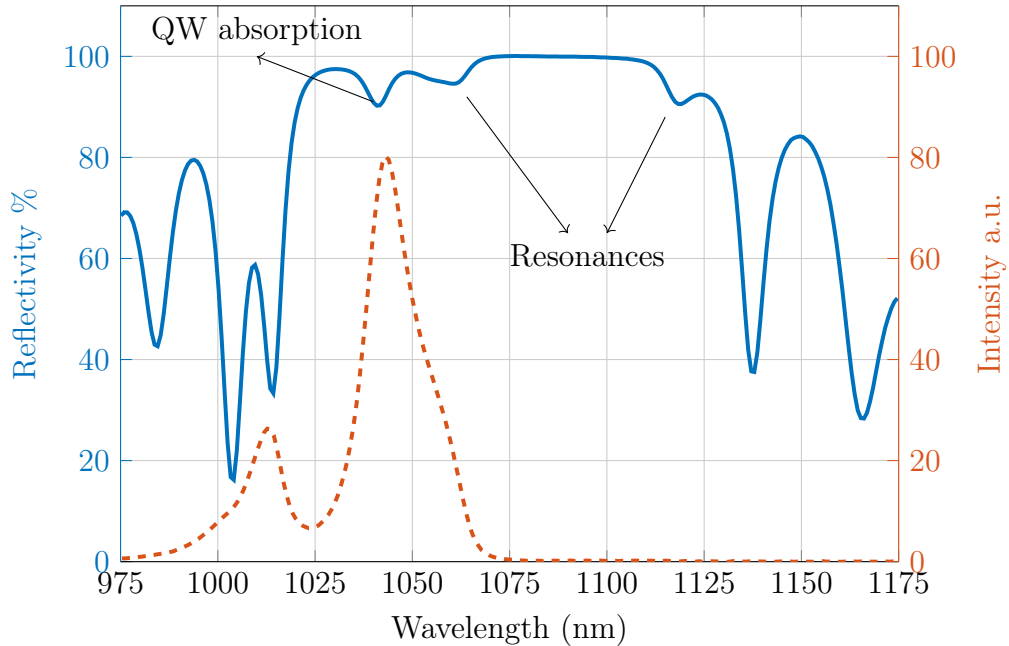


Figure 3.9: Measure reflectivity for the high gain design using FTIR method and measure QWs photoluminescence spectrum.

3.2.2 Growth process

The control of the epitaxial growth is a key point for the development of 1/2-VCSEL structures. It is indeed fundamental to be able to produce reproducible active zone emitting at the desired wavelength and to precisely control the thickness of each layer. At present, GaAs is a mature and widely industrialized platform, allowing for great semiconductor device quality with low defects density and QW relaxation.

The growth is done in the “*Centre de nanosciences et de nanotechnologies*” by Gregoire Beaudoin within the team of Isabelle Sagnes through the MOCVD (Metalorganic Chemical Vapor Deposition) epitaxy process.

Metal-organic precursor source (TMGa, TMAI, TMIIn, AsH₃) mixed with non-reactive gases (such as hydrogen) are injected into a high-pressure reactor

chamber (60 *mTorr*) where pyrolysis at high temperature (700 °C) allows the chosen semiconductor to bond on the wafer substrate surface. With this process, it is possible to achieve high-growth speed (to 10 $\mu\text{m}/\text{h}$) with a few monolayers precision. Alloy composition can be controlled through gas flow adjustment, allowing a great reproducibility. All semiconductor structures were designed at the IES and grown in the C2N. The FTIR measurement was also done at the C2N.

3.2.2.1 Large-scale inhomogeneity

The growth process can introduce large-scale inhomogeneity from uneven radial growth of each layer. It will impact the thickness of the active region and lead to a radial variation of the micro-cavity resonance.

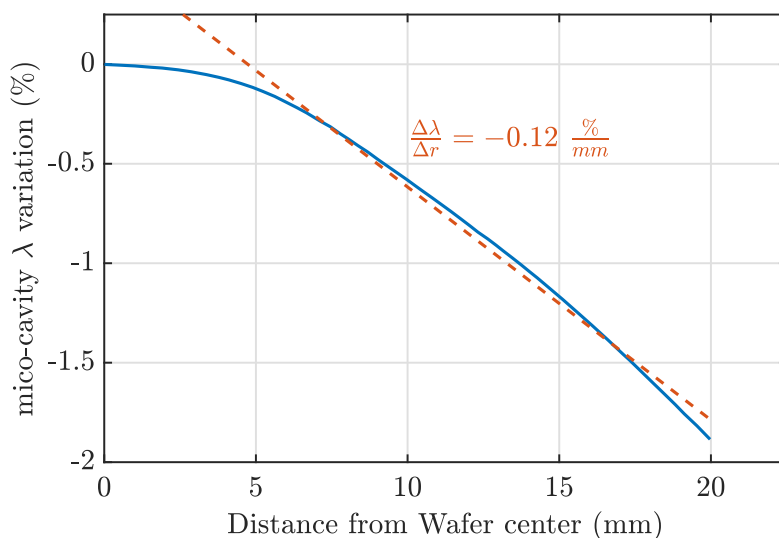


Figure 3.10: Measured micro-cavity resonance variation along the radial axis of the semiconductor wafer.

From figure 3.10 we see that further from the wafer center the micro-cavity resonance shifts to the blue ($\Delta\lambda/\Delta r \approx -0.12\% \text{ mm}^{-1}$), meaning that a reduction of the layer thickness has occurred. This variation can be used in practice to precisely tune the laser wavelength emission by transversally shifting the pumped region. In our case, this effect can be used to help match the SESAM and Gain resonances. In the scale of our pumped region around, 100 μm this effect is small $< 0.012\%$.

3.2.2.2 Small-scale inhomogeneity

We have also observed a small-scale inhomogeneity of the QWs gain. Figure 3.11 shows the transverse field emission pattern on the surface of a very high gain 1/2-VCSEL with a large micro-cavity enhancement factor $\Gamma_{\mu c} = 11$ placed inside a self-imaging optical cavity close to the threshold. The small laser spots were found to follow the 1/2-VCSEL gain mirror after transverse translation. Meaning that they were “gain pinned” by some small-scale inhomogeneity or “puddles” of the optical gain.

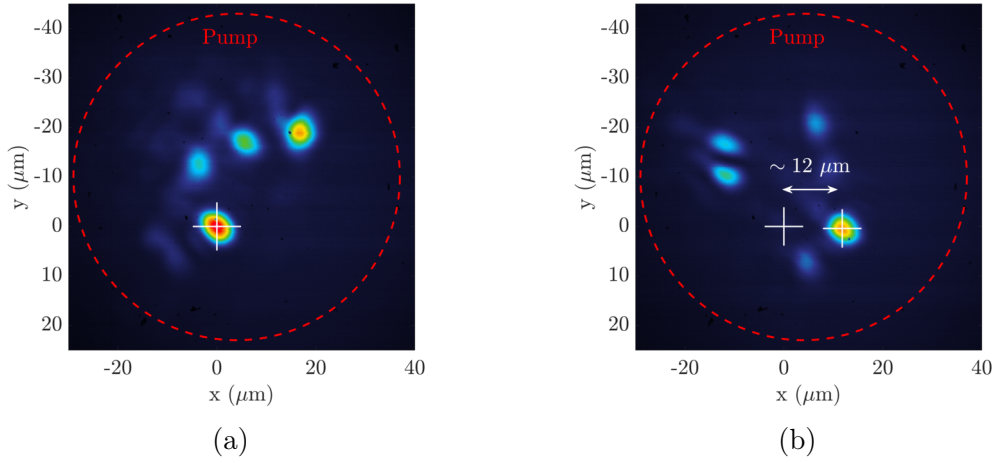


Figure 3.11: Near-field intensity profile of a very High gain 1/2-VCSEL in a self-imaging cavity without saturable absorber, $\Gamma_{uc} > 10$. (a) Small spots ($\omega \sim 4 \mu\text{m}$) seen close to threshold. (b) $12 \mu\text{m}$ translation in the positive x-direction of the structure. The small spots are following the gain translation. They are gain pinned by small gain modulation.

This gain modulation is small ($< 10\%$) and found to be around $5 \mu\text{m}$ to $10 \mu\text{m}$ in scale. It is believed that they originate from the QWs nanostructure interface inhomogeneity due to the inherent diffusion process of the MOCVD growth. For large transverse structure or cavity confined transverse modes, this QWs gain “puddles” does not impact NL modes structures. The quantum efficiency is not impacted for small or large light structure. However, for 3D light structuration and non-linear localized structure of the same scale as gain modulation, “puddles” can have an impact by pinning the structuration, or modulating the local potential and thus limiting SLS freedom. Reducing the light-matter interaction and the micro-cavity enhancement factor will naturally reduce the impact of the QWs gain puddles.

3.2.3 First order characterization

The analysis of the 1/2-VCSEL reflectivity spectrum is the first step to ensure a good growth of the semiconductor structure and respect of the design. The next step is to use a simple laser set-up to characterize its properties. For that, we can measure the laser output power (threshold, efficiency) and the optical spectrum. These measurements provide us with good information about the gain properties of the 1/2-VCSEL.

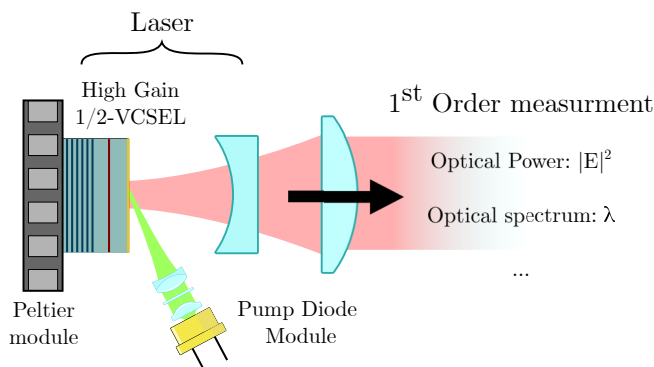


Figure 3.12: Set-up for first order characterization of the 1/2-VCSEL using a plano-concave laser cavity.

Figure 3.12 represents the laser set-up used for this characterization. The 1/2-VCSEL is optically pumped by a laser diode positioned at the Brewster angle, both to circularize the pump spot and to maximize the transmitted power into the active zone. We use a $\lambda/2$ polarizing plate to tune the pump polarization to a TM state. The structure is used as one end-mirror of the laser cavity and is mounted on a Peltier cooler module to control its temperature. The cavity is closed with a spherical mirror of 90% reflectivity and radius of curvature, $R_c = 10$ mm creating a few millimeters long plano-concave optical resonator. The laser light is then collimated using an off-the-shelf lens and is sent to the different measurement devices such as an optical power-meter and an optical spectrum analyzer.

3.2.3.1 Output power

The laser output power versus pump power density curve shown in figure 3.13a gives us access to important information such as the 1/2-VCSEL gain, internal losses and temperature sensibility. Since for laser action, gain must equal losses, we can use the pump power density at the threshold to estimate the structure modal gain using the curves of figure 3.7. For this design, we expected around 3.5 kW/cm^2 power density for 10% losses, and we measure 3.3 kW/cm^2 and 3.6 kW/cm^2 respectively for 20°C and 30°C Peltier cooler temperature. This means we have achieved the

correct micro-cavity enhancement factor and there is no considerable mismatch on the QWs positioning.

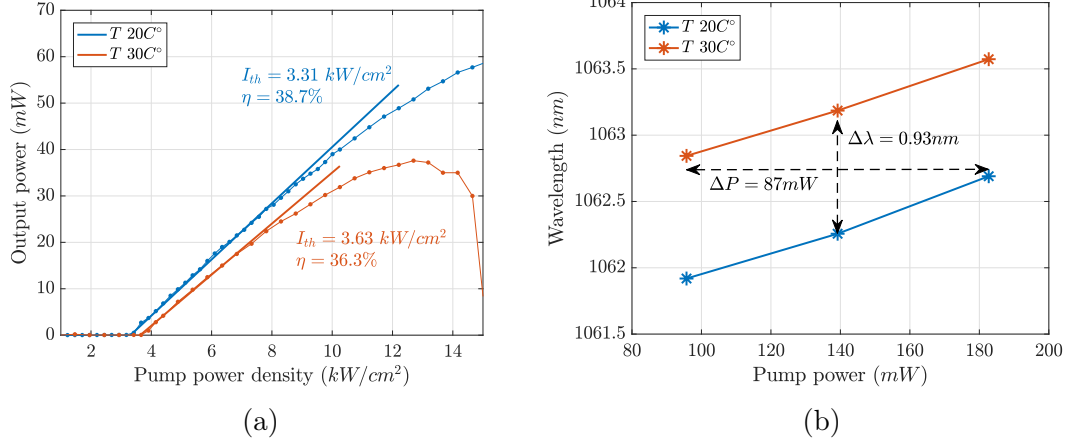


Figure 3.13: (a) Laser output power vs. pump power density for two temperature 20°C and 30°C. (b) Measured wavelength variation from Peltier temperature variation and pump power variation. In both measure $\omega_0 \simeq \omega_p$ with $\omega_p = 23.5 \mu\text{m}$.

The laser efficiency given by $(1 - \eta_T)\eta_d$ in equation 3.15 can be used to check the internal losses of the device. This formula links the laser output power with the incident pump power through the efficiency factor. This factor can be separated into several individual efficiency. First $(1 - \eta_T)$ is the fraction of the pump power used for light amplification, while the rest is converted into heat. For a design onto GaAs at, $\lambda = 1064 \text{ nm}$ the useful pump fraction is around 70% [Laurain 2010].

$$P_{out} = (1 - \eta_T)\eta_d (P_p - P_{th}) \quad (3.15)$$

Then the differential efficiency η_d is as follows:

$$\eta_d = \eta_{ab}\eta_q\eta_i\eta_{ext}\Gamma_{x,y} \quad (3.16)$$

where $\eta_{ab} = T_r A_b$ is the fraction of incident pump power absorbed inside the active zone, T_r is the transmitted power fraction inside the semiconductor and A_b the absorption in the barrier. $\eta_q = \lambda_p/\lambda_l$ is the quantum defect efficiency and η_i the internal quantum efficiency whose value is 1 above threshold. $\Gamma_{x,y}$ is the transverse confinement factor and depends on the pump and laser beam size. Then the output coupling efficiency η_{ext} is given by:

$$\eta_{ext} = \frac{-\ln(R)}{-\ln(R) + \alpha_{\mu c}\Gamma_{\mu c}} \quad (3.17)$$

where $-\ln(R)$ is the output coupler losses and $\alpha_{\mu c}$ the internal losses of the semiconductor. Its importance is enhanced by the micro-cavity factor $\Gamma_{\mu c}$. From this, we can see that a high-efficiency means that, $-\ln(R) \gg \alpha_{\mu c} \Gamma_{\mu c}$ which reflects a good structure quality with low defect and internal losses. We find with our measurements an overall efficiency of 38% with $R = 10\%$ thus we can estimate $\alpha_{\mu c} = 0.35\%$.

In figure 3.13a we can also see the impact of temperature from the increase in threshold (meaning a gain reduction) between $T = 20^\circ\text{C}$ and $T = 30^\circ\text{C}$. At high pump power, the QWs temperature also rises, leading to the roll-over effect seen in the measurements. This gain reduction also comes from the detuning between the cavity resonance drifting at 0.07 nm/K by thermal variation of the optical index and the drift of the gain spectrum at 0.3 nm/K . It is conventional to describe those effects with the following equation:

$$P_{th}(T_2) = P_{th}(T_1)e^{\frac{T_2-T_1}{T_0}} \quad (3.18)$$

Using the characteristic temperature T_0 as a figure of merit. For $\Delta T > T_0$ when the temperature rise equals, T_0 then the output power starts to saturate and the laser threshold increases quicker than the useful pump power, leading to a roll-over. On the other end, for $\Delta T \ll T_0$ the threshold does not change, and high output power can be reached. However, at high carrier density, Auger effect can start to degrade the quantum internal efficiency. A large T_0 is then important for high-power application and temperature sensitivity of the system. In our case, for 10% at 20°C we can estimate $T_0 = 100\text{ K}$ which is coherent with GaAs based 1/2-VCSEL [Laurain 2010].

3.2.3.2 Lasing wavelength tunability

Another impact of the rise of temperature can be seen on the laser spectrum and can be used as a way to tune the laser emission wavelength. The temperature rise is impacted by the thermal resistance of the semiconductor structure and the pump size, as seen in § 2.4.2. The optical spectrum offers us a way to estimate its value:

$$R_{th} = \frac{\Delta T}{\Delta P} = \frac{\Delta T}{\Delta \lambda} \times \frac{\Delta \lambda}{\Delta P} \quad (3.19)$$

From this equation, we can see that the thermal resistance in K/W can be separated into two wavelength dependent components. The wavelength variation through pump power and the inverse wavelength variation with the Peltier cooler temperature. From the measurement with $\omega_p = 23.5\ \mu\text{m}$ in figure 3.13b we find that $\frac{\Delta \lambda}{\Delta P} = 8.8\text{ nm/W}$ and $\frac{\Delta \lambda}{\Delta T} = 0.09\text{ nm/K}$. Those variations follow the variation of the micro-cavity resonance. Using those measures, we can calculate $R_{th} = 98\text{ K/W}$.

This high value is coherent with the small pump size and the previous simulation, but it also means that a high-temperature rise occurs, this explains the measured roll-over for high excitation.

All relevant properties and parameters of the high gain 1/2-VCSEL design are combined into table 3.1.

Material gain	g_0	570 cm ⁻¹
Puddles modulation	Δg_0	<10%
Losses in chip	α_{uc}	0.35%
Pump power density at transparency per QW	I_{tr}	0.11 kW/cm ²
Characteristic temperature	T_0	100 K
Quantum well width	L_{QW}	8 nm
Number of quantum well	N_{QW}	12
Confinement factor	Γ_{uc}	4.5
FWHM resonance bandwidth	$\Delta\lambda_{\mu c}$	8.35 nm
Resonance wavelength shift (T°)	$\frac{\Delta\lambda}{\Delta K}$	+0.09 nm/K
Resonance wavelength shift (Inhomogeneity)	$\frac{\Delta\lambda}{\Delta r}$	-0.12 %/K
Pump wavelength	λ_p	808 nm
Pump absorption coefficient	A_b	92%
Transmission pump chip	T_r	100%
Heat conversion	η_{th}	30%
Quantum defect	η_q	76%
Diffusion length at transparency	$L_d(N_{tr})$	3 μ m
Lifetime at transparency	$\tau(N_{tr})$	3 ns
Mono-molecular recombination coefficient	A	1 \times 10 ⁶ s ⁻¹
Bi-molecular recombination coefficient	B	1 \times 10 ⁻¹⁰ cm ³ /s
Auger recombination coefficient	C	1 \times 10 ⁻³⁰ cm ⁶ /s
Ambipolar diffusion coefficient	D_{np}	30 cm ² /s

Table 3.1: Main parameters of the High gain structure.

3.3 SESAM Design

To create the optical bi-stability essential for localized structure, saturable losses are needed. Using the GaAs platform, it is possible to design what is called a Semiconductor Saturable Absorber Mirror (SESAM). Typically, it consists of a Bragg mirror and a single quantum well as the absorber layer. The main differences

from the 1/2-VCSEL being that it is not used in the gain regime and carrier lifetime is usually shorter. As with the 1/2-VCSEL and the semiconductor technology, it is possible to engineer to a certain degree its physical properties. In the case of the SESAM the important properties are the modulation depth or the maximum change in reflectance, the amount of non-saturable loss, the saturation fluence or saturation intensity and the carrier lifetime.

3.3.1 SESAM interest

SESAM are mainly used for passive mode-locking (PML) in a wide range of lasers. Three fundamental models can explain passive mode-locking, the slow saturable absorber with dynamic gain saturation [Haus 1975a], the fast saturable absorber mode-locking [Haus 1975b] and soliton mode-locking [Kärtner 1995]. The speed adjective referring here to the recovery time of the absorber versus the gain. For semiconductors, this implies that we have a recovery time in the ps range for “fast” SESAM and the ns range for “slow” SESAM. In all those models, the SESAM is used to open a small positive net gain window where only the pulse is amplified. The window size and pulse width is then dependent on the pulse intensity, SESAM recovery time and gain bandwidth. The exception being that for soliton mode-locking, the pulse is further shortened by the self-phase modulation and kept stable through the balance of SPM with group velocity dispersion.

To reduce the recovery time, the excited carrier lifetime must be short, and thus we must create a large density of state inside the energy gap to quickly trap the excited carrier. For this, different processes have been developed in the past. Low temperature III-V semiconductor growth by molecular beam epitaxy (LT-MBE) creates an excess of group V atoms and the carrier lifetime is dramatically reduced due to the trapping and subsequent recombination of carriers at these centers [Gupta 1992]. High-energy ions irradiated QWs after growth also lead to fast carrier lifetime as short as 5 ps [Gopinath 2001]. This process is usually more delicate to fabricate and has relatively high non-saturable losses. Another method compatible with a standard MOCVD growth consists in increasing the surface recombination rate by quantum tunneling effect. For this, the QW of the SESAM must be placed close to the semiconductor surface (≤ 2 nm) [Garnache 2003].

In our case, it has been proven that temporal localized structure can arise from a passive mode-locked system where the round-trip time is greater than the recovery time of gain ($\tau_{RT} \gg \tau_g$) [Marconi 2014]. Then a “fast” SESAM is needed for this application. The rest of this manuscript is focused on the spatial non-linear structuration and use a “very-slow” SESAM design to free ourselves from the temporal dynamics. By using a SESAM with similar or longeur lifetime than the gain, no temporal window of net-gain can be open for pulse formation, and the SESAM saturation will simply follow the gain. For spatial structuration, a

“very-slow” SESAM allows us to keep the effect of spatial self-amplitude modulation without worrying with longitudinal dynamics.

To achieve this, no need to try to add a recombination center and using the same growth process than with the 1/2-VCSEL design is enough. In this case, the same care with accumulated strain and crystal interfaces quality must be taken.

3.3.2 Very-slow lifetime design

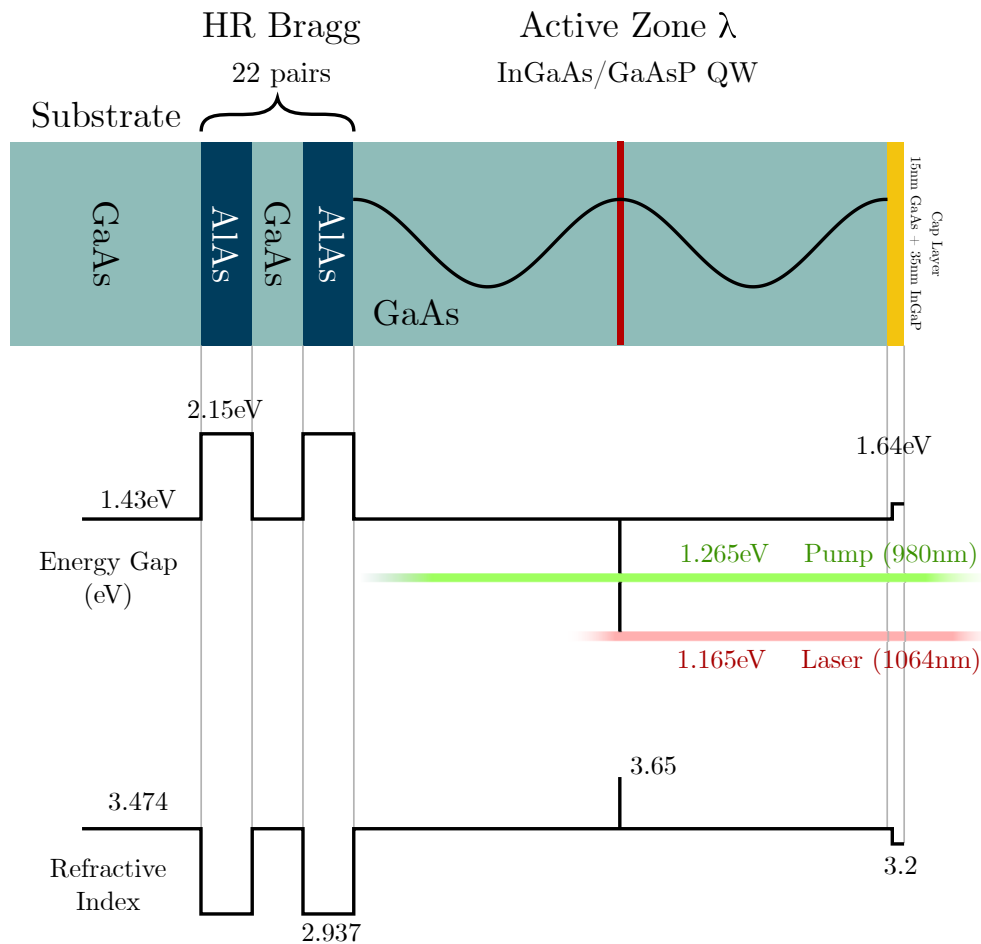


Figure 3.14: Structure design for slow saturable absorber semiconductor mirror at 1064 nm. Structure numbered V0598

The SESAM was designed on an undoped GaAs substrate to keep it transparent at the working wavelength ($\lambda = 1064$ nm) for use as an output coupler. The bottom Bragg mirror was made of 22 AlAs/GaAs pair with a max reflectivity of ($R = 99\%$). The active zone was made one wavelength long and a single InGaAs/GaAsP strain

compensated QW placed on the standing wave anti-node. This QW was made to have an absorption peak at ambient temperature around 1064 nm. This design is thus a simple resonant design, slightly enhancing the field inside the micro-cavity $\Gamma_{\mu c} = 3.5$. Pumping at $\lambda_p = 980$ nm is also possible to externally control the QW absorption while minimizing thermal effect.

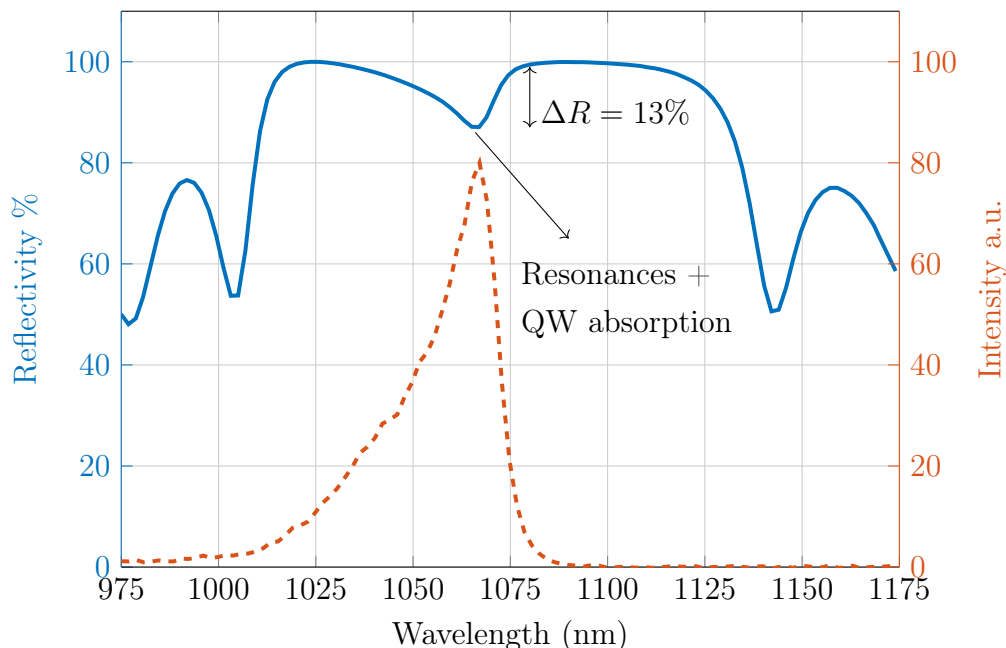


Figure 3.15: Measure reflectivity for the slow SESAM design using FTIR method and QWs photoluminescence spectrum.

Despite the resonant design, the bandwidth remains large thanks to the short length ($\Delta\omega_{\mu c} = 40$ nm). This allows for a simpler matching between the laser emission and absorption than with a highly resonant system such as in [Camelin 2018]. Considering the absorption coefficient of a single QW and the resonant design, we expect around 13% peak absorption. Both of those properties can be checked in figure 3.15 where contrary to the high gain design case, the absorption peak of the QW is matched with the micro-cavity resonance since no “red-shift” due to pumping is expected.

3.3.2.1 Saturable absorption measurement

The main goal of the SESAM is to provide saturable absorption for SAM effect, thus characterizing this behavior was important. Figure 3.16 describes the full set-up used for this measurement. We used a home-made laser emitting at 1064 nm as our laser source to probe the SESAM. The laser beam was collimated by an

$f = 50$ mm achromatic lens before isolating the source from possible feedback by an optical isolator. The incident laser beam was split by a 55:45 pellicle Beamsplitter, sending one part to the device under test and the other part to an HR dielectric mirror (*Layertech : 146440*) used as a reflective reference surface. Both reflected beams will then be combined by the beamsplitter onto a Silicon photodiode. In this way, both the HR dielectric mirror path and the SESAM path will undergo one transmission and one reflection on the beamsplitter, rendering its effect on power void.

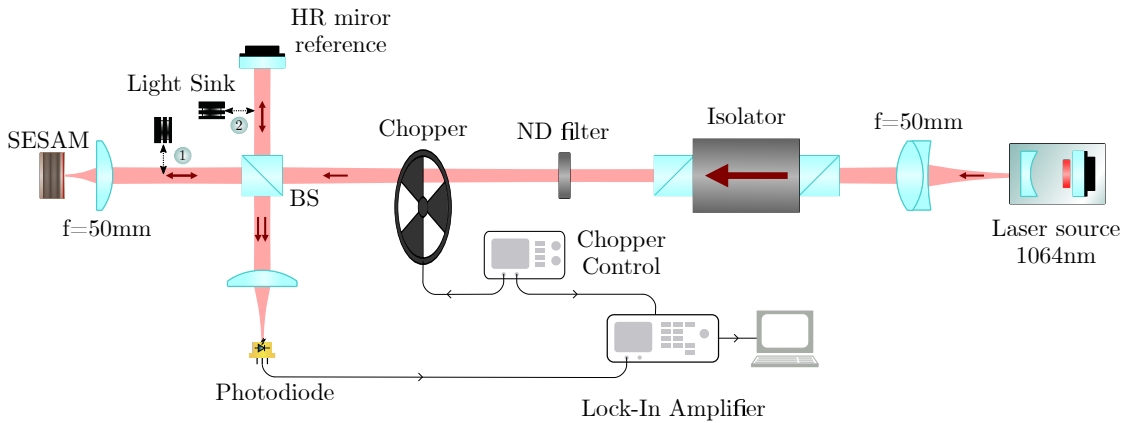


Figure 3.16: Set-up for the non-linear reflectivity measurement using a laser source at 1064 nm and high reflectivity dielectric mirror as a reference.

To measure the real reflectivity of the SESAM for different incident power density, the laser source was kept at a constant output power and wavelength while a set of neutral density filter was used before the beamsplitter to vary the input power over a few decades. The maximum incident power being, 48 mW with an attenuation range from 3 to 43 dB. A $f = 30$ mm achromatic lens was used to achieve a focused Gaussian spot on the SESAM of $\omega_o = 10 \mu\text{m}$ waist. To separate the useful signal from the noise, a lock-in amplifier with a chopper at 300 Hz on the main beam path was placed. An average of $N = 400$ points was taken for each measurement. To discriminate between the reference mirror and the SESAM, two measures were made, one with the SESAM path blocked (number one on the figure) and the other with the reference mirror blocked (number two on the figure). This process was repeated at least three times for each ND filter to ensure no outlier measurement. The measurement protocol was first calibrated using a gold mirror with known reflectivity instead of the SESAM.

Figure 3.17a shows the result of this measurement process, where the absolute non-linear reflectivity is plotted. The error bar represents the confidence at 95% from the multiple measurement variances. The power density was obtained using

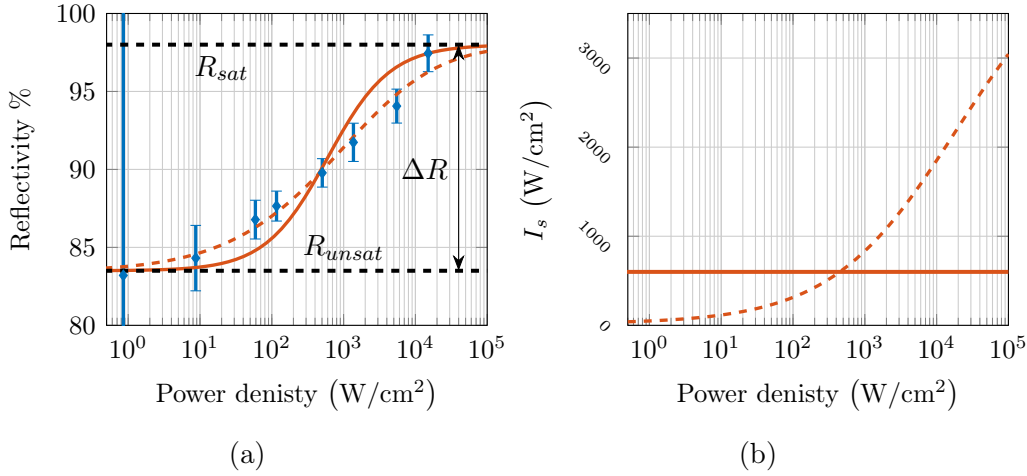


Figure 3.17: a) Measure of the non linear reflectivity for the slow SESAM design using a 1064 nm laser, (solid) fit with a constant $I_s = 600 \text{ W/cm}^2$, (dashed) fit with a variable $I_s(I) = I_{min} + I_{max}(1 - 1/(1 + \sqrt{I/I_0}))$ and $I_0 = 18.5 \text{ kW/cm}^2$. b) Variation of I_s for both fit curve, (solid) constant I_s , (dashed) variable I_s .

the disk area approximation for a Gaussian beam or $I = P/(\pi\omega^2)$. The solid curve represents a fit from a simple stationary two level rate equation:

$$R(I) = R_{max} - \frac{\Delta R}{1 + \frac{I}{I_s}} \quad (3.20)$$

In our case, this allows us to estimate key parameters such as the modulation depth $\Delta R = 14.5\%$, the saturated reflectivity $R_{sat} = 98\%$, the unsaturated reflectivity $R_{unsat} = 83.5\%$ and the saturation intensity $I_s = 600 \text{ W/cm}^2$.

Some disparity from the simple two level model are present. It could simply be explained by a non-constant saturation intensity. Looking at equation 2.14, we see that for low carrier density, the lifetime is long while for high carrier density the lifetime decreases until saturation. The saturation intensity being highly dependent on the level lifetime, $I_s = \frac{h\nu}{\sigma\tau}$ this can explain a non-constant value. By using a power density dependent I_s following this trend (see figure 3.17b, dashed line) we can improve our correlation with the data points. In the end, for reducing by half the saturable losses, we still have $I_s = 600 \text{ W/cm}^2$ but it quickly goes up delaying the fully saturated state.

3.3.2.2 Diffusion length measurement

Another interesting property to know for both the gain and absorber is the diffusion length of the carriers inside the QWs. For passive mode-locking, the size

of the net gain window opened by the saturable absorber dictates the size of the pulse (without soliton mode-locking effect). In the same way, the diffusion length will give us a limit on the window open by SAM and the spatial size of the “pulse”.

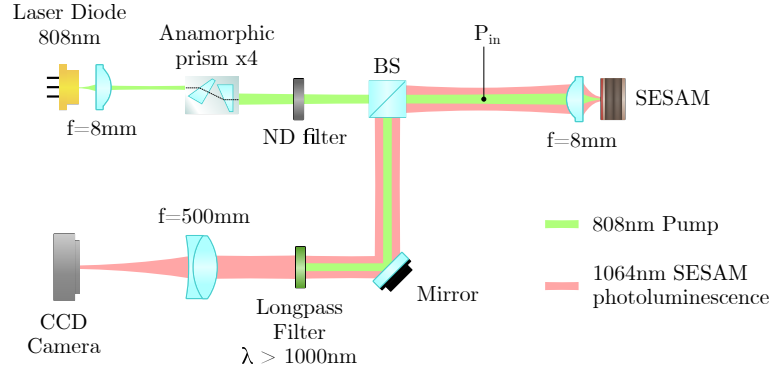


Figure 3.18: Set-up for the diffusion length measurement using a 808 nm laser diode as a pump while imaging the emitted photoluminescence.

We measured the diffusion length in both structures by pumping the QWs with a 808 nm laser diode and then looking at the spatial intensity profile of the QW photo-luminescence on the device surface with a 2D CCD camera. Using different neutral density filter to change the pump power, we were able to get data for different pump power density. Figure 3.18 shows the set-up for measuring the SESAM QW photo-luminescence.

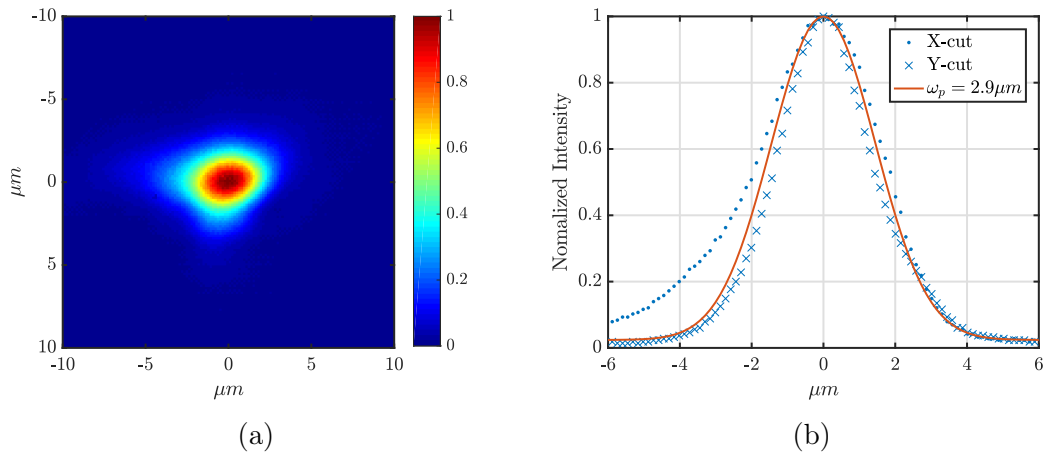


Figure 3.19: (a) 2D intensity profile of the pump beam on the measured device. (b) x,y cut of the 2D profile with a Gaussian fit of waist $\omega_p = 2.9 \mu\text{m}$.

To circularize the laser diode spot, an anamorphic prism of $\times 4$ magnification was used before focalizing the pump spot on the device at normal incidence. Figure 3.19

shows the resulting spot intensity. To have a meaningful measurement, the pump spot had to be smaller than the expected diffusion, thus a spot of $\omega_p = 2.9 \mu\text{m}$ waist was used.

Since the photo-luminescence intensity is proportional to the carrier density, n we used the diffusion equation [Crank 1979]:

$$\frac{\partial n(\vec{r}', t)}{\partial t} = D_{np} \nabla^2 n(\vec{r}', t) - \frac{n(\vec{r}', t)}{\tau} + g(\vec{r}') \quad (3.21)$$

Where D_{np} is the ambipolar diffusion coefficient and is assumed to be spatially invariant. L_d is the diffusion length, and is related to the carrier lifetime and ambipolar coefficient by $L_d = (\tau D_{np})^{1/2}$. And $g(\vec{r}')$ is the source term related to our pump profile by:

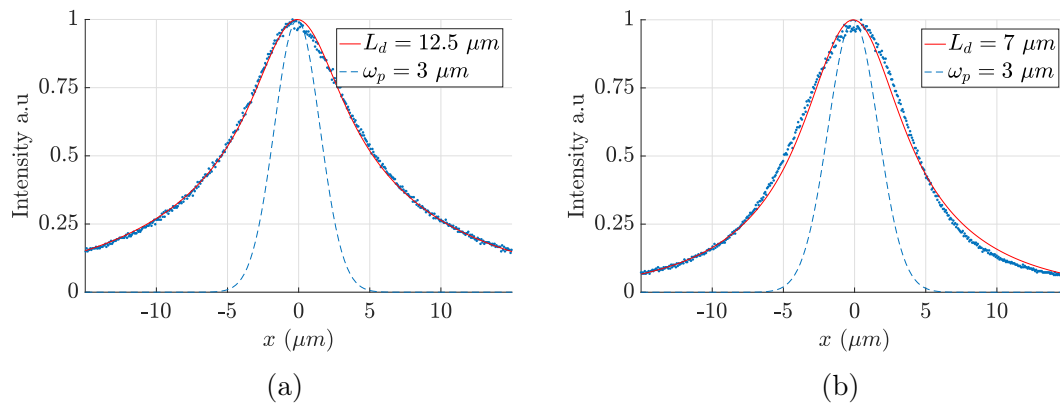


Figure 3.20: Fit of the photoluminescence profile (x, y cut) of the measure device (SESAM) using the solution of the diffusion equation. (a) for $I = 2.8 I_{tr}$ and (b) for $I = 16 I_{tr}$. The dashed line is the Gaussian source of $\omega_p = 3 \mu$ used for the simulation.

$$g(r) = \frac{G_0}{D_{np}} e^{-2 \frac{r^2}{\omega_p^2}} \quad (3.22)$$

with ω_p being the pump waist and G_0 a normalized amplitude. Following the work of Bierker et al. [Bieker 2015] we can find an analytic stationary solution of this differential equation under continuous excitation.

$$n(\vec{r}') = [G(\vec{r}') * g(\vec{r}')](\vec{r}') \quad (3.23)$$

$$G(\vec{r}') = \frac{1}{2\pi D_{np}} K_0 \left(\frac{r'}{L_d} \right) \quad (3.24)$$

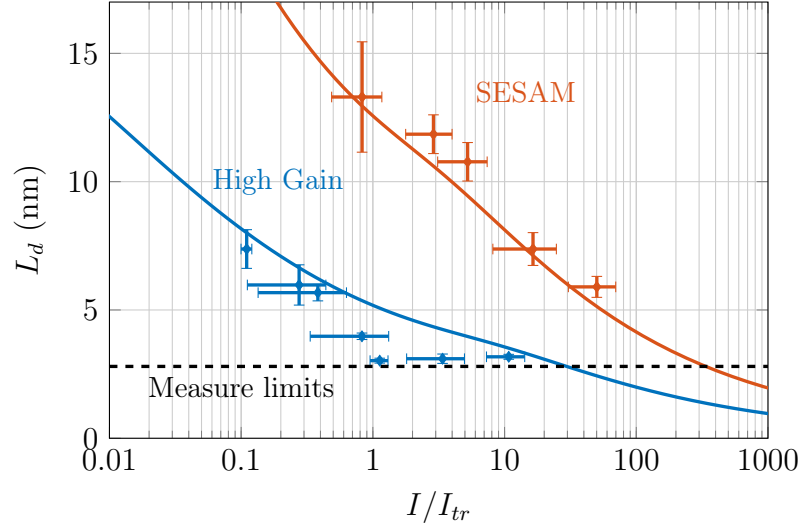


Figure 3.21: Measure diffusion length versus the incident power density of the pump beam for (red) the SESAM and (blue) the High Gain structure.

The 2D solution is the convolution of the source terms, with the Green function defined as the zeroth rank K-Bessel function $K_0(z)$. Figure 3.20 shows two examples at two different pump excitations. A 1D-cut from the symmetric 2D spatially resolved photo-luminescence was used and fitted with a 1D cut of the analytical model.

From different pump power density excitation, we were able to extract several data points that are shown in figure 3.21. The measurements were made on both the High Gain structure and the SESAM. Using the relation $L_d = (\tau D_{np})^{1/2}$ and equation 2.14 for the lifetime, we can also roughly fit the data with realistic parameters. All parameters are in table 3.1 and table 3.2 for the high gain structure and the SESAM respectively.

The main give away here is the two to three times ratio between both structures, with $L_d = 13 \mu\text{m}$ at transparency for the SESAM. Although the two devices have the same growth process, there is a large disparity between them. This is mainly due to a change in the QW indium concentration, which reduces the radiative recombination process. There is also a larger ambipolar coefficient, but this alone does not explain the large change. To ensure the GaAs spacer does not impact the transverse diffusion, a new measurement could be made at 980 nm. As said earlier, the diffusion length gives us a fundamental limit for the net gain window a spatial pulse can open. Depending on the optical cavity configuration, the SESAM diffusion length could be a limiting factor. And reducing its value by using a fast SESAM and temporal Mode-locking could be a solution. Table 3.2 combines all the important SESAM parameters.

Pump power density at transparency per QW	I_{tr}	0.11 kW/cm ²
Quantum well width	L_{QW}	8 nm
Number of quantum well	N_{QW}	1
Confinement factor	Γ_{uc}	3.5
FWHM resonance bandwidth	$\Delta\lambda_{\mu c}$	40 nm
Saturable absorption/Loss	ΔR	14.5%
Saturated reflectivity	R_{sat}	98%
Resonant Saturation intensity	I_s	600 W/cm ²
Diffusion length at transparency	$L_d(N_{tr})$	13 μ m
Lifetime at transparency	$\tau(N_{tr})$	28 ns
Mono-molecular recombination coefficient	A	$1 \times 10^6 \text{s}^{-1}$
Bi-molecular recombination coefficient	B	$0.5 \times 10^{-10} \text{cm}^3/\text{s}$
Auger recombination coefficient	C	$1 \times 10^{-30} \text{cm}^6/\text{s}$
Ambipolar diffusion coefficient	D_{np}	60 cm ² /s

Table 3.2: Main parameters of the SESAM structure.

3.4 Air-semiconductor interface functionalization

The 1/2-VCSEL technology, by its nature, introduces an intra-cavity air-semiconductor interface. We can take advantage of this fact to control the intra-cavity light state generation of the laser.

One way is to use an anti-reflection coating to remove the micro-cavity resonance. For that, we need to add a $\lambda/4$ layer of a material with close to $\sqrt{n_{sc}}$ refractive index. In this case, we can have a design with a comparable bandwidth to the anti-resonant system while keeping a larger effective gain (see figure 3.22).

Another way was to use the previously developed meta-surfaces masks technologies [Seghilani 2015, Sellahi 2014] to select a light state. These meta-surfaces can be used to transversely modulate both the net gain amplitude and the reflected phase of the structure by varying the spatial distribution of the effective refractive index. Two main technologies are available for that:

- Amplitude modulation is done by adding selective transverse losses through the use of a sub-wavelength metallic absorber or by localized diffraction (abrupt phase step). This will affect the effective transverse gain of the structure and thus the wavefunction intensity.
- Phase modulation is achieved through a transparent dielectric meta-material (sub-wavelength periodic dielectric pattern). This meta-material allow spatial

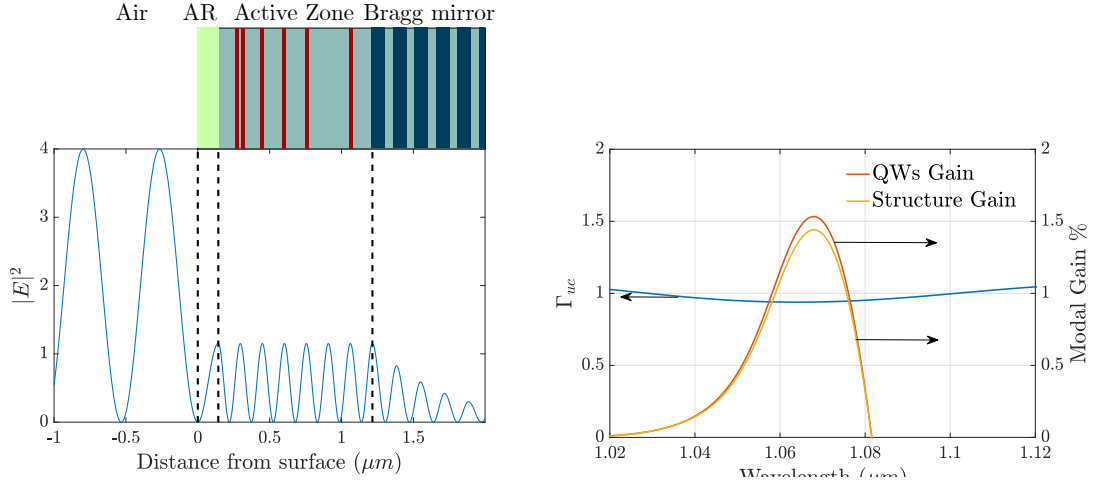


Figure 3.22: (Left) Calculation of the intra-cavity field intensity $|E|^2$ for an anti-resonant structure ($7.5\lambda/2$ length). (Right) Confinement factor Γ_{uc} and the effective gain of the structure.

control of the reflected phase on the 1/2-VCSEL multilayer structure. This phase pattern can be used to select higher order mode.

In our work, only the amplitude modulation was used to introduce selective losses and boundary conditions. However, the use of phase mask to further or control over the real and imaginary potential in a self-imaging system is of great interest.

3.4.1 Amplitude mask

An intensity mask is used to spatially control the net gain of the laser by adding a small absorbent metallic layer on top of the 1/2-VCSEL structure. This layer is made of chromium because the imaginary part of its refractive index gives a strong absorption $\alpha_{cr} = 4.46 \times 10^5 \text{ cm}^{-1}$ at, 1 μm while the real part is close to the GaAs optical index $n_{cr} \sim 3.5$. The chromium also forms a strong bond with GaAs, allowing for good quality mask in a thin layer. The advantage of the high losses means that a small chromium thickness $\sim 10 \text{ nm}$ leads to large single pass losses $\sim 35 \%$. The thickness being well below the laser wavelength $e \ll \lambda$ ensure that no diffraction occurs on the mask edge. In this way, the metallic layer acts solely as transverse losses.

This technology was previously experimented by M. Selahi to create an intra-cavity mode selection. He demonstrated the possibility to generate, intra-cavity, in a VCSEL system a higher order Laguerre-Gauss [Sellahi 2014]. The chromium layer adds selective transverse losses to suppress the appearance of other modes. The

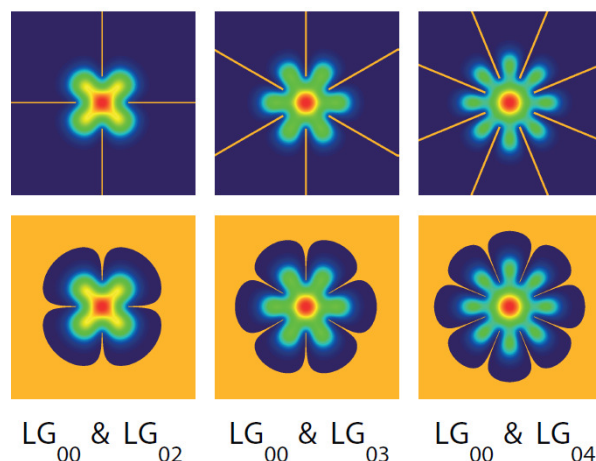


Figure 3.23: Design example of the chromium mask geometry for the bi-mode LG00 & LG02, LG00 & LG03 and LG00 & LG04 configuration. [Paquet 2016]

same method was also used by R. Paquet et al. for a continuous wave bi-frequency laser [Paquet 2016]. This time, the intensity mask design allowed for the existence of both the fundamental Gaussian TEM_{00} mode and a higher-order Laguerre-Gauss mode. By adjusting the pump size and the resulting thermal gradient, both modes were able to lase simultaneously at two different frequencies with THz separation. The fact that it is generated inside a single VeCSEL as the advantage of correlating mechanical and optical noise. Figure 3.23 shows the geometry of the different mask layout proposed. This system is currently used with a photo-antenna for THz signal generation. It has the advantages of providing very low THz signal noise thanks to the coupling of the optical noise [Abbes 2021].

Figure 3.24 shows some masks design used in our works. For instance, the “A” shape was designed to test the ability of the laser system to lase onto arbitrary shaped wave-function. This can also be used as a measurement of degeneracy. The “holes” shape was intended to restrict the transverse area by adding a strong absorptive boundary condition. The aim is to add one degree of transversal control and to vary the Fresnel number for light structuration. This design was also declined with a 2D periodic structure to create a transverse matrix of lasers. A one dimensional periodic structure was also designed to allow a single direction of freedom for localized structure. Other designs were made to simulate random absorptive defects by placing a random distribution of small chromium circles. All the different design types were declined in different size (diameter / period ...).

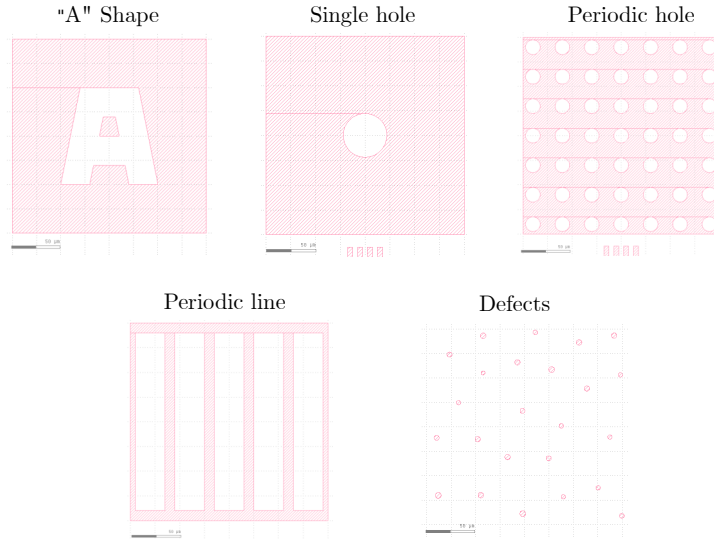


Figure 3.24: Chromium mask design for testing spatial degeneracy and non-linear localized structure.

3.4.2 Phase mask

To fabricate a phase mask, we must be able to control the reflected phase of the gain mirror, leading to a spatially non-uniform phase variation $\Delta\phi(x, y)$. One way to achieve this is through the use of a metamaterial where the optical refractive index can be spatially modulated ($neff(x, y)$). A metamaterial is an artificial periodic structure with an elementary cell smaller than the operating wavelength ($a \ll \lambda$). In this case, the periodic structure behaves, from the light perspective, like a homogeneous material with specific properties (optical index for example). By engineering the periodic structure and the elementary cell, it is possible to transversally modulate the effective refractive index and thus the transverse phase of a light beam. Thanks to the maturation of these types of components, M. Seghilani et al. have demonstrated a Vortex laser [Seghilani 2016], where the metasurface provides an azimuthally varying phase coupled with a phase step at the center to math the intensity “doughnut” shape and the characteristic helical phase of a vortex mode. The selection process happens through laser competition, the vortex mode has good purity compared to external cavity methods with spiral phase plate [Beijersbergen 1994].

3.4.3 Technological steps

All our designs were manufactured at the C2N (*Centre de nanosciences et de nanotechnologies*) under the team of Pr Isabelle Sagnes. The fabrication process

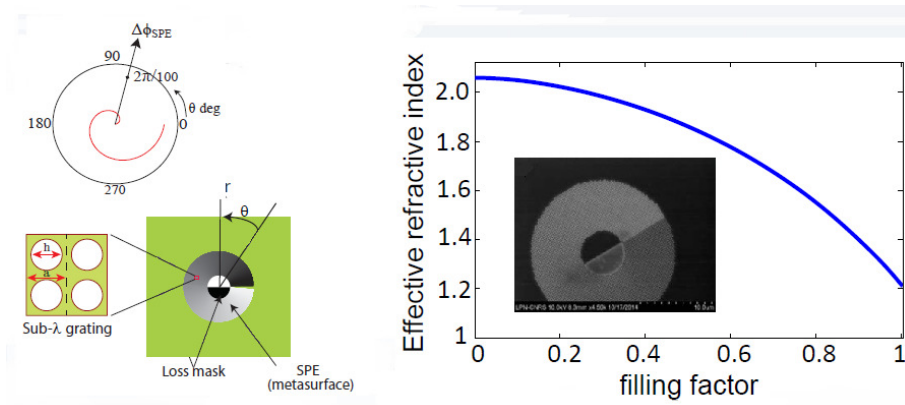


Figure 3.25: (Left) Schematic representation of the phase mask structure and the elementary cell shape. (right) Effective refractive index of the artificial material made of a Si_3N_4 layer perforated by a 2D periodic array of air holes placed on a square lattice. (Insert) SEM photo of the fabricated phase mask for vortex generation.

for the metallic mask layer is schematically described in figure 3.26. Firstly, a polymethyl methacrylate (PMMA) resin is spin-coated on the wafer and patterned by electron beam lithography (Vistec EBPG 5000 at 100 kV) with a resolution of 1.25 nm. A PEC (proximity effect correction) method is used to improve the quality over a wide range of possible design. After PMMA development in methylisobutylketone (MIBK) solution, a thin layer (5 nm-20 nm) of chromium is deposited using physical vapor deposition (PVD), and finally the structure is cleaned from residual chromium and PMMA leaving us with the desired chromium layer.

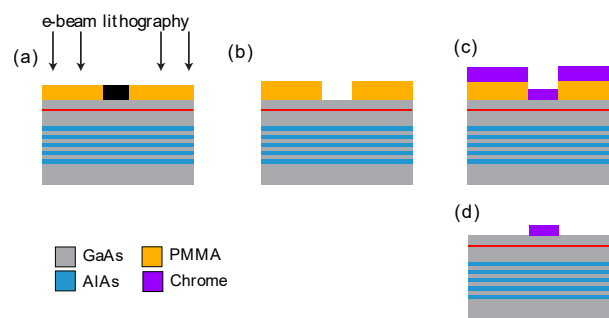


Figure 3.26: Technological process of fabrication of the metallic mask integrated on the VECSEL gain-mirror. a) e-beam lithography; b) PMMA development; c) chromium deposition; d) lift-off.

Several repetitions of the same mask design are made on the surface of the 1/2-

VCSEL structure to have some redundancy. Each mask is usually implemented with several design variations to test different functions in situ (same structure, same pump, same cavity configuration and so on). Figure 3.27 shows SEM (Scanning Electron Microscopy) photos of the different masks realized for non-linear light structuration. The chromium layer of each mask is estimated to be around 10 nm thick.

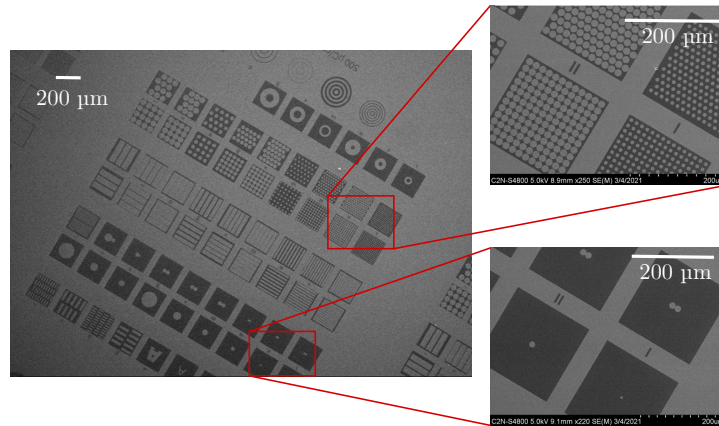


Figure 3.27: SEM picture of the chromium mask realized on a 1/2-VCSEL structures

3.5 Perspective: MIXSEL (Two in one)

We decided to separate into two different devices, the gain and the saturable absorption. However, it could be possible to combine both aspects into a single semiconductor structure. One advantage of this configuration would be to reduce the complexity of the optical cavity and improve our ability to integrate the complex optical system. This set-up could then resemble the monolithic configuration used in previous cavity soliton experiment [Barland 2002] with the added bonus of an integrated saturable absorber. The downside, however, will be a lack of control of intensity saturation ratio from gain to saturable absorber. This ratio will be fixed by the design, instead of being adjustable by the magnification ratio within the external optical system.

For this, we propose a simple design of a pseudo coupled cavity by placing the absorber QW close to the HR Bragg mirror, using an intermediary Bragg mirror to reflect the pump and then placing the gain active zone. In this case, the intermediate Bragg mirror must be designed at the pump wavelength for an incidence angle in the air at the Brewster angle while keeping the reflectivity at the laser wavelength low enough to limit the field enhancement on the QW. Too large of an enhancement and the saturable losses could be larger than the available gain,

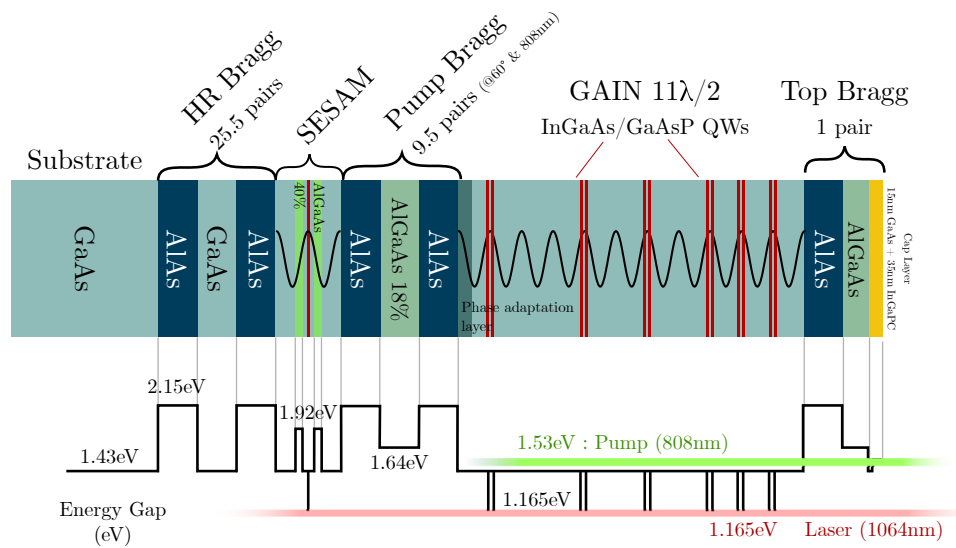


Figure 3.28: Design example for the MIXSEL two in one structure combining a SESAM and a GAIN section. Structure numbered V0599.

for this reason, it should be kept between 1 and 1.5 more than the enhancement factor on the gain section. A phase layer should also be added in front of the intermediary Bragg to properly adjust the micro-cavity length by considering the intermediary Bragg reflection phase shift.

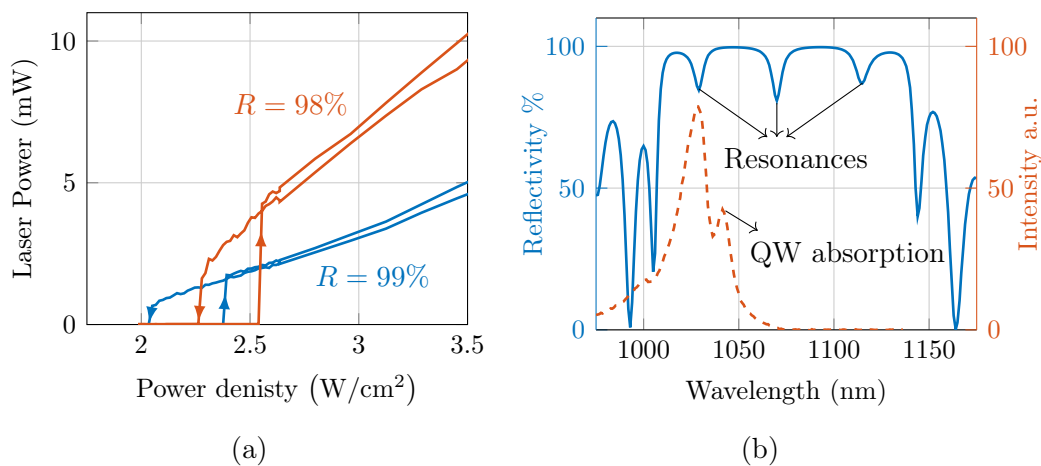


Figure 3.29: a) Measure of the power output as a function pump power density for two different mirror reflection, the cavity was a simple plano concave cavity. b) FTIR and photo-luminescence measurement for the structure.

In this case, a AlAs/AlGaAs Bragg mirror was used after an $11\lambda/2$ active gain region with 12 QWs to reflect $> 60\%$ of the remaining pump power and two

$\text{Al}_{40\%}\text{GaAs}$ layers sandwiched the QW to limit the remaining carrier diffusion into the well, assuring a negligible excitation of the absorber.

A simple characterization (see figure 3.29) was done on this two in one structure, validating the proposed design. We observe an optical bi-stability for output coupler of up to 2% losses. The bistability is proof that the structure exhibits saturable absorption. It remains to be used in a dedicated system for non-linear light structuration, but the proof of concept for an integrated slow SESAM is done.

3.5.1 Conclusion

In this chapter, we have described the design for two active components based on the GaAs III-V semiconductor technology. One design was made for a high gain mirror and the other for a saturable absorber mirror. We opted for a surface emission as in disk laser to take advantage of the small Dirac like light matter interaction and ease of integration into a complex external optical system.

Two key elements were considered: a high gain with low threshold system and a homogeneous system in phase and amplitude. To achieve a high gain, a classic method consists of increasing the light-matter interaction by enhancing the micro-cavity factor. However, with a large enhancement, parasitic effects such as the resonance spatial frequency filtering, gain “puddles” modulation and thermal lensing reducing the homogeneity of our system, a compromise was made. In the end, a 12 QWs active zone layout with a micro-cavity enhancement factor of $\Gamma_{\mu c}$ to reach up to 15% gain while keeping a low threshold limiting the effect of the thermal lens was made. This resulted in a 8.33 nm spectral bandwidth for possible temporal structuration and > 0.4 numerical aperture filtering for high Fresnel number operation. The compromise also limits the impact of the amplitude and phase inhomogeneity from the gain “puddles”.

The SESAM design was also made in accordance with the gain design and the added consideration of lower saturation density than the gain. The saturation ratio should, however, not exceed 10 to not oversaturate the SESAM and nullify the effect of SAM and reduce the gain SPM. Being made from the same technology, a QW in the absorption regime will naturally exhibit lower saturation density due to its slightly longer level lifetime. However, too long of a lifetime and carrier diffusion might limit the smallest obtainable size from purely self-amplitude modulation. In our case, using a unique QW inside a simple resonant micro-cavity design allowed us to reach up to 14.5% saturable losses with 600 W/cm^2 saturation density. The carrier diffusion length was measured 2-3 times larger than in the gain structure for around an order of magnitude on the level lifetime. The limiting effect on the small non-linear size can in part be compensated with the cavity design. On the other hand, for TLS structuration, a fast SESAM ($\tau < 2 \text{ ns}$) is needed to create a PML system. In this case, the discussion about carrier diffusion length becomes

irrelevant. One such design was made in relation with the BLASON ANR and in partnership with the INPHYNI for their work on TLS system.

The growth of semiconductor device was made at the RENATECH C2N using MOCVD technology. The resulted structure exhibited low defect density and a good spatial homogeneity. It was also possible to design and fabricate absorptive metasurface onto the device surface. In the context of 3D light structuration, those metasurface can be used to shape the near field light pattern or define a transverse area with a sharp boundary, creating a “waveguided like” area.

Part III

Design of a spatially modeless optical cavity

Optical resonator design for 3D light structuration

4.1 Introduction

In this chapter, we will touch on the design and properties of a laser resonator for 3D Structured coherent light state and localized structure. A laser system is composed of two main components, an active material providing optical gain to the system and an optical resonator or optical cavity. An optical resonator possesses a self-repeating field both in phase and amplitude as a stable solution of the system[Siegman 1986]. The resulting 3D eigenvectors are called the mode basis of the cavity. It is important to define the desired modes properties (spatially and spectrally) of the laser system before choosing the type of resonator.

The goal of this chapter is to find the best design for structured light and non-linear spatial localization. For that purpose, we will need to define the requirement and tolerances on a few key parameters, such as the cavity stability. The design and properties of a self-imaging system fulfilling the requirements will be explored in the following chapter, after we define the basic properties of an optical cavity.

4.1.1 Different types of laser cavities

In the world of lasers, different types of cavities coexist, each with their advantages and downsides. The choice of a particular design will be influenced both by the choice of the gain technology and the type of targeted application. For example, a single mode continuous wave laser and a passively mode-locked laser do not have the same requirements. The first one needs high selectivity of a single mode (spatially and longitudinally) while the other needs intra-cavity saturable absorption and dispersion management. However, most laser systems can be categorized into two

broad resonator technologies (free space and waveguide) and two broad designs (linear or ring).

Free space resonator: They are mostly used with solid-state bulk gain media or for more complex laser applications. They are composed of a multiple of optical elements, where light propagates in free space between them. The resonator can range from a simple two mirrors system with a laser crystal medium for single mode continuous wave application [Chomet 2019, Laurain 2010] to multiple mirrors system integrating saturable absorber for passive mode-locking [De Silvestri 1984, Heritage 1978, Hoogland 2005], non-linear crystal for intracavity frequency doubling [Liew 2017, Polzik 1991] or a wavelength tuning element [Lan 2004, Vainio 2008]. Each of these systems requires specific resonator modes property. For PML, suitable mode size in the active elements for good saturation and/or transverse mode selection and the appropriate length for the desired frequency mode spacing or pulse repetition rate. This category of resonator is the more diverse one, allowing a wide range of active mediums and application.

Waveguide resonator: This type of resonator is used when the gain medium is integrated inside a waveguide. For solid-state lasers, external mirrors are coupled to the waveguide and for semiconductors they are usually integrated in the waveguide [Webb 2020, Mackenzie 2007]. Multiple types of gain medium can also be used, but doped fiber and semiconductor double heterostructure are the most common. For semiconductor laser most technology is based on waveguide resonator such as edge-emitting laser diode (Fabry-Perot laser diode, distributed Bragg reflector laser [Fricke 2010]), monolithic surface-emitting semiconductor lasers [Iga 1988]. This as the advantage of a good miniaturization with versatility in wavelength and power to allow for various applications. For the most part, the fields resonances are the same as the propagating mode of the waveguide, but not easily tunable without an external optical system.

Linear resonator: A linear resonator reflects the light between two end mirrors. The propagative and contra-propagative generated waves interfere together. This creates a longitudinal standing wave pattern and discretize the resonating frequency (wavelength) to a fraction of the cavity length.

Ring resonator: A ring resonator has no end mirror, and the light circulates in two counter-rotating propagation. This leads to some different behavior from the linear case. Mainly that an optical component is only hit once per round-trip and that the non-normal incidence of the light on the optical elements can lead to astigmatism. Furthermore, a single rotating propagation can be selected,

removing the contra-propagative wave and spatial-hole burning effect. This can be advantageous for mono-frequency operation [Kane 1985].

4.1.2 Design guidelines for transverse structuration

For classical laser system such as edge-emitting laser diode or solid-state system, the cavity volume is more or less equal to the field volume ($a^3 \simeq \omega_s^3$). In this case, see figure 4.1a, the transverse size of the system is close to the transverse size of the field with a well-defined propagation direction. The longitudinal length tends to be long in front of λ ($L \gg \lambda$), meaning large diffraction for free space cavities. These kinds of systems generate a discrete set of eigenfunctions represented in blue in the dispersion diagram of figure 4.2. It is useful for applications needing a strong discrimination between the different laser states. For example, to select a particular resonating wavelength, such as single mode laser [Zayhowski 1989] or transverse mode selection for bi-frequency operation [Paquet 2016].

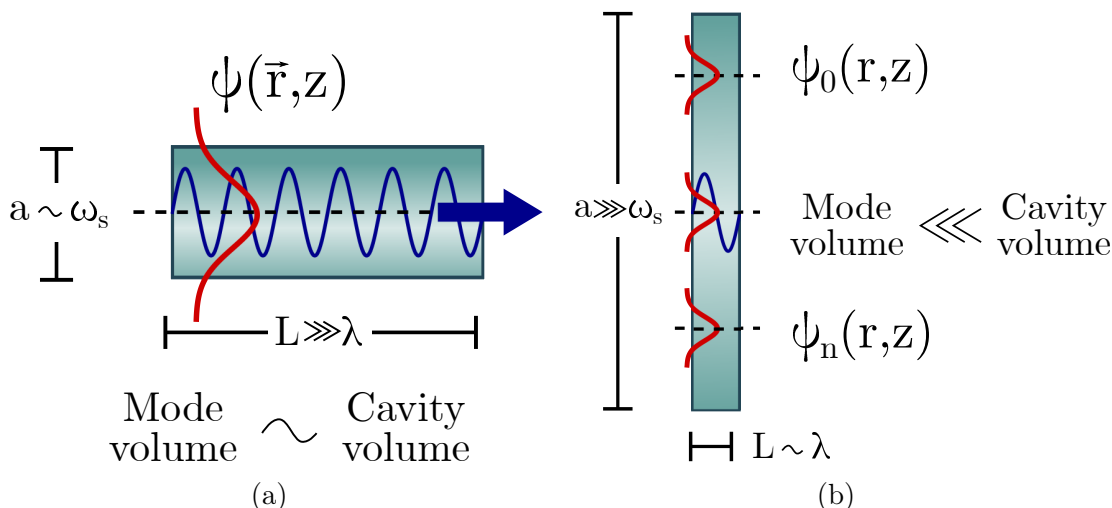


Figure 4.1: Schematic representation of a classical single transverse mode laser cavity (a) versus the target system for spatially localized structure (b).

In our case, for transverse structuration of the light and localized structure, these systems are not good enough. We want to reach a transverse degenerate state in the dispersion diagram of figure 4.2 (red lines). In this context, the optical cavity can allow arbitrary eigenfunction to resonate, including the spatially localized structure. By definition, localized structure also implies the need for the following requirements:

- Bi-stable system.

- Broad area system.
- Equilibrium between non-linear dispersive / diffractive effects.

To meet these conditions, we need to adapt the optical cavity, we will first focus on the transverse localization requirement, then we will see that the proposed system is also suited for temporal localization. For the first condition, having a bi-stable system means that we need to introduce saturable absorption. This will create a hysteresis where both the On and Off lasing state can exist within the same parameter range. The cavity then needs to accommodate two active mediums, one for the optical gain and one for the saturable losses. To be able to have coexistence of several localized structures, both of these active mediums need to fulfil the broad area requirement and the telecentric condition (off axis normal incidence emission). For that, they need to be on conjugate focal plane and image into each other.

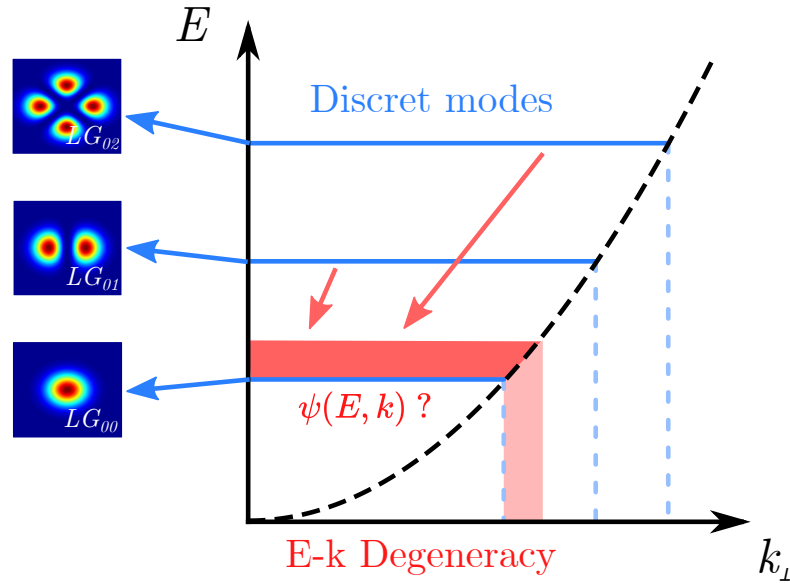


Figure 4.2: Energy-momentum diagram of the transverse cavity eigenvectors from the classical system (blue) to the targeted system (red)

Coming back to figure 4.1b we can see what form such a system should take. To have a broad transverse area system is to have a large aperture, then the localized structure needs to be smaller compared to it ($a \gg \omega_s$). In other words, the volume of the cavity needs to be larger than the volume of the localized structure. One way to represent this criterion is to use the Fresnel number, $F = a^2/L\lambda$ where a is the aperture, L is the distance to the aperture or the diffraction length, λ is the wavelength. By defining the elementary structure size with, $w_s = \sqrt{L\lambda}$ we

can have a direct comparison between the Fresnel number, the aperture and the elementary structure size. This means that the Fresnel number is proportional to the number N of structure of size ω_s through the following relation:

$$N = \frac{a^2}{w_s^2} = \frac{a^2}{L\lambda} = F \quad (4.1)$$

Then for our system to be able to support $N = 10 \times 10$ structure, the Fresnel number needs to be $F > 100$.

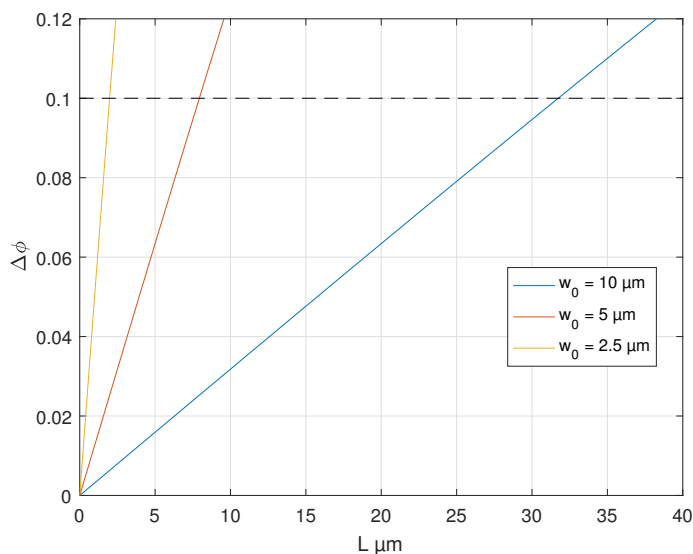


Figure 4.3: Transverse phase variation of a Gaussian beam at $1/e^2$ due to the diffraction length L for three different Gaussian size (2.5, 5 and 10 μm).

To meet the second and third criterions, the system needs to operate with minimal diffraction or well within the first Fresnel zone. This can be explained by the amount of non-linear phase the active mediums can provide to compensate for diffraction. Since the gain and the saturable absorption are achieved using a III-V semiconductor with a quantum well (QW), the main $\chi^{(3)}$ mechanism is expected to be the amplitude-phase coupling effect through the Henry factor α_h . Where $\Delta\phi \simeq -\frac{\alpha_h}{2} \Delta g$ is the phase variation due to the Δg gain variation. The gain will then exhibit a self-focusing effect while the absorber a small defocusing effect, resulting at the maximum with a 0.1 rad focusing phase variation. In fig.4.3 where the transverse Gaussian phase variation due to diffraction is plotted for different Gaussian beam size, we can see that we need around 10 μm or smaller diffraction

length to compensate the 0.1 rad or smaller non-linear phase. This is computed for a typical size of $\omega_0 = 5 \mu\text{m}$.

One implication of the previous condition is the need for a high numerical aperture system to support small structure size. For a lens used for beam collimation, the typical numerical aperture is its radius a over the focal length f . So to avoid beam truncation leading to excessive losses and wavefront deformation, we can set a limit for the beam waist on the lens such that the lens radius must be 2 times greater than the beam waist. Written in terms of numerical aperture, we have $NA_{lens} > 2NA_{Gauss} = 2\lambda/\pi\omega_0$. For a beam waist of, $\omega_0 = 5 \mu\text{m}$ the numerical aperture limit is, $2NA_{Gauss} = 0.14$ which corresponds to more than 99.9% power transmission.

As seen in the previous chapter, the active medium also has a limiting effect on the numerical aperture. The microcavity nature of the gain device leads to spectral and spatial filtering of the resonating field. To not be limiting, it should follow the same requirement as the intra-cavity elements, meaning $NA_{\mu c} \gg \gg 0.14$.

Coming back to the Fresnel number, we can now find limits on the aperture size using the previous Gaussian size of $\omega_0 = 5 \mu\text{m}$. If we want to support more than 10×10 optical structure, we need an aperture of at least $a = \sqrt{N}\omega_0 = 50 \mu\text{m}$ of diameter. The table 4.1 summarizes the different needed key parameters for the optical system.

Parameter	Value	unit
F	> 100	-
a	> 50	μm
L_d	< 10	μm
NA	> 0.2	-

Table 4.1: Summary of key parameters in the design of an optical cavity for non-linear structuration.

In this chapter, we will look at the properties of a cold cavity and select the important ones for 3D light structuration. We will also look at how to compute a cavity stability and the limits of that approach for a self-imaging system.

4.2 Concept of stable optical cavity

A passive optical cavity (i.e., with no active medium) imposes a discrete set of electromagnetic modes through the mirror boundary conditions. The mode basis possesses spectral, spatial, and polarization properties that the generated photon

must couple into it if it wants to resonate inside the cavity. We can then expand the electromagnetic field inside the cavity into an orthonormal spatial basis $u_\lambda(x, y, z)$ [Khanin 2012].

$$\vec{\mathcal{E}}(x, y, z, t) = \text{Re} \left(\sum_{\lambda} A_{\lambda}(t) u_{\lambda}(x, y, z) e^{-i\omega_{\lambda}t + i\beta_{\lambda}z} \cdot \vec{x}'_i \right) \quad (4.2)$$

with $\lambda = n, q, i$ representing the longitudinal index q , the transverse index n and the polarization index i . $u_{\lambda}(x, y, z)$ is the complex spatial distribution of the field. $A_{\lambda}(t)$ is the slowly varying temporal evolution of the field with frequency ω_{λ} and wavenumber β_{λ} . We'll look in the following section at the resonant properties ω_{λ} and the transverse field profile $u_{\lambda}(x, y, z)$.

4.2.1 Longitudinal modes

An optical cavity creates a series of resonating longitudinal modes or resonating frequency from its limited physical size. A simple model to explore the spectral properties is to take two plane mirrors of reflecting coefficient $R_1 = |r_1|^2$ and $R_2 = |r_2|^2$ separated by a distance L_c . This formalism is also known as the Fabry-Perot interferometer [Fabry 1897]. We can then calculate the intensity transfer function of the system as being:

$$T(\delta\phi) = \frac{(1 - R_1)(1 - R_2)}{(1 - \sqrt{R_1 R_2})^2} \frac{1}{1 + \frac{4\sqrt{R_1 R_2}}{(1 - \sqrt{R_1 R_2})^2} \sin^2 \left(\frac{\delta\phi}{2} \right)} \quad (4.3)$$

With $\delta\phi = 2knL_c \cos(\theta)$ being the phase difference between the multiple reflections of the light with an incident angle θ in the Fabry-Perot interferometer of optical length nL_c . So for an optical cavity at normal incidence $\cos(\theta) = 1$, the phase-shift is equivalent to the round-trip phase. We can see from equation 4.3 that a maximum of transmission occurs when $\sin^2(\delta\phi/2) = 0$ or $\delta\phi/2 = q\pi$, with q as an integer, creating a resonant longitudinal mode. We can then express the separation of each longitudinal resonance by the free spectral range:

$$FSR = \frac{c}{2nL_c} \quad (4.4)$$

Where c is the speed of light. However, in reality, the resonator is made up of partially reflecting mirrors creating losses. On each reflection, the photons have a probability of $1 - R$ to escape. These optical losses create a broadening of the resonance from not having an infinity of waves taking part in the interferometer. We can then define the full width half maximum of the resonance by:

$$\delta\nu_c = \frac{FSR}{\mathcal{F}} \quad (4.5)$$

where \mathcal{F} is the cavity finesse defined as 2π over the half maximum phase. For small round-trip losses ($< 10\%$) it becomes equivalent to [Siegman 1986]:

$$\mathcal{F} = \frac{2\pi}{Loss} \quad (4.6)$$

By introducing the cavity photon lifetime τ_c as the average time a photon remains in the cavity, we can see that the finesse can also be an indicator for the average number of round-trip N of the system.

$$\tau_c = \frac{1}{2\pi\delta\nu_c} \quad (4.7)$$

$$N = \frac{\tau_{ph}}{\tau_{ar}} = \frac{FSR}{2\pi\delta\nu_c} = \frac{\mathcal{F}}{2\pi} \quad (4.8)$$

With the spectral properties, we can now explore some design and understand their interest for certain applications. For example, to design a single longitudinal mode laser with semiconductor QWs gain, the VCSEL platform is interesting. The typical cavity is formed by two high reflectivity ($R > 99\%$) Bragg mirrors and a semiconductor multi-quantum well gain layer with around 3 THz of gain bandwidth and thickness of around 1-3 μm . The resulting cold properties of the resonator are a FSR ranging from 15 THz to 40 THz with very high finesse $\mathcal{F} \gg 1000$. This ensures that only one longitudinal mode can coexist within the gain, thus having a monochromatic laser emission. However, transverse mode selection in this case cannot be done by diffraction alone and without proper care transverse multi-modal operation can arise, especially in the so called broad-area VCSEL [Chang-Hasnain 1990].

4.2.2 Transverse eigenstates

The transverse modes of an optical cavity correspond to a transverse field profile that reproduces itself after one round-trip. For comparison, an arbitrary travelling wave will undergo changes during a round-trip due to losses, aperture effects (optical element edges), and diffraction. While a transverse eigenmode conserves the same shape. We can write this condition as [Siegman 1986]:

$$u^{n+1}(x, y) = \gamma u^n(x, y) \quad (4.9)$$

In this case, $u^n(x, y)$ represent the complex transverse profile of the field at a round-trip n and $u^{n+1}(x, y)$ at a round-trip $n + 1$. γ is the complex eigenvalue

with $\arg(\gamma)$ being the round-trip phase and $1 - |\gamma|^2$ is the power losses for one round-trip.

4.2.2.1 Gaussian propagation

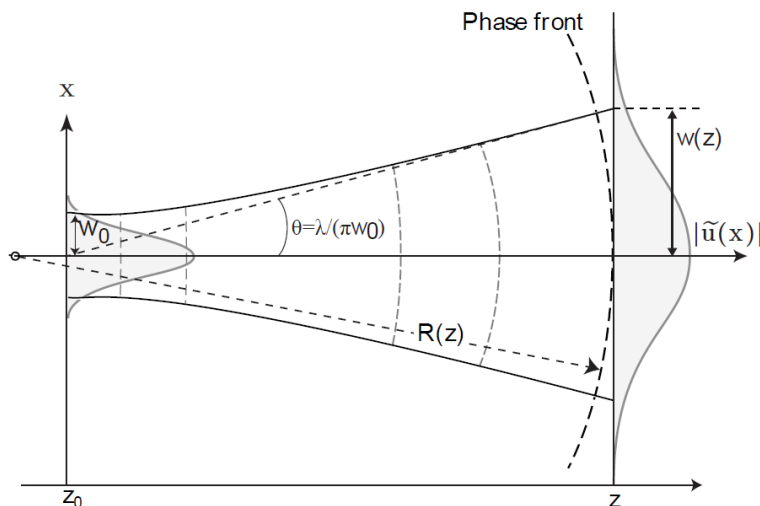


Figure 4.4: Schematic representation of the fundamental Gaussian beam TEM₀₀.

The simplest solution for transverse modes in a stable laser resonator is a Gaussian beam. For that reason, a quick overview of the nature of Gaussian beam propagation is important, since it will describe the propagation of most transverse laser modes. The normalized field expression for a Gaussian beam travelling in the $+z$ direction with its minimal size in $z = 0$ in cylindrical coordinate is [Siegman 1986]:

$$\begin{aligned} u(r, z) &= \sqrt{\frac{2}{\pi}} \frac{\tilde{q}_0}{\omega_0 \tilde{q}(z)} \exp \left[-jkz - jk \frac{r^2}{2\tilde{q}(z)} \right] \\ &= \sqrt{\frac{2}{\pi}} \frac{1}{\omega(z)} \exp \left[-\frac{r^2}{\omega(z)^2} \right] \exp \left[-jkz - j \frac{kr^2}{2R(z)} - j\varphi(z) \right] \end{aligned} \quad (4.10)$$

Where the complex beam parameter $\tilde{q}(z)$ describe the fundamental properties of the beam such as its beam waist $\omega(z)$ (radius at $1/e$ amplitude) and the wavefront curvature radius $R(z)$ following this equation:

$$\frac{1}{\tilde{q}(z)} = \frac{1}{R(z)} - j \frac{\lambda}{\pi \omega(z)^2} \quad (4.11)$$

For $z = 0$ the beam parameter is purely imaginary and provides us information about the size of the beam.

$$\tilde{q}_0 = j \frac{\pi \omega_0^2}{\lambda} = j z_R \quad (4.12)$$

Where ω_0 is the small beam waist and z_R is the Rayleigh length that characterizes the distance for which the beam area is multiplied by 2. Knowing these two parameters (ω_0 and z_R) allows for the calculation of the physically relevant parameters anywhere along its propagation.

$$\omega(z) = \omega_0 \sqrt{1 + \left(\frac{z}{z_R}\right)^2} \quad (4.13)$$

$$R(z) = z + \frac{z_R^2}{z} \quad (4.14)$$

$$\varphi(z) = -\arctan\left(\frac{z}{z_R}\right) \quad (4.15)$$

Eq. 4.13 calculates the beam waist at any point z . Eq. 4.14 gives us the beam curvature radius for any z . And lastly, Eq. 4.15 expresses the Gouy phase of the beam, which is an additional phase offset accumulated during propagation compared to a perfect spherical wave. This parameter will later be important to estimate the frequency separation of transverse modes and estimate the cavity degeneracy.

Using Eq. 4.13, we can also define the angle θ as the divergence angle of the beam as $z \gg z_R$ in the small angle approximation.

$$\theta = \frac{\lambda}{\pi \omega_0} \quad (4.16)$$

However, in real beam, the divergence angle may be different from the ideal case from wavefront deformation. In this case, we can introduce the M^2 factor in Eq. 4.16 to give us Eq. 4.17 where M^2 is an indication of the beam quality. A M^2 factor close to one means a near diffracted limited beam, while a $M^2 > 2$ indicates a poor beam quality.

$$\theta_{Laser} = M^2 \frac{\lambda}{\pi \omega_0}, \quad \text{with } M^2 > 1 \quad (4.17)$$

For higher order beam the M^2 factor scales linearly with the mode number, this indicates that higher order mode diffract quicker.

4.2.2.2 Higher order modes : Spherical wave cavity

In a spherical resonator, meaning a resonator which only affects the spherical or parabolic (in the paraxial approximation) part of the eigenfunction phase, we find two main mode families. For a cavity with rotational symmetry, the higher order modes are of the Laguerre-Gaussian (LG) family. While for a resonator which breaks this symmetry, then the Hermite-Gaussian (HG) family describes the eigenfunction.

4.2.2.2.1 Higher order modes : LG & HG

For both mode basis, the Gaussian beam is the fundamental HG_{00} or LG_{00} solution. Higher order modes are simply a more complex transverse propagating pattern. It is important to note that they are both solutions of the paraxial wave equation. The general expression of non-degenerate LG and HG modes are given by Eq. 4.18 and Eq. 4.20 respectively.

$$u_{pl}^*(r, \theta, z) = \sqrt{\frac{2}{\pi}} \frac{1}{\omega(z)} \sqrt{\frac{p!}{(p+|l|)!}} \left(\frac{\sqrt{2}r}{\omega(z)} \right)^{|l|} L_p^{|l|} \left(\frac{2r^2}{\omega(z)^2} \right) \times \exp \left[-jk \frac{r^2}{2\tilde{q}(z)} \right] \exp [-jkz + jl\theta - j\varphi(z)(2p + |l| + 1)] \quad (4.18)$$

For LG modes, the cylindrical (r, θ, z) coordinate system is used with $p \geq 0$ as the radial mode number and l the azimuthal one. $L_p^{|l|}$ is the generalized Laguerre polynomial given by Eq. 4.19. $\omega(z)$ and $\tilde{q}(z)$ are respectively the Gaussian waist and complex beam radius from the propagations properties of a Gaussian beam seen in § 4.2.2.1. The Gouy phase shift is modified as $(2p + |l| + 1)\varphi(z)$. This transverse mode basis has a phase singularity in the mode center, leading to a donut-shaped intensity profile and a helical wavefront carrying orbital momentum for mode with $l \neq 0$ and $p = 0$. These types of modes are also known as ‘‘Vortex’’ and can be useful in certain applications, notably the trapping of particles in optical tweezers[Yao 2011].

$$L_p^{|l|}(X) = \sum_{i=0}^p (-1)^i \frac{(p+l)!}{(p-i)!(l+i)!} \frac{X^i}{i!} \quad (4.19)$$

For degenerate LG beam the azimuthal phase $\exp[jl\theta]$ transform into $\cos(l\theta)$ leading to the more common petals shape modes. To explain this transformation, we can consider a LG degenerate mode as being a coherent combination of two non-degenerate LG modes of same indices p and $|l|$ but with opposite handedness ($\pm l$). Thanks to the Euler formula, we go back to $\exp(+il\theta) + \exp(-il\theta) = 2 \cos(l\theta)$.

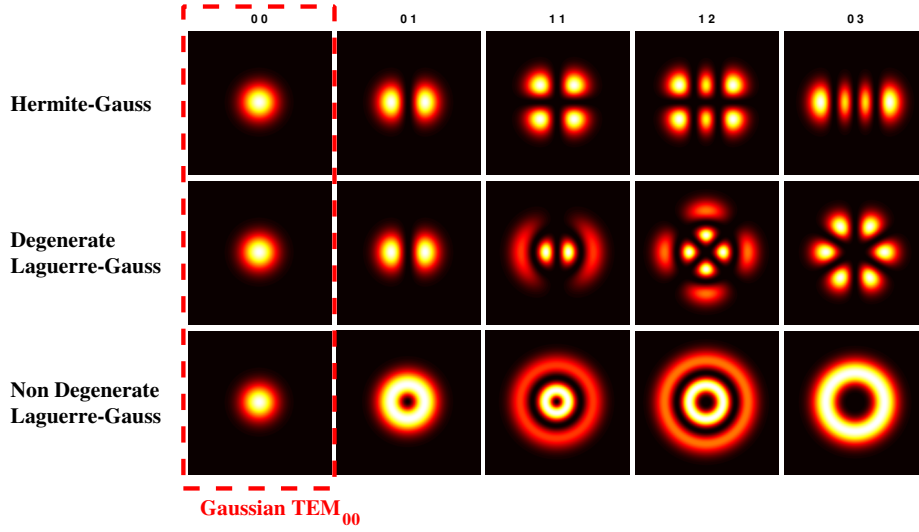


Figure 4.5: Transverse intensity distribution of some possible transverse modes of Fabry-Perot spherical like cavities.

The HG beam used the Cartesian (x, y, z) coordinate system, and the same way as for LG beam they can be expressed as Gaussian beam modulated by a polynomial function:

$$u_{nm}(x, y, z) = \sqrt{\frac{2}{\pi}} \frac{1}{\omega(z)} \sqrt{\frac{1}{(2^{n+m} n! m!)}} H_n \left(\frac{\sqrt{2}x}{\omega(z)} \right) H_m \left(\frac{\sqrt{2}y}{\omega(z)} \right) \times \exp \left[-jk \frac{(x^2 + y^2)}{2\tilde{q}(z)} \right] \exp [-jkz - j\varphi(z)(n + m + 1)] \quad (4.20)$$

In this case, it uses the Hermite polynomial of order n $H_n(X)$ for both x and y . The Gouy phase shift is modified as $(n + m + 1)\varphi(z)$

$$H_n(X) = n! \sum_{m=0}^{\lfloor \frac{n}{2} \rfloor} \frac{(-1)^m}{m!(n-2m)!} (2X)^{n-2m} \quad (4.21)$$

Inside a resonator, the additional axial Gouy phase shift for each transverse pattern will lead to the shift of the transverse mode resonance.

4.2.2.3 Conical wave cavity: Bessel-Gauss Beam

For cavities with a conical phase dependence as well as a spherical one, the HG and LG are not the best suited mode families to describe the eigenfunc-

tion. For this type of system, using the Bessel-Gauss representation is better [Gutiérrez-Vega 2003, Khilo 2001].

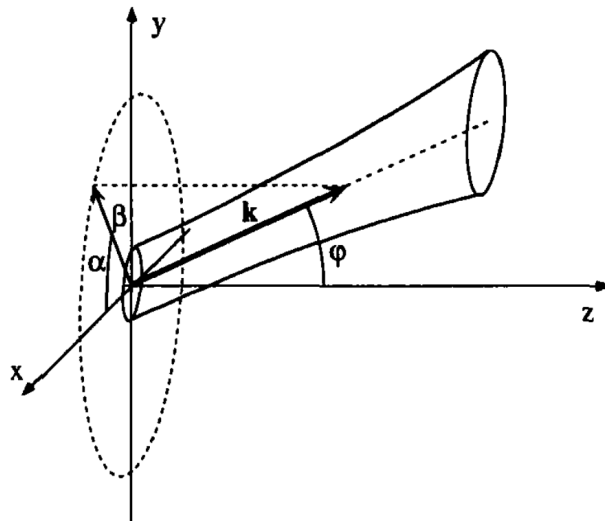


Figure 4.6: Representation of the geometry for generalized Bessel-Gauss beams from Bagini et al [Bagini 1996].

Bessel-Gauss modes can be thought of as a superposition of an infinity of Gaussian beams emitted on a cone of semi-aperture ϕ from the propagation direction z . This can be written as a transverse component of the wavevector $\beta = k_0 \sin(\phi)$ (see figure 4.6). The transverse field can be expressed as a function of r and z [Bagini 1996]:

$$u(r, z) = \frac{\omega_0}{\omega(z)} \exp\left(j[kz - \varphi(z)] - j\frac{\beta^2}{2k}z\right) \exp\left(-\frac{1}{\tilde{q}(z)}\left[r^2 + \frac{\beta^2 z^2}{k^2}\right]\right) \times 2\pi J_0\left[\frac{2r}{\tilde{q}(z)}\frac{\beta z}{k} + i\beta r\right] \quad (4.22)$$

Where we used the Gaussian parameter $\omega(z)$, $\tilde{q}(z)$ and $\varphi(z)$ as well as the zeroth order Bessel function of the first kind $J_0(x)$ to describe the transverse beam. This equation makes the assumption that the infinity of Gaussian beam have the same amplitude. Higher order Bessel mode, on the other hand, can be composed with a variety of amplitude or even using Hermite-Gaussian beam instead of simple Gaussian beam [Schimpf 2012]. In all cases, this mode family carries a conical phase component βr . The modified Gouy phase shift is also dependent on the transverse wavevector by $\Phi_G = \varphi(z) + \frac{\beta^2}{2k}z$.

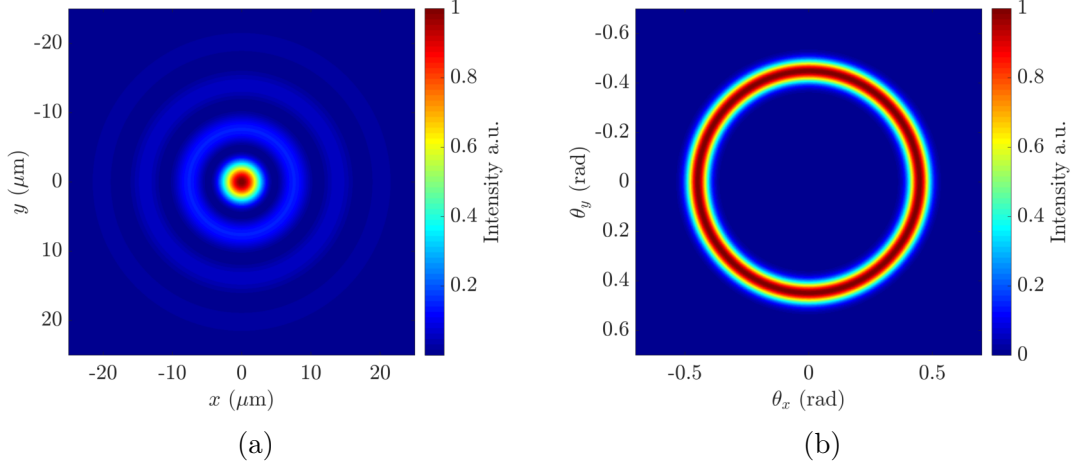


Figure 4.7: Example of a Bessel gauss beam with $\beta = 0.5$, $\omega_0 = 30 \mu\text{m}$. a) Representation for $z = 0$. b) Spatial spectrum of the beam in a).

Figure 4.7 shows a 2D intensity profile for $z = 0$ of a Bessel-Gauss with $\beta = 0.5$ as well as its spatial spectrum. This picture shows the characteristic interference pattern for when all Gaussian beams converge, and its characteristic annular spatial spectrum. One particularity of Bessel-Gauss beam is the appearance of diffraction free propagation around its focus. Indeed, through the interference most of the beam energy is concentrated in the first lobe (which is smaller than ω_0), making it interesting for non-linear optics where strong field-matter interaction is needed.

When a cylindrical step like transverse confinement is present, such as in step index wave-guide, the eigen-wavefunction becomes a pure Bessel basis. Contrary to the conical part of Bessel-Gauss beams, Bessel beams exhibits a plane wave phase function in real space and not a conical one.

4.2.2.4 Transverse modes frequency spacing

Inside an optical cavity, each transverse mode will resonate on a slightly different frequency due to its Gouy phase shift. By reusing the condition in Sec. § 4.2.1 for a resonating mode but with the complete axial phase from the higher order mode basis we can write the resonating frequency for each longitudinal q and HG modes n, m . The same derivation can be done for LG modes with p and l mode number, giving the factor $(1 + |l| + 2p)$ beam [Siegman 1986].

$$\nu_{nmq} = qFSR + (1 + n + m) \frac{\varphi_{GRT}}{2\pi} FSR \quad (4.23)$$

The $qFSR$ term comes from the plane wave longitudinal phase and the last term arises from the Gouy phase of higher order modes with $\frac{\varphi_{GRT}}{2\pi} FSR$ being the

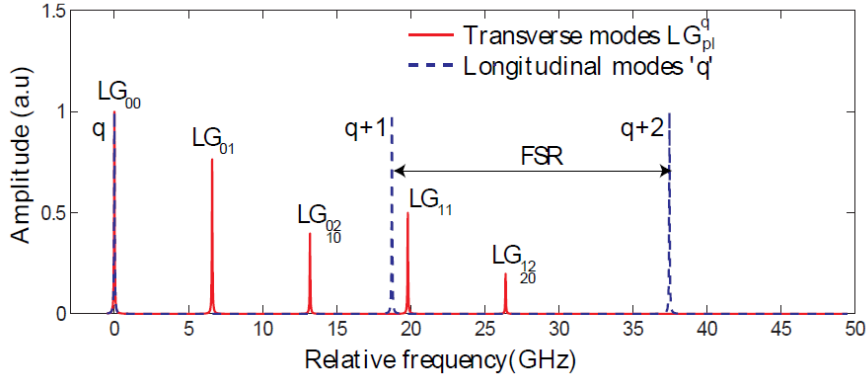


Figure 4.8: Frequency of transverse modes for a plane-concave cavity, calculated for a resonator length $L_c = 8$ mm and spherical mirror with $R_c = 10$ mm.

transverse mode spacing frequency. This means that for each longitudinal mode q there is an associated set of discrete frequencies corresponding to transverse modes with different mode number as shown in figure 4.8.

In the transverse dispersion diagram for a free space resonator, for each longitudinal mode q we have a set of (n, m) transverse modes. In the longitudinal direction the system is akin to a “well” like potential thus having a sinusoidal wavefunction and an energy-momentum dispersion relation following $E_q/\hbar = 2\pi qFSR = qv_gk_0$ where the energy is discretized following a linear relationship with the wavevector. In the transverse space, we will have the following relationship:

$$E_{n,m}/\hbar = (n + m)\varphi_{GRT}FSR = \frac{\beta^2}{2k_0} \quad (4.24)$$

where the energy is discretized following a parabolic relationship with the transverse wavevector β . For the special case of the BG family, the Gouy phase shift carrying a conical phase component, βr is added, and the dispersion relation becomes a mix of parabolic and linear dependencies.

It is important to note that in this equation, the axial mode spacing or FSR derived earlier is the result of the physical length of the resonator. While the transverse mode spacing is dependent on the round-trip Gaussian Gouy phase shift, which is not directly dependent on the resonator length but on the resonator configuration. For a two spherical mirror cavity of a same given length, the Gouy phase will not be the same for a near-planar or a near-confocal configuration. The accumulated Gouy phase for a near planar configuration is small (large stable mode size) thus leading to the clustering of the transverse mode frequency around the axial mode. On the other end, moving the configuration toward a confocal system

(small stable mode size) will increase the Gouy phase and increase the transverse mode frequency separation independent of resonator length.

4.2.3 Polarisation modes

The polarization state of a beam is completely characterized by its electric field vector. In the case of plane waves, this vector lies in the transverse plane and can be written as a combination of two mutually independent components:

$$\begin{aligned} E_x &= A_x e^{(-i\omega t + i\beta z + i\Phi_x)} \\ E_y &= A_y e^{(-i\omega t + i\beta z + i\Phi_y)} \end{aligned} \quad (4.25)$$

The polarization state of the electric field depends on the phase difference $\Delta\varphi = \varphi_x - \varphi_y$ between the two components. The electric field vector oscillates linearly along one direction at an angle ψ with respect to the x-axis, when the two components are either in phase ($\Delta\varphi = 0$) or have opposite signs ($\Delta\varphi = \pi$). The light is circularly polarized when ($\Delta\varphi = \pm\pi/2$) in this case, the vector field describes a circle as time evolves. If we look in the direction of propagation, the field rotates in a clockwise direction (right-handed) for ($\Delta\varphi = +\pi/2$) and in a counter-clockwise direction for ($\Delta\varphi = -\pi/2$). For any other phase difference value, the polarization of the light is elliptical.

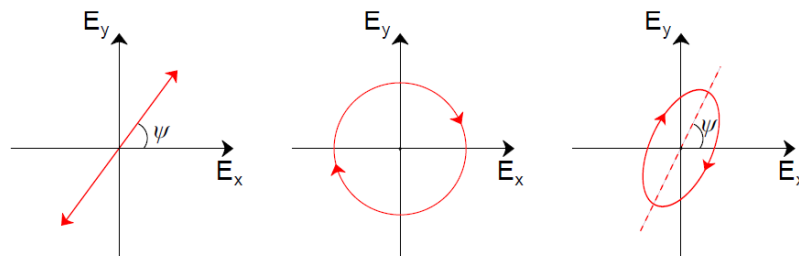


Figure 4.9: Different polarization states, from the left to the right: linear, circular and elliptical.

We note that the introduction of a linear birefringent element inside a laser cavity defines two linear polarization modes oriented parallel to the ordinary and the extraordinary axis of the element, regardless of the birefringence value [Seghilani 2015]. Nevertheless, the birefringence value will induce a frequency difference between the two oscillating waves.

4.2.4 Cavity stability

We described the different properties of a propagating field in free-space using the fundamental Gaussian parameter $\tilde{q}(z)$. However, not every cavity parameters fulfills the self-replicating beam requirement. ABCD matrix stability analysis can be used to find the Gaussian beam parameter $\tilde{q}_{RT}(z)$ for certain resonator configuration (See figure 4.10). This analysis is usually performed in the paraxial approximation using ray transfer matrix [Yariv 1991].

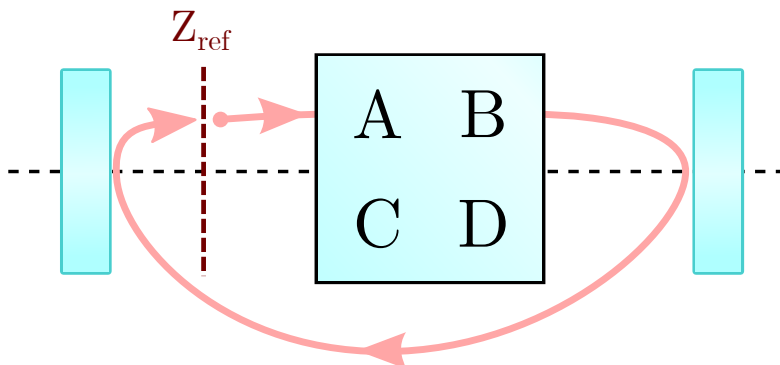


Figure 4.10: Schematic representation of the calculation of cavity stability using complex Gaussian parameter and ABCD matrix describing the round-trip.

4.2.4.1 ABCD matrix formalism

The ray transfer matrix or ABCD matrix are useful to describe an optical system including an optical resonator. They come from a geometrical description of optical rays in paraxial optical elements. The matrix links the slope and position of the input ray to the slope and position of the output ray in relation with the optical axis of the system. From this, we can relate each element of the matrix to the properties of the system. If we define r_1 and θ_1 as the input height and slope of the ray and r_2 and θ_2 as the output height and slope of the ray, we can write:

$$\begin{bmatrix} r_2 \\ \theta_2 \end{bmatrix} = \begin{bmatrix} A & B \\ C & D \end{bmatrix} \cdot \begin{bmatrix} r_1 \\ \theta_1 \end{bmatrix} \equiv \begin{matrix} r_2 = Ar_1 + B\theta_1 \\ \theta_2 = Cr_1 + D\theta_1 \end{matrix} \quad (4.26)$$

From equation 4.26 we see that the coefficient A represents the transverse magnification of the system while D is the angular magnification. While the coefficient B can be seen as an equivalent propagation length of the system. $B\theta_1$ represents a change of height in the output ray. And C gives us the focusing power of the optical system, or in other words, the change in the output slope versus the

input height. Several optical elements can then be represented as an ABCD ray matrix. Some elements used in this work are presented in the table 4.2

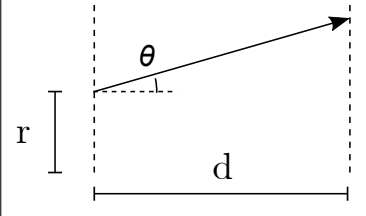
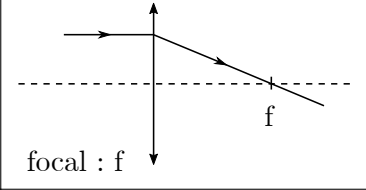
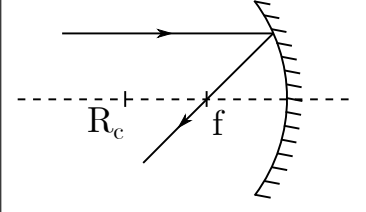
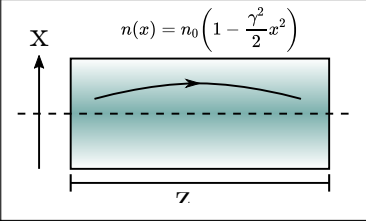
Propagation		$\begin{bmatrix} 1 & d \\ 0 & 1 \end{bmatrix}$
Thin lens		$\begin{bmatrix} 1 & 0 \\ -\frac{1}{f} & 1 \end{bmatrix}$
Spherical Mirror		$\begin{bmatrix} 1 & 0 \\ -\frac{2}{R_c} & 1 \end{bmatrix}$
Waveguide		$\begin{bmatrix} \cos(\gamma z) & \frac{1}{n_0 \gamma} \sin(\gamma z) \\ -n_0 \gamma \sin(\gamma z) & \cos(\gamma z) \end{bmatrix}$

Table 4.2: Summary table of ABCD matrix for four key optical element.

ABCD matrix can also be used for optical resonator. A geometric stability condition can be derived when after N round-trip no ray escapes the system. This condition is expressed for an ABCD matrix M_r in equation 4.27

$$\frac{|tr(M_r)|}{2} = \frac{|A + D|}{2} \leq 1 \quad (4.27)$$

Instead of geometrical rays, the ABCD matrix lets us work with spherical waves by defining the radius of curvature of the wave as $R = r/\theta$. Then, by replacing R with the complex Gaussian parameter $\tilde{q}_{RT} = \tilde{q}_1 = \tilde{q}_2$ defined earlier, we can transform equation 4.26 as:

$$\frac{1}{\tilde{q}_{RT}} = \frac{A + B \frac{1}{\tilde{q}_{RT}}}{C + D \frac{1}{\tilde{q}_{RT}}} \quad (4.28)$$

This equation expresses the fact that the complex Gaussian parameter must be the same before and after a round-trip, and is schematized in figure 4.10. From equation 4.28 we can derive Eq. 4.29 to calculate the size of the stable fundamental TEM_{00} mode in the cavity. It is done by extracting the waist ω_0 from q_{RT} , since after a round-trip the mode must be the same. The higher order mode size can then be calculated from the fundamental mode using Siegman definition adapted for a Hermite-Gauss basis[Siegman 1986]: $\omega_{m,n} = \omega_0 \sqrt{1 + m + n}$.

$$\omega_0 = \sqrt{\frac{\lambda}{\pi} |B|} \cdot \left[\left| \left(\frac{A+D}{2} \right)^2 - 1 \right| \right]^{-\frac{1}{4}} \quad (4.29)$$

We can also use the round-trip ABCD matrix to calculate the total Gouy phase shift. Using equation 4.15 we see that it is dependent on the propagation length and the Rayleigh length. By substituting the propagation distance with the B coefficient of the round-trip matrix and using equation 4.29 to get the Rayleigh length as a function of the ABCD parameters, we find:

$$\varphi_G = -\arctan \left(\text{sign}(B) \sqrt{\left| \left(\frac{A+D}{2} \right)^2 - 1 \right|} \right) \quad (4.30)$$

4.2.4.2 Diffractive cavity: Plano-Concave example

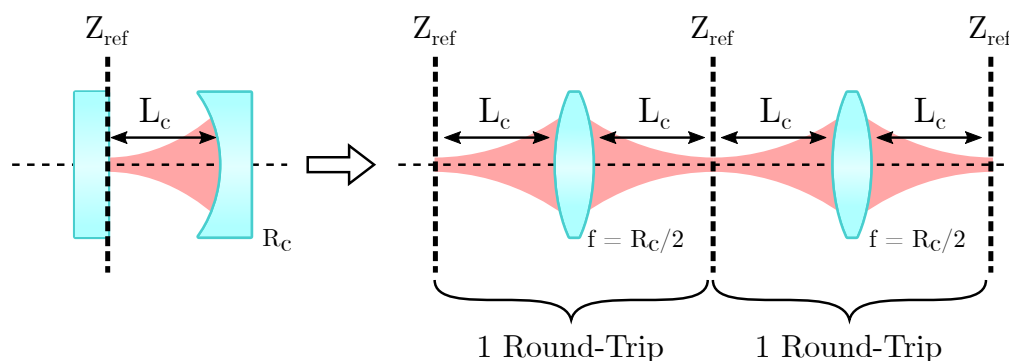


Figure 4.11: Schematic representation of a plano-concave optical cavity and its propagating equivalents by unwrapping each round-trip.

Using the previously developed tools, we can analyze the stability and behavior of a simple plano-concave cavity used mainly in VeCSEL system. Figure 4.11 shows us this cavity, and its development with paraxial elements, the reference for

development is on the plan mirror. Using that, we can write the ABCD round-trip matrix as:

$$M_{RT} = \begin{bmatrix} 1 & L \\ 0 & 1 \end{bmatrix} \begin{bmatrix} 1 & 0 \\ -\frac{2}{R_c} & 1 \end{bmatrix} \begin{bmatrix} 1 & L \\ 0 & 1 \end{bmatrix} = \begin{bmatrix} 1 - \frac{2L}{R_c} & 2L\frac{R_c-L}{R_c} \\ \frac{2}{R_c} & 1 - \frac{2L}{R_c} \end{bmatrix} \quad (4.31)$$

Using this matrix, it is possible to compute the stability region using equation 4.27. In this case, the parameters A and D are the same, and thus the condition become $0 < L/R_c < 1$ meaning the length of the cavity must not exceed the curvature radius of the mirror. Knowing the stability region, we can estimate the properties of the cold modes inside the cavity by calculating the size of the fundamental waist and the Gouy phase shift. Figure 4.12 shows the resulting calculation for, $R_c = 10$ mm with the fundamental mode size on the left and the Gouy phase on the right. An example of the longitudinal mode spacing for this type of cavity has also been given in section 4.2.1.

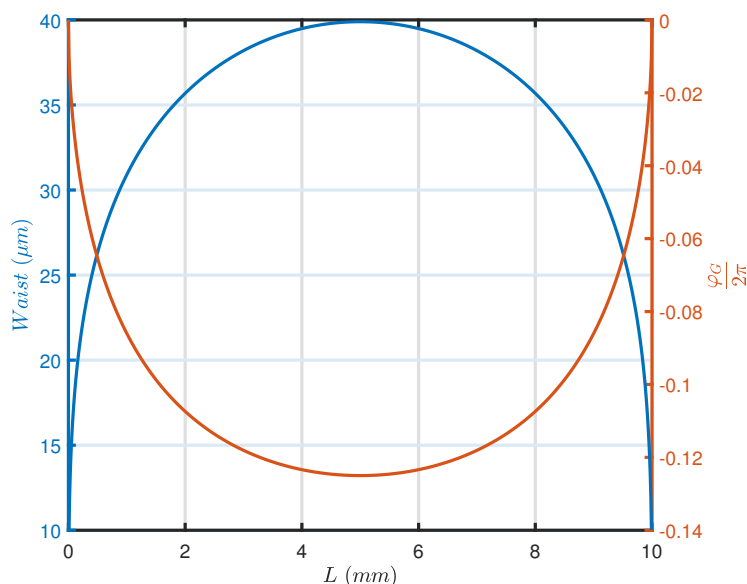


Figure 4.12: Waist size and Gouy phase shift versus the cavity length of a plano-concave system with $R_c = 10$ mm.

From this figure, we can observe the correlation between large mode size and large Gouy phase or strong discretization of the transverse modes. However, on the stability edge, when $L = R_c$ we see both the Gouy phase shift and the mode size going to zero. In our case, those conditions are interesting since we want to reach degeneracy in the transverse plane (we get closer to a con-focal configuration

where there is no effective diffraction). However, the plano-concave system is not telecentric (extended transverse area) and does not offer two separate conjugate focal planes to place both gain and SESAM. The cavity length is also dependent on mirror curvature, and long cavity for TLS are impossible to implement.

4.3 Conclusion

For 3D light structuration and localized structure generation, we have defined three main requirements. The extended transverse area, expressed by the Fresnel number and/or the NA limit of our system. The need to have access to two conjugate focal planes to place both the gain and saturable absorbing medium. And lastly the needs to reach high transverse degeneracy, meaning a small Gouy phase shift, thus a small effective diffraction. We can summarize those three conditions by restricting the cavity geometry to a bi-telecentric system. The object plane is imaged onto the image plane while conserving the same angular direction regardless of object height. The imaging system ensures two conjugate focal planes and low effective diffraction while keeping an extended transverse area.

To find a solution to this problem, we have introduced the general properties of a cold cavity. An optical resonator is considered stable when an eigenfunction after one round trip remains the same. From these properties and the cavity geometry, we can derive the shape and resonant frequency of the resonating modes. For spherical system two main mode families exist, the Laguerre and Hermit-Gaussian modes, while in conical wave system the Bessel-Gaussian mode best describes the resonating field. The stability analysis of a diffractive plano-concave cavity showed us that this system is inadequate for all of our needs. Mainly the conjugate focal plane and extended transverse area. We will see in the next section the description of a self-imaging system fulfilling all the requirements.

Spatially modeless cavity: Self-imaging optical system

The self-imaging optical cavity at first glance is ideal for 3D light structuration and localized structure generation. Indeed, the fact that it is an imaging system will produce very low effective diffraction and thus high spatial degeneracy. However, those systems are operating close to or at the marginally stable point. This means in part that it will become more sensitive to effects previously considered as perturbative, such as thermal lensing or optical aberration. An optical system that images itself onto itself after each round-trip does not impose a condition on the resonating field, and can be thought of as transparent. Therefore, any perturbative effects that were smaller than the cavity structuration before will now become important.

The stability of this optical cavity with low diffraction, a wide area across the transverse direction, and a high numerical aperture can be changed by different potentials in the real space (Near field) and the space of spatial frequencies (Far field). In near field, thermal lensing, self-focusing, gain modulation will tend to keep the light in place, while in far field the optical aberration will make the phase profile deviate from the paraxial parabolic one.

$$\phi(\beta) = \phi_0 + D_1\beta + D_2\beta^2 + D_3\beta^3 + D_4\beta^4 + \dots \quad (5.1)$$

Equation 5.1 described the paraxial far-field phase linearization relative to the transverse wavevector $\beta \approx k\theta$. With all orders different from β^2 being deformation due to aberration. By ignoring all odd orders that break rotational symmetry and keeping only the second and fourth order, we can derive an effective second order coefficient $D_{2_{eff}} = D_2 + D_4\beta^2$. Where $D_2 = -L_d/2k$ is the diffraction coefficient that will tend to zero in a self-imaging system. It leaves us with an effective diffraction from the spherical aberration. We can derive the condition that

$D_4\beta^2 \lll 2\pi$ to lessen the aberration impact. This term is also dependent on the divergence angle through β .

A similar expression as equation 5.1 can be written to express the Fourier plane amplitude filtering corresponding to diffusion effects in real space.

In this chapter, we will describe a self-imaging optical system and look at the effect of thermal lensing and misalignment on the cavity stability. We will also introduce optical aberration, more specifically spherical aberration, to explain the observed behavior of this system. In the end, we will summarize the key parameters to design a good self-imaging optical cavity.

5.1 Self-imaging interest

A self-imaging degenerate optical cavity is a system that images a plane on itself after a round-trip or when an arbitrary ray retraces its path [Arnaud 1969]. The ABCD matrix formalize implies that after a round-trip:

$$\begin{aligned} A &= D = 1 \\ B &= C = 0 \end{aligned} \quad (5.2)$$

The important parameter here is $B = 0$, since it means that the reference plane is imaged onto itself and the system exhibits no diffraction. $C = 0$ also means that the system has a null vergence. From this condition, it is possible to design different possible configurations of optical elements, leading to a self-imaging system. We show in figure 5.1 three different configurations for a self-imaging system.

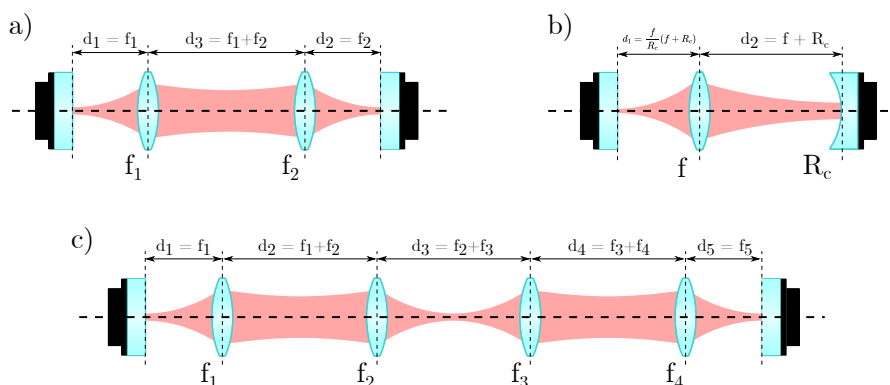


Figure 5.1: Example of three self-imaging cavity. a) Two lenses cavity. b) One lens, one mirror cavity. c) Four lenses cavity.

The configuration a) is made up of two plan mirrors and two lenses. By setting $d_1 = f_1$, $d_2 = f_1 + f_2$ and $d_3 = f_3$ we are in a 4-f telescopic configuration respecting the self-imaging conditions. In this case, the two plane mirrors are image onto themselves and the other. We can control the magnification on each plane with the choice of the focal length where $M = f_2/f_1$. The configuration b) is made of one lens and one spherical mirror. The conditions to respect in this case are $d_1 = f(1 + f/R)$ and $d_2 = R + f$. The configuration a) and c) are essentially the same, with an added pair of lenses for an 8-f configuration. This allows for longer cavity length and broader magnification control.

5.1.1 Extended transverse broad area

For 3D light structuration and spatially localized structure, we need a wide transverse area compared to the laser spot size. Like explained in section 4.1.2, for that, we want a large numerical aperture and Fresnel number. In our case, the three configurations can fulfil those requirements. The lenses used can be with large NA, and in the passive cavity case the Fresnel number of such a system is near infinite since $B = 0$.

The other advantage of the self-imaging cavity is the telecentric configuration. Any ray emitted from the gain mirror with transverse offset r at normal incidence $\theta = 0$ will be imaged on the opposite plane with the same angle and return after a round-trip with the same parameters. This theoretically extends our transverse area to the full lens diameter. In reality, we must consider the beam divergence and the lens truncating effects reducing this range.

5.1.2 Extended longitudinal area

For temporally localized structure (temporal pulse) it is important to have a round-trip time longer than the recovery time of the active mediums. In other words, the cavity length must be long so that after a round-trip the travelling pulse sees an unsaturated gain and absorption. For that, the self-imaging system and in particular the c) configuration is the most interesting. With the 8-f lenses systems, we can have a spatially degenerate cavity with low diffraction while keeping the physical length and the round-trip time long. For example, a system with $f_1 = f_4 = 8$ mm, $f_2 = 100$ mm and $f_3 = 200$ mm in a 8-f configuration has a length of $L_c = 632$ mm and a round-trip time of $\tau_{rt} \simeq 4$ ns. Thus, a gain medium with quick recovery time < 4 ns could be used for temporal localized structure [Camelin 2018]. The other two configurations are less suited for this application since using long focal length will inherently reduce the maximum numerical aperture, so the limit of transverse degeneracy.

5.1.3 Active component placement

We need to both place the gain and the saturable absorber in conjugate focusing planes. For both configuration a) and c) the two plane mirrors allow adequate placement (see figure 5.2). The added benefit of those configurations is the possibility to control the magnification of the image of one plane onto the other. For the configuration a) the magnification corresponds to $M = f_2/f_1$ while for the configuration c) it becomes $M = f_2f_4/f_1f_3$. The resulting zoom is an important parameter to be able to control. Since the gain and saturable absorber are integrated on each mirror, we can adjust the relative size of the localized structure on each of them to maximize or minimize the saturation and non-linear effect without affecting other parameters such as the effective diffraction (B parameter of ABCD matrix).

However, for the configuration b), only one plane is accessible for gain and absorption placement, leading to the added requirement of combining them into one device. In this case, we also lose the ability to adjust the saturation parameter independently. For this reason, we choose to use a 4-f configuration for spatially localized structure that can be expanded into a 8-f system for combining spatial and temporal localization.

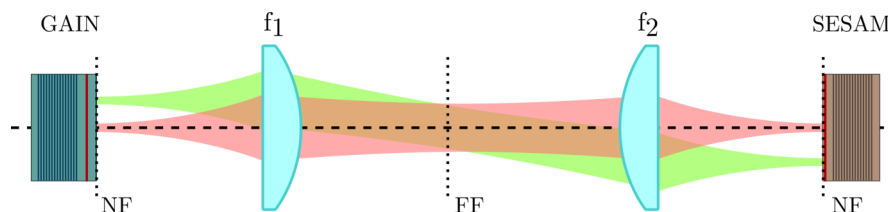


Figure 5.2: Placement of the active component (Gain and SESAM) inside a 4-f cavity.

In the 4-f configuration, the active elements will be placed on the near field of the resonating field. This placement means that the lenses must have a large numerical aperture, to allow for the coexistence of multiple resonating transverse spots.

5.2 System stability

In this section, we will look at the self-imaging stability using configuration a). By design, the round-trip matrix of such a system is an identity matrix, thus $A + D = 2$. According to the stability criterion, such a system is then marginally stable. In reality, this kind of system is not achievable and several effects such as

small offset/misalignment, thermal lensing, optical aberration can strongly impact the stability.

5.2.1 Thermal lensing: local anharmonic potential

In all pumped systems, thermal effect can play on the resulting cavity stability. In our case, the optical pumping of semiconductors induces a three-dimensional refractive index variation proportional to the temperature. We can estimate the resulting phase variation using $dn/dT = 2.7 \times 10^{-4} \text{ K}^{-1}$ for the GaAs. After one round trip in the structure, the laser wave undergoes a phase shift due to the variations of the optical path, which is now spatially inhomogeneous. For the 1/2 VCSEL structure, given the small thickness of penetration length and the small temperature variations over this distance, we can neglect the longitudinal variation of the index, so the phase shift will be mainly transverse and generates a “thermal lens”.

$$\Delta\varphi(x, y) = 2kL_p(n - 1) + 2kL_p \frac{dn}{dT} \Delta T(x, y) \quad (5.3)$$

where $\Delta T(x, y)$ is the thermal distribution induced by the pumping. This thermal lens will distort the resonator stability condition. If the temperature profile can be approximated by a parabola around the axis of the pump, then the phase shift will have the effect of a lens called a “thermal lens.” For a uniform pump profile with rotational symmetry, the focal length of the equivalent thermal lens can be calculated with the following formula [Laurain 2010][Yariv 1991]:

$$F \sim \frac{\sigma^2}{2ln(2)L_p} (R_{th}P_p \frac{dn}{dT})^{-1} \quad (5.4)$$

where σ is the half-width at half maximum (HWHM) of the pump beam, L_p the penetration length in the 1/2 VCSEL chip, R_{th} the thermal impedance and dn/dT the change of the refractive index with temperature. Other pump profile can lead to a differently shaped “thermal lens”. Using the tool in section § 2.4.2 to compute the thermal profile, we can estimate the equivalent paraxial lens and wavefront aberration of any pump shape.

The paraxial thermal lens on the gain can be introduced in the round-trip matrix calculation by multiplying the identity matrix with a thin lens matrix, where $C_{th} = -1/f_{fth}$ gives us the following result:

$$M_{RT} = \begin{bmatrix} 1 & 0 \\ C_{th} & 1 \end{bmatrix} \times \begin{bmatrix} 1 & 0 \\ 0 & 1 \end{bmatrix} = \begin{bmatrix} 1 & 0 \\ C_{th} & 1 \end{bmatrix} \quad (5.5)$$

This leads to a non-null C coefficient for the ABCD round-trip matrix, meaning that our system is not perfectly telecentric anymore. Indeed, for a beam emitted

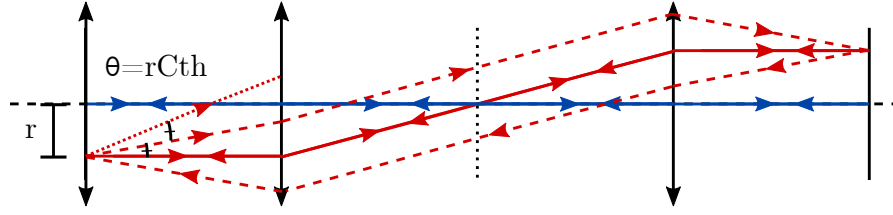


Figure 5.3: Schematic representation of the angle shift experienced by a ray after one round-trip.

at normal incidence $\theta = 0$ with a transverse offset on the gain mirror plane $r \neq 0$ it will, after a round-trip, accumulate an angle rC_{th} (see figure 5.3) then $2rC_{th}$ for the second round-trip and NrC_{th} for the N round-trip.

As an example, let's take a cavity with a finesse of, $\mathcal{F} = 100$ then the average number of round-trip is $N = \mathcal{F}/2\pi$. For an off-axis beam $r = 50 \mu\text{m}$, if we want the total angle deviation to be $|NrC_{th}r| < 10 \text{ mrad}$, we need the thermal lens contribution to be $|C_{th}| < 2.5 \times 10^{-2} \text{ mm}^{-1}$. Or in terms of focal length $|f_{th}| > 40 \text{ mm}$. However, this is true only for a paraxial lens contribution, in reality the thermal phase profile deviates from this simple approximation especially on the edge of the pumping region.

For a Gaussian pumping profile, we can approximate the induced temperature and phase profile by a Lorentzian, following:

$$\Phi_{th}(r) = \frac{\Delta\phi}{1 + \frac{r^2}{(0.9\omega_p)^2}} \sim 1 - \frac{kC_{th}r^2}{2} \quad (5.6)$$

where $\Delta\phi = k \cdot 2e \cdot dndT \cdot \Delta T$, is the induced phase shift from ΔT temperature difference, $dndT$ is the optical index variation from temperature and e is the gain active region thickness. ω_p is the pump waist. Approximating the equation with a Taylor expansion and ignoring the constant phase term, we can deduce the paraxial equivalent focal. This equation represents the phase potential seen by a resonating electromagnetic field in real space on the gain mirror plane.

5.2.2 Longitudinal misalignment: non-local parabolic phase diffraction tuning

Starting from the perfect 4-f configuration, we can add misalignment in the system to investigate the effect on the cavity stability. In addition, we look for misalignment in d_2 and d_3 shown in figure 5.4.

We end up with the round-trip matrix with the reference plane on the side of the thermal lens:

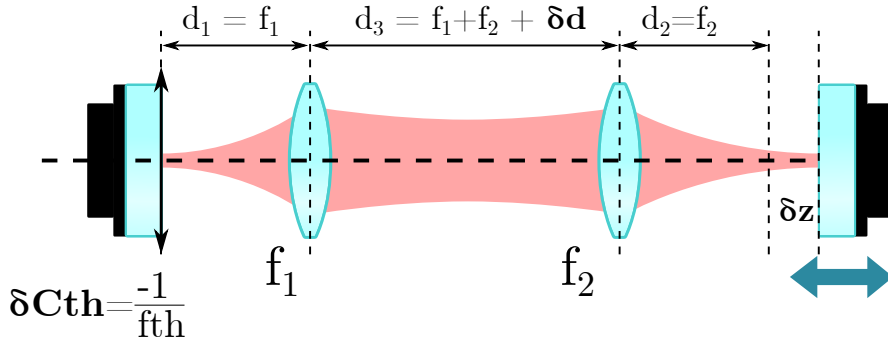


Figure 5.4: Self-imaging cavity in 4-f configuration with the thermal lens $C_{th} = -1/f_{th}$ and misalignment in $d_2 = f_1 + f_2 + \delta d$ and $d_3 = f_2 + \delta z$

$$M_{RT} = \begin{bmatrix} 1 - \frac{2\delta d \delta z}{f_2^2} & 2\delta z \frac{f_1^2}{f_2^2} \\ C_{th} - 2\frac{\delta d}{f_1^2} + \frac{2\delta z \delta d}{f_1^2 f_2^2} (\delta d - C_{th} f_1^2) & 1 - \frac{2\delta d \delta z}{f_2^2} + 2\delta z C_{th} \frac{f_1^2}{f_2^2} \end{bmatrix} \quad (5.7)$$

To simplify the matrix and understand what are the physical effects of each misalignment, and since they are small perturbations, we remove the second order terms (C_{th}^2 , δd^2 , δz^2) and the cross products to get the matrix in equation 5.8. This optical system can also be represented as a small micro-cavity of length $B/2$ with a parabolic phase profile of curvature $-\frac{\pi C}{\lambda} r^2$ (see figure 5.5).

$$M_{RT} \simeq \begin{bmatrix} 1 & 2\delta z \frac{f_1^2}{f_2^2} \\ C_{th} - \delta d \frac{2}{f_1^2} & 1 \end{bmatrix} \quad (5.8)$$

Typically, the A and D coefficient are not impacted at first order, meaning that there is no change in magnification from small longitudinal variation. As seen previously, the thermal lens adds some phase profile in the near field, leading to a vergence destabilizing off-axis emission. On the other hand, tuning the distance δd also allows adjusting of the total vergence of the system. It is then possible to use the distance δd to cancel or minimize the impact of the thermal lens on the round-trip stability. Together, this gives us some small control over the residual focusing power of the system. In figure 5.5 we can represent those effects as a parabolic phase profile in the micro-cavity.

On the other hand, tuning the distance δz affects the effective length of the system. In this case, since the reference plane is on the opposite side of the variation,

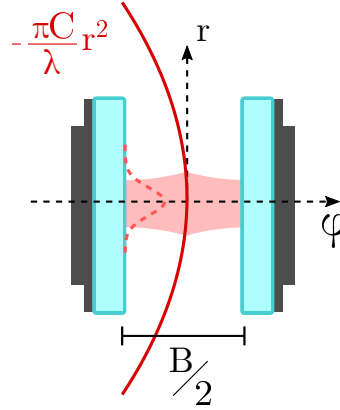


Figure 5.5: Schematic representation of the SI 4-f cavity with the thermal lens and small longitudinal misalignment.

the magnification divides its effect by $M^2 = f_2^2/f_1^2$. If the reference plane was on the same side as the variation, then the result would have been $B = 2\delta z$. This equivalent distance correlates directly with the offset from the self-imaging position and can be linked to the round-trip length of the micro-cavity in figure 5.5. In practice, this variation is easily tunable with a micro-metric translation stage.

Using the non-simplified matrix, we can study the different regions of stability of such a system. Figure 5.6 shows the calculation of the on-axis Gaussian mode size versus the value of the B parameter for different configurations. The black line corresponds to the marginally stable case with no thermal lens and $\delta d = 0$. This case is not physically realistic and serves to illustrate the self-imaging point in the plot. When the contribution of C_{th} and δd results in a negative C parameter, then stability occurs for $B > 0$. This regime is the regime of normal diffraction. The other case when $C > 0$ the stability occurs in the anomalous diffraction regime $B < 0$. The properties of this system to be able to function in both regimes is interesting, since it could be possible to balance any sign of non-linearity.

This result also shows us that too big of an offset from the self-imaging position leads to large stable mode size, incompatible with our requirement for small degenerate transverse modes. To look at the tolerance for this degeneracy, we need to go back to the Gouy phase shift.

5.2.3 Transverse degeneracy tolerances

Two aspects are important to define the level of spatial degeneracy. First the transverse frequency mode separation given by the Gouy phase shift φ_G of the system and the width of the resonance given by the Finesse \mathcal{F} . We want to have a

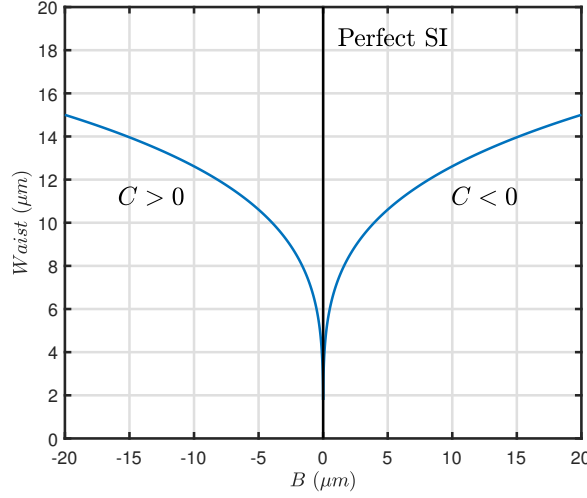


Figure 5.6: Gaussian mode size ω_0 versus the parameter B .

continuum of transverse states around one longitudinal resonance. Figure 5.7 shows two examples of a dispersion diagram with the superposition of the longitudinal resonance width for each transverse mode. The first example is for a discrete transverse mode basis with large Gouy phase shift like in the previously shown plano-concave cavity, while the other is an example of the targeted self-imaging cavity with a continuum of transverse state.

A simple way to evaluate the degeneracy is to calculate the number of transverse resonance one longitudinal mode width can accommodate.

$$N_{dege} = \frac{\text{mode width}}{\text{mode separation}} = \frac{FSR 2\pi}{\mathcal{F} |\varphi_G| FSR} = \frac{2\pi}{\mathcal{F} |\varphi_G|} \quad (5.9)$$

In the self-imaging case, it is also possible to simplify the Gouy phase expression from equation 4.30 using since $A = D \simeq 1$ and $AD - BC = 1$.

$$\varphi_G = -\arctan \left(\text{sign}(B) \sqrt{\left| \frac{BC}{2} \right|} \right) \quad (5.10)$$

It is then possible to represent the number of degenerated modes N_{dege} versus the B and/or C coefficient for a 4-f self-imaging cavity. For our needs, we can set the subjective criterion of $N_{dege} > 10$ to define the self-imaging region of our system. Figure 5.8 depicts the number of degenerated on-axis mode verse the B coefficient for the 4-f system and different C values. We see that the width of the degenerated region is impacted by the strength of the thermal lens, and the smaller

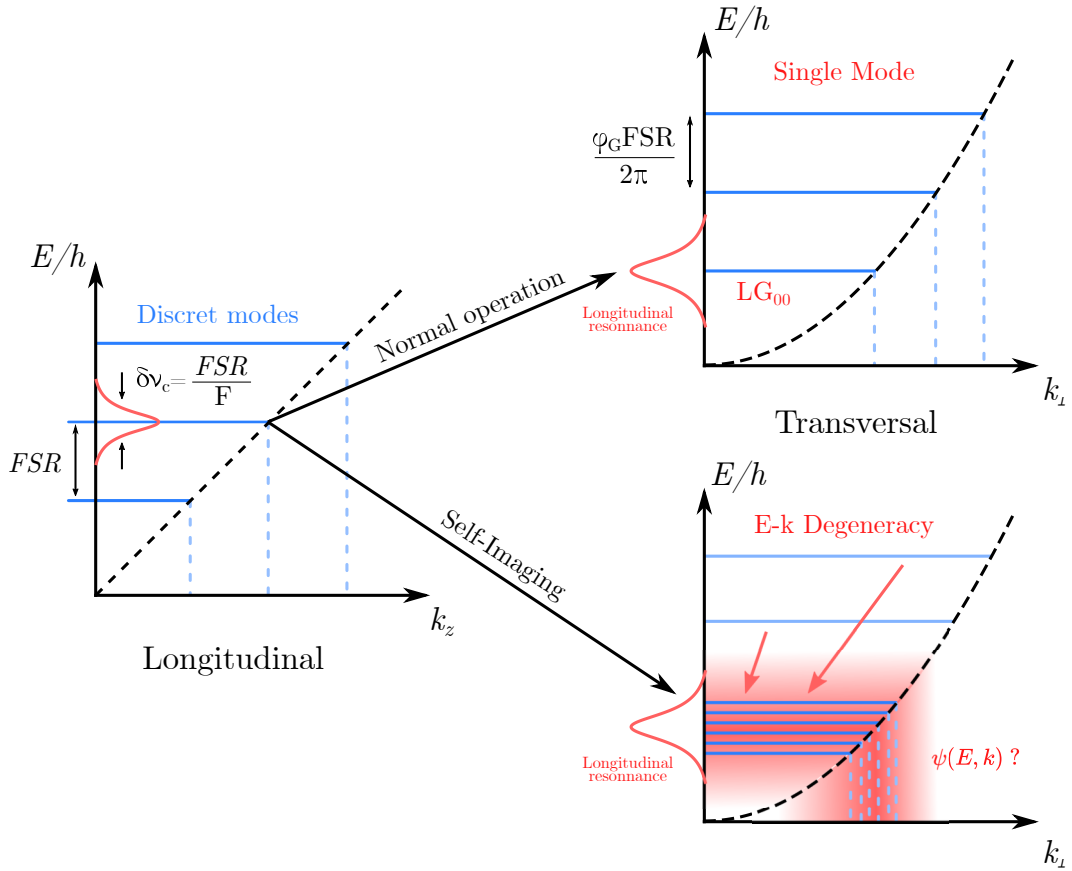


Figure 5.7: Resonance frequency versus transverse wavevector dispersion diagram depicting a cavity with a discreet mode basis (Left) and a cavity with a transverse continuum of state (Right).

it is, the larger it becomes. For a thermal lens of $f_{th} = 25$ mm to $f_{th} = 100$ mm the range of the degeneracy varies from $\Delta B = 2$ μm to $\Delta B = 8$ μm .

For now, we have analyzed the optical cavity in the paraxial ABCD approximation. However, this analysis shows some limits. In figure 5.9 we show a real example of the optical modes sizes resonating inside a two lenses cavity with $f_1 = 20$ mm and $f_2 = 15$ mm. The pumping scheme for this measurement amounted to a thermal lens around, $f_{th} = 15$ mm leading to δ_z a variation of around 400 μm . The simple model can explain the spherical wave variation. However, it falls short for the conical wave (Bessel-Gauss family). In the degenerate position, the ABCD system also falls short to explain the measured degenerated wavefunction. We will develop in the next chapter a tool to analyze the system in those conditions. To achieve this analysis, we need to consider the more complex phase transfer function, including

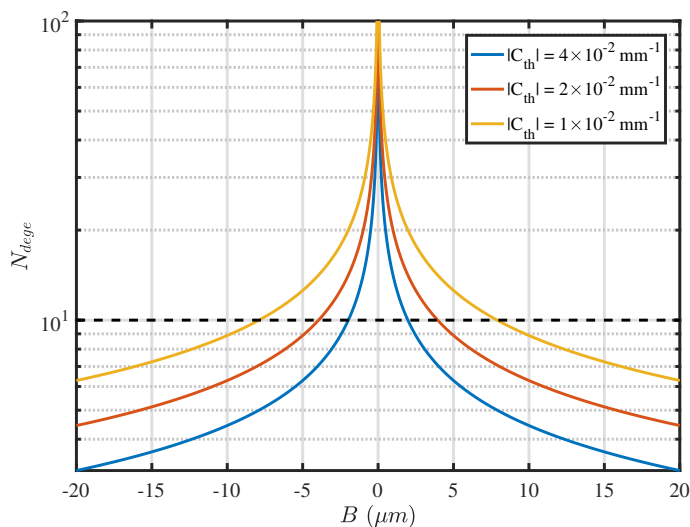


Figure 5.8: Number of degenerated on-axis mode verse the B coefficient for the 4-f system and different C values. The dotted line represents the criterion $N_{dege} = 10$.

higher order perturbation than the parabolic phase. We refer to these perturbations as the aberration of the optical system.

5.3 Aberrations effects on self-imaging system

The optical aberrations are usually defined as the performance departure from the paraxial optical system. In classical paraxial optics the phase effects are limited to the second order or parabolic term while all other terms are considered as aberration. For an optical system with circular symmetry, we can write the complex pupil function as:

$$P(\rho, \theta, h) = A(\rho, \theta)e^{ikW(\rho, \theta, h)} \quad (5.11)$$

Where (ρ, θ) are the normalized polar coordinates in the exit pupil plane of the optical system and h the object height. $A(\rho, \theta)$ is the pupil transmission function and $kW(\rho, \theta, h)$ is the phase transfer function. This term is directly proportional to the wave aberration following the corresponding power expansion[Welford 1986]:

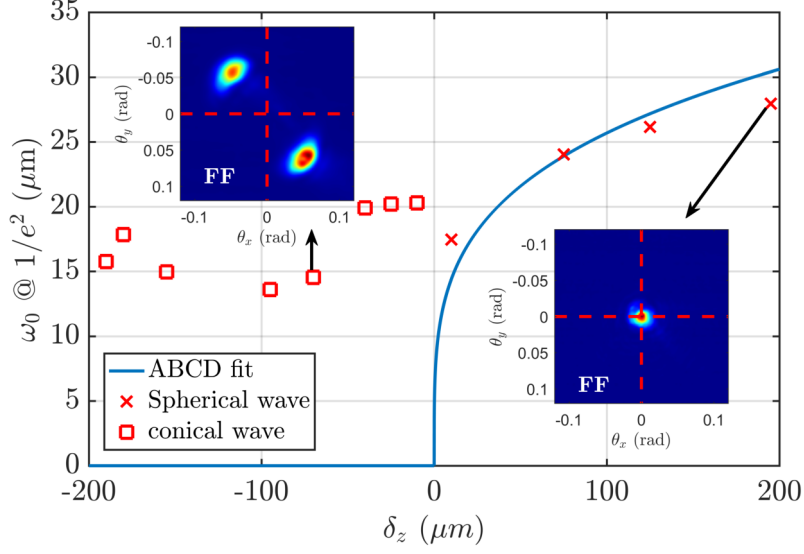


Figure 5.9: (solid line) Expected waist size on the gain versus effective cavity length. (cross / square) Measured waist size on the gain side. The square point indicates conical waves, while the cross indicates spherical Gaussian waves. The two inserts are the 2D intensity profile of the far field.

$$\begin{aligned}
 W(\rho, \theta, h) = & W_{000} + W_{020}\rho^2 + W_{111}h\rho \cos(\theta) + W_{040}\rho^4 + W_{131}h\rho^3 \cos(\theta) \\
 & + W_{222}h^2\rho^2 \cos^2(\theta) + W_{220}h^2\rho^2 + W_{311}h^3\rho \cos(\theta) \\
 & + W_{060}\rho^6 + W_{151}h\rho^5 \cos(\theta) \\
 & + \dots
 \end{aligned} \tag{5.12}$$

The explanation for the different terms is listed in table 5.1. The first five terms, excluding the piston, are usually referred to as the primary aberration since they describe the most important effect. Figure 5.10 schematize the principal parameters for aberrated optical system, the exit pupil position, the reference sphere and aberrated wavefront.

In our case, we will neglect the Tilt and coma since or object offset height is small compared to the pupil size ($h \ll \rho$), but we will focus on the effect of the spherical aberration for the stabilization of conical waves.

5.3.1 Spherical aberration

Most optical elements have spherical surfaces, in large part due to the simplicity of the manufacturing process. The surface shape follows a parabola close to the

Coefficient	Power expansion	Name
W_{000}	1	Piston
First order terms		
W_{020}	ρ^2	Defocus
W_{111}	$h\rho \cos(\theta)$	Tilt
Third order terms		
W_{040}	ρ^4	Spherical aberration
W_{131}	$h\rho^3 \cos(\theta)$	Coma
W_{222}	$h^2\rho^2 \cos^2(\theta)$	Astigmatism
W_{220}	$h^2\rho^2$	Field curvature
W_{311}	$h^3\rho \cos(\theta)$	Distortion
Fifth order terms		
W_{060}	ρ^6	Fifth order spherical aberration
W_{151}	$h\rho^5$	Fifth order linear coma
\vdots		

Table 5.1: List of the different wavefront aberration terms and their meaning.

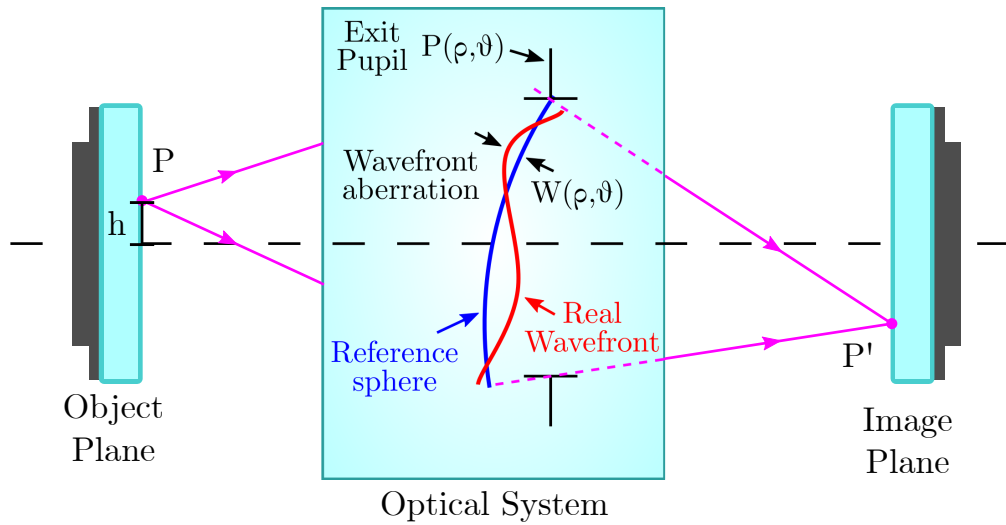


Figure 5.10: Schematic representation of an imaging system with the representation of the real wavefront (with aberration) and the reference sphere in the exit pupil.

center, but quickly breaks down, leading to large variation from the paraxial approximation. It is easy to see this effect for a simple plano-convex lens using a geometrical ray tracing (see figure 5.11).

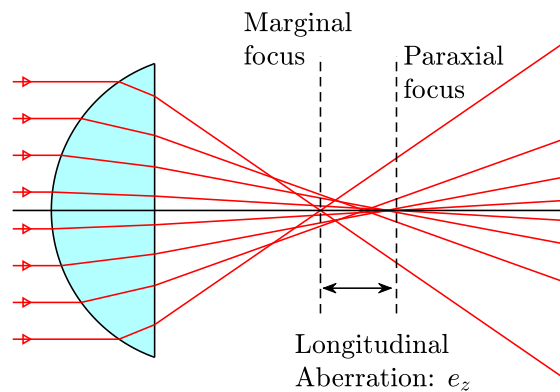


Figure 5.11: Spherical aberration in plano-convex lens.

In this example, where a plano-convex lens is used to focus the incident collimated light, the marginal ray near the edge of the lens will cross the optical axis before the paraxial ray which is closer to the lens center. Looking at the wavefront aberration function, the term $W_{040}\rho^4$ corresponds to the spherical aberration. This is only dependent on ρ meaning a small phase variation at the center of the pupil

and a large phase variation at the edge. This will have the effect of increasing the focusing power on the edge of the lens.

From this view, it is also useful to define the longitudinal aberration coefficient e_z as the distance between the paraxial focus point and the marginal focus. Using the optical distance convention, if the marginal focus is before the paraxial focus, then $e_z < 0$ and inversely.

5.3.1.1 Seidel coefficient

The primary aberrations are inherent to the shape of the surfaces, so Seidel derived a way to link the wavefront aberration function with the surface shape [Welford 1986]. For the spherical aberration, this leads to:

$$W_{040} = \frac{1}{8} S_1 \text{ with } S_1 = \sum_{\text{All surf}} \text{Surface geometry impact} \quad (5.13)$$

This shows that the impact of each surface adds up into the full aberration of the system. This enables us to use a single aberrated element representing the full system aberration while keeping all others as paraxial elements, as we will see in section 5.3.2. The usual convention for the sign of S_1 is to take it positive if the marginal ray focuses before the paraxial ray and inversely.

5.3.1.2 Off-axis incident beam

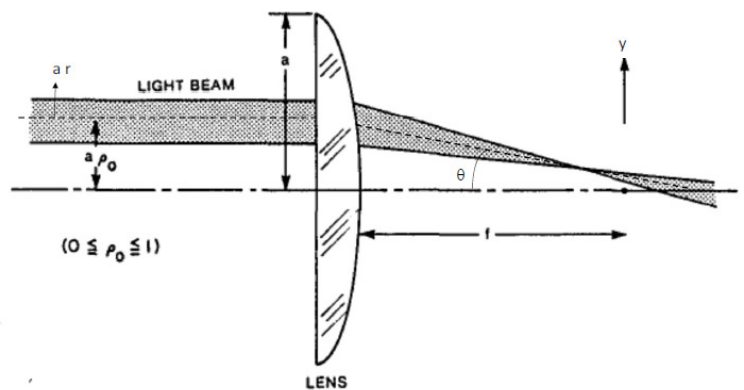


Figure 5.12: Schematic representation of a decentered Gaussian beam and lens aberration effects [Yoshida 1982].

We want to calculate the effect of the spherical aberration on the focus of the off-axis beam. Following the development of Yoshida [Yoshida 1982] we write the aberration function for a incident beam parallel to the optical axis with a plane wavefront.

$$W(r, \phi) = \frac{S_1}{8}\rho_0^4 + \frac{S_1}{2}\rho_0^3 \cos(\phi)r + \frac{S_1}{4}\rho_0^2(2 + \cos(2\phi))r^2 + \frac{S_1}{2}\rho_0 \cos(\phi)r^3 + Sr^4 \quad (5.14)$$

The offset referential is (r, ϕ) where r is the normalized (by the lens radius a) local radius on the beam axis and ϕ is the azimuth angle. The normalized offset from the optical axis is ρ_0 , figure 5.12 schematize this geometry. For a Gaussian beam, we assume that the aperture is large in front of the beam waist to avoid any truncation issue. This can be written as $2\omega < (1 - \rho_0)$. Since the local beam variation is small, $r \ll 1$ we neglect the effect of the induced coma r^3 and spherical aberration r^4 on the beam itself. We also neglect the r term corresponding to a small anisotropic tilt, since the term is also proportional to $\rho_0^3 \ll \theta \simeq \rho_0/f_0$. We are left with:

$$W(r, \phi) = \frac{S_1}{8}\rho_0^4 + \frac{S_1}{4}\rho_0^2(2 + \cos(2\phi))r^2 \quad (5.15)$$

The first term gives us the shift in path length from the offset optical path due to spherical aberration. While, the second term allows us to calculate the anisotropic focal variation for an offset beam. By denormalizing $r' = r.a$ and $\rho'_0 = \rho_0.a$ and using, $\theta \simeq a\rho_0/f_0$ we can express equation 5.15 with the incident angle on the image plane. Now we can write the complete phase transfer function, including the paraxial focusing element of focal f_0 , the calculated aberration and neglecting the constant (not depending on r) phase term, we find:

$$\Phi(r, \phi) = -\frac{kr^2}{2f_0} \left(1 + \frac{S_1\theta^2}{2a^4} f_0^3(2 + \cos(2\phi)) \right) \quad (5.16)$$

From this, we can see that the equivalent vergence $C = -1/f + \delta C_{SA}$ of an offset incident beam on a lens with spherical aberration corresponds to the paraxial focal plus a parabolic angle variation from the spherical aberration. According to the Seidel definition, a positive coefficient corresponds to a marginal ray crossing the optical axis before the paraxial one, thus is equivalent to reducing the focal length and inversely. We can also see the induced anisotropy from the beam offset, where x , is the sagittal plane $\phi_x = \pi/2$ and y the tangential plane $\phi_y = 0$. This results in a vergence variation with a strong astigmatism of 1 : 3

$$\delta C_{SA_{x,y}} = -\frac{S_1\theta^2}{2a^4} f_0^2(2 \pm 1) \quad (5.17)$$

The tangential plane corresponds to the incident angle plane, while the sagittal plane is at 90 deg from it. From the anisotropic focal length variation due to aberration, it is then possible to recalculate the stability for the off-axis emitted beam.

5.3.2 Stability analysis with spherical aberration

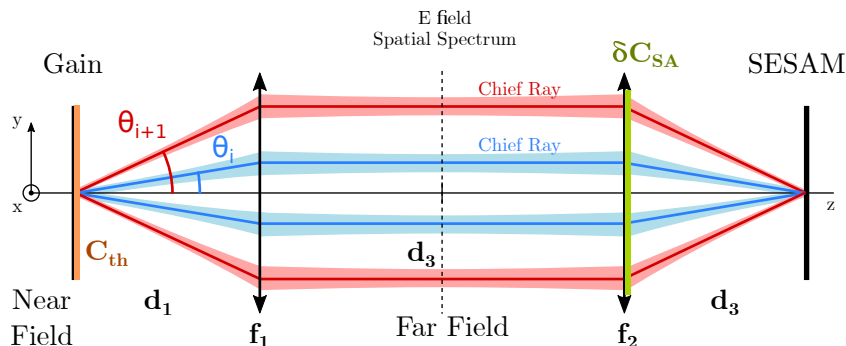


Figure 5.13: 4-f optical cavity schematics with thermal lensing effect and focal variation aberration effect. An off-axis bidirectional rotating beam is included as a reference for the off-axis angle θ .

To consider the spherical aberration in a near self-imaging cavity using ABCD matrix, several hypotheses must be met:

- We assume a quasi continuum of off-axis cavity systems that circulate radially in a ring-like path (see figure. 5.13) at angle θ_i in a self-imaging telecentric configuration (uni-directional travelling wave or bidirectional standing wave states).
- Only spherical aberration are taken into account. All lenses are computed as paraxial element. The round-trip focal length variation due to spherical aberration is placed at the NA limiting lens.
- We assume our system to be close to self-imaging such that the angular magnification from the gain to the SESAM does not vary and is equal to $\alpha_m = f_1/f_2$. Thus, the incident angle θ_2 on the SESAM is equal to $\theta_2 = f_1/f_2\theta$.
- Each angle θ_i propagates a possibly anisotropic Hermite-Gauss like basis of weak divergence $\Theta_G < NA$ compared to the paraxial system $NA < 0.5$. The possible angular separation between two stable off-axis mode must be greater than the beam divergence $2/k\omega_0 < \theta < NA$.

Using ABCD matrix, we can now write the single pass system matrix for the sagittal and tangential plane. A cavity stability corresponding to a unique system can then be calculated for each angle θ_i .

$$M_{SP_{x,y}}(\theta) = \begin{bmatrix} 1 & 0 \\ \frac{C_{th}}{2} & 1 \end{bmatrix} \begin{bmatrix} 1 & d_1 \\ 0 & 1 \end{bmatrix} \begin{bmatrix} 1 & 0 \\ -\frac{1}{f_1} & 1 \end{bmatrix} \begin{bmatrix} 1 & d_2 \\ 0 & 1 \end{bmatrix} \begin{bmatrix} 1 & 0 \\ -\frac{1}{f_2} & 1 \end{bmatrix} \quad (5.18)$$

$$\times \begin{bmatrix} 1 & 0 \\ \delta C_{SA_{x,y}}(\theta \frac{f_1}{f_2}) & 1 \end{bmatrix} \begin{bmatrix} 1 & d_3 \\ 0 & 1 \end{bmatrix}$$

Following Siegman [Siegman 1986] we can calculate the round-trip matrix using the reverse matrix from SESAM to Gain $M_{RT} = M_{SP}M_{SP}^T$. In this system, d_1 , d_2 and d_3 correspond to the distance between lenses with $d_3 = f_2 + \delta_z$ and C_{th} is the vergence from the thermal lensing effect and $\delta C_{SA}(\theta_2)$ is the vergence variation from spherical aberration.

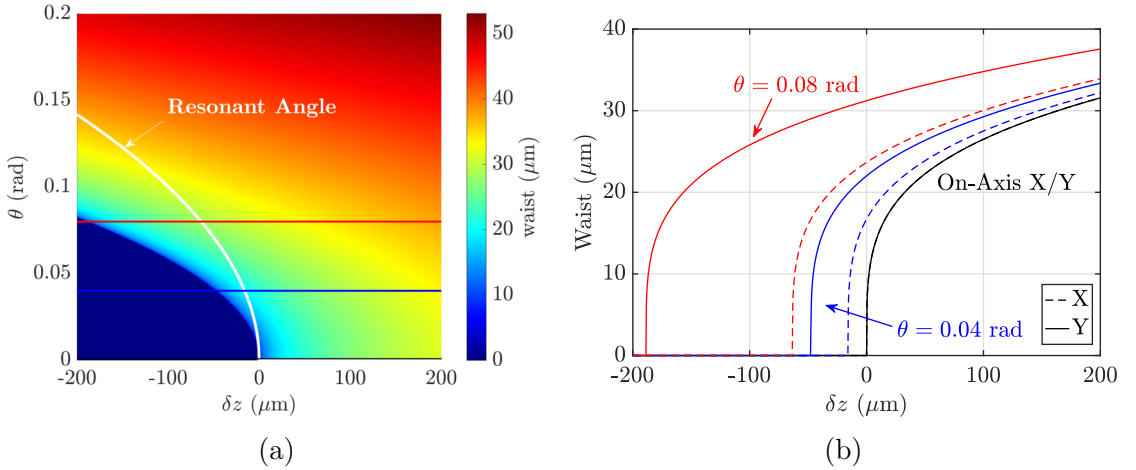


Figure 5.14: Off-axis ABCD stability analysis with $f_1 = 20$ mm and $f_2 = 15$ mm and $S_1 = 1.2$ mm with $a = 8.25$ mm. a) 2D representation of all stable angles. Each line represents a new cavity with θ incidence angle. b) Stability for the On-axis (black) and for two different θ angles. X represents the sagittal plane and Y the tangential one.

On figure 5.14 we show the result of the stable fundamental waist size (color scale) for different incident angle θ and $f_1 = 20$ mm, $f_2 = 15$ mm, a thermal lens $f_{th} = 12$ mm and a Seidel coefficient of $S_1 = 1.2$ mm. From this example, each horizontal line corresponds to the stability of a cavity with θ_i angle. On figure 5.14b we show the sagittal and tangential stability for angles 0.08 rad and 0.04 rad. We

remark that for each angle, the self-imaging point (waist null) shifts according to the sagittal/tangential focal variation of equation 5.17.

The highlighted white line marks the “resonant angle”. It shows the exact angle for when the off-axis focal (in the sagittal plane) equals the distance d_3 . In the case of spherical aberration, this follows the longitudinal spherical aberration[Welford 1986]:

$$e_z = -\frac{S_1 f_0^4}{2a^4} \theta^2 \quad (5.19)$$

This value characterizes the distance at which the marginal ray of angle θ cross the optical axis from the paraxial one. A negative value implies that the marginal ray crosses the axis before the paraxial one.

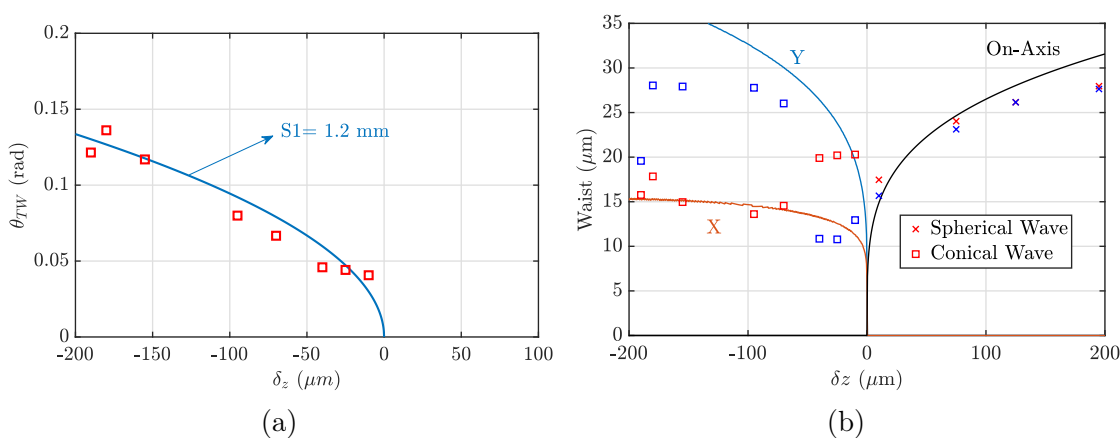


Figure 5.15: Off and On axis stability with the ABCD matrix and spherical aberration with $f_1 = 20$ mm, $f_2 = 15$ mm, $f_{th} = 12$ mm and $S_1 = 1.2$ mm with $a = 8.25$ mm corresponding to the system shown in figure 5.9. a) Plots of the measured TW angle with the hard angle ABCD condition fit giving $S_1 = 1.2$ mm. b) Plots of the near field stability with the On-axis and Off-axis ABCD fit.

We can use this condition for limiting the infinity of cavity stability by only picking the fundamental waist for the “resonant angle”. Plotting the fundamental waist in the sagittal and tangential plane for each $(\delta z, \theta)$ satisfying it, we have figure 5.15b. This simulation was done to fit the measured waist of figure 5.9 for a cavity with $f_1 = 20$ mm and $f_2 = 15$ mm. The Seidel coefficient was adjusted with the measured angle of the off-axis modes following equation 5.19 (see figure 5.15a). In this configuration, the NA limit lens was the $f_2 = 15$ mm thus the angled used to estimate S_1 was $\theta_2 = f_1/f_2\theta$. The measured Seidel coefficient is equivalent to the aberration effect of the whole system.

From those graph, we can see the on-axis ($\theta = 0$ rad) stability for positive δz and the strongly astigmatic stability for off-axis beam for negative δz . In this

representation, each point along the off-axis stability line corresponds to an incident angle, θ which itself is the result of a whole stability analysis. Even if the off-axis stability appears to be for anomalous diffraction, going back to figure 5.14 shows that we are still in the normal diffraction regime given that the self-imaging point has shifted.

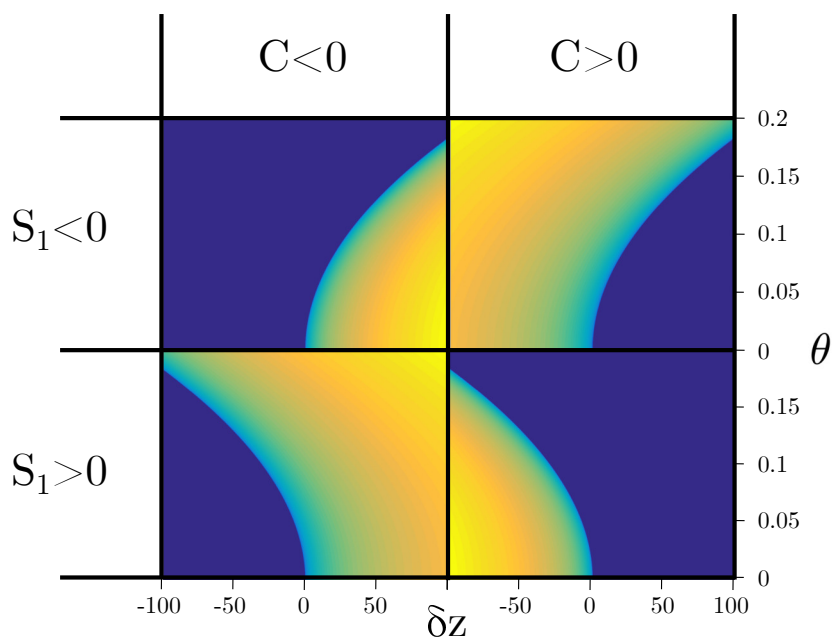


Figure 5.16: Summary of the different Off-axis stability, depending on the sign of both the aberration (S_1) and the parameter C .

To summarize the expected behavior for telecentric optical cavity near self-imaging with spherical aberration, we can look at figure 5.16. It displays the result of the ABCD calculation (large waist yellow, small waist blue) for a stability in the normal ($C < 0$) or anomalous ($C > 0$) diffraction regime with a positive or negative Seidel coefficient. We see here that stability shift for the off-axis beam is not affected by the C parameter (toward larger focal for $S_1 < 0$ and toward smaller focal for $S_1 > 0$ but the stable region is given by the sign of the C parameter. To reduce TW competition near the self-imaging being in the top right and bottom left quadrants is better since the resonant angle condition is opposite the on-axis stability. Using this fact in practice also allows us to quickly identify the on-axis self-imaging position by looking for the transition between on-axis and off-axis emission.

5.3.2.1 Spherical aberration limits

In practice, the wavefront aberration of commercially available lenses rarely consists of only fourth order variation (i.e., spherical aberration) but can show a much more complex pattern. Figure 5.17 (taken from Thorlabs) shows the difference in wavefront error between three lenses of similar focal and diameter but different design (aspherical and achromatic) and polishing methods. Spherical polishing for the achromatic lens (only spherical surfaces). CNC-Polished and MRF-Polished method for the aspheric lens. Their measurements show a strong deviation from only spherical aberration (lens b and c) and thus some higher aberration order term. The measured peak to peak value for the aspheric lens (lens b) is even stronger than for the achromatic lens (lens c). This difference can be explained by the fact that the aspheric is inherently more difficult to polish. Using the more precise MRF-polished method (Magnetorheological Finishing) it is possible to reduce by a factor of ten the aberration amplitude but not all the higher order aberration oscillation. Those large differences are due to manufacturing process and tolerances [Malacara 2001].

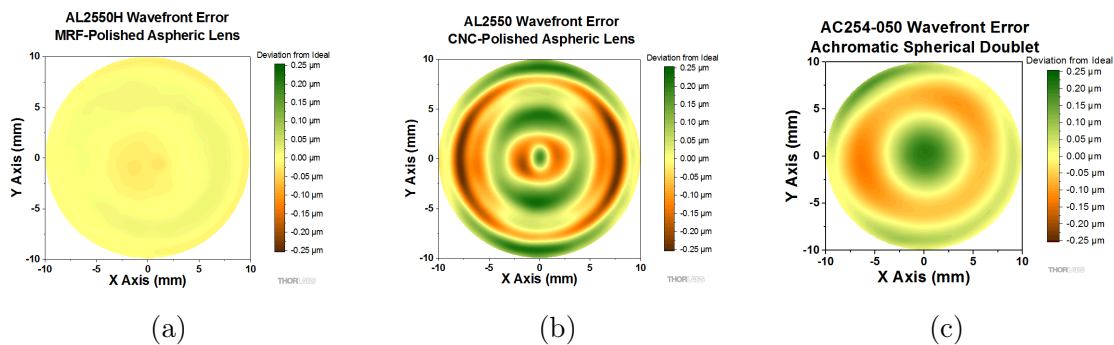


Figure 5.17: Example of measured wavefront error from the Thorlabs lenses catalog. (a) AL2550H, MRF polished aspheric lenses. (b) AL2550, CNC polished aspheric lenses. (c) AC254-050, achromatic doublet lens

The presence of higher order aberration term will deform the simple spherical aberration response. To investigate their effects, we use a ray-tracing software (Zemax) with the fitted wavefront error shape from figure 5.17 applied to the NA limiting lens of a 4-f paraxial system. The longitudinal aberration being related to the “resonant angle” of Off-axis emission, by computing those values we can see how higher order aberration terms can deform the off-axis stability.

Figure 5.18 shows the comparison of the longitudinal aberration (i.e., resonant angle position) for a round trip in a 4-f optical system with the fitted wavefront error of the AL2550 (aspheric lens b) and AC254-05 (achromatic lens c). The dotted lines are a fit for only spherical aberration. The equivalent Seidel coefficient

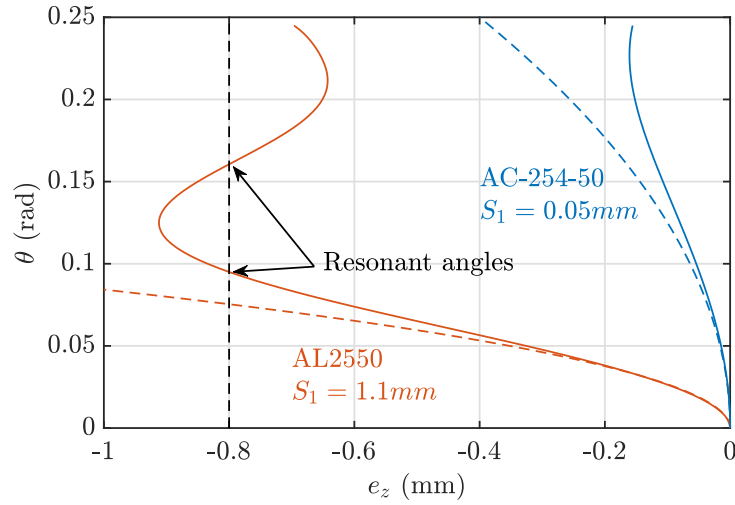


Figure 5.18: Longitudinal aberration for a round-trip 4-f system with one paraxial lens of focal $f_1 = 50$ mm and a lens with the fitted wavefront error of AL2550 and AC254-50.

is $S_1 = 1.2$ mm and $S_1 = 0.05$ mm for the aspheric and achromatic lens, respectively. We see that the wavefront modulation is deforming the resonant angle response to the point where multiple angles could resonate for a same detuning δz .

Code	Lens Type	f	CA	NA	WE	S_1
AC-254-050	Achromatic	50 mm	22.86 mm	0.22	No Data	0.05 mm
AL-2550	CNC Aspheric	50 mm	23 mm	0.23	$< 0.5 \mu\text{m}$ (RMS)	1.1 mm
AL2550J	MRF Aspheric	50 mm	21.3 mm	0.2	< 100 nm (P-V)	< 0.05 mm
AL1225J	MRF Aspheric	25 mm	10.6 mm	0.2	< 100 nm (P-V)	< 0.05 mm
AL2520-C	CNC Aspheric	20 mm	22.5 mm	0.54	$< 0.5 \mu\text{m}$ (RMS)	~ 1.2 mm
AL1815-C	CNC Aspheric	15 mm	16.5 mm	0.53	$< 0.5 \mu\text{m}$ (RMS)	~ 1.2 mm

Table 5.2: Thorlabs datasheet of the lenses used in this work. CA: Clear Aperture. NA: Numerical Aperture. WE: Wavefront error. And estimated equivalent S_1 coefficient.

Table 5.2 summarizes the datasheet of the lenses used in this work. We see that for an equivalent numerical aperture, the MRF polished asphere gives the least amount of aberration both in the Thorlabs datasheet and in the estimated S_1 coefficient. However, from the datasheet alone we do not have any information on the regularity or modulation of the wavefront error. For this, we can refer to figure 5.17 to have a general idea of the wavefront error shape according to the manufacturing and design process.

5.3.3 Numerical aperture

The finite aspect of the lens provides a physical limit for the numerical aperture that can be written, $NA_{max} = \arctan(a/f)$ where a is the clear aperture radius and f the lens focal length. To maximize this limit, we can choose a large diameter lens with short focal. However, in practice, mechanical limitations such as the minimum distance from the gain to the lens mount while being able to still optically pump our sample at Brewster angle or the minimum space required by the translation and mount between the two lenses, put limits on those choices. As seen at the beginning of this chapter, to have more than 99.9% power transmission through the lens for a Gaussian spot of $5\ \mu\text{m}$ on the gain, we must use a lens with at least $NA > 0.14$. This result come from [Siegman 1986] by using the power transmission of a Gaussian beam through a circular aperture of radius a formula: $T = 1 - e^{-2a^2/\omega^2}$. Thus, to ensure good operation for spot size as small as, $5\ \mu\text{m}$ we have to use lenses with minimum 0.14 NA. With this limit set, the choice of focal length available becomes quite large and one inch 50 mm focal length lenses with $NA = 0.2$ are an adequate option.

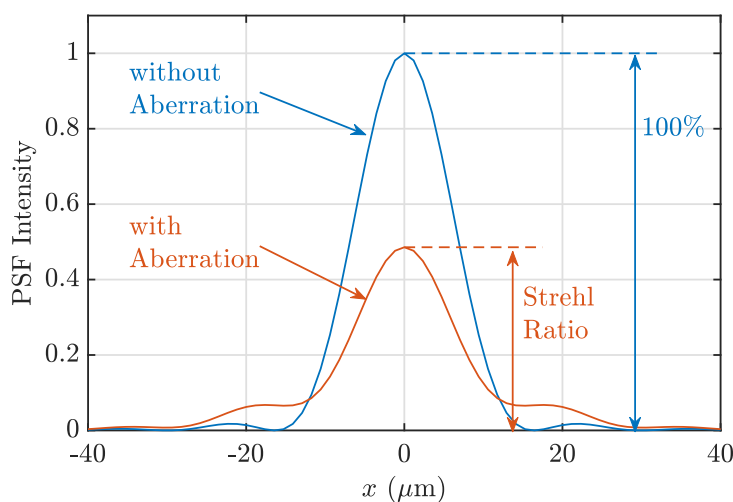


Figure 5.19: Point Spread Function (PSF) for a given aperture size without aberration (blue) and with aberration (red). The blue PSF give the diffraction limited and the 100% Strehl ratio, while the red one is the real PSF with a lower Strehl ratio.

This criterion, only looks at the power transmission of the optical element, but wavefront deformation from aberration can also dramatically reduce the achievable spot size. This effect is even amplified by the intra-cavity nature of the optical element, where phase deformation will strongly shape the resonating beam. To investigate the phase aberration effects, we look at the Strehl ratio.

5.3.3.1 Strehl ratio

The Strehl ratio, first proposed by astronomer Karl Strehl [Strehl 1895] is commonly used to define image quality in various optical systems through the Maréchal criterion [Maréchal 1948]. It states that for a Strehl ratio of 0.8 or above, we can consider the optical system to be diffraction limited, meaning that aberration has close to no impact on the image size and quality.

The Strehl ratio is defined as the ratio from the max intensity of the real system PSF (Point Spread Function) over the theoretical PSF without aberration [Mahajan 1983]. The PSF being the image through the optical system of an infinitesimally small point source. In signal processing terms, the impulse response of the optical system. Figure 5.19 shows the two PSF used to define the ratio. The aberration of the optical system tends to broaden the PSF and thus reduce its peak intensity, leading to lower than 1 Strehl ratio.

5.3.3.2 Aperture limits for On-axis beam

In our case, we investigated the aberration effect of this criterion to have a better picture of the NA limit of our system. Using a ray tracing software, we were able to compute the Strehl ratio for different apertures in our system from 0 to the full aperture given by the lenses size. Around 0.2 NA for 25.4 mm diameter lenses of 50 mm focal.

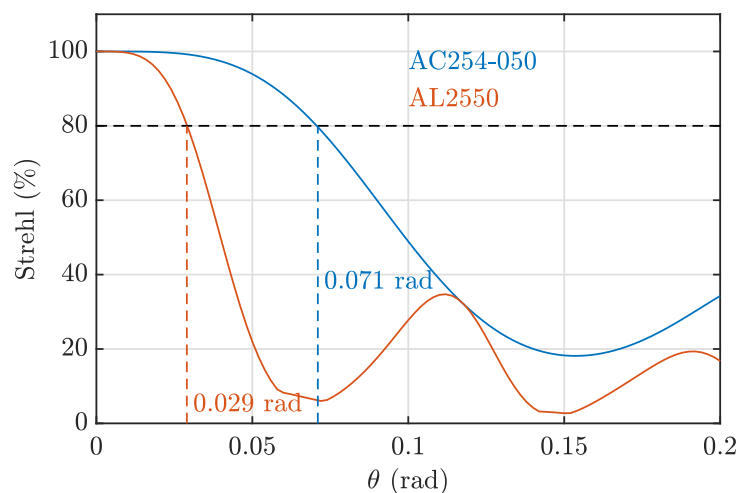


Figure 5.20: Strehl ratio computation for two different lenses as a function of the aperture, given as the marginal ray angle on the gain size. The blue curve is for the Thorlabs AC-254-050 achromatic lens and the red curve is for the Thorlabs AL-2550 aspherical lens. Both lenses have a $f = 50$ mm focal length.

Figure 5.20 shows the results for the achromatic AC254-50 lens (blue curve)

and the aspheric AL2550 one (red curve). For both those lenses, we see a sharp drop-off of the Strehl ratio the larger the aperture gets. However, despite being an aspheric lens, the higher order aberration terms lead to a quicker cut-off. For a $5\ \mu\text{m}$ Gaussian spot size with $0.067\ \text{rad}$ divergence angle only the achromatic lens is still considered diffraction limited while the wavefront modulation of the aspheric one will lead to a large broadening of the spot size. This limits from the 0.8 Strehl ratio criteria does not mean the laser cavity cannot stabilize larger diffracting spots. However, it is a good approximation for when the transition between the on-axis and off-axis emission occurs, since on-axis mode are no longer diffraction limited and multiple round-trip in the system would lead to a large broadening.

5.4 Conclusion

In this chapter, we have studied the self-imaging 4-f optical cavity. We explained why this optical system was ideal for 3D light structuration and localized structure generation. Indeed, by design the optical system is telecentric with two conjugate focal planes. This allows us to be in an extended transverse system where we can have multi-axis stability. Looking at the round-trip matrix for such design, we can see that the effective diffraction length of the simplified micro-cavity is tunable by the longitudinal detuning from the self-imaging position. This in effects allows us to reach a system with no diffraction (at the SI position) and high Fresnel number. In this condition, the Fourier space phase transfer function (energy-momentum dispersion diagram) should be flat, meaning that:

$$\frac{\delta\varphi}{\delta\beta} = 0 \quad \text{and} \quad \frac{\delta^2\varphi}{\delta\beta^2} = 0 \quad (5.20)$$

In this condition, we have reached the transverse degeneracy regime, where any arbitrary wavefunction could be projected on any transverse mode-basis. However, in reality, reaching this marginally stable point is impossible, and perturbative effects becomes the main stabilizing factor. We studied two of them, one in real space with a local effect on the EM field (thermal lensing) and another with a non-local effect (spherical aberration).

Figure 5.21 synthesize the two stabilizing effects in a self-imaging cavity by tracing the phase in real space (thermal lens) and in spatial frequency space (aberration). The optical aberration limits the range of on-axis transverse wavevector Δk compared to the SI position.

Thermal lensing both helps to stabilize paraxial optical modes and limit the high degeneracy operating regions. The stronger thermal lensing is, the harder it is to degenerate a large number of transverse modes. This can be explained by the confining/waveguiding effect of this phenomenon, thus making it harder to

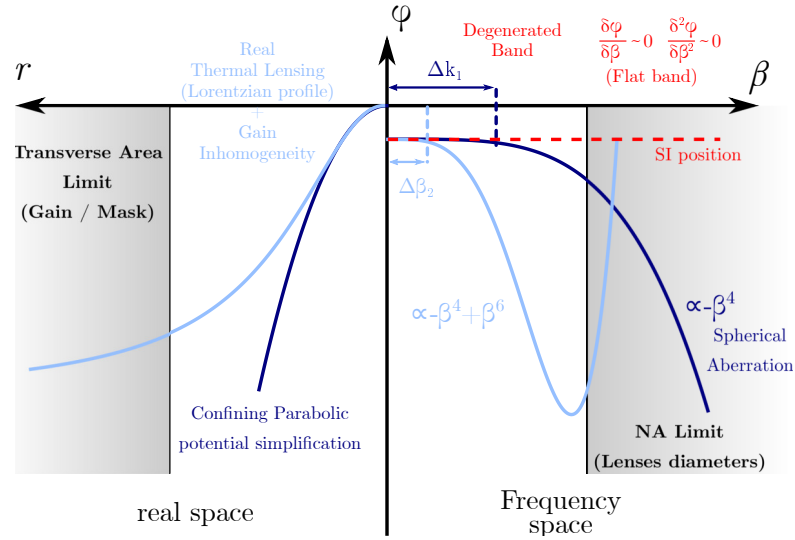


Figure 5.21: Local and non-local phase potential from thermal lensing, cavity detuning and optical aberration.

collapse all transverse resonances. For a cavity composed of lenses $f_1 = 20$ mm and $f_5 = 15$ mm the transversally degenerate region for several degenerate modes $N_{dege} > 10$ ranged from an effective round-trip length of $B = 2 \mu\text{m}$ to $B = 8 \mu\text{m}$ corresponding to a thermal lensing of $f_{th} = 25$ mm to $f_{th} = 100$ mm. As a general rule, having a thermal lens larger than the max focal length of the optical system is important to be able to reach the degenerated state.

On the other hand, optical aberrations, are non-local effects that limit the achievable flatness of the transverse Fourier phase profile. For a large numerical aperture, the wavefront error leads to a spot size broadening, limiting the effective numerical aperture of the optical system. Looking at the Strehl ratio, we can quantify this limitation. For commercially available lenses, diffracted limited design such as MRF polished lens or achromatic lens appears to be the least limiting. Higher order aberration which modulates the optical system wavefront error decreases significantly the lens quality. By carefully selecting the lens, we can still design a system with a flat on-axis phase response. The spatial frequency bandwidth is then not limited by the numerical aperture of the system (lens diameter) but by the residual aberration shape.

Beyond this limit, the optical aberration, especially the spherical one, will separate the stability diagram for the on-axis and off-axis modes (Gaussian with tilted emission). This degeneracy lift is both limiting for high degeneracy operation and useful in practice to estimate the SI position. In practice, we can also use the conical-wave regime to estimate the spherical Seidel coefficient S_1 for each cavity configuration. The amplitude of this coefficient provides us information about

the maximum NA bandwidth ($\Delta\beta \propto 1/|S_1|$) possible and the sign of the residual diffraction (normal for $S_1 > 0$ and anomalous for $S_1 < 0$). Typically, for having a sufficient bandwidth to support as small as $5\ \mu\text{m}$ waist spot, $|S_1| < 0.1\ \text{mm}$ is needed and with a positive sign to be compensated by non-linear self-focusing effect. From the studied lenses, a combination of MRF and achromatic lenses are viable options.

To conclude, the 4-f SI configuration is a good choice for light structuration, but careful consideration must be taken in the choice of optics and pumping scheme. A simple paraxial ABCD matrix stability analysis can be made to have a global vision of the system behavior. However, in the degenerate region this model fails, and a more complete model is needed. In the next part of this manuscript, we will describe such physical model which will be used to understand linear and non-linear behavior in the degenerate region.

Part IV

Experimental results and analysis

Analysis tools: Multi-harmonic Schrödinger Non-linear like equation

For now, we have described the gain structure properties as well as the saturable absorber. We design one of each with the goal of 3D light structuration and spatially localized structure generation. For this, we also explored the relevant properties of an optical cavity and their limits for large transverse extended area in a self-imaging configuration. Now to complete our understanding and help us analyze the experimental data, deriving a simple model encompassing the semiconductor and cavity properties is essential.

Figure 6.1 schematize such a system, where a gain mirror is image with some magnification through an optical system onto a saturable absorber mirror. Each of those elements will impact the transverse wavefunction propagation. The local effects from near-field (here the near field is defined as the gain or SESAM plane) interaction with the active medium. It will affect both the phase (self-focusing, thermal lensing) and the amplitude (localized losses, self-amplitude modulation) of the wavefunction. While, the non-local effect is applied onto the Fourier (here also defined as the Far field) space of the wavefunction. In turn, they will also change the wavefunction through diffusion, diffraction, or aperture effects and deviation from the ideal wavefront. As seen in chapter 1, describing this system in the SVE and paraxial approximation will lead to an inhomogeneous traveling wave model. In the following chapter, we will simplify this model to a single equation describing the change of the transverse field per round-trip, following the same description and assumption made for pulse propagation in time.

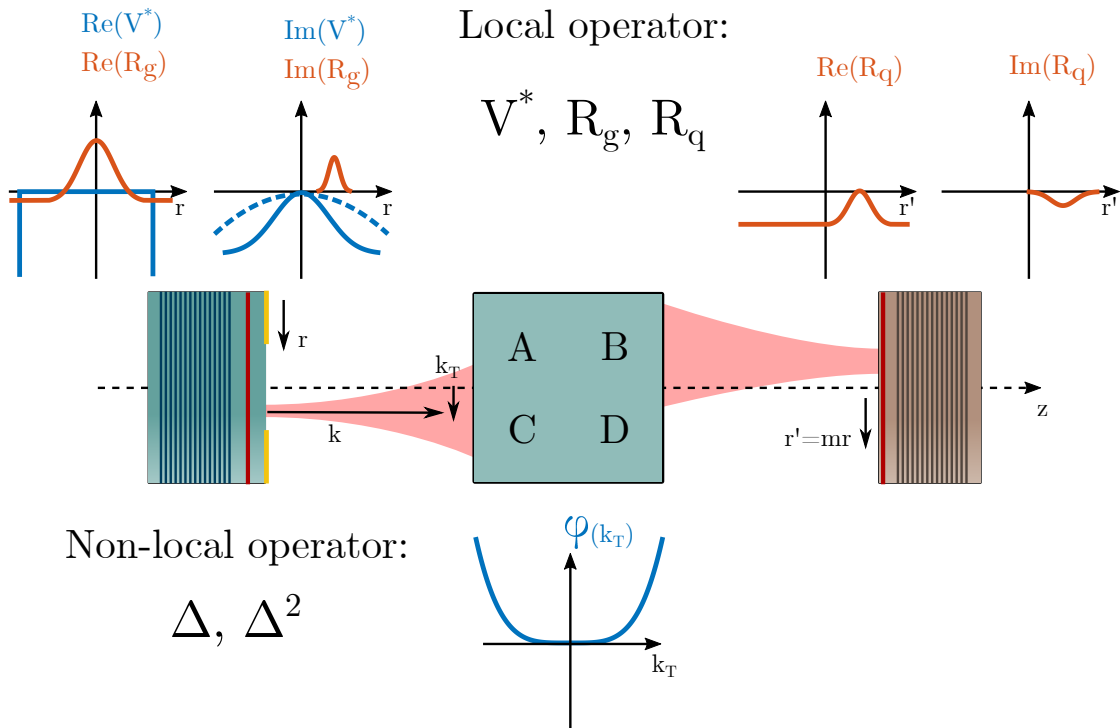


Figure 6.1: Laser system, with the main physical operator playing a role in the transverse structuration of the laser beam.

6.1 Derivation of multi-harmonic Schrödinger like non-linear equation

For a long time, temporal dynamics inside a laser cavity have been studied using both simple rate equation and more complex Schrödinger like model. Furthermore, the field of passive mode-locking using saturable absorber has made use of a discrete model of the different cavity element to derive a master equation for individual pulse propagation [Haus 1975a, Haus 1975c, New 1974]. For this, they used the Fourier space to describe the pulse behavior with group delay dispersion and the pulse shape with third order dispersion [Keller 2021]. However, from a simply mathematical standpoint, dispersion in time is equivalent to diffraction in space and higher order dispersion to higher order diffraction. Based on this simple analogy, we aim to establish a multi-harmonic Schrödinger like non-linear equation to analyze a self-imaging laser cavity.

6.1.1 Simplified system and hypothesis

To follow the same kind of derivation as for passive mode-locked pulse propagation equation, first some assumptions and approximations needs to be made.

- We make the slowly varying envelope approximation (SVEA) on the electromagnetic field \vec{E} propagating as a continuous wave (mono-frequency). We also work in the paraxial approximation, where the wave propagates in the \vec{z} direction. From those approximations, we can say that the transverse field profile variation per round-trip is small, while the CW regime allows us to neglect the time dependency.

$$\vec{E}(x, y, z, t) = A(x, y, z).e^{k_z z - \omega_0 t}.\vec{e} \quad (6.1)$$

From this, we also defined the spatial spectrum as the 2D Fourier transform following:

$$\tilde{A}(k_x, k_y, z) = \int \int A(x, y, z).e^{-i(k_x x + k_y y)} dx dy \quad (6.2)$$

and its inverse:

$$A(x, y, z) = \int \int \tilde{A}(k_x, k_y, z).e^{i(k_x x + k_y y)} dk_x dk_y \quad (6.3)$$

where, $k_{x,y}$ is the transverse component of the wavevector of magnitude $k_0^2 = k_z^2 + k_x^2 + k_y^2$. They can be thought of as the spatial frequency and can be related to the Fraunhofer divergence angle by:

$$k_{x,y} = k_0 \sin(\theta_{x,y}) \quad (6.4)$$

The field in real space can be thought of as the superposition of an infinity of plane waves, each travelling at a different angle θ from the z direction.

- Our optical system is in self-imaging condition or close to it. Thus, the object plane (in this case the gain mirror) is imaged onto the image plane (here the SESAM) with only a transverse scaling factor. The reciprocal is also assumed true. From this assumption, we can simplify the system by combining in the same plane the gain and SESAM effects $r(x) = g(x) + q(x * M)$. Where M is the magnification from the gain plane to the SESAM plane.

- The saturable absorber and gain medium are assumed to be instantaneous to the incident field. The round trip modification of the field through them is assumed to be small (less than 20% amplitude gain or loss). The exponential nature of gain and loss on the field can be expanded in first order.
- The optical system round-trip transfer function can be written on the field spatial spectrum. Its effect per round-trip is also small enough (less than 20% amplitude filtering and less than 2π phase modification) to be linearized up to fourth order.

With this, we can schematize the field propagation for a round-trip inside our cavity, following figure 6.2. The field $A_0(x, y, z)$ is the starting field just outside the active medium. $A_1(x, y, z)$ is the field after almost one round-trip around the optical cavity just before the active medium. The field $A_3(x, y, z)$ is then the field after a complete round-trip.

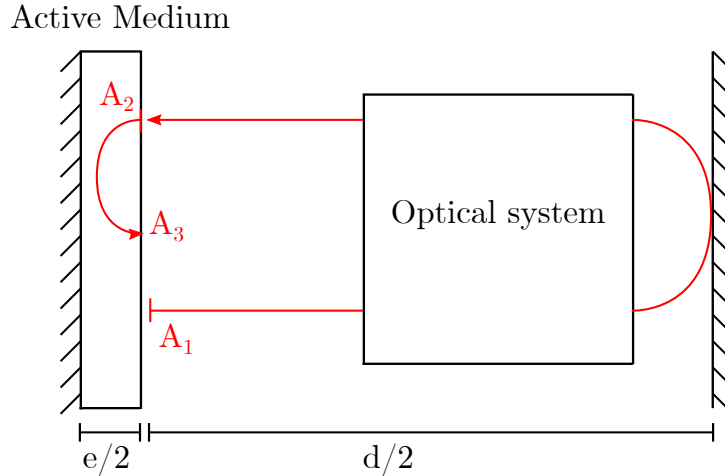


Figure 6.2: Schematize propagation of the field inside the laser system.

6.1.2 Master equation

The first step is to connect the field A_1 and A_2 . For that, we can use the Fourier transform $\tilde{A}_1(k_x, k_y, z)$ of field $A_1(x, y, z)$ and the complex pupil function $\tilde{H}(k_x, k_y)$ of the imaging system. It follows from Fourier optics and the diffraction integral that we can write:

$$\tilde{A}_2(k_x, k_y, z) = \tilde{H}(k_x, k_y) \cdot \tilde{A}_1(k_x, k_y, z - d) \quad (6.5)$$

The function $\tilde{H}(k_x, k_y)$ corresponds to the Fourier transform of the impulse response of the system. In frequency space, it will describe the bandwidth limits

by the filtering of the spectrum amplitude. And the phase transfer function, where $\varphi(k) = k_0.W(k)$ is the aberrated phase induced by the wavefront error of the optical system:

$$\tilde{H}(k_x, k_y) = P(k_x, k_y).e^{-i\varphi(k_x, k_y)} \quad (6.6)$$

Since we assume our optical system to be in self-imaging, all misalignment from the tuning of the SESAM and lenses position can be considered as defocus aberration. The same goes for higher-order terms introduced from any deviation with the ideal wavefront, such as spherical aberration. For simplicity's sake, we will consider only even order terms. This assumes axial symmetry in the system, and thus no Tilt (first order) or coma (third order) are present. Spectral filtering is produced by the numerical aperture limit of the optical system. In this case, no filtering occurs below this limit and 100% after (Top hat shape). This can be approximate either by a super Gaussian of waist $\Gamma = k_0NA$. Thus, we can write using $\beta = k_{x,y}$:

$$\tilde{H}(\beta) = \exp \left[-i \left(D_0^* + D_2^*.\beta^2 + D_4^*.\beta^4 + \dots \right) \right] \quad (6.7)$$

with the real part of the D_{2n} coefficient are:

$$D_{2n} = \frac{1}{2k_0n!} \frac{\delta^{2n}W(\beta)}{\delta\beta^{2n}} \quad (6.8)$$

It described the diffraction coefficient of the optical system and is connected to the aberration coefficient of the wavefront error function. The coefficient D_0 represents a constant phase factor across the field, akin to a propagation distance already taken into account into e and d . It will be ignored for the next step. The imaginary part of D_n^* describes the diffusion coefficient and is related to the amplitude filtering of the spatial spectrum. For the rest we will assume $P(\beta)$ as a super-Gaussian of fourth order, thus only the fourth order term will possess an imaginary part such that $Im(D_4^*) = 1/\Gamma^4$. For the next part, we limit the expansion to the fourth order term to consider only spherical aberration. By using the property of an inverse Fourier transform stating $\frac{\delta}{\delta x} \Leftrightarrow ik_x$ and our previous assumption, we then have the relation:

$$A_2(x, y, z) = \exp \left[i \left(-D_2\nabla_{\perp}^2 + \left(D_4 - i\frac{1}{\Gamma^4} \right) \nabla_{\perp}^4 \right) \right] A_1(x, y, z - d) \quad (6.9)$$

where $\nabla_{\perp} = \frac{\delta}{\delta x} + \frac{\delta}{\delta y}$ is the transverse differential operator and $\exp(\nabla_{\perp}^2 + \nabla_{\perp}^4)$ has to be interpreted as an operator describing the exponential expansion in $i\beta$ of $H(\beta)$ as long as we stay in the first Fresnel zone ($\varphi < 2\pi$) [Haus 1975c].

When the field passes in the thin active medium (delta like) the envelope becomes:

$$A_3(x, y, z) = e^{r(x, y, |A|^2)} A_2(x, y, z - e) \quad (6.10)$$

where $r(x, y, |A|^2) = V(x, y) + R(x, y, |A|^2)$ is the active medium coefficient encompassing local potential effect $V(x, y)$ from the matter-light interaction and/or localized non-saturable losses and the reactive part $R(x, y, |A|^2)$ describing the saturable gain and losses. By assuming the spectral bandwidth in equation 6.7 to be sufficiently narrow, the phase effects small in front of 2π and the variation of the field after passing in the active medium to be small, we can expand the exponential to first order.

$$A_3(x, y, z) = \left[1 + i \left(-D_2 \nabla_{\perp}^2 + \left(D_4 - i \frac{1}{\Gamma^4} \right) \nabla_{\perp}^4 \right) + r(x, y, |A|^2) \right] \times A_1(x, y, z - L_{RT}) \quad (6.11)$$

where we have replaced all intermediate fields by A_1 and set $L_{RT} = e + d$ as the optical length of the optical cavity. Since for a resonating wavefunction the field must not change after a round-trip, we write $A_3(x, y, z) = A_1(x, y, z - L_{RT})$, and we expand A_1 to first order in L_{RT} . Lastly, for better understanding, we transform the variable z in a slow time $T = z/c$ and $T_{RT} = L_{RT}/c$. We can finally write the equation as:

$$T_{RT} \frac{\delta A(x, y, T)}{\delta T} = [iD_4^* \nabla_{\perp}^4 - iD_2 \nabla_{\perp}^2 + V^*(x, y) + R(x, y, |A|^2)] A(x, y, T) + F(x, y, T) \quad (6.12)$$

This equation describes the small change in the transverse envelope of the electromagnetic field after each round-trip, where D_4^* is the complex coefficient that describes both fourth order diffraction from spherical aberration and diffusion from spectral filtering. It follows the same derivation as the Haus master equation describing a mode-locked pulse, and is quite similar to it if the transverse coordinate were replaced by the fast time of the pulse. One added element is the bi-Laplacian operator ∇_{\perp}^4 coming from the expansion of the spectral phase transfer function to the fourth order instead of the commonly used second one. In addition, we take into account the quantum nature of light (spontaneous quantum noise), by adding a stochastic Langevin force $F(x, y, t)$ (spatio-temporal source) as an external source in a semi-classical model of E-field, with the well-known properties:

$$\langle F(x, y, T) \rangle = 0 \quad (6.13)$$

$$\langle F(x, y, T) F(x', y', t') \rangle = D_E \delta_{xx'} \delta_{yy'} \delta(T - T') \quad (6.14)$$

where D_E , homogenous to s^{-2} is the diffusion coefficient (and variance) of the delta correlated quantum process. This coefficient used in simulations is $D_E = 10^{-4}$ expressed in normalized variables ($\times T^2/I_s$). We now need to relate all functions and coefficients to the physical properties of the system.

6.2 Physical interpretation of the operators

6.2.1 Non-local operator

The non-local operators are the ones coming from eq 6.7 and are local to the spatial spectrum of the field. There are best described in the Fourier coordinate space (Far field). All set of coordinates (x, y) play a part in all spatial frequency, thus any local effect on Fourier space is applied to all real space, making it a non-local operation.

In equation 6.12 this is the case for both Laplacian operators. In space, their effects are to broaden the field for both the classic Laplacian ∇_{\perp}^2 and the bi-Laplacian ∇_{\perp}^4 . For the normal Laplacian (second order) those effects are called diffraction when the cause of the broadening is the spectral phase, and called diffusion when it is the spectral amplitude. For the bi-Laplacian, we simply called them fourth order diffraction/diffusion effects. A parallel can be made with time when the second order phase effects are called chromatic dispersion or group delay dispersion (GDD) and spectral filtering for amplitude effect.

We now want to express both coefficient D_2 and D_4^* in terms of physical parameters of the optical system. Looking back at eq 6.6 we have defined the phase of the pupil function as the wavefront error of the optical system. We also considered any misalignment δz to be considered as aberration of the self-imaging system. We can then relate both D_2 and the real part of D_4^* to the effective length of the optical cavity and the spherical Seidel coefficient, respectively.

6.2.1.1 Diffraction coefficient

Looking at the free space propagating transfer function of eq 1.12 we can equate with the β^2 term of equation 6.7 giving us:

$$D_2 = \frac{-2\delta z}{2k_0} = \frac{-B}{2k_0} \quad (6.15)$$

where $2\delta z = B$ corresponds exactly to the effective length of our system found using the ABCD matrix formulation. We can also verify that fact, by writing the Fourier transform of the generalized Fresnel transforms with ABCD coefficients [Palma 1997]:

$$\tilde{U}(\beta, z) = \sqrt{\frac{i\lambda A}{C}} \exp\left(-i\frac{A}{2k_0 C}\beta^2\right) \otimes \sqrt{A}\tilde{U}(A\beta, z-d) \exp\left(-i\frac{AB}{2k_0}\beta^2\right) \quad (6.16)$$

we find $D_2 = \frac{AB}{2k_0}$ which reduce to the same as eq 6.15 in our case since for the round-trip matrix $A = 1$. The detuning δz of the cavity introduces a parabolic transfer phase profile corresponding to simple free space propagation. We call D_2 the diffraction coefficient, and it can take positive (normal diffraction) or negative (anomalous diffraction) values depending on the cavity detuning δz . To remain in the first Fresnel zone, the effect of D_2 must be small compared to 2π . Thus, we can set the condition:

$$|B| < 4\pi \frac{k_0}{\beta^2} \quad (6.17)$$

thus for a small spot of 0.2 numerical aperture, the detuning must be smaller than $53 \mu\text{m}$ and for 0.1 numerical aperture this goes up to $212 \mu\text{m}$. The assumption made means that the equation is valid only for close to self-imaging position.

6.2.1.2 Fourth order diffraction coefficient

The real part of D_4^* is the fourth order diffraction coefficient arising from spherical aberration in the transfer phase function. As with D_2 , we can equate it to some physical parameter using this time the wavefront error equation in spatial frequency space. Limiting this to only spherical aberration, we can do the Fourier transform of equation 5.11 in frequency space as [Goodman 2005]:

$$k_0 W(\beta) = \frac{S_1 f^4}{8a^4 k_0^3} \beta^4 \quad (6.18)$$

where we have used the denormalized pupil coordinate $x = a\xi$ and the transform to frequency space using $x = \lambda f \beta / 2\pi$ following Goodman. The a parameter represents the pupil radius and f is the focal length of the reference sphere corresponding to the pupil position from the image plane. We can now find the real part of the fourth order coefficient:

$$D_4 = -\frac{S_1 f^4}{8a^4 k_0^3} \quad (6.19)$$

It is clear from this equation that the fourth order diffraction depends solely on the spherical aberration of the round-trip optical system through Seidel spherical coefficient S_1 . Contrary to second order diffraction, D_4 is not tunable, except by limiting the effective pupil size (thus tuning a). However, this operation also reduces the NA of the optical system.

The imaginary part of D_4^* was found previously by approximating the top hat filtering of the optical system (from the lens clear aperture) to a super-Gaussian of fourth order. However, a Taylor expansion could be made to approximate any pupil shape. It has for effect to filter the amplitude of the spatial spectrum, thus limiting the system bandwidth.

6.2.1.3 Combined diffraction effects

Those two types of diffraction are the non-local operators affecting our system. They both will tend to broaden the beam size in real space. In figure 6.3 we show the phase transfer function of the optical system for different tuning of B and a fixed Seidel coefficient. To remain in the first Fresnel zone, the combine effect of D_2 and D_4 must be smaller than 2π or λ .

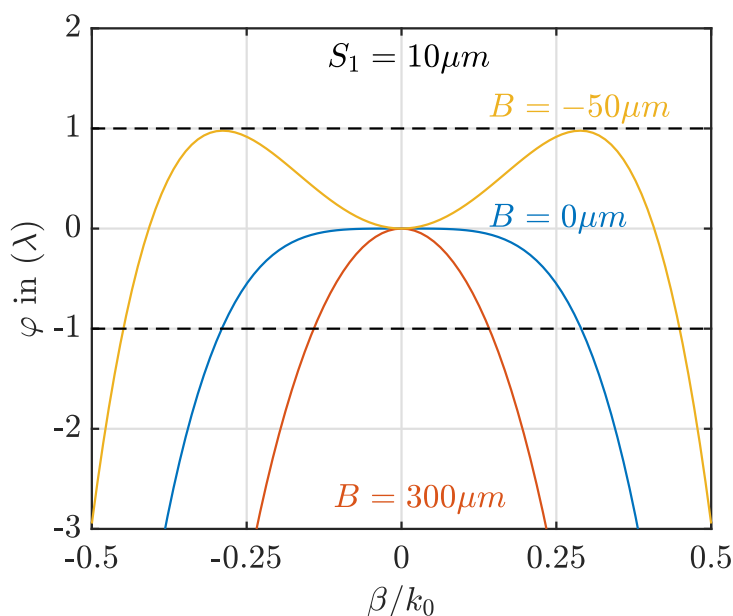


Figure 6.3: Example of the transfer phase function for $B = -50 \mu m$, $B = 0$ and $B = 100 \mu m$ and with $S_{11} = 5 \mu m$.

For an ideal self-imaging system, the phase transfer function should be null and does not impact the EM field. In the case of $B = 0 \mu m$ (at perfect SI position) only the effect of spherical aberration remains, where large variation occurs at large angles. This is the limiting effect of the numerical aperture discussed earlier. Small bandwidth spot (large spot in the near field) sees almost no effects, but larger bandwidth spots (small in the near field) start to see large phase variation, leading to their broadening in near field. However, the model assumptions are only valid

for small enough angle. For the case in figure 6.3 for a numerical aperture over 0.25 we start to go out of the first Fresnel zone.

For large detuning from SI (i.e., for $B > 100 \mu\text{m}$), the spherical aberration effect is small compared to diffraction effect. This is because for large values of B , the parabolic phase variation from diffraction becomes strong in front of the spherical aberration. The case of strong diffraction can also be explained by the ABCD matrix, and as seen earlier, is true in our equation only for a small numerical aperture.

And lastly, in the case of anomalous diffraction (for positive S_1 , normal diffraction for $S_1 < 0$), the opposite sign variation of the β^2 and β^4 term leads to a special behavior. Where in the center, small bandwidth spots will see anomalous diffraction and small bandwidth spots with angle emission see normal diffraction. This is another view of the conical-wave cavity, where, depending on the stability region, we could see on-axis emission or conical-wave.

6.2.2 Local operators

The local operators are coming from the light-matter interaction of the EM field in the active medium. Contrary to the non-local operator, they are best described in the real space coordinate system (Near Field). Their effect, in this case, can be localized in space, and losses at the (x, y) point does not imply losses at (x_1, y_2) . In equation 6.12 we identified the two main components as the potential $V^*(x, y)$ and the reaction $R(x, y, |A|^2)$. This distinction was made to separate static effect placed in the potential and instantaneous non-linear effect placed into the reaction.

6.2.2.1 Complex potential

The static part of the local effect is the complex potential $V^*(x, y)$. Its complex nature means that it can affect both the phase and the amplitude of the propagating field. The first static effect of the active medium interaction that we saw in earlier chapters was thermal lensing. Amplitude effect could come from spatially localized losses, such as the chromium mask of section § 3.4.1. We can then write:

$$V^*(x, y) = -L_{local}(x, y) + i\Phi_{local}(x, y) \quad (6.20)$$

where the real part $L_{local}(x, y)$ is a function describing local losses from unsaturable losses or chromium masks or defects. The imaginary part regroups all the potential phase effects. In Gaussian pumping, thermal lensing can be approximated by a Lorentzian using the thermal simulation described in § 2.4.2 or further expanded into a parabolic phase profile like the ABCD matrix. In the end, we have in the parabolic approximation:

$$\Phi_{local}(x, y) \cong -\frac{k_0}{2}(C_{th_x}x^2 + C_{th_y}y^2) \quad (6.21)$$

where $C_{th_{x,y}}$ is the astigmatic equivalent vergence from the thermal effects, and it must be small enough in front of the spot size to warrant the exponential expansion assumption. As for the non-local operator, we can compare this effect to the generalized Fresnel transforms with ABCD coefficient, but this time in real space we have:

$$U(x, z) = \exp\left(-i\frac{k_0 C}{2A}x^2\right) \times F^{-1}\left[\sqrt{A}\tilde{U}(A\beta, z-d)\exp\left(-i\frac{AB}{2k_0}\beta^2\right)\right] \quad (6.22)$$

From this equation, we can see that after we apply the transfer function in the Fourier space, we apply another parabolic potential, which corresponds to the effect of the parameter C in an ABCD matrix. In the SI position, we have $A = 1$. We see that in fact, not only the thermal lens but all other elements in the optical system that change the C parameter can be measured with a parabolic imaginary potential. More generally, any phase profile, such as an accurate thermal lens or manufactured phase gradient from metasurfaces could be inserted into this potential.

$$L_{local}(x, y) = Q_{sat} + f_{msk}(x, y) \quad (6.23)$$

Secondly, the real part $-L_{local}(x, y)$ of the complex potential will affect the wavefunction amplitude. The first component is the saturated losses Q_{sat} and then the local effect from the chromium mask $f_{msk}(x, y)$. If all other effects are small, mainly very low diffraction, the near field filtering can lead to a waveguiding like effect confining the field. However, this pushes the limit of our previous assumption, where the amplitude effect must be small in front of 1 to warrant the exponential linearization. Indeed, chromium absorption for small thickness still leads to around 50% amplitude losses.

6.2.2.2 Complex reaction

The final operator for the local effect is the reaction. It encompasses both the gain and the saturable losses, which are non-linear effects. As stated in the assumptions/hypothesis, we will assume that they are instantaneous:

$$R^*(x, y, |A(x, y)|^2) = \frac{(1 - i\alpha)}{2}G(x, y, |A(x, y)|^2) - \frac{(1 - i\beta)}{2}Q(Mx, My, |A(Mx, My)|^2) \quad (6.24)$$

where both gain G and saturable losses Q can be written following the saturation equation:

$$G(x, y, |A|^2) = \frac{G_0(x, y)}{1 + \frac{|A(x, y)|^2}{s}} \quad (6.25)$$

$$Q(x, y, |A|^2) = \frac{Q_0}{1 + |A(Mx, My)|^2} \quad (6.26)$$

The gain $G_0(x, y)$ represent the pumped region with Gaussian shape for Gaussian pumping or top hat shape for top hat pumping. The saturable absorption Q_0 is homogeneous along the SESAM plane, but is locally saturated by the field intensity $|A(Mx, My)|^2$. Here we have taken into account the possible scale factor M from the magnification of the optical system. Finally, the saturation parameter s was added to the gain equation because the field intensity was normalized to the saturation intensity of the SESAM. We can express it following:

$$s = \frac{\Gamma_Q \cdot \tau_Q}{M^2 \Gamma_G \cdot \tau_G} \quad (6.27)$$

where M is the field magnification from gain to SESAM, $\Gamma_{Q,G}$ are the micro-cavity enhancement factor of the SESAM and gain structure and $\tau_{Q,G}$ the excited level lifetime.

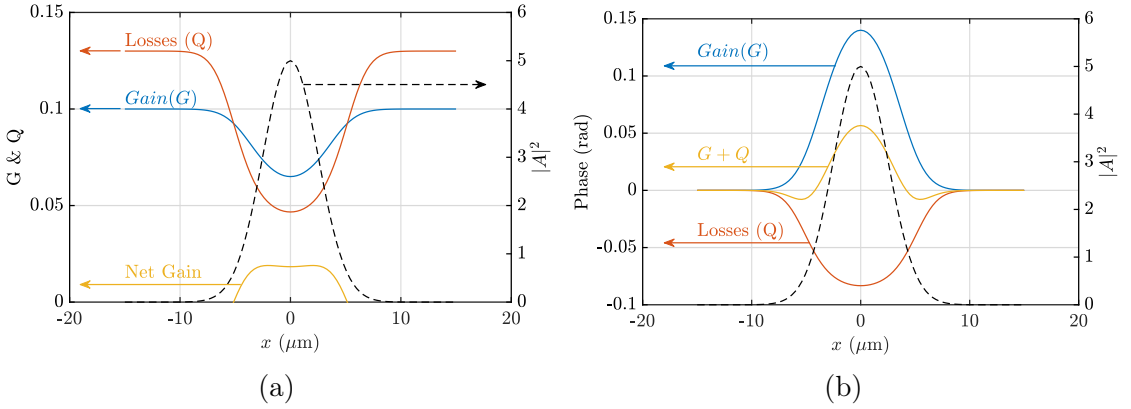


Figure 6.4: Amplitude and phase effect of the instantaneous non-linear reaction for $G_0 = 0.1$, $Q_0 = 0.13$, $\alpha = 4$, $\beta = -1$, $s = 5$ and a Gaussian spot of $\omega_0 = 5 \mu\text{m}$ waist and $I_0 = 5I_s$. (a) Amplitude effect with (left) gain and saturable losses and (right) Gaussian spot intensity (b) Phase effect with (left) gain, saturable absorber and their sum and (right) the Gaussian spot intensity.

Equation 6.24 also considers the phase amplitude coupling effect of the semiconductor medium for the gain α and for the SESAM β . Thanks to those effects,

the resonating field will experience positive self-amplitude modulation (SAM>0) from the gain and the SESAM by opening a net positive gain window. The Gain saturation will generate positive self-phase modulation (SPM>0) that will dominate the SPM from the SESAM, as long as the SESAM is not too saturated. Thus, we should not use an S factor too large in front of 1 to exploit SPM>0. Similarly to passively mode-locked lasers, the saturable absorption will open a net gain window around a spatial pulse, and the SPM effect could lead to soliton mode-locking by balancing diffraction effects. For normal diffraction ($B > 0$ or $D_2 < 0$) the SPM must be positive to compensate the pulse broadening and the reverse for anomalous diffraction ($B < 0$ or $D_2 > 0$). With our optical cavity, the diffraction is a tunable parameter, allowing us to reach the preferred regime. Figure 6.4 summarizes the non-linear saturation effect. On the left, we see the net gain window (SAM) opened by a Gaussian spot of 5 times the saturation intensity of the SESAM. On the right, we see the residual self-focusing (SPM > 0) effect from the Gain saturation ($\alpha = 4$ and $\beta = -1$)

However, those simple models for Gain and Saturable losses are not considering the effect of carrier diffusion. They'll lead to a larger coherence range of the local saturation, which could prevent a spatially stable localized structure. We saw that the SESAM provides most of the carrier diffusion. A different spatio-temporal differential equation for the absorption should be added. In the steady-state with instantaneous media (compare to cavity photon lifetime), we can write:

$$Q(x, y, |A|^2) = \frac{Q_0 + L_d^2 \nabla^2 Q(x, y, |A|^2)}{1 + |A(Mx, My)|^2} \quad (6.28)$$

where the Laplacian operator takes carrier diffusion into account with the diffusion length L_d . In our case, the long photon lifetime of the large cavity length in front of matter recovery time, sets our system in class A dynamics where we can consider the saturation instantaneous compared to field formation. However, for class B laser dynamics (i.e., fast photon lifetime compared to matter lifetime) the matter equation is time dependent and the field formation occurs before the full gain and absorption saturation. The delay in saturation will lead to more complex dynamics and can even prevent from any pattern formation.

6.3 Eigenvalue problem : Bi-Harmonic Helmholtz like equation

We can also take advantage of the master equation to express an eigenvalue problem, allowing us to compute the eigenvector and eigenvalue of a close to degeneracy. First, we must assume a stationary system where the transverse field

does not change with time:

$$\frac{\delta A(x, y, T)}{\delta T} = 0 \quad (6.29)$$

Secondly, we assume no non-linearity, and thus we remove the $|A|^2$ dependency of the Gain and Absorption. However, we keep the transversal dependent part of the Gain. The complex reaction thus becomes:

$$R(x, y, |A|^2) = (1 - i\alpha)G_0(x, y) - (1 - i\beta)Q_0 \quad (6.30)$$

Since we remove the saturation, the phase amplitude coupling parameter β for the absorption will only create a constant phase shift, while for the gain we will have a diverging “electronic lens” effect. In the laser system, this effect will be attenuated and even reversed by the gain saturation.

In the end, we have the following Eigenvalue problem:

$$[iD_4^*\nabla_\perp^4 - iD_2\nabla_\perp^2 + V^*(x, y) + (1 - i\alpha)G_0(x, y) - Q_0] A(x, y) = \Omega A(x, y) \quad (6.31)$$

where D_4^* and D_2 are the previously defined diffraction coefficient. $V^*(x, y)$ is the complex local potential describing the thermal lens profile (Lorentzian profile), the residual cavity C parameter (parabolic profile) and localized losses. While, only the net gain profile remains from the complex reaction. From this equation, we can find the stable wavefunction $A(x, y)$ (transverse mode basis) of the linear optical system. Those will be the mode basis with which will be generating localized structure. The real part of the complex eigenvalue Ω is equivalent to the gain of the eigenfunction. It tells us which function is more likely to appear first. The imaginary part carries the constant phase shift of the eigenfunction, which is equivalent to a frequency shift (Gouy phase shift) of each transverse mode. It can be used to evaluate the number of degenerated transverse modes. It is analogous to the energy-momentum dispersion diagram where the shift is proportional to the resonant frequency (i.e., the energy) and the mode number to a transverse wavevector (i.e., momentum).

6.4 Conclusion

In this chapter, we derived an equation describing the transverse field variation per round-trip for an optical system close to self-imaging. This derivation was done following a similar treatment as for temporal propagation of mode-locked pulse inside a laser system, but for the transverse profile of a spatial pulse. From this equation, we found both local and non-local operators. The entire system can be

summarized as a small micro-cavity with a complex transfer function in real space and Fourier space (see figure 6.5).

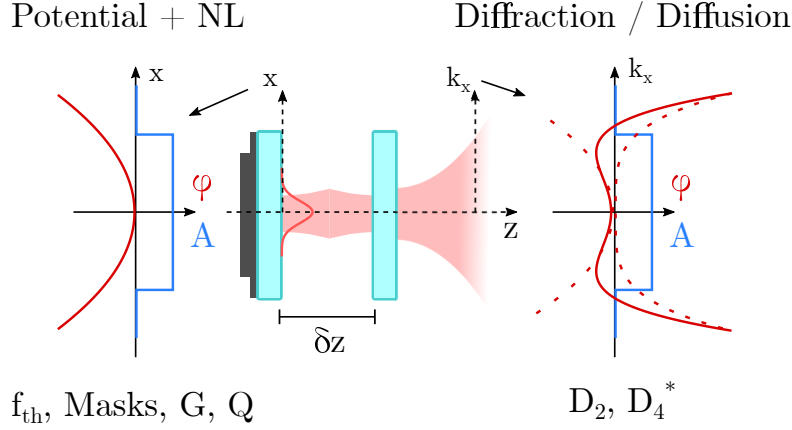


Figure 6.5: Summary schematics of the equivalent laser cavity modelled by the developed equation. Local and Non-local linear potential are both displayed.

The non-local operators are the second order diffraction and the fourth order diffraction. The first one, originates from the small cavities detuning of the self-imaging position. The second originates from spherical aberration of the optical elements. This means that D_2 is tunable with the SESAM plane position (δz detuning) and D_4 is fixed by the choice of the optics. However, to remain in the approximation validity (first Fresnel zone) both the detuning and spherical aberration must be small enough in front of 2π . For example, taking a Gaussian spot of $5\ \mu\text{m}$ waist and $\sin(\theta) = 0.07$ of Gaussian numerical aperture, the tuning of D_2 is limited to $|\delta z| < 217\ \mu\text{m}$ to remain in the correct approximation. At the perfect SI position ($D_2 = 0$) one can define a numerical aperture limit from the spherical aberration following the small phase perturbation $D_4\beta^4 < 2\pi$:

$$\sin(\theta) < \frac{1}{k_0} \sqrt[4]{\frac{2\pi}{|D_4|}} \quad (6.32)$$

For the same Gaussian spot, the Seidel coefficient needs to follow $|S_1| < 1.4\ \text{mm}$ to respect the approximation. The computation was done with a lens of $50\ \text{mm}$ focal length and $25.4\ \text{mm}$ optical diameter. As seen in the previous chapter, those limits are well above the targeted amount of spherical aberration $|S_1| < 0.1\ \text{mm}$ and the degenerate range.

On the other hand, the local operators came from the light-matter interaction of the field with the active medium and can be separated into two components. The first one is the complex potential, consisting of static effects such as thermal lensing or localized losses from chromium metasurfaces. The second is the instantaneous

Non-Local effect				
Parameter	Effect on	Typical value	Tunable	
δz	D_2	$< 100 \mu\text{m}$	Yes	-
S_1	D_4	$< 0.1 \text{ mm}$	No	Design

Local effect				
Parameter	Effect on	Typical value	Tunable	
f_{th}	$\Phi_{local}(x, y)$	$\sim 50 \text{ mm}$	Yes/No	Design + Pump
s	SPM	~ 5	No	Design
α	SPM	~ 4	No	Technology
β	SPM	~ -1	No	Technology
Q_0	SAM/SPM	$\sim 10\%$	No	Design
G_0	SAM/SPM	$\sim 10\%$	No	Design

Table 6.1: Summary of the Local and Non-local parameters of our system and their tunability.

non-linear reaction from the optical gain and saturable losses. As for passive mode-locking, they can provide the necessary phenomenon to obtain spatial localization (self-phase and self-amplitude modulation). The reactive part of the local effects are primarily affected by the active medium design (max gain, max saturable absorption, saturation parameters) and in our case are small to allow linearization. While for the complex potential, the thermal lens is also dependent on the optical pump shape. For the local phase potential, the first Fresnel zone limit ($\varphi < 2\pi$) is reached for a $5 \mu\text{m}$ waist Gaussian beam when the thermal lens is small $f_{th} < 15 \mu\text{m}$. In practice, we aim to reduce the thermal lens impact, and thus we will never reach this limit. However, the amplitude part of the complex potential coming from the chromium mask may start to approach the limit of the approximation. Indeed, for small chromium thickness ($e \sim 5 \text{ nm}$) we can have up to 50% amplitude loss, meaning a 20% error on the approximation.

Table 6.1 summarized the important parameters of the system and their order of magnitude for a typical 4-f optical system and the V0450 1/2-VCSEL gain and V0598 SESAM. For cases where all parameters agree with assumption/approximation, it is possible to directly numerically solve equation 6.12. Otherwise, outside those limits, we can keep the exact formulation and separate the equation into a split-step method where local effects are calculated in real space and non-local effects in Fourier space. The advantage of this model compared to the much simpler ABCD matrix approximation is its ability to give us insight into a self-imaging laser transverse dynamic inside the targeted degeneracy range. It will be used for the rest of the manuscript to analyze and predict certain behavior.

6.4.1 Passive Eigenfunctions

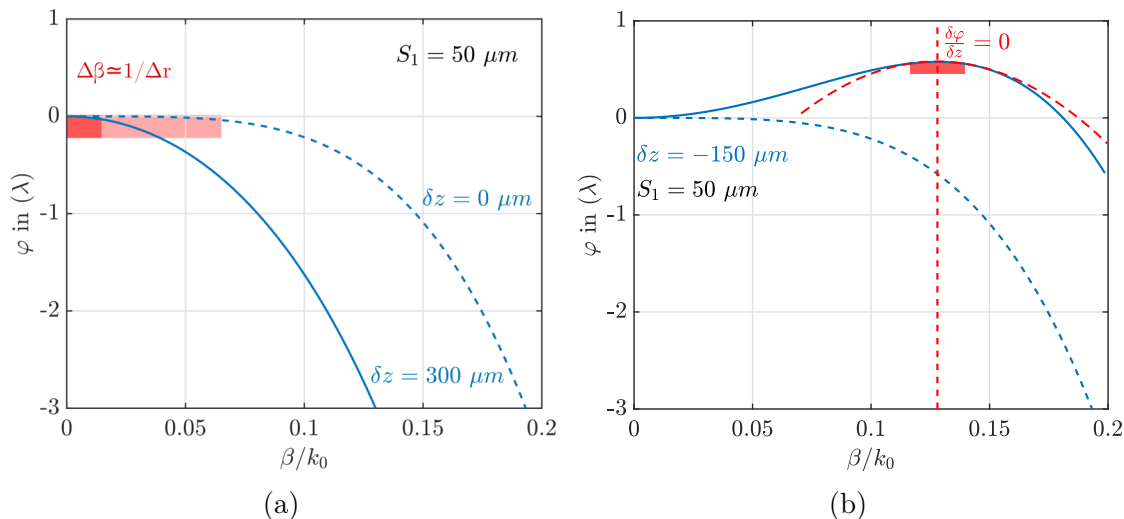


Figure 6.6: E-k Dispersion diagram of the non-local effect for static real space confining phase potential ($C < 0$). a) On axis stability for large normal (solid curve) diffraction and for only negative fourth order diffraction (dashed curve). b) Off-axis stability for anomalous diffraction at the position of zero first order derivative. Locally, the field sees normal diffraction.

From the non-local operator and the transverse E-k dispersion diagram, we can have insight into the passive wavefunction of the system. For example, figure 6.6 shows that the wavefunction would be stable in the negative curvature region for a confining static potential with $C < 0$ or positive thermal lensing in near field. The reverse is also true, for $C > 0$ the wavefunction would be stable in the positive curvature region. From the quantum-mechanical analogy standpoint, it would correspond to a particle of positive mass ($C < 0$) or negative mass ($C > 0$).

Thus, for normal diffraction and confining static real space potential stability should be on axis. Depending on the amount and sign of the fourth order diffraction coefficient (i.e., spherical aberration) we also find an off-axis stability region. For $C < 0$, $D_4 < 0$ ($S_1 > 0$) and normal diffraction $D_2 < 0$ the stability remains on-axis but for anomalous diffraction we find an off-axis stability region. The emission angle corresponds to $\frac{\delta\varphi}{\delta t} = 0$ where locally the curvature is still negative, thus equivalent to normal diffraction. This regime is the conical-wave cavity region, and we find the same conditions as for detail in the previous chapter with the modified ABCD matrix stability.

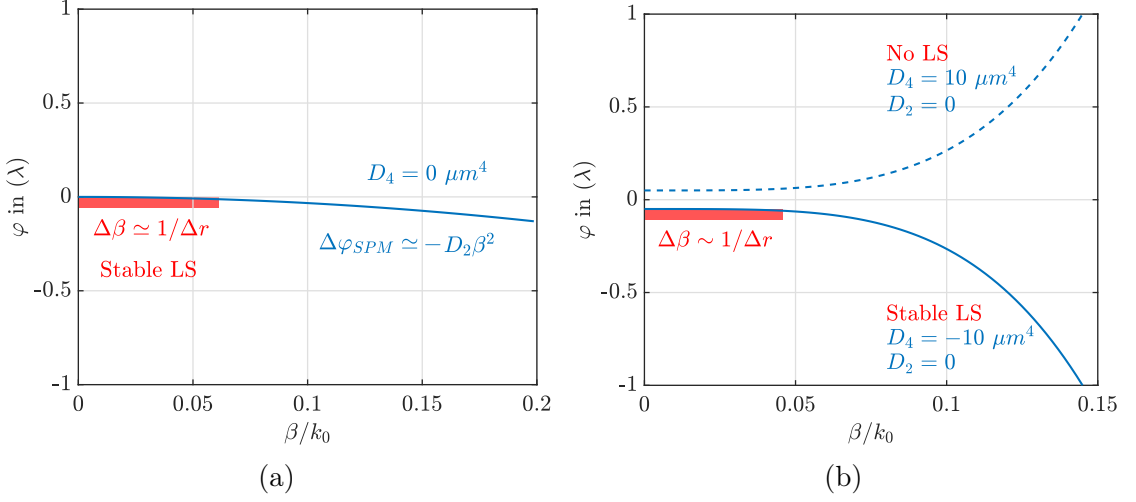


Figure 6.7: E-k Dispersion diagram of the non-local effect for NL localization. A broad ($\Delta r \times 10$) flat potential was assumed in real space. a) For the ideal case, $D_2 = D_4 = 0$ the whole spatial bandwidth is available and D_2 tunable to compensate the SPM. b) For the realistic case, D_4 is fixed by the optical system aberration. The NL localization is only possible for $D_4 < 0$ and still small enough to allow for a large spatial bandwidth. For the $D_4 > 0$ on axis, compensation of SPM is not possible.

6.4.2 Non-linear localization

The reactive parameters are important to achieve non-linear structuration of the transverse field. Indeed, the Gain and SESAM will provide SPM an SAM of the field. SAM is positive thanks to the net gain windows opened by the SESAM, while the SPM is positive through self-focusing by the gain saturation. In order to compensate for its effect, the diffraction must be normal, meaning that the effective diffraction comprised of both second and fourth order terms $D_2^{eff} = D_2 + D_4\beta^2$ must be negative. The condition can be expressed as:

$$\Delta\varphi_{SPM} \sim -D_2^{eff} \Delta\beta^2 \quad \text{with} \quad \Delta\beta \sim 1/\Delta r \quad (6.33)$$

where the transverse bandwidth $\Delta\beta$ is inversely proportional to size in real space. With $\Delta\varphi_{SPM} \leq 0.1$ and D_2 being tunable to zero, the remaining diffraction effect is coming from the spherical aberration. To have normal effective diffraction for a real space size around $\Delta r \sim 5 - 10 \mu\text{m}$, the condition on fourth order diffraction becomes $-50 \mu\text{m}^4 \leq D_4 \ll 10 \mu\text{m}^4$. Figure 6.7 displays the non-local transverse phase dispersion diagram for the ideal case $D_2 = 0$ and $D_4 = 0$ and the more realistic case with $D_4 \neq 0$. The non-linear spatially localized appears only for normal effective diffraction when the bandwidth is sufficient. In real space, a broad,

flat potential of more than times the non-linear structure size was assumed.

Non-linear self-imaging laser cavity modes topology

This chapter will present the experimental results obtained with a self-imaging laser based on a 1/2-VCSEL Gain mirror and a saturable absorber. All the results presented have been done using the 4-f cavity system. This system allows us to reach a low diffraction regime (self-imaging) while keeping a large Fresnel ratio for the broad transverse area condition.

7.1 Experimental set-up

The figure 7.1 describes the full set-up used during this work. The 4-f laser system is composed of the previously described 1/2-VCSEL, two intra-cavity lenses and a SESAM. The lenses L1 and L2 can be chosen from either large numerical aperture aspheric lenses (Thorlabs CNC polished or MRF polished for lower aberration) or achromatic lenses. The choice is made to achieve the correct magnification while reducing the impact of higher-order diffraction. The laser cavity was folded using a short pass dichroic mirror (Thorlabs DMSP102B) with high reflectivity in the laser wavelength ($>99\%$ at 1064 nm) and still permit the transmission of both the pump for the gain (at 808 nm) and the injection for the SESAM (at 980 nm).

An alignment protocol was developed to correctly place each element of the cavity. The optical axis was defined using a “green” laser diode. Alignment was made by matching the reflection on each optical element’s surface to the optical axis and by a repeating cycle of translation and tilting of the lenses. Both lenses were placed on a micro-translation stage to finely adjust each distance during the alignment process. The SESAM was placed on a three axis translation stage with differential adjusters and a micro-metric resolution coupled to a theta/phi gimbals.

It was the last element to align and was used to finely tune the system diffraction, thus the higher translation resolution.

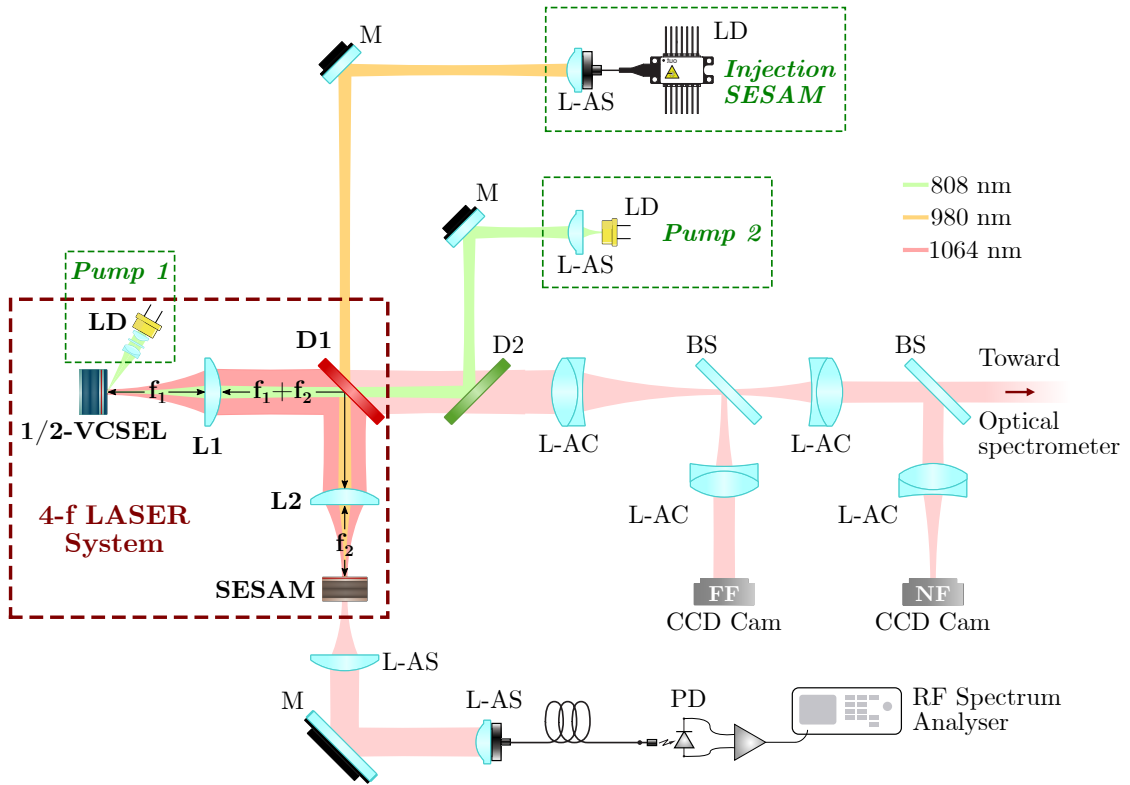


Figure 7.1: Full set up with the 4-f laser system, the pumps, and the external detection system. LD (Laser Diode), D (Dichroic mirror), M (Mirror), L-AC (Achromatic lens), L-AS (Aspheric lens), BS (Beam splitter), PD (Photodiode).

7.1.1 Instrumentation

To fully characterize this laser system and understand its different modes family and behavior, we will need to monitor several key aspects of the laser emission. The folded 4-f laser system allows for two outputs from the dichroic mirror, and one from the mirror/SESAM (with small transmission $\sim 1\%$). From those possibilities, only two will be used to monitor the laser system.

The main branch is coming from the dichroic mirror output, and two CCD cameras are used to monitor the laser profile. The images produced by the CCD camera are intensity time average profile. One camera is dedicated for imaging the gain plane that we call the Near-Field (NF). The other is to image the Fourier transform of the NF that we call the Far-Field (FF). Using a beam splitter, we can

also inject the residual power into an optical spectrometer using a 600 line/mm grating to achieve 0.034 nm spectral resolution on the first order. Our cavity being usually long (from 100 to 200 mm with 0.005 to 0.003 nm free spectral range), we cannot resolve individual cavity modes but only the spectral envelope.

We also replace the CCD camera measuring the NF or the FF by a wavefront sensor (Phasics SID4). It allowed us to also have information about the transverse phase profile of the emitted laser beam.

The secondary branch from the SESAM output is mainly used to either measure the average output power on a broad area photodiode (Thorlabs PM100D with PD S120C) or to look at the relative intensity noise (RIN) in the RF domain using a fast photodiode (PDA8GS) combined with RF spectrum analyzer (Rohde & Schwarz FSV 10 Hz to 30 GHz).

7.1.2 Pumping profiles

The 1/2-VCSEL can be pumped either by a single mode laser diode (Pump 1: LD808-SE500) or by a large core fiber coupled laser diode array (Pump 2: UNIQUE MODE UM8K/200/20). Both of them emitting at 808 nm. Pump 1 is placed into an in-house module with a half-wave plate and refocused onto the gain mirror at the Brewster angle. This angle allows us to maximize transmission into the semiconductor and to circularize the Gaussian profile. Figure 7.2 shows the resulting 2D intensity profile of the spontaneous emission from pump 1 and the horizontal (X) and vertical (Y) cuts of the profile. The resulting pumped area is a Gaussian of 52 μm waist with good circularity.

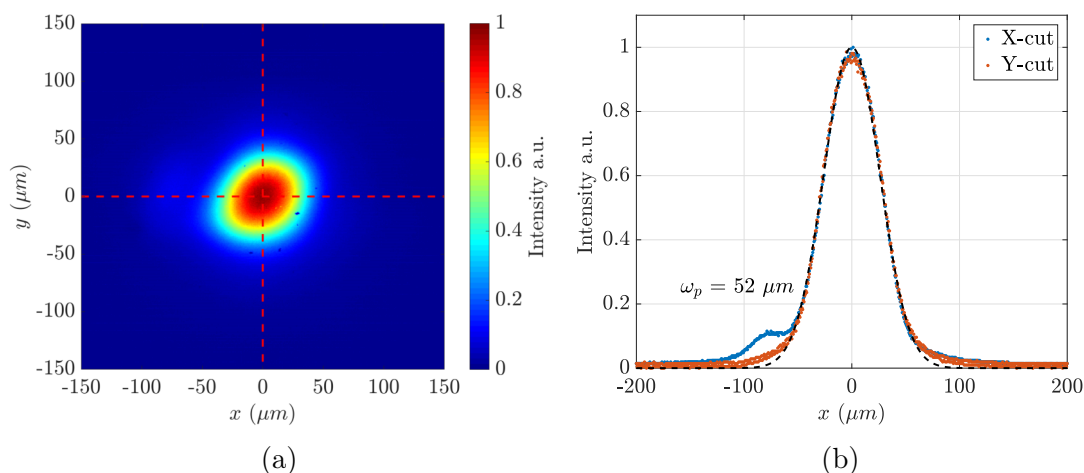


Figure 7.2: (a) 2D intensity profile of the Gaussian pump on the 1/2-VCSEL. (b) 1D cut in X and Y.

Pump 2 is injected into the 1/2-VCSEL at normal incidence, using the same path as for detection. To not block the detection path, a long-pass dichroic mirror (D2) is used reflecting the pump but letting through the laser, while the short-pass dichroic mirror (D1) is used for the reverse effect in the cavity. This pump used the cavity lens L1 to refocus the pump beam onto the gain mirror. The fiber core of pump 2 being 200 μm diameter, a similar focal than L1 must be used to collimate the pump beam to have a 200 μm focus spot onto the gain mirror. Figure 7.3 shows the resulting 2D intensity profile of the spontaneous emission from pump 2 with L1 $f = 25$ mm and the collimation lens $f_c = 30$ mm. On the X/Y-cuts, we measured the FWHM at 170 μm and around 10% residual modulation of the top-hat flatness. The top hat profile comes from the multi-modal operation of the fiber, leading to a refocus top hat profile.

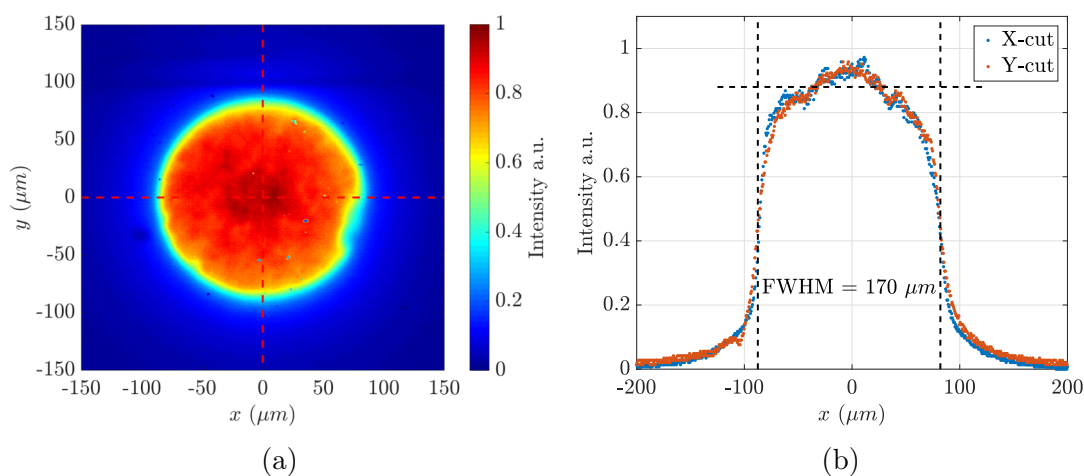


Figure 7.3: (a) 2D intensity profile of the top hat pump profile on the 1/2-VCSEL. (b) 1D cut in X and Y.

Lastly, a 980 nm fiber grating stabilized laser diode (3SP Technologies 2000CHP) was used to locally inject the SESAM and giving us the ability to locally saturate the losses. The same technics then with pump 2 was used to focus a small spot on the SESAM, this time using lens L2. In this case, the fiber used was mono-mode with a core of 6 μm . To have the same spot size or smaller on the SESAM, the same focal or smaller than L2 must be used. In our case, the smaller the spot is, the better to localize the saturation. However, we have seen in § 3.3.2.2 that the diffusion length of the SESAM is around, 10 μm thus a target spot of 3 μm is sufficient. So, the collimator must always be half or less the focal length of L2.

7.2 Study of the spatial morphology in a 4-f self-imaging laser

We start to explore the typical transverse solution of our system, and its dependence on the controllable parameters (longitudinal detuning, thermal lensing, chromium masks) to classify the different types of emission. From this, we will be able to define a target area for the non-linear structuration of light. We can first define the two types of spatial emission encountered as:

- Spherical wave with an emission on the cavity axis. Meaning the main propagating wave-vector as no transverse component and is positioned at the zero spatial-frequency point, thus HG or LG mode basis.
- Conical-wave with an angle of emission compared to the cavity axis. We thus have either two contra-propagative wave-vector with a transverse component and not positioned on the zero spatial-frequency point, or a multitude of contra-propagative off-axis waves forming a ring in the spatial frequency domain, thus Bessel-gauss like mode basis.

The following results have been obtained using the 4-f laser cavity with the same lens ($f = 50$ mm, MRF polished) for L1 and L2 and by replacing the SESAM with a high reflectivity mirror in order to focus the analysis onto the transverse mode family of our system. The Gaussian pump was used.

7.2.1 On-axis spherical wave emission.

7.2.1.1 Without chromium mask: Thermal lens based potential stabilization.

First, we look at the spatial pattern in the 4-f self-imaging cavity and the Gaussian pump for different pumping power without any chromium masks. Figure 7.4 and figure 7.5 represent the overall size of the spatial pattern on the 1/2-VCSEL surface as a function of the detuning δz (position of the mirror).

By using the on-axis emission, we can fit the near field using the previously shown ABCD model with our system parameter (gold curve). Figure 7.4 uses a thermal lens of $f_{th} = 16.4$ mm and an electronic lens of $f_e = -200$ mm. In this case, the thermal lens corresponds to an absorbed power of 392 mW on a pump waist of 50 μ m, while the negligible electronic lens comes from the residual unsaturated gain, being at a relatively high pumping rate of $r \sim 2$ the electronic lens is small. In this case, the stability occurs for positive detuning (i.e., normal diffraction).

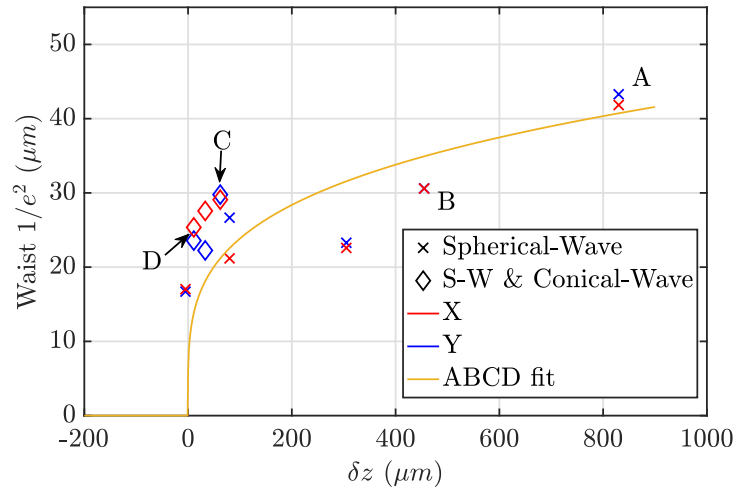


Figure 7.4: Measured waist on the 1/2-VCSEL surface versus the longitudinal detuning δz . Pumping rate $r \sim 2$.

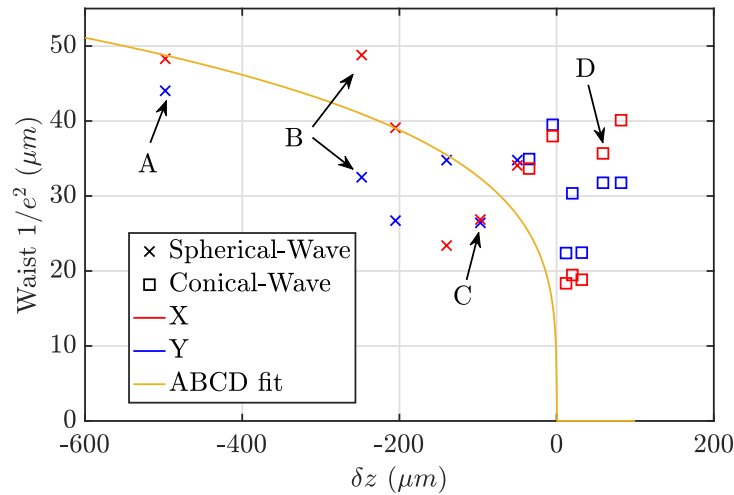


Figure 7.5: Measured waist on the 1/2-VCSEL surface versus the longitudinal detuning δz . Pumping rate $r \sim 1$.

On the other end for figure 7.5 the thermal lens is $f_{th} = 33.6$ mm, for an absorbed power of 192 mW, which corresponds to a pumping rate close to unity. In this case, the electronic lens due to the unsaturated gain modulations is high, $f_e = -20$ mm leading to a shift of the stability towards negatives detuning (i.e., for anomalous diffraction).

In both cases, the larger the detuning from self-imaging, the larger the NF size. And in both cases, the on-axis emission is similar to a Hermite/Laguerre-gauss basis. On figure 7.6 and 7.7 illustration of the NF and FF profile are shown for

$r = 2$ and $r \sim 1$ respectively. We found that there is a strong stability dependence on the thermal and gain induced potential. Depending on the curvature potential sign, the system can be stable on-axis for positive (normal) or negative (anomalous) diffraction.

The self-imaging position is not affected by this potential variation and can still be approached from positive or negative diffraction. Looking at figure 7.6 and 7.7 we can also see the evolution of the on-axis emission NF and FF profile in conjuncture with the simple ABCD fit to estimate the exact self-imaging position. As expected, the closer to the self-imaging point, the smaller the NF modulation consists of larger spatial frequency (FF). However, in this region, we have observed strong competition between the on-axis spherical mode emission and the off-axis conical-waves.

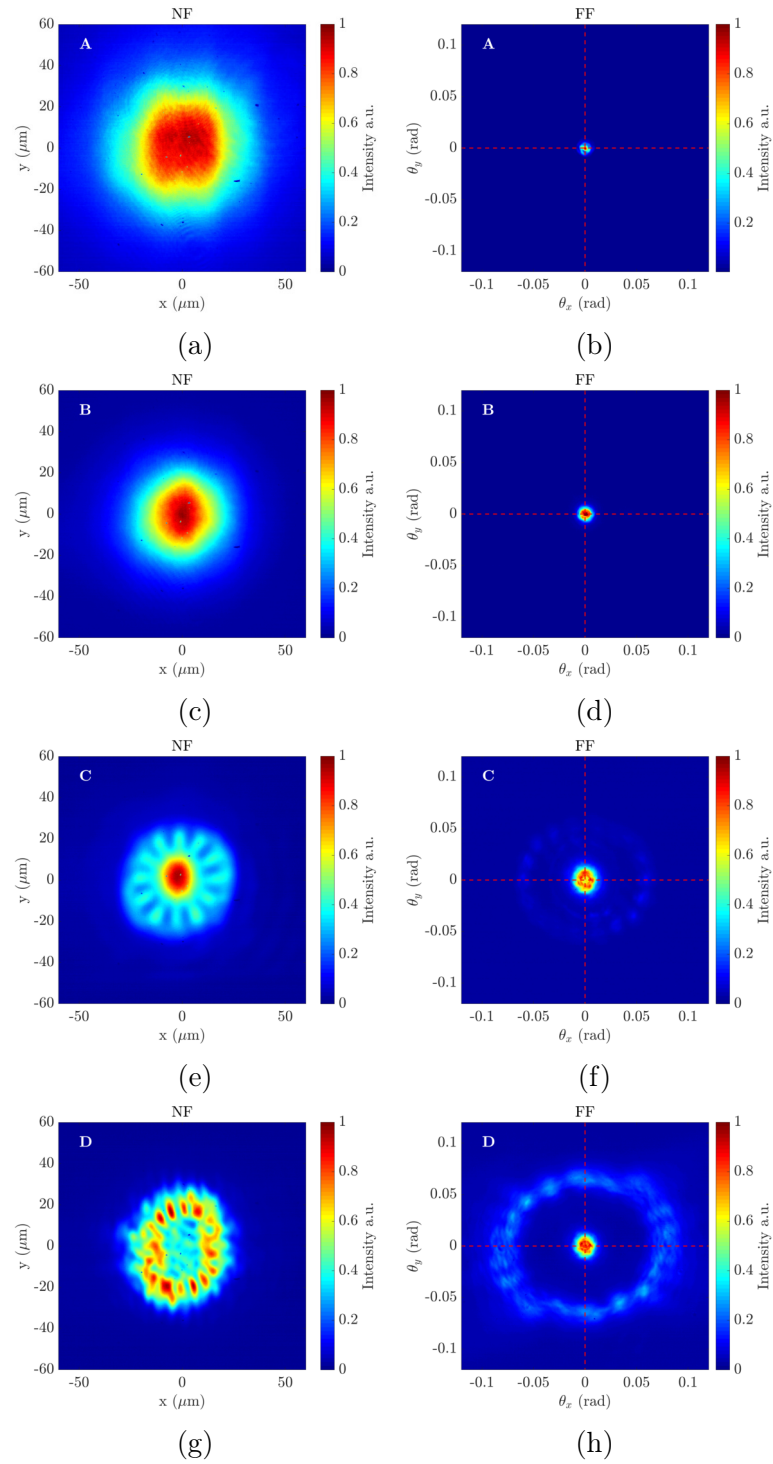


Figure 7.6: 2D NF intensity profile (a, c, e, g) and the corresponding 2D FF intensity (b, d, f, h) for the position A, B, C, D of figure 7.4.

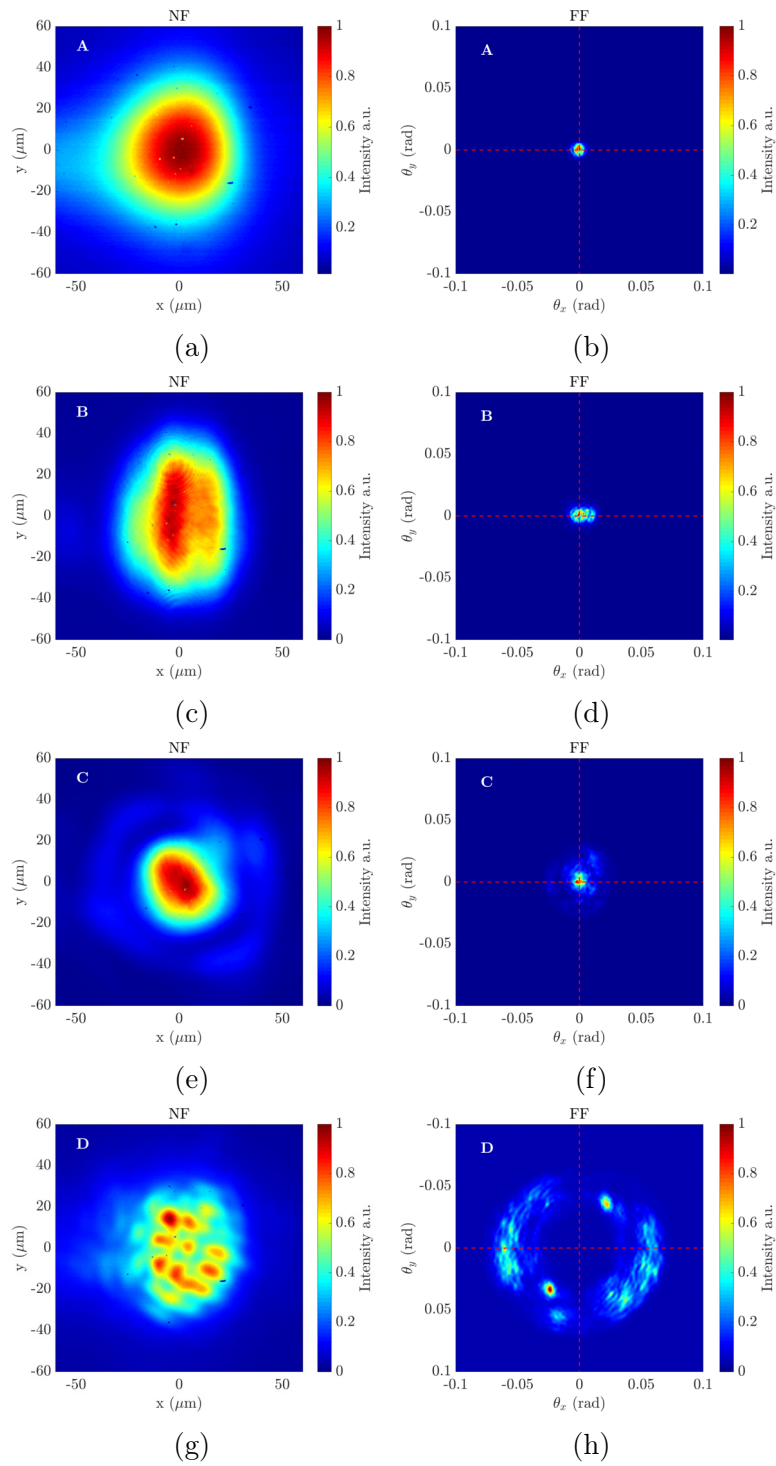


Figure 7.7: 2D NF intensity profile (a, c, e, g) and the corresponding 2D FF intensity (b, d, f, h) for the position A, B, C, D of figure 7.5.

7.2.1.2 With chromium mask: Guided mode stabilisation.

Adding a chromium mask on the gain surface with a $30\ \mu\text{m}$ diameter clear aperture on the same configuration with a pumping rate of $r \sim 2$ results in a different behavior. On figure 7.8 we show the resulting large-scale waist as a function of the detuning and on figure 7.11 the corresponding NF and FF profiles.

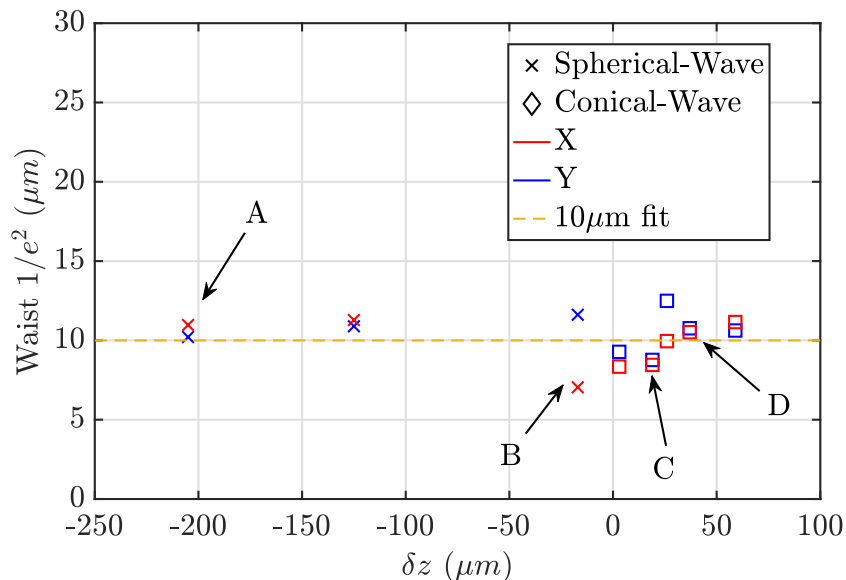


Figure 7.8: Measured waist on the 1/2-VCSEL surface versus the longitudinal detuning δz . Pumping rate $r \sim 2$, chromium mask of $30\ \mu\text{m}$ diameter.

The first observation is that the stability is reversed compared to without the mask, and the on-axis emission occurs for anomalous diffraction. And the second observation is the lack of variation from the overall envelope, which remains close to an equivalent waist of $10\ \mu\text{m}$.

Using a thermal profile ($\omega_p = 50\ \mu\text{m}$) that was created by Gaussian pumping on a circular mask with a clear aperture of, $30\ \mu\text{m}$ (see figure 7.9), we can show that the thermal lens that is created is of the opposite sign. This is because 100% of the optical energy is converted into heat in the chromium layer, instead of 30% in the semiconductor. The hot-spot is then on the mask perimeter and thermal diffusion smooths the variation.

As previously, the stabilizing process is fixed by the thermal and electronic lensing effect, and thus we find on-axis emission for anomalous diffraction regardless of pumping power. The restricted transverse area also helps confine the transverse modes, and a simple ABCD simulation does not accurately describe the mode sizes.

We are closer to a guided micro-cavity cavity where the longitudinal size is larger than the transverse one. We can still get close to the self-imaging point, but

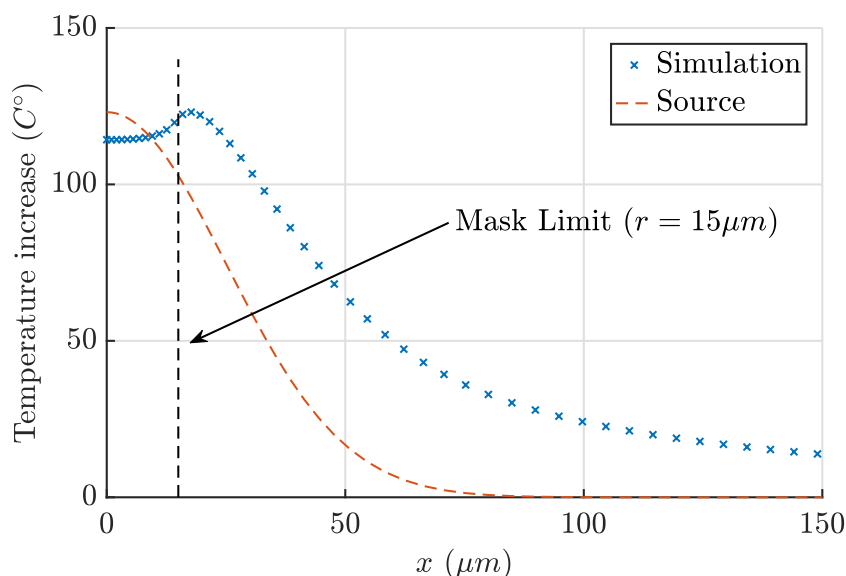


Figure 7.9: Finite element simulation illustrating the effect of the chromium mask on the optically induced thermal profiles by a Gaussian pump.

the competition with spherical-wave and the conical wave emission makes finding the exact position more difficult.

7.2.2 Off-axis, conical-wave behaviour

The conical-wave is a type of emission where the beam is not emitted perpendicular to the gain section but at an angle leading to a ring pattern emission in FF or a couple of spots offset from the optical axis and an interference pattern in the NF. This behavior is seen in both cases close to the self-imaging position, and sometime overlaps with an on axis emission, see figure 7.7g and 7.7h.

On figure 7.10a we show the measured max angle emission for both pumping rate and two clear tendencies can be seen. The first one is a slowly increasing max FF angle the closer we get to self-imaging, and the second is a sharp increase in the maximum angle and larger angle variation for small δz detuning. The first one is following the expected behavior of a simple on axis cavity stability (ABCD fit) while the second part is indicative of the conical-wave emission. Another point is that the conical-wave emission stability region does not appear to change between the two pumping rates, like with the on-axis emission. This appears to be indicative of another process than the near-field potential from thermal lensing for their stability, such as optical aberration.

By using a different set of lenses with more aberration than the MRF polished one such as an achromatic doublet ($f = 50$ mm) we find a different behavior for

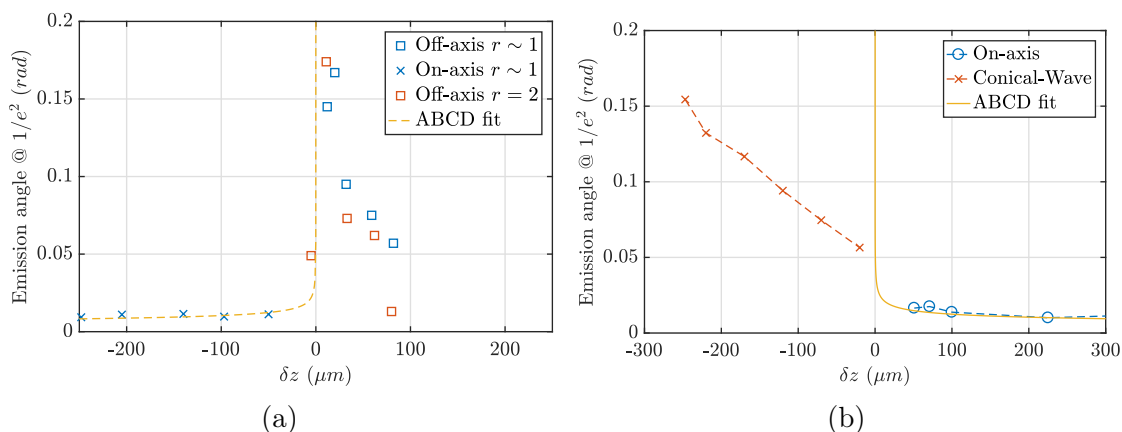


Figure 7.10: a) Measured max emission angle in FF for both 7.6 ($r = 2$) and 7.7 ($r \sim 1$). b) Measure max emission angle in FF for a cavity with L2 replaced by an achromatic doublet of same focal length as L1. For on-axis mode the angle is taken at $1/e^2$ while for conical-wave the emission angle is taken.

the conical-waves emission such as a slower and more continuous angle variation as we can see in figure 7.10b. This reinforces the idea that conical-wave stability comes mainly from optical aberration of the external cavity system.

We can link the angle variation properties with the spherical aberration and the related Seidel coefficient. As seen in the previous chapter, the spherical aberration introduces a focal variation for a small diverging beam and an offset incidence onto the lens. This focal shift with incidence angle explains the measured angle variation, and the slope can be related to the Seidel spherical coefficient.

A negative slope means a positive Seidel coefficient and thus a strong possibility of on-axis competition with the anomalous stability region, since a positive Seidel coefficient means a focal reduction with increasing incidence angle. The reverse is true for a positive slope. The strength of the slope is inversely proportional to the strength of the aberration. Lower aberration means a lower focal variation for the same incident angle, thus a smaller detuning and a large slope. This can be encapsulated using the longitudinal spherical aberration formula:

$$|S_1| = \frac{4a^4}{f_0^4(\Delta\theta)^2} \Delta z \quad (7.1)$$

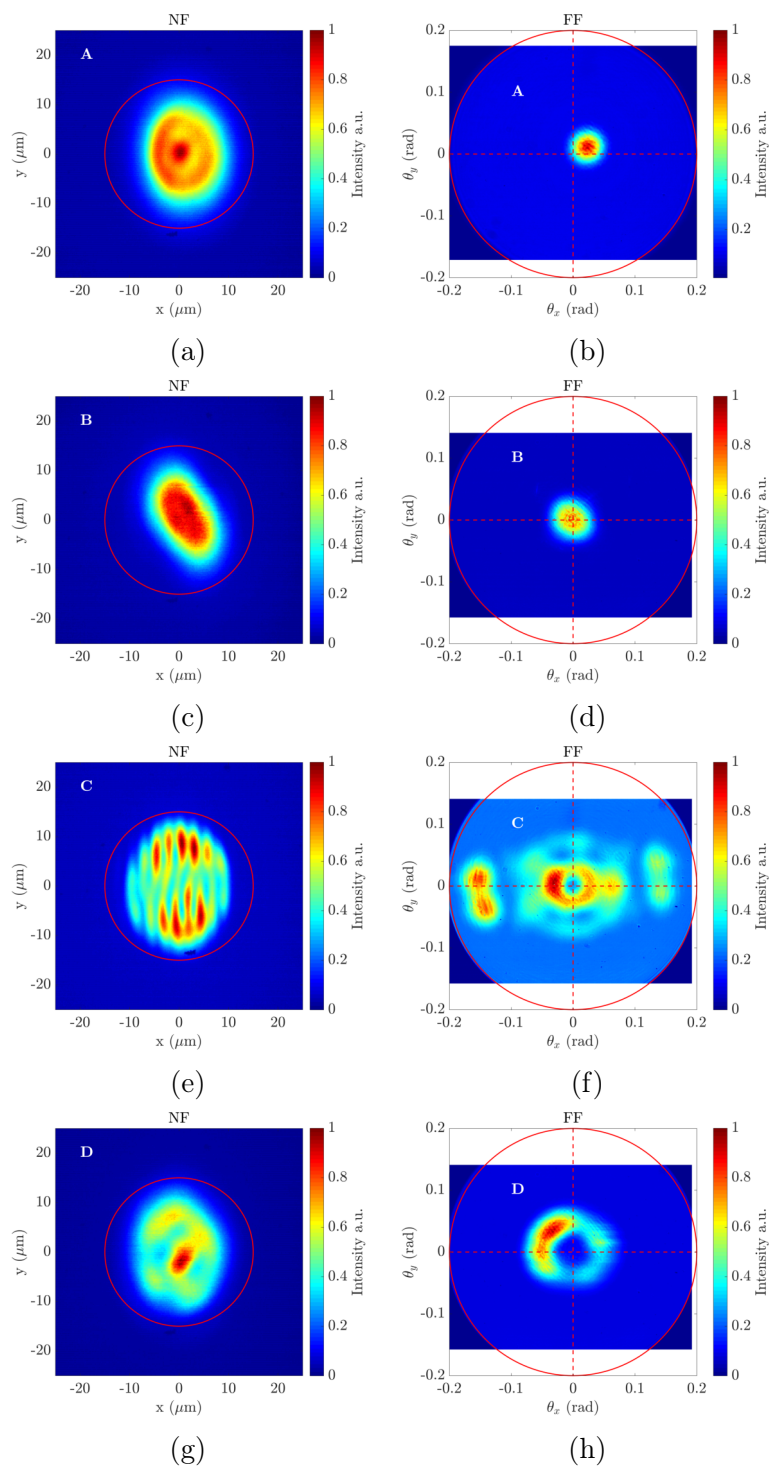


Figure 7.11: 2D NF intensity profile (a, c, e, g) and the corresponding 2D FF intensity (b, d, f, h) for the position A, B, C, D of figure 7.8.

7.2.3 Summary of the different emission behaviour

In conclusion, we have identified two main operating regimes, the on-axis one with a standard mode basis, the conical-wave one depending on the optical system aberrations. We also find this distinction when looking at the optical spectrum (see figure 7.12).

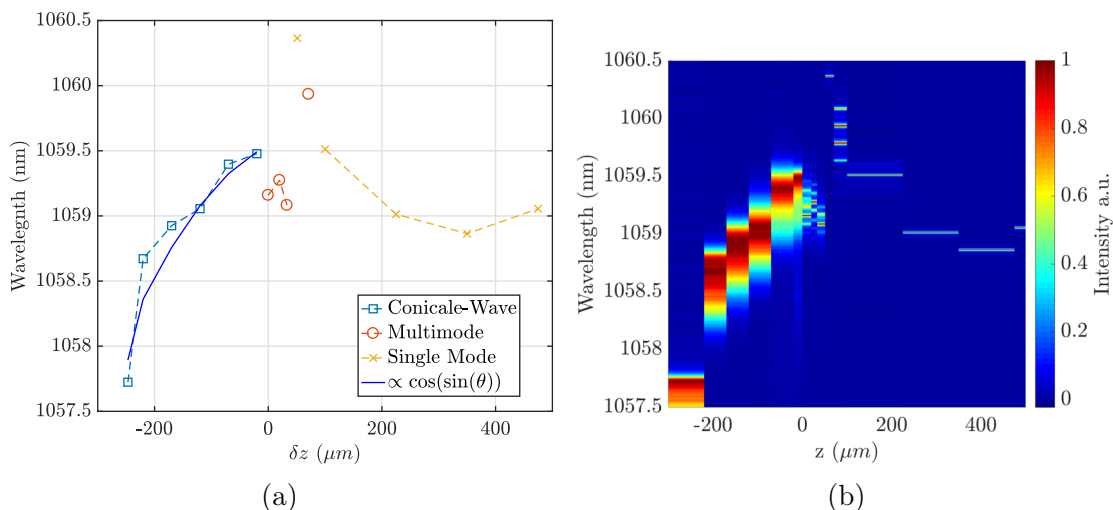


Figure 7.12: a) Maximum of each optical spectrum codify by their type of emission versus the detuning δz . b) 2D representation of the optical spectrum intensity versus the detuning δz .

Indeed, we see here the single mode optical spectrum in the normal diffraction regime, corresponding to the on-axis emission. The red-shift occurring the closer we are to the self-imaging point can be explained by the increased local heating due to the decreasing size (thus increasing power-density) of the fundamental mode until spatial degeneracy occurs and longitudinally multimode operation appears.

Then for anomalous diffraction we have the conical-wave emission following a wavelength blue-shift with their emission angle. The longitudinal resonating part follows $\lambda_0 \cos(\sin(\theta)/n_{sc})$ with θ being the emission angle from the normal of the gain in the air and λ_0 the wavelength for on-axis emission, in this case $\lambda_0 = 1059.6$ nm.

As seen in the previous chapter, we can equate the 4-f system as a small micro-cavity with an extended transverse plane and a complex potential representing both the net-gain and the focusing effects (thermal lens, SPM). This can be expressed by a stationary linear eigenvalue problem using the Bi-Harmonic Helmholtz like equation (see section § 6.3). Where the bi-Laplacian represents the spherical aberration, the normal Laplacian, the diffraction and the complex potential describing the thermal lens profile (Lorentzian profile), the electronic lens profile (Gaussian profile), the

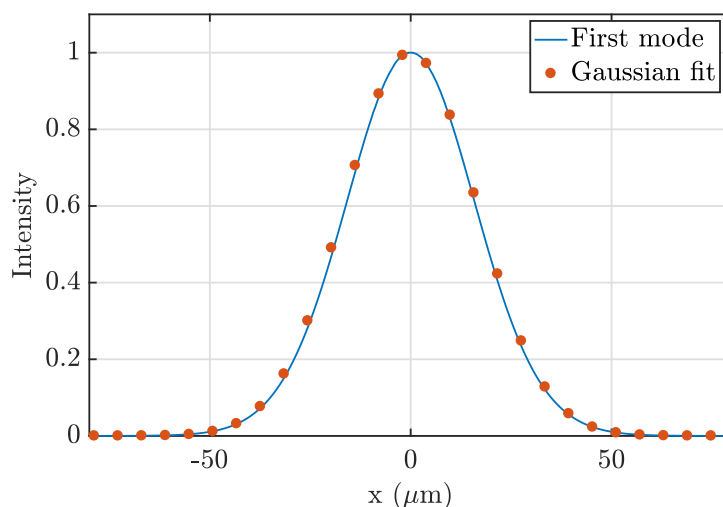


Figure 7.13: Near field intensity for the fundamental mode calculated with the simulation parameter of point B in figure 7.4. The Gaussian fit is of $33\ \mu\text{m}$ waist.

residual cavity C parameter (Parabolic profile) and the net gain profile (Gaussian profile). By solving this eigenvalue problem, we can explore the effect of each parameter on the stabilized profile.

Solving this Eigenvalue problem results in a series of transverse modes supported by the cavity for a parameter set. It is possible to confirm the existence of the two emission regimes. Using the parameter of section § 7.2.1 with a phase profile equivalent to a $f = 16\ \text{mm}$ lens and around 4% losses, we can look at the fundamental mode of the system with the fewer losses or higher net gain.

Figure 7.13 displays the NF intensity resulting from the simulation with a detuning equivalent to $\delta_z = 400\ \mu\text{m}$ and a Seidel coefficient for spherical aberration of $S_1 = 1\ \text{mm}$ equivalent to the point B in figure 7.4. Both the measured beam and the simulation give a close result, similar to the more simple ABCD fit. On the other hand, for detuning of $\delta_z = -50\ \mu\text{m}$ the equation 6.31 predicts the stabilization of conical-waves. Figure 7.14 displays both the NF and the FF of the fundamental solution, which is a conical-wave.

With this eigenvalue problem, we now can define a detuning range for the degenerated region, useful for non-linear structuration. In figure 7.15 we show the real and imaginary part of the solved eigenvalues for detuning $\delta_z = 5\ \mu\text{m}$. And looking at the imaginary part (Gouy phase) we can see that we reach degeneracy for the first 10 cavity transverse modes. Indeed, the phase of each of those modes is included into a single resonance of a Fabry-Perot cavity of finesse 150.

It is also better to have the on-axis stability separated from the off-axis one to reach as close as $5\ \mu\text{m}$ the self-imaging point. For this, having a positive spherical

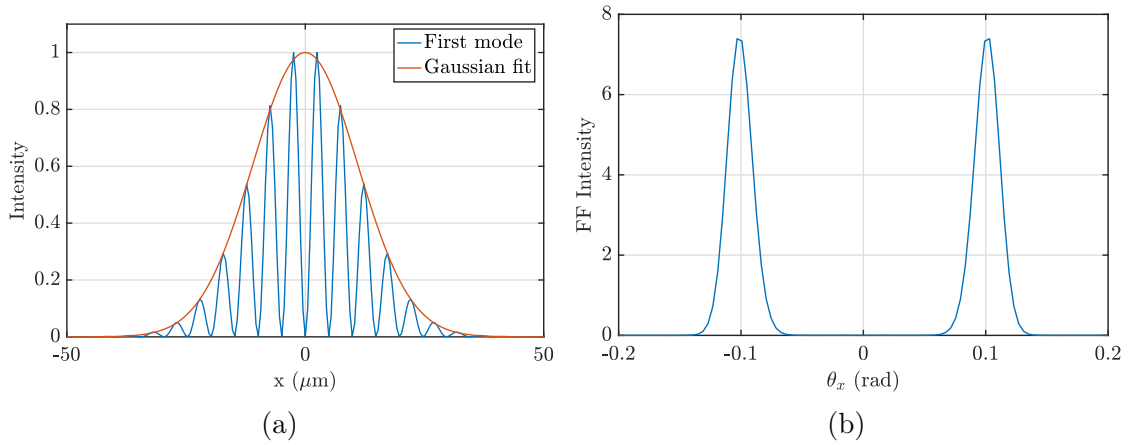


Figure 7.14: a) Near field intensity and b) Far field intensity for the fundamental mode, calculated with the simulation parameter of figure 7.4 and $\delta_z = -25 \mu\text{m}$ detuning. The Gaussian envelope fit is of $22 \mu\text{m}$ waist.

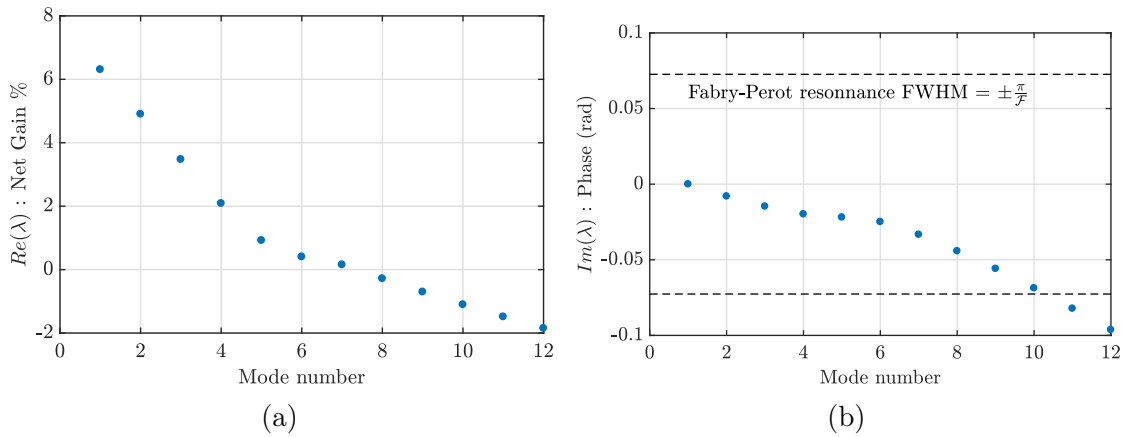


Figure 7.15: Eigenvalue result for a detuning $\delta_z = 5 \mu\text{m}$ and the equivalent potential as figure 7.4. In this configuration, we reach 10 degenerate modes. a) Real part of the eigenvalue corresponding to the net gain. b) Imaginary part of the eigenvalues corresponding to the transverse mode Gouy phase.

Seidel coefficient for the normal on-axis stability and negative spherical Seidel coefficient for the anomalous on-axis stability. This means that the marginal ray defining the off-axis stability will cross before (after) the self-imaging point for normal (anomalous) on-axis stability.

7.3 Arbitrary wavefunction

For the rest of the manuscript, we place ourselves in the high transverse degeneracy region around the self-imaging position. We first explore the potential of this region to generate arbitrary transverse wavefunction by using other chromium mask design such as the “A” shape, while adding the SESAM as one end mirror. The larger losses mean lower finesse and thus better degeneracy.

7.3.1 Chromium mask "A"

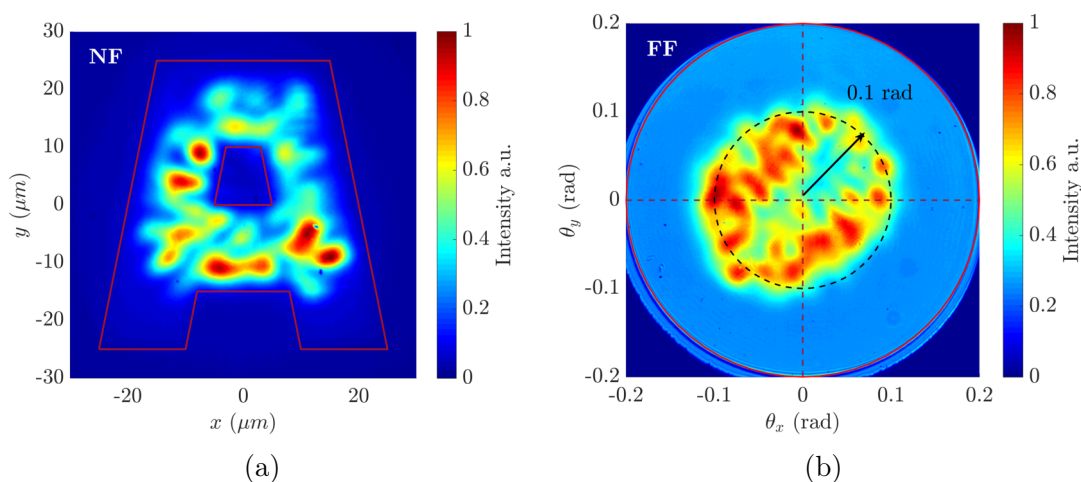


Figure 7.16: Example of arbitrary/complex wave pattern occurring near the self-imaging position for high pump power. Chromium mask simulating a “A” shape. (a) Near field intensity. (b) Far field intensity.

Using the “A” shape chromium mask with width and height of $50\ \mu\text{m}$ and spacing of $15\ \mu\text{m}$ in combination with the Gaussian pump, we manage to achieve lasing on an arbitrary pattern. Figure 7.16 displays the NF and FF 2D intensity distribution of this beam. The NF profile follows roughly the mask contours, with modulation from 3.5 to $6\ \mu\text{m}$ Gaussian waist. The FF also shows an on-axis modulated emission with max angle of 0.1 rad corresponding to the Gaussian divergence angle for a $3.5\ \mu\text{m}$ spot at $1.064\ \mu\text{m}$. The FF modulation has a mean value of 0.028 rad waist

at, $1/e^2$ which in turn corresponds to the Gaussian divergence angle of a $12\ \mu\text{m}$ waist spot.

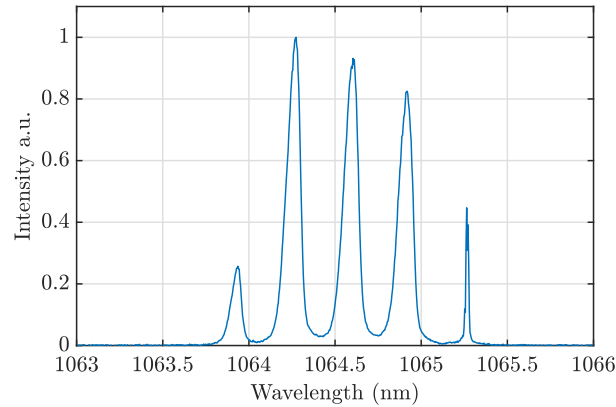


Figure 7.17: Optical spectrum for the arbitrary wave on a “A” shaped chromium mask/

In figure 7.17 We see a strong longitudinal multimode operation where each of the peaks represents a SESAM transmission resonance. And each of those resonances can fit up to 26 longitudinal cavity modes. This makes this emission pattern strongly multi-modal, both transversally and longitudinally.

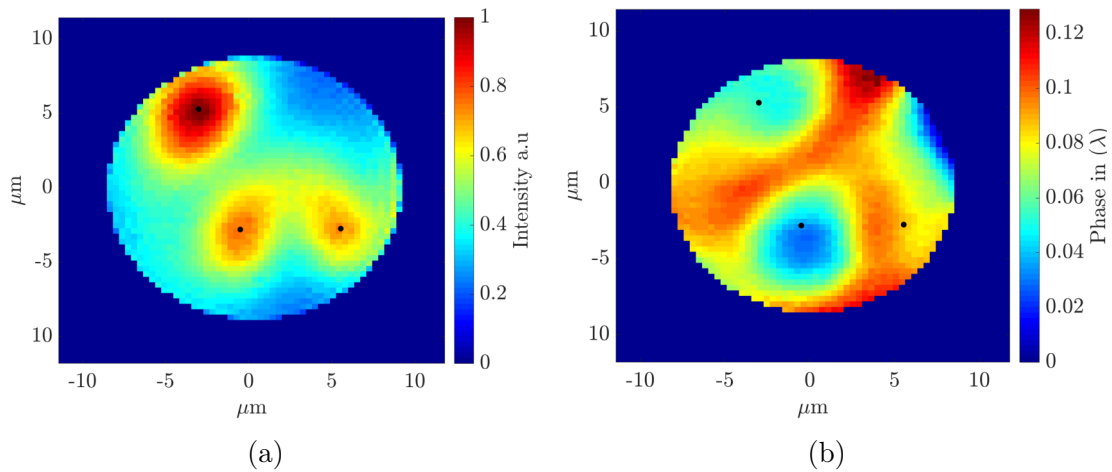


Figure 7.18: Zoom on a few modulations in NF measure with a wavefront sensor (Phasics). (a) Near field intensity. (b) Corresponding wavefront.

We used the Phasics SID4 4-wave Shearing Interferometer wavefront sensor camera to look at a zoomed in portion of the NF. Figure 7.18a shows the intensity

distribution inside the measurement pupil, while figure 7.18b shows the corresponding transverse phase (the max intensity is marked with a black dot). From this, we can correlate phase valley with intensity peak, indicating some small self-focusing effect ($< \lambda/10$ phase variation over the small beam radius). However, the max/min of intensity and phase do not match perfectly, indicating of a spatial chirp in the transverse phase.

7.3.2 Chromium defects

For the next example, we changed the “A” mask to a random assortment of small chromium dots ($5 \mu\text{m}$ diameter). It is used to simulate some local defects. The top hat pump (FWHM $170 \mu\text{m}$) was preferred to the Gaussian pump, enlarging the pumped transverse area.

Figure 7.19 shows the 2D intensity NF (FF) profile on the left (right) for three different pumping rates ($r = 1.6$ for the top, $r = 1.1$ for the middle one and $r = 0.9$ for the bottom one).

For large pumping rate, both the NF and FF almost fill all the available space with some randomly modulated intensity pattern. This pattern clearly does not belong to a single transverse mode of any base, and resembles more the output of multimode fiber [Čižmár 2011]. We thus have, in this case, a high spatial degeneracy.

Lowering the pumping rate, the laser emission is concentrated on the maximum gain, but still largely multimode. We can note that under the threshold the FF becomes less uniform, but we start to see a strong on-axis emission coupled with lower high-frequency components. This can be the result of lowering the thermal lens and thus the NF confining potential and switching to the FF or aberration confinement of the field, as well as the start of non-linear structuration.

7.3.3 Degenerated conical wave

Using the top-hat pump without mask in the conical regime, we show an azimuthally degenerated tilted-wave emission. We used a cavity set-up with the one achromatic lens and one MRF lens to increase the aberration and range of conical-wave emission. We pump the gain without mask with the Gaussian pump at a high pumping rate. In this condition, the separation of the on-axis emission and tilted wave is clear, and we manage to observe a fully azimuthally degenerated beam.

Figure 7.20 displays this emission. On the right, we see a complex interference pattern arising from a multitude of tilted-waves. The mean period of the interferences fringes is $3.2 \mu\text{m}$. On the left, the 2D FF intensity shows a multitude of spots arranged in a ring at 0.14 rad emission angle. Some pairs of spots have been

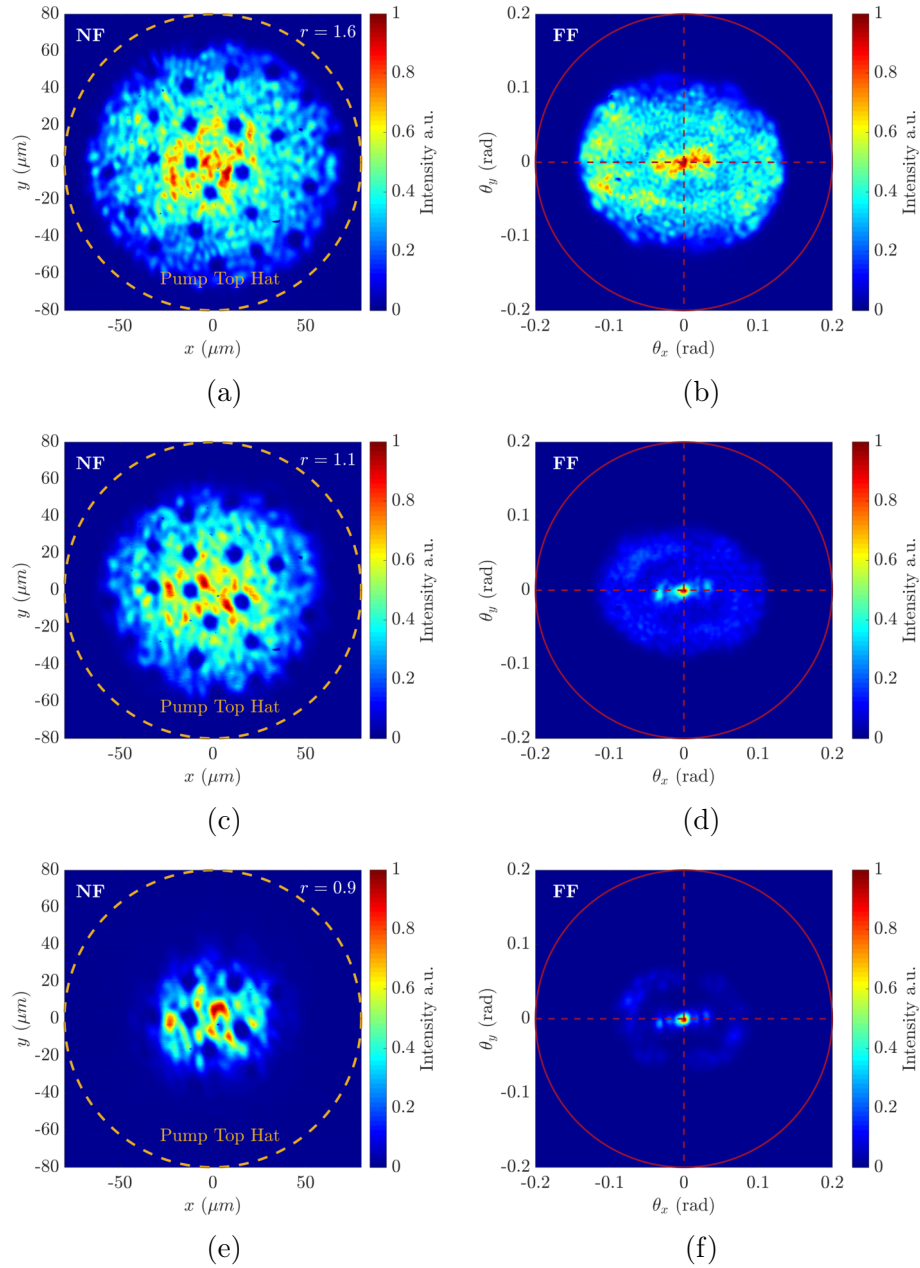


Figure 7.19: Example of an arbitrary/complex wave pattern occurring near the self-imaging position for three pump rates. $r = 1.6$ for (a) and (b). $r = 1.1$ for (c) and (d). $r = 0.9$ for (e) and (f). Chromium mask simulating random $5 \mu\text{m}$ defects. (a),(c),(e) Near field intensity. (b),(d),(f) Far field intensity.

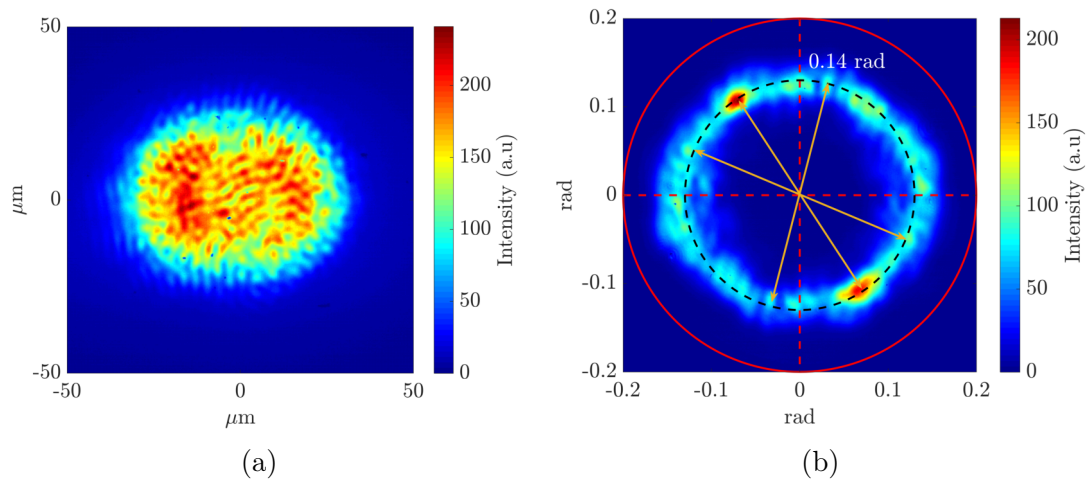


Figure 7.20: Example of azimuthally degenerated complex wave pattern occurring near the self-imaging position for high pump power with top hat pump. (a) Near field intensity. (b) Far field intensity.

marked by an arrow. Each of those pairs interfere in the NF to give rise to this complex pattern.

By simple trigonometry, we can calculate the expected interference period given this emission angle. Using $T = \lambda/2 \sin(\theta)$ we find for $\lambda = 1.064 \mu\text{m}$ and $\theta = 0.13 \text{ rad}$, $T = 3.8 \mu\text{m}$. This is coherent with the measure interferences fringes period in NF.

Non-linear light structuration in the spatial domain

In this chapter, we will describe and analyze the non-linear behavior observed in our system by adding the saturable absorber. We aim to demonstrate the possible existence of a spatially localized state. The resulting wavefunction takes the form of a unidirectional travelling wave with a small off-axis component, similar to a unidirectional ring cavity. The transverse dynamics can be compared to a quantum-mechanical system with a heavy mass particle and small momentum inside a close to flat potential.

We used a 4-f self-imaging cavity with one lens (MRF polished) for low optical aberration and the other as an achromatic lens to better control to conical cavity regime. As seen previously, the achromatic lens introduces mainly spherical aberration and almost no higher order one. From this, it is possible to better separate the on-axis and off-axis stability region. We also used the V0450 Gain section with the V0598 saturable absorber presented in part 2.

To characterize the field properties, we measured both the NF and FF spatial intensity profiles using a time average CCD camera, giving us insight for the spatial properties. We also looked at the optical spectrum using a diffraction grating spectrometer and the relative intensity noise for temporal properties. And lastly, a polarizer to verify the polarization properties of the generated laser emission.

8.1 Non-linear travelling wave

8.1.1 Dynamically instable NL travelling wave

8.1.1.1 Without mask, magnification: 2

At first, let's investigate the bi-stable behavior of the system. Figure 8.1 shows the measured output power versus pump power density curve for this system using the Top Hat pump near the self-imaging position. Several inserts of the 2D field intensity in both NF and FF are also shown. The laser threshold from low to high power is measured at 2.6 kW/cm^2 which is equivalent to around 6% losses according to figure 3.7 and the threshold from high power to low power is measured at 2.3 kW/cm^2 equivalent to 4% losses. The last point roughly corresponds to the unsaturated losses of the system, while the first point to the total losses. The small loss modulation, in this case, is due to a bad matching of micro-cavity resonance and the maximum of the gain of the semiconductor device. Because of its large size, the Top hat pump requires a higher power to reach the power density needed to cross threshold and generate a large red-shift of the gain spectrum. The top hat pump, despite its lower impact on the thermal lens, is not the best suited pump to achieve large modulation depth of the saturable losses.

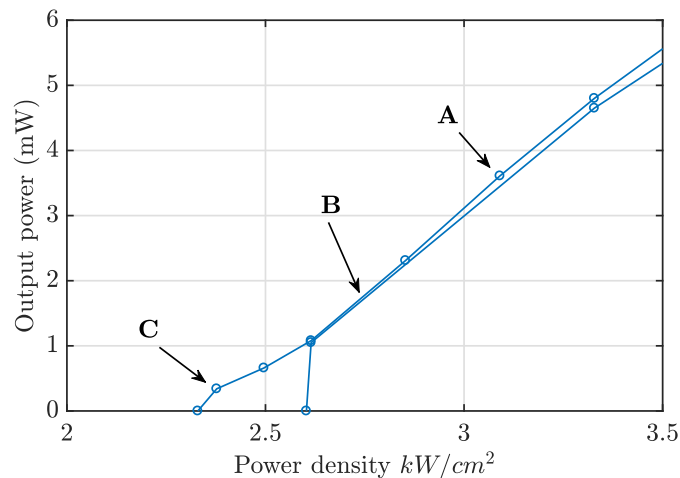


Figure 8.1: Output power versus pump power density for the 4-f cavity ($f_1 = 25 \text{ mm}$ and $f_2 = 50 \text{ mm}$) without chromium mask near Self-imaging. The pump used is the Top Hat pump.

The 2D intensity profiles were taken for different pump power excitations and show the beam evolution from high above the threshold to inside the bistability. In the near field, the dotted circle delimit the pumped area. We observed a downsizing

of the lasing area when pump excitation is going down. This is explained by the fact that the top hat pump is not entirely flat, and thus the net gain region is actually decreasing in size. On the other hand, the FF does not evolve a lot, and most of its energy is found on the cavity axis except for the last point where a strong off-axis component appears. An important observation is that the emitted pattern does not collapse onto a singular localized spot.

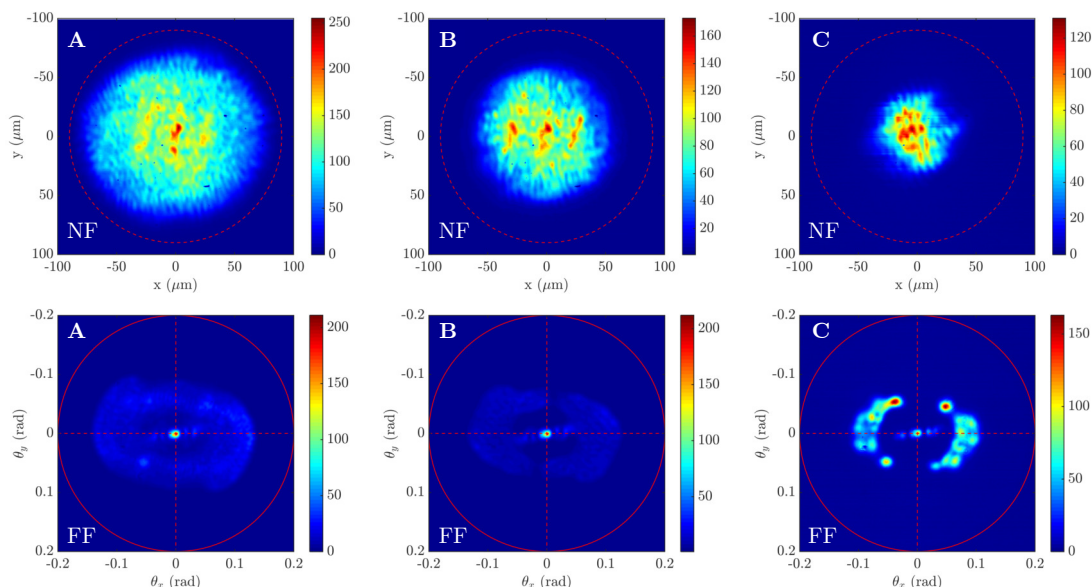


Figure 8.2: 2D NF and FF intensity for the position marked A, B, C in figure 8.1.

Despite having a large Fresnel number (large pumped transverse area in front of the maximum numerical aperture of the system) and optical bi-stability, the system does not naturally collapse onto the SLS state. One reason is that the system has a lot of freedom to choose a wavefunction that resonates near the self-imaging position. This freedom of choices and the near-field phase potential induces spatial dynamical instabilities.

To reduce this freedom, we choose to use the chromium mask filtering the field amplitude to limit the transverse area. Meaning both the Fresnel number and the maximum phase potential height. We also choose to work with the Gaussian pump to improve the losses modulation and thus the self-amplitude modulation and self-phase modulation effect.

8.1.1.2 Chromium mask 30 μm , magnification: 2

In order to restrict the transverse plane and to have a flatter near field phase profile, we decided to use the circular chromium mask. For this, we used a

$f_1 = 25$ mm MRF polished lens in front of the gain section V0450 and an achromatic lens $f_2 = 50$ mm in front of the saturable absorber V0598. We end up with times 2 magnification on the SESAM. The chromium mask diameter was $30\ \mu\text{m}$.

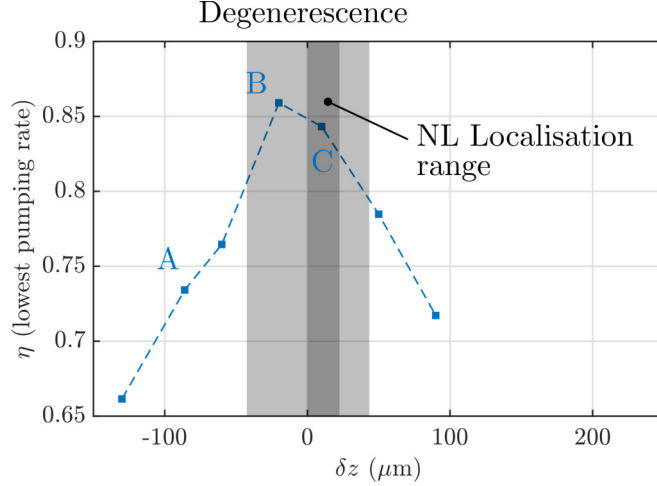


Figure 8.3: Minimum pumping rate versus the cavity self-imaging detuning with chromium mask $30\ \mu\text{m}$. The range of the transversally degenerate position is shown, with the smaller range for non-linear structuration.

Figure 8.3 shows the degenerate range of the system as well as the range where non-linear localization occurred. The figure displays the lower threshold pumping rate versus the self-imaging detuning δz , meaning the pumping rate at which laser emission stops when starting with the laser On and decreasing the pump power. This is calculated following:

$$\eta = \frac{P - P_{tr}}{P_{th} - P_{tr}} \quad (8.1)$$

where P_{tr} is the pump power needed to reach transparency, and P_{th} is the laser threshold when starting from the Off solution and increasing pump power. This threshold is then equivalent to pumping rate, $\eta = 1$ and the lower threshold display on figure 8.3 is a measure of the size of the optical bistability. We see that the bistability range varies according to the cavity detuning. When the laser is at the SI position, the bistability is the smallest and then increases with the detuning. This is easily explained with chromium masks on the gain side by the fact that for larger detuning, the effective mode size grows. Thus, it sees more losses from the chromium layer. The high threshold increases faster than the low threshold (better loss saturation from larger mode size). For the SI position, the chromium losses are less impactful since the resonating wavefunction adapts its shape to the loss mask. We find a similar emission profile as the ones described in the cavity

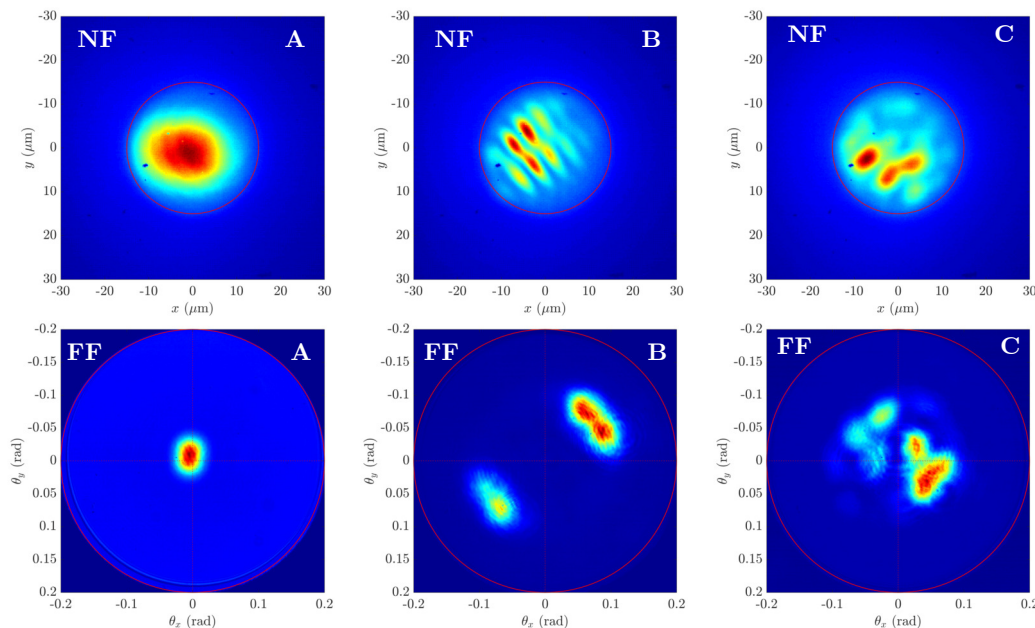


Figure 8.4: 2D NF and FF intensity for the position marked A, B, C in figure 8.3.

topology. With Gaussian emission for large detuning, conical emission for smaller detuning mixed with on-axis degenerate emission.

The degenerated range was taken for less than $|\delta z| < 50 \mu\text{m}$ detuning. While the NL localization range corresponds to the small window $\sim 10 \mu\text{m}$. Figure 8.4 displays the 2D NF and FF intensity profiles of the position marked A, B, C with a pumping rate close to the low threshold.

On figure 8.4, the picture C corresponds to parameters where the non-linear localization should appear. The system parameters were: $D_2 = -0.42 \mu\text{m}^2$ with $D_4 = -11.1 \mu\text{m}^4$. The static near field phase potential was estimated around a maximum of $\Delta\varphi = 0.025$ wave using the pump thermal profile and the chromium mask. Figure 8.6 displays the near field and far field phase diagram of the system. In this configuration, we should be able to balance the SPM for a spatially localized structure.

However, we do not see a single localized state, but rather a “random” pattern of emission. Using the injection laser to turn on a single spatial pulse of this pattern results in turning on the entire pattern. Simulation of a similar configuration confirms the difficulty in observing a single NL state.

Figure 8.5 shows a series of simulated NF 2D intensity profile for different numbers of round-trip as well as the time integrated profile for 1024 round-trip. We clearly see that transverse emission is not temporally stable and oscillate between different patterns.

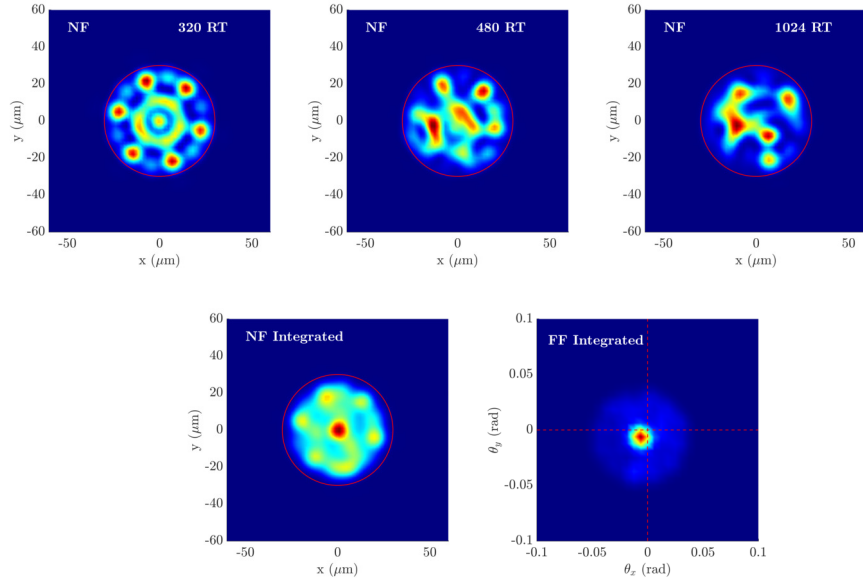


Figure 8.5: 2D NF intensity simulation for the round-trip number $N=200$, $N=500$ and $N=1000$ as well as the NF and FF on the integrated simulation over 1024 RT. The simulation is scaled on the SESAM plane. Simulation parameters: $D_4 = -20 \mu\text{m}^2$, $D_2 = 1 \mu\text{m}^2$, $\eta = 0.92$, $S = 5$, Gain to SESAM magnification $m = 2$.

The carriers diffusion is limiting the saturated size of the transverse spot at around $10 \mu\text{m}$ on the SESAM. The magnification from Gain to SESAM being 2 we can expect spot as small as $5 \mu\text{m}$ on the gain. The small spot size is too small in front of the mask radius and the near field phase variation to find a stable position. This freedom means that any perturbation such as ASE, gain modulation will transfer some energy and start some transverse motion of the NL spot, the same way as for the no-mask case.

8.1.2 Stable NL travelling wave

8.1.2.1 Chromium mask $30 \mu\text{m}$, magnification: 0.75

The next step to observe a NL spatial localization was to adjust the spot size versus mask size ratio. For this, we changed the cavity magnification while keeping the other parameters the same. We choose the lens $f_1 = 20 \text{ mm}$ in front of the gain and lens $f_2 = 15 \text{ mm}$ in front of the SESAM. This results in a 0.75 magnification from Gain to SESAM.

The $30 \mu\text{m}$ chromium mask on the gain then corresponds to a $22.5 \mu\text{m}$ diameter circle on the SESAM. The size of the 980 nm injected spot was measured around $3 \mu\text{m}$ waist, resulting in a Lorentzian saturated losses window of around $10 \mu\text{m}$

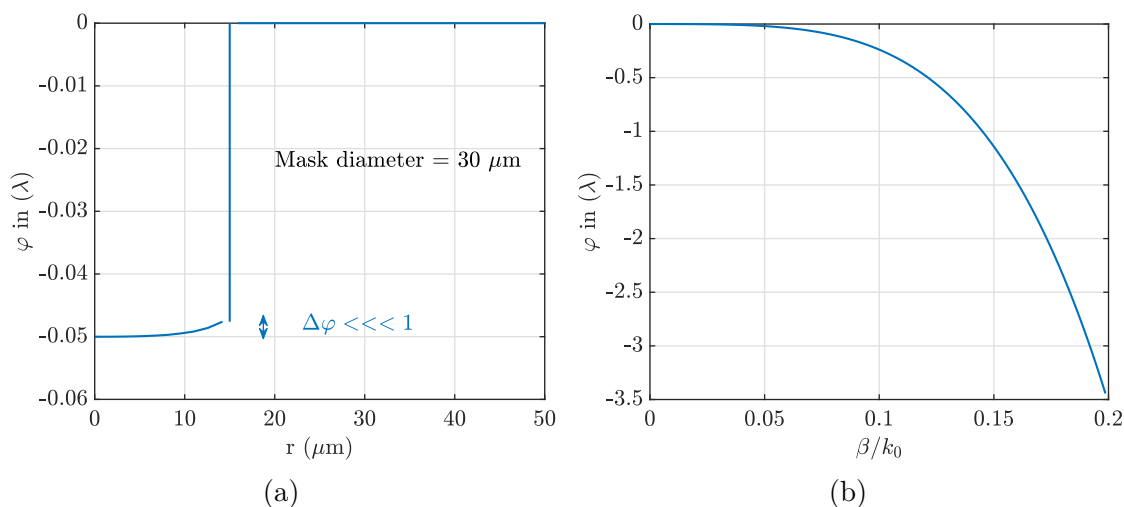


Figure 8.6: Dispersion diagram in (a) real space and (b) Fourier space for the 30 μm chromium mask and $D_2 = -0.42 \mu\text{m}^2$ with $D_4 = -11.1 \mu\text{m}^4$.

due to carrier diffusion. With the effective size of the chromium mask, it was then possible to saturate at least two distinct positions with minimum coupling. The expected NL spot size was then to be around 13 μm or two to three times larger than in the previous configuration. The other parameters were kept as close as possible to the other configuration, meaning $D_2 = -0.84 \mu\text{m}^2$, $D_4 = -8 \mu\text{m}^4$ and the same amount of near-field phase variation. The previous figure 8.6 still summarizes quite well the NF and FF phase dispersion diagram.

In this configuration, we observed a single NL localized light state under the threshold pumping rate (i.e., inside the optical bistability). We crossed the Off to On state using an injection laser emitting at 980 μm to locally saturate the losses of the SESAM by generating carrier inside the QW.

Figure 8.7 shows the NF 2D intensity chronology of generation. The red circle marks the chromium mask limit. The pictures coordinate were taken to the gain side. First we are in the off state (left image) then we locally saturate the SESAM losses at the position marked by the injection arrow. We then end up at the top right picture (follow the black arrow to “A”), where we have crossed the threshold at the injected position. Turning off the injection laser does not turn off the laser emission, which remains in place. From this state, we can either go back to the off state by lowering the pumping rate (red arrow), or switch to a different position in NF by moving the injection laser to another position (black arrow to “B”). In position “B” the laser emission also remains stable with or without the injection laser. From this position, we can either go back to the Off state by lowering the pumping rate or go back to position “A” by moving the injection laser.

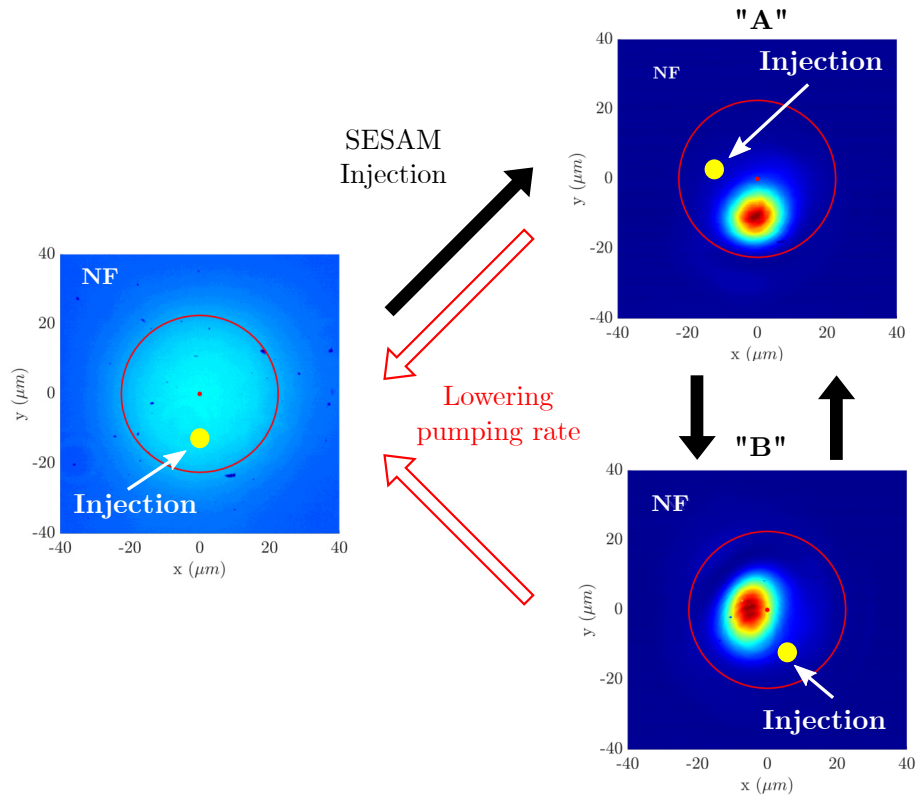


Figure 8.7: Transition from the off state to one of two possible non-linear localized states. 2D NF intensity profiles are shown. The position of the injection laser dictates the NL state that appears. It is also possible to switch from one state to the other directly with the injection laser.

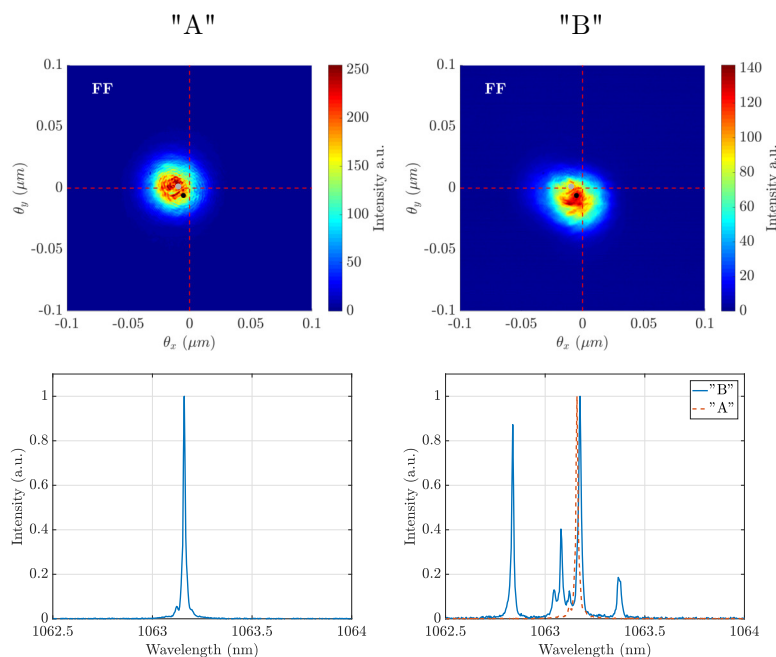


Figure 8.8: 2D FF intensity profile and optical spectrum corresponding to the positions “A” and “B” of figure 8.7.

The corresponding FF intensity profile and optical spectrum of position “A” and “B” are shown in figure 8.8. A gray dot marks the centroid of position “A” and a black dot, the centroid of position “B”. We see that they are both offset from the on-axis emission by 10 mrad and, 5.5 mrad respectively. Furthermore, the separation between them is 8.6 mrad. The laser cavity being telecentric, all transverse positions should emit at normal incidence. This small measured offset could be due to some cavity misalignment (i.e., small tilt) however it should result in the same offset for the two positions. We can say that both light states are not simple linear solution of the optical system. A non-linear force stabilizes to two positions and allows them to follow a unidirectional ring path in the system.

The corresponding time integrated optical spectrums are also displayed on figure 8.8. For position “A” we see a single mode at the resolution limit of the optical spectrometer ($\Delta f \sim 4$ GHz) and thus only one longitudinal mode exists since in this case $FSR = 2.2$ GHz. The optical spectrum for the position “B” is less stable, thus the time average trace result in a multi-modal emission. The optical spectrum of position “A” is superposed onto the optical spectrum of position “B” and we see that despite the unstable behavior of position B it does mainly lase onto a separate longitudinal mode. Both those light states are linearly polarized following the [110] axis of the Gain semiconductor device.

Using the *Phasics SID4* wavefront sensor, we also measured the transverse

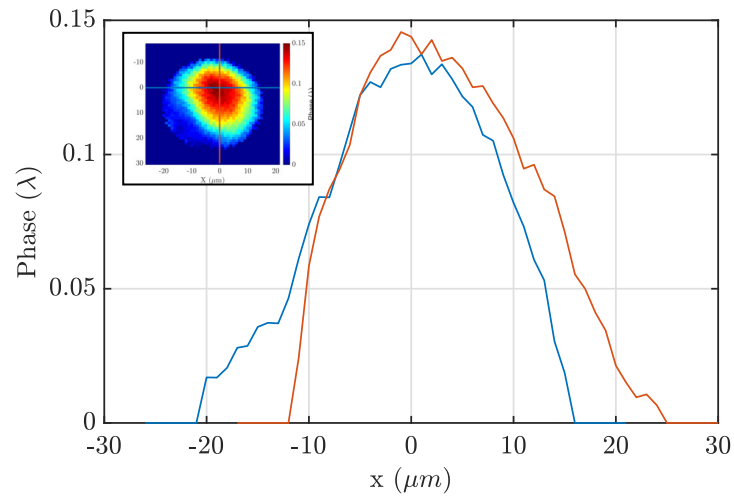


Figure 8.9: X/Y cut of the transverse phase profile of position “A”. Insert of the 2D phase profile.

phase profile in the near-field of the non-linear localized light state “A”. Figure 8.9 displays the X/Y cut of the transverse wavefront, showing a residual focusing phase of around $\lambda/10$ for $10\ \mu\text{m}$. This phase is the trace of the phase-amplitude coupling self-phase modulation.

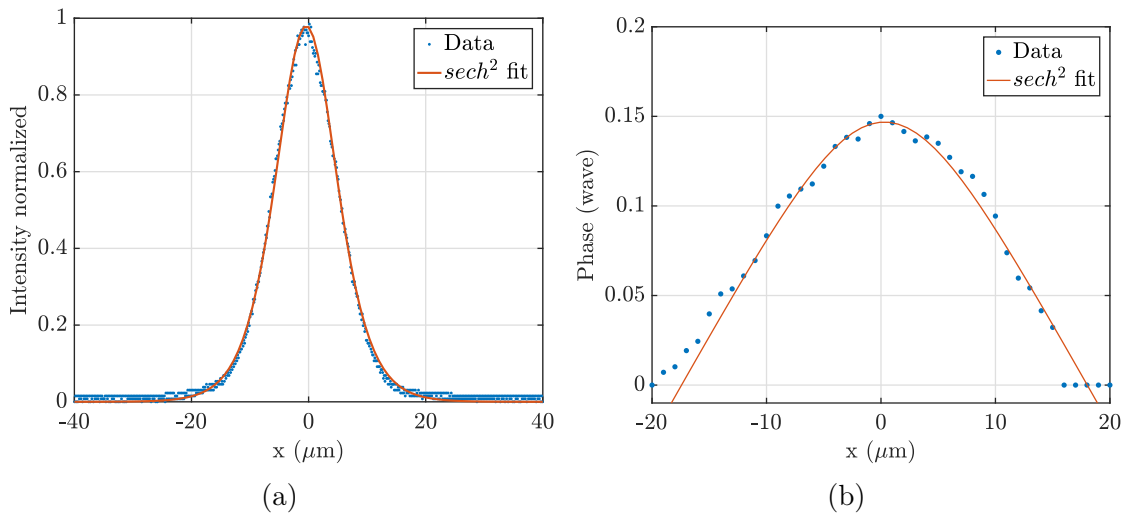


Figure 8.10: a) 1D x -cut of the NF intensity of spot “A” with a sech^2 fit of radius $r_s = 7\ \mu\text{m}$ or FWHM $12.3\ \mu\text{m}$. b) 1D x -Cut of the transverse phase profile measure with the Phasics SID4 wavefront sensor and the sech^2 fit with the soliton parameter $\beta_s = 0.5$.

We can use a sech-squared profile to fit and extract the NL parameters.

$$A(r) = \operatorname{sech} \left(\frac{r}{r_s} \right)^{1+i\beta_s} \quad (8.2)$$

Where the Sech-squared profile is the typical profile for soliton like-pulse in time, here we complete this analogy in space. r_s is the soliton radius and β_s the soliton chirp, positive for focusing SPM and negative for defocusing SPM. Figure 8.10 shows the Intensity and phase x-cut profile and their corresponding sech-squared fit. We find a radius of $r_s = 7 \mu\text{m}$, equivalent to $12.3 \mu\text{m}$ FWHM and a soliton parameter $\beta_s = 0.5$. Those values are in concordance with the soliton pulse size adapted for with SPM stabilization for the spatial case [Keller 2021]:

$$r_s^2 = \frac{-16D_2^{eff}}{\alpha G_0 \frac{F_p}{S}} \quad (8.3)$$

where α is the phase amplitude coupling factor of the Gain, G_0 is the gain modulation and F_p/S is the pulse saturation fluence normalized on the SESAM. Plugging the value $D_2^{eff} = -1 \mu\text{m}^2$, $\alpha = 4$ and $F_p/S = 3/5$ we find $r_s \simeq 8 \mu\text{m}$.

8.1.2.2 Chromium mask $15 \mu\text{m}$, magnification: 2

To test if the spot size vs. chromium mask size ratio does impact the single NL localized light state stability, we went back to the previous configuration with two times the magnification using the $f_1 = 25 \text{ mm}$ MRF aspheric lens and the $f_2 = 50 \mu\text{m}$ achromatic lens. This time, instead of the $30 \mu\text{m}$ mask, we used a $15 \mu\text{m}$ diameter one to have a mask diameter to number of spots ratio of 2 to 3, similar to the former section. As previously, we used parameters compatible with NL localization. Here, $D_2 = -0.42 \mu\text{m}^2$, $D_4 = -11.4 \mu\text{m}^4$, and a good phase flatness in near field $\Delta\varphi < 0.0025 \lambda$. Figure 8.11 displays the corresponding NF and FF phase dispersion diagram.

In this case, shown in figure 8.12 we find the same behavior as in the previous cavity configuration (figure 8.7). The red circle delimit the chromium mask, and the coordinates are taken on the gain side.

We show that starting from the Off state, it is possible to turn on a spatial pulse at two different positions depending on the injection direction. When approaching the injection laser from the left, a spot on the left of the mask turns on, while approaching the injection laser from the right, a spot on the right turns on. Similarly, the FF emission shows an off-axis component different for each position. The large shift in angle (0.08 rad) cannot be explained only with cavities detuning and misalignment, and thus another non-linear force must be at play.

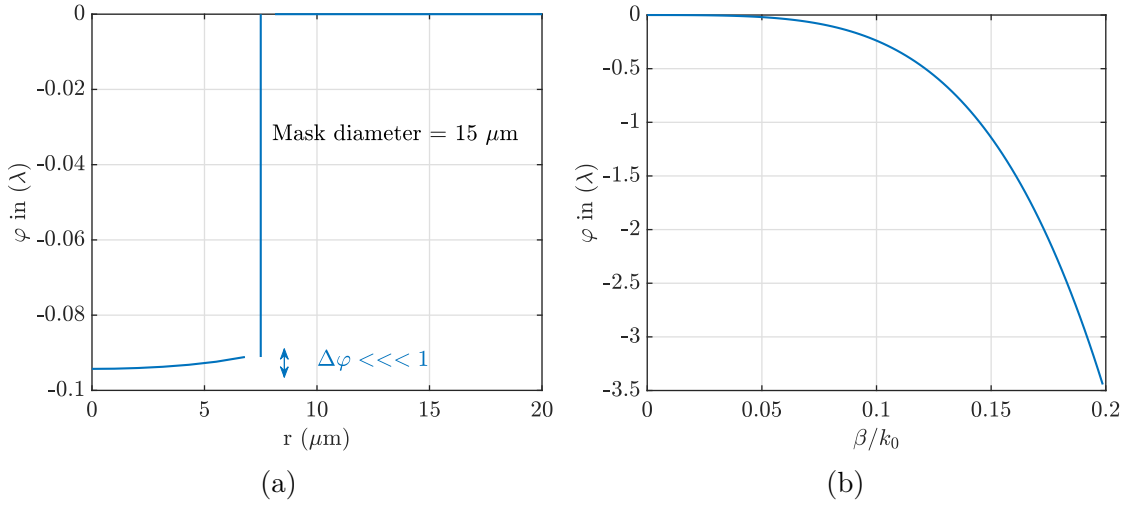


Figure 8.11: Dispersion diagram in (a) real space and (b) Fourier space for the 15 μm chromium mask and $D_2 = -0.42 \mu\text{m}^2$ with $D_4 = -11.4 \mu\text{m}^4$.

We also remark that the switched between two different positions only works on a certain range of the bi-stability. Figure 8.13 shows the Output power versus pump power curve where the low to high and high to a low threshold are marked by arrows and the range where the position selection works is indicated by dashed lines. This figure was taken for the configuration $f_1 = 15 \text{ mm}$, $f_2 = 20 \text{ mm}$ and the 30 μm chromium mask. The selection process only works for parameters at the higher end of the bi-stability. This is also true for the two times magnification configurations, where the selection process only works for the highest 40% of the bi-stability. One reason could be that at lower pumping rate the intra-cavity power is too small, thus non-linear effects such as self-phase modulation are too small to balance linear effects such as diffraction or the near field phase potential.

To better understand the origin of those singular light states, we looked in figure 8.14 at the NF and FF 2D intensity transition from above the bi-stability to inside the NL localization region. We remark that the singular light state appears to be the collapse into a single spot of a larger pattern. In this case, from a modulated doughnut like pattern in NF and FF to a single offsetted spot in NF and FF with the same position as the modulated pattern. The black dot represents the centroid for the single light state.

8.1.3 Experimental limits

The question is now, why do we see this behavior in only certain cases, mainly when we restrict the transverse space using a sharp absorptive boundary condition?

A beginning of a response can be found by looking at the relative intensity

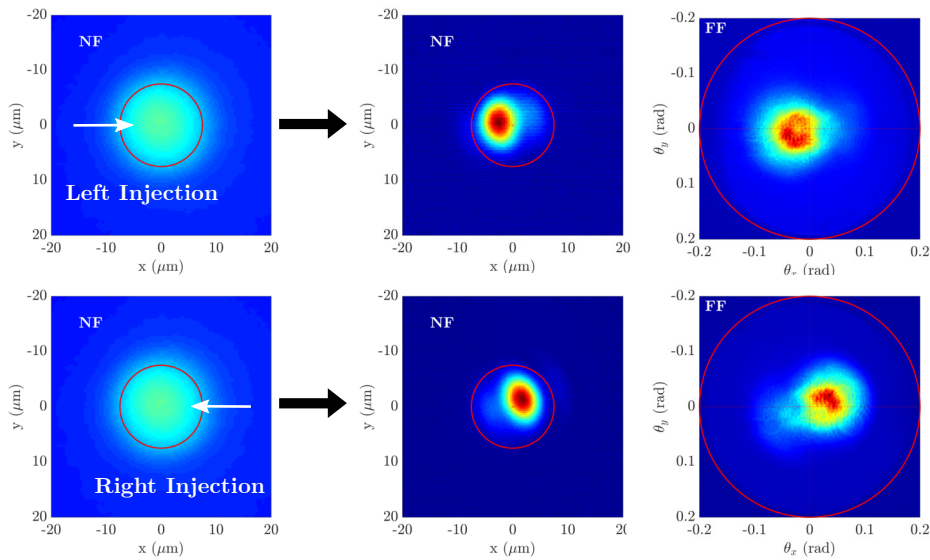


Figure 8.12: Transition from the off state to one non-linear localized state. 2D NF and FF intensity profile are shown. (Top line) When the injection laser comes from the left. (Bottom line) When the injection laser comes from the right.

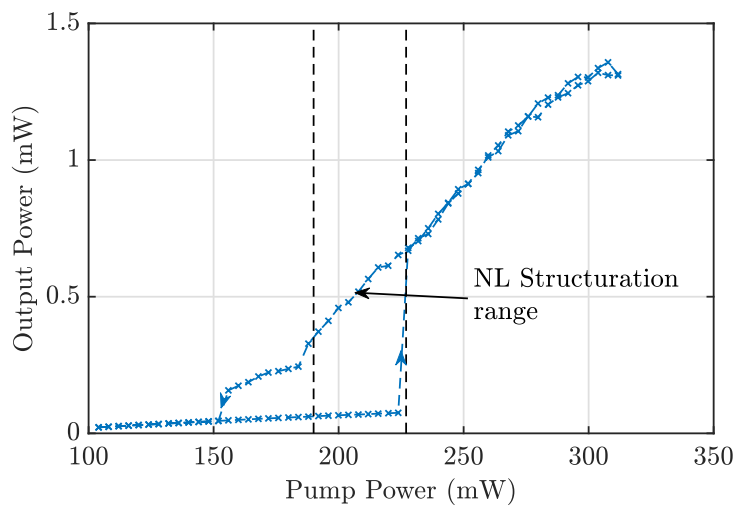


Figure 8.13: P-P Curve at the Non-linear structuration position, showing the optical bistability and the controllable range of the non-linear structure.

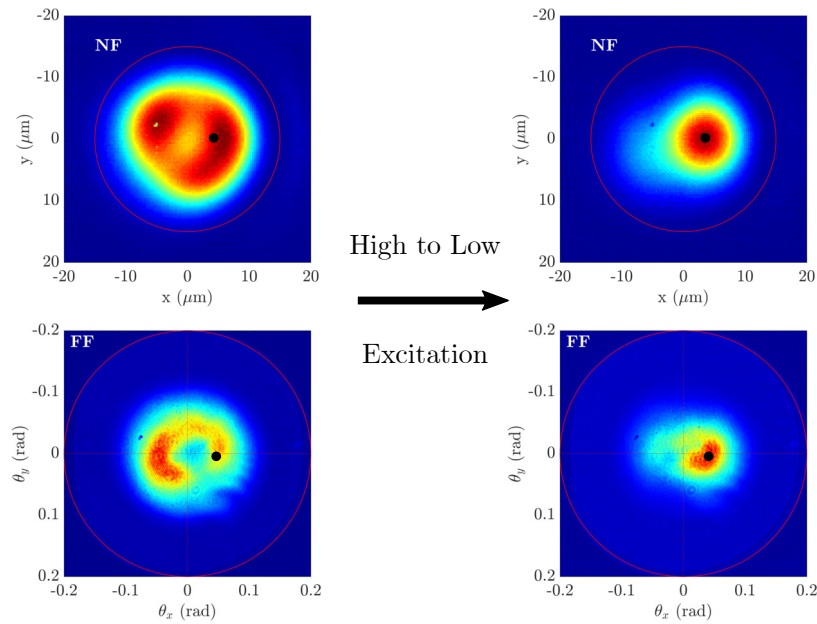


Figure 8.14: 2D NF and FF intensity pattern transition from high pump excitation to low pump excitation.

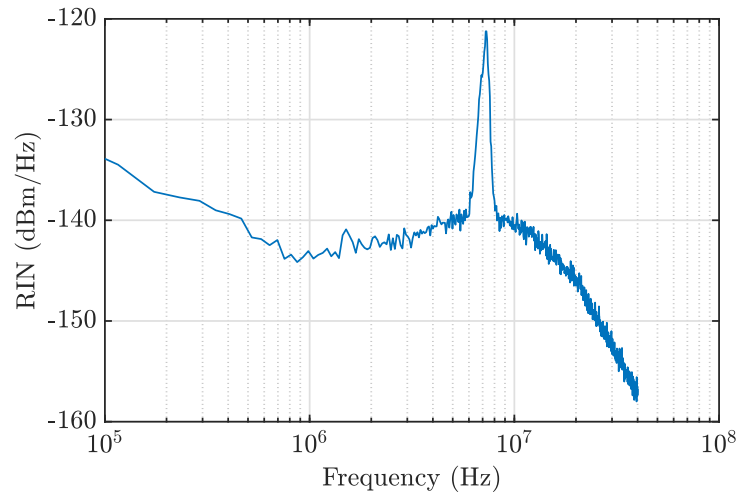


Figure 8.15: Relative intensity noise (RIN) from the single state of figure 8.14.

noise for the single light state in figure 8.15. We observe a strong frequency around, 7 MHz which should not exist for a single light state. This frequency could be a signature of some spatio-temporal instability of the system. Indeed, in this configuration where the Finesse is around 100 and the round trip time is 1 ns, the characteristic frequency is 7 MHz corresponds to dynamics around the photon

lifetime. Meaning that some spatio-temporal instability is destabilizing the system during its generation.

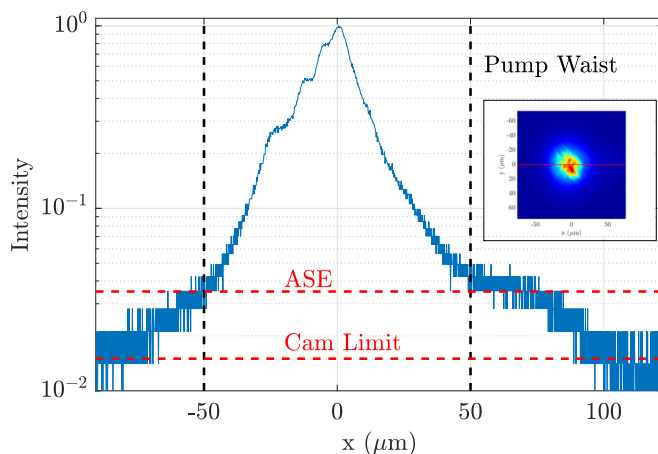


Figure 8.16: X-cut of the NF intensity for emission at the self-imaging position with no chromium mask and $\eta = 0.9$. Insert of the 2D profile.

The nature of those instabilities could be diverse. At the beginning, we aim to design a system offering the maximum of freedom to generate SLS. Doing so means that we would have a flat non-local potential by reducing the impact of optical aberration and reaching self-imaging in a telecentric system, and a flat local potential, thus limiting any near field phase and amplitude variation. In those conditions, the SLS should be free to move and exist at any positions. In reality, some variations still exist from thermal lensing or QW gain inhomogeneity having an impact on the SLS drift, or from optical aberration having an impact on the available spatial frequency. Lastly, the stochastic effect from amplified spontaneous emission (ASE) can also be seen as a strong perturbation in both phase and amplitude.

Figure 8.16 shows a cut of the NF emission at the SI position without chromium mask. The y-axis is in the log scale to show the limit of the camera dynamics and the power of the ASE, which is less than 20 dB below the laser emission inside the bi-stability. This will cause some phase and amplitude instability for the localized state, which will prevent it from finding a stable position. Limiting the transverse area with a chromium mask helps to limit this effect, but also prevents the localized state from escaping the gain region from drifting away, by quantum reflection on the chromium mask (amplitude barrier).

8.1.3.1 Quantum particle analogy

Following the quantum-mechanical analogy for the transverse wavefunction developed in the first part of the manuscript. We can compare the single non-linear state to a cold fermion particle with heavy mass near the SI degeneracy position. Indeed, the transverse non-local potential is close to a flat energy band, thus a heavy mass particle. In other terms, we are in the slow light condition in the transverse plane, since the transverse wavevector is longer than the light state size ($1/\beta \gg r_s$) [Khurgin 2010]. In this case, we can also view the absorptive barrier as a reflective potential following quantum reflections (see figure 8.17a).

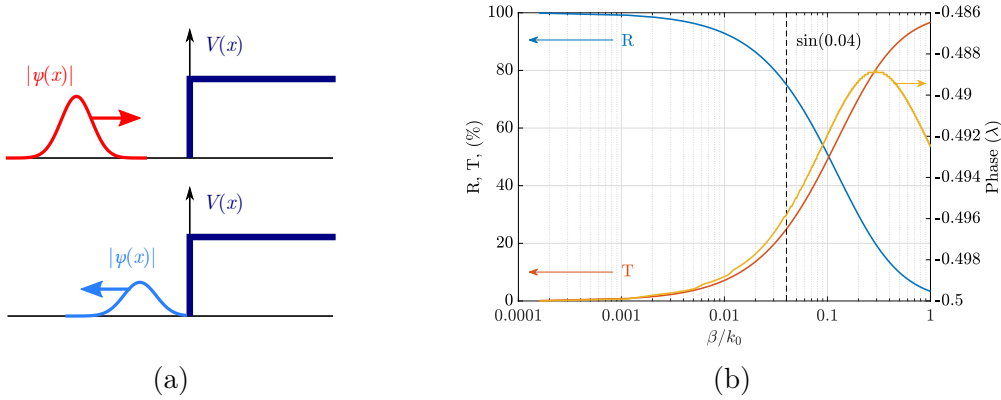


Figure 8.17: a) Schematics representation of a quantum reflection on a slow light wave-packet. b) Transmission and Reflection coefficient and phase of an absorptive barrier $\alpha_m = 0.8$ with $D_2^{eff} = -1 \mu\text{m}^2$ versus the particle impulsion (transverse wavevector β). The black dotted line represents the transverse wavevector for section § 8.1.2.2.

From this and the model of chapter § 6 applied to the optical cavity Hamiltonian, we can define the transverse wave vector outside the barrier (β) and inside the barrier (κ) following:

$$\kappa^2 = \beta^2 + \frac{V}{D_2^{eff}} \quad (8.4)$$

where V is the absorptive potential with $V = 0$ outside the barrier and $V = \alpha_m/2$ inside it and D_2^{eff} is the effective diffraction coefficient considering D_4 if needs to. From that, we can define a transmission, and reflection coefficient of the barrier versus the light particle impulsion (transverse wavevector), see figure 8.17b.

We see from figure 8.17b that for small impulsion the barrier provides a very high reflection and the more kinetic energy the particle has the less effective the barrier is until we reach a point where more energy is transmitted than reflected. In

a parabolic optical cavity, we can define the particle speed using the Hamiltonian kinetic energy following:

$$v_p = \frac{\beta D_2^{eff}}{T_{rt}} \quad (8.5)$$

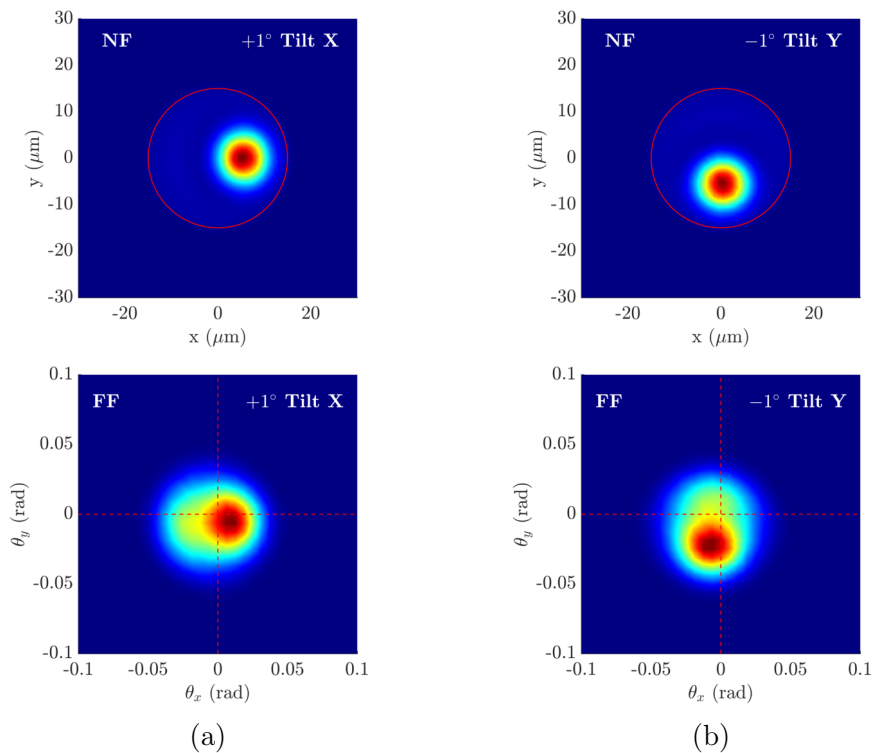


Figure 8.18: 2D NF and FF simulated and intensity profile at round-trip number 1024. The simulation is scaled on the SESAM plane. (a) A positive tilt on the horizontal axis was added. (a) A negative tilt on the vertical was added. Simulation parameters $15 \mu\text{m}$ chromium mask and $D_2 = 1 \mu\text{m}^2$ with $D_4 = -20 \mu\text{m}^4$, $\eta = 0.95$, $S = 5$, Magnification Gain to SESAM $m = 2$.

We see a linear proportionality with the light transverse wavevector β . The transverse behavior of this light state can then be thought of in terms of a mechanical system with speed v_p and momentum β . Small perturbations can generate transverse dynamics, destabilizing the system by supplying kinetic energy to the light particle, who then bounces back on the potential. Such mechanisms could be from mechanical origin, thermal lensing, gain amplitude gradient/modulation, optical system tilt, or amplified spontaneous emission on both the phase and amplitude.

The stable position seen in the previous section which was neither at the mask center nor at the on-axis emission can be explained by this phenomenon. The

destabilizing forces supplied kinetic energy to the light particle, who bounced back on the chromium potential until reaching a balance between the reflective force and the induced tilt.

We can see from figure 8.18 which is the result of a simulation using the parameters of section § 8.1.2.2 with a constant tilt to the right (a) and to the bottom (b). The simulation shows the NF and FF intensity after the spot stabilize to its final position (1024 round-trip). The initial beam was injected at the mask center. Looking at the transient, we see multiple reflections on the mask edge before its stabilization. This is coherent with the quantum reflection analysis. Secondly, the final position of the spot is only dependent on the perturbation applied to it. In our case, the kinetic energy was provided by changing the phase/amplitude potential using the injection laser, which moved the light particle position.

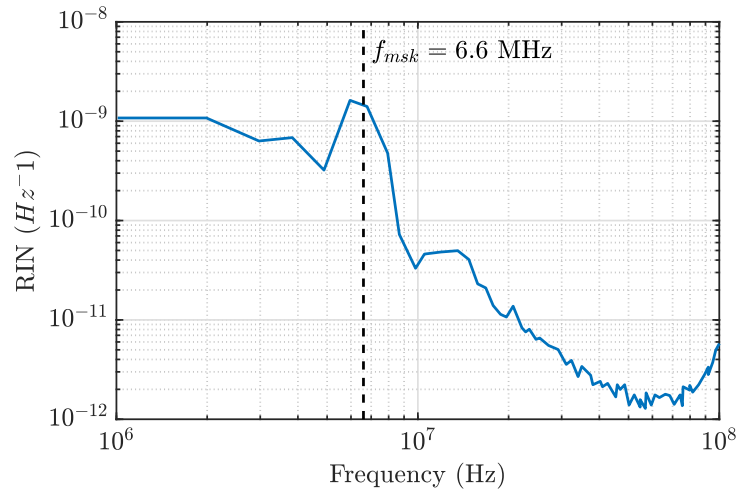


Figure 8.19: Relative intensity noise of the simulation in figure 8.18b.

Lastly, another marker of this dynamic can be found by estimating the time it takes a light particle to travel across the chromium mask. This characteristic time can then be related to a dynamical trace of the system. From the mask diameter and the particle speed of equation 8.5 we can get the time $T_{msk} = d_{mask}/v_p$. Using typical the typical value of section § 8.1.2.2, $d_{msk} = 15 \mu\text{m}$, $D_2 = -0.42 \mu\text{m}^2$ and measured angle $\theta = 0.04 \text{ rad}$ and $T_{rt} = 1 \text{ ns}$ we find a time of $T_{msk} = 151 \text{ ns}$. This time corresponds to slow intensity fluctuation of $f_{msk} = 1/T_{msk} = 6.6 \text{ MHz}$. We find those typical frequencies while looking at the RIN in practice (see figure 8.15) but also in simulation (see figure 8.19). The intensity variation corresponds to approximately 10% of the mean value.

To complete our understanding of those behaviors, a more in-depth analysis of the spatio-temporal transverse dynamics remain to be done. Currently, limitation

in output power has prevented us to image this behavior using time-resolved equipment such as a Streak camera.

8.2 Laser multiplexing

In the current system, it was not possible to simultaneously have several NL localizations. Indeed, a transverse restriction in the form of a loss mask has to be added to stabilize the NL state. Thus, a single state at a same time could be obtained in a single mask. However, by taking advantage of the telecentric nature of the self-imaging cavity and by using a matrix of losses potential, we could obtain multiplexing of lasers inside the same system.

8.2.1 Two lasers in one

We used the same optical system with an MRF lens $f_1 = 25$ mm on the gain side and an achromatic lens $f_2 = 50$ mm on the SESAM side. However, instead of the chromium mask with a single hole, we used a periodic system with a hole diameter of $15\ \mu\text{m}$ and different periods from $30\ \mu\text{m}$ to $16\ \mu\text{m}$.

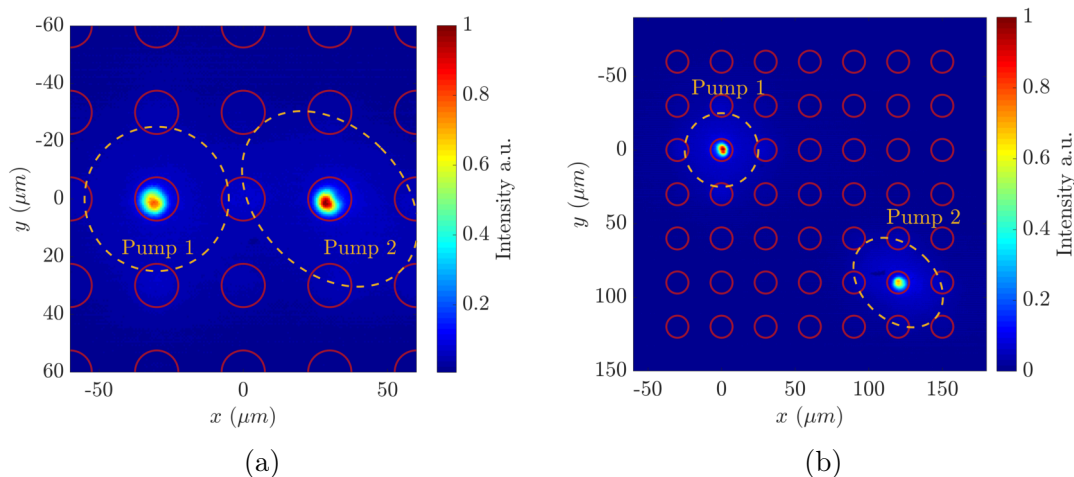


Figure 8.20: Representation of the multiplexing ability of the 4-f laser system using chromium ($15\ \mu\text{m}$ diameter, $30\ \mu\text{m}$ period) mask and two Gaussian pumps. (a) Two pumps in a close to each other. (b) Two pumps far from each other.

We also used two different Gaussian pumps to separately control to different positions. In this case, we are not at the self-imaging position but slightly detuned in order to obtain a Gaussian on-axis emission.

8.2.1.1 Large separation : Independent system

For the case where the circular holes have a large separation between them ($30\ \mu\text{m}$ period) we managed to control two lasers independently (one for each pump) across a large section of the gain (Chromium mask of $200\ \mu\text{m}^2$). Figure 8.20 shows the near field intensity for two cases, (left) when the two pumps are close to each others and (right) when they are far from each others. The red circles mark the chromium limits. Here, both spots are independently stabilized by the chromium mask and the thermal potential of each pump.

Both spots are also independently controllable by varying the pumping rate of each pump and each are lasing on different longitudinal modes (see figure 8.21a). This is also a proof of the good telecentricity of the optical system, since despite a large transverse separation, the spatial spectrum remains centered around the on-axis position (see figure 8.21b). Confirming the fact that each laser lase on a different longitudinal mode, the FF intensity profile does not show any interference pattern. The two lasers are uncorrelated.

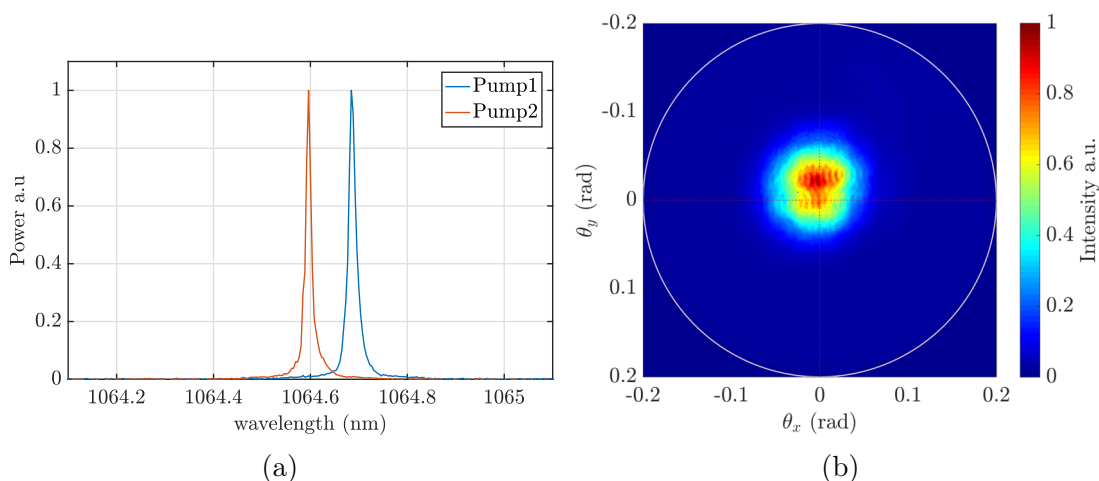


Figure 8.21: a) Optical spectrum of the two spots from pump 1 and pump 2 in the close from each other configuration in figure 8.20a. b) Far-field intensity for both laser spots in figure 8.20b.

8.2.1.2 Small separation: coupled system

To see if the independent nature remains for small separation, we used the chromium mask with a $15\ \mu\text{m}$ diameter hole separated by $1\ \mu\text{m}$. In this condition, a single Gaussian pump was used to create gain for several holes. Figure 8.22 shows the NF and FF 2D intensity for this configuration. We see that we still

have emission on several spots, where their intensity differences come from the gain gradient of the Gaussian pumping. However, by looking at the FF emission profile, we can infer that the four spots are coherent with each other since we observe an interference pattern in FF.

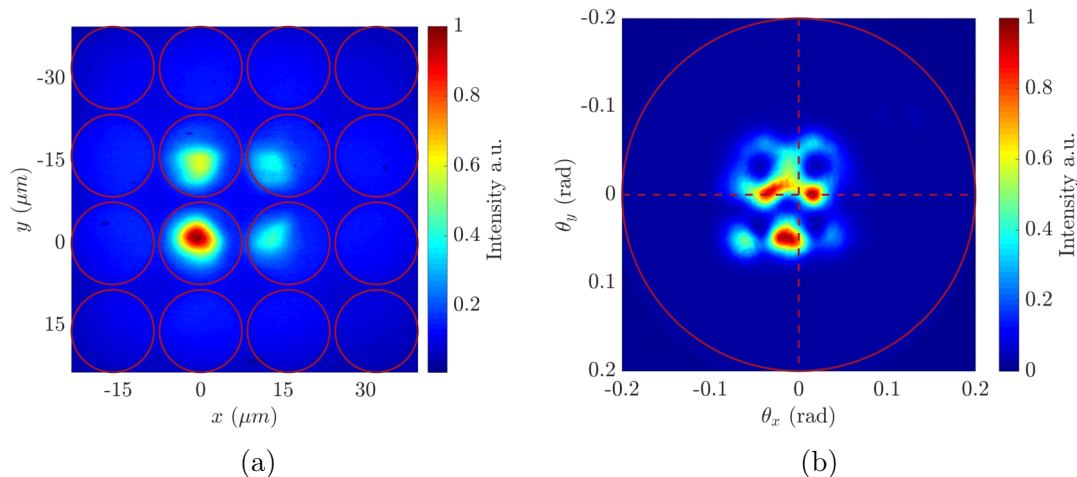


Figure 8.22: Gaussian pump on a periodic Cr mask with holes of diameter $15\ \mu\text{m}$ and periodicity of $16\ \mu\text{m}$. The smallest separation consists of $1\ \mu\text{m}$ chromium strip. (a) NF 2D intensity. (b) FF 2D intensity.

We can conclude that a $1\ \mu\text{m}$ chromium separation between two adjacent holes is not enough to prevent coupling either by the evanescent wave of the wavefunction or by the diffusion of the carriers in the SESAM, coupling two adjacent spots through loss saturation.

8.2.2 Multiplexed NL localized structure

Using the large diameter top hat pump, we wanted to confirm the independent nature of the multiplexed laser and extend it to the non-linear structuration region, meaning close to self-imaging and inside the optical bi-stability. For this, we went back to a mask with large separation ($15\ \mu\text{m}$) illuminated only with the top hat pump. This way, each spot was not stabilized through independent thermal lens and independent gain, but with the same pump.

Using the same methods as for the single hole mask, and with the same parameters, we used the $980\ \text{nm}$ injection laser to turn on the first spot by starting from the Off state (figure 8.23a) and saturating the losses inside one hole to cross onto the On state at this position (figure 8.23b). Then, moving the injection laser, we also manage to cross the On state on a different position (figure 8.23c). However,

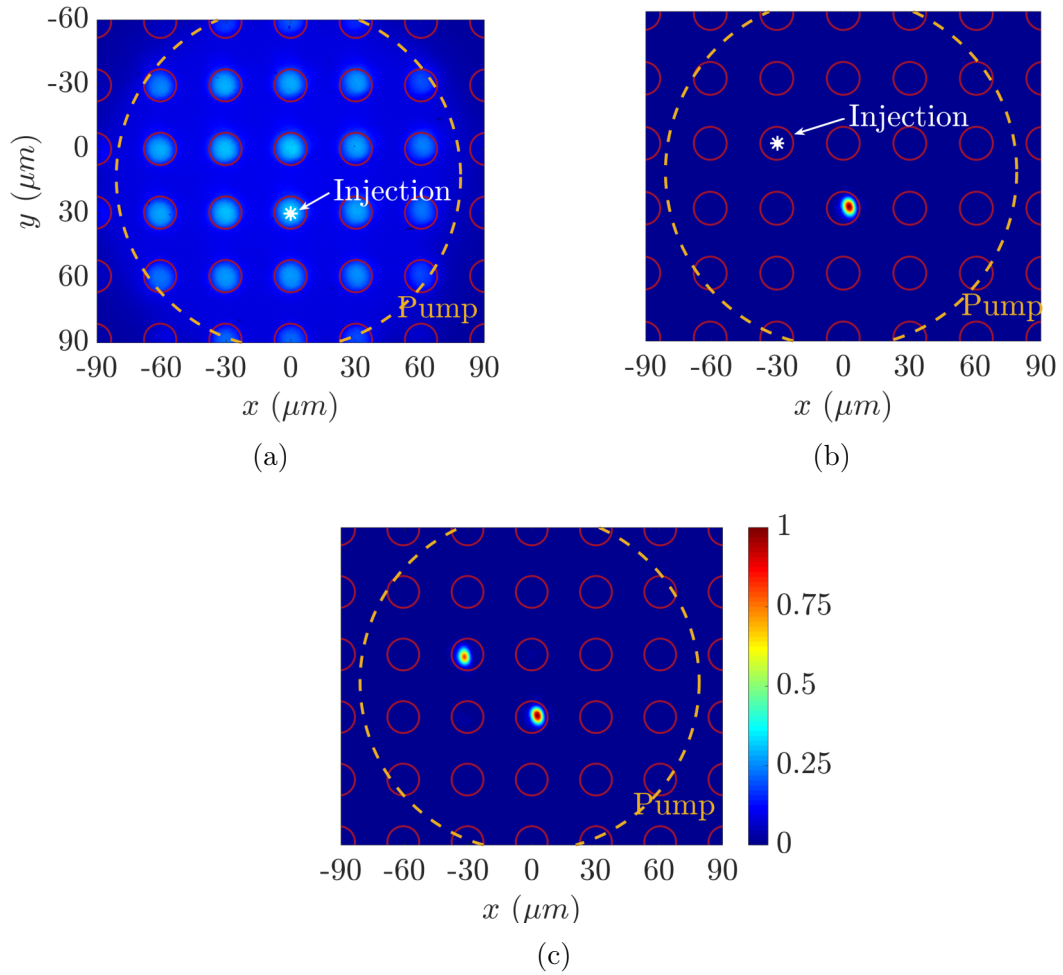


Figure 8.23: Representation of the multiplexing ability of the 4-f laser system using chromium mask and large area top hat pump. (a) The system starts in the off state, we saturate the losses at a specific point. (b) One laser spot appears at the previous point, we now saturate the losses at another point. (c) Both spots coexist.

turning off a single spot was not achieved. Only by reducing the pumping rate can we go back to the Off state for both spots.

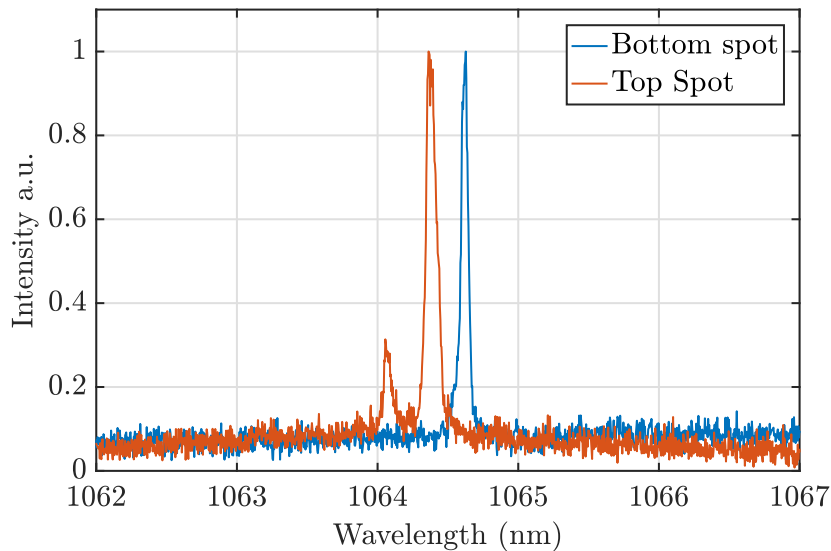


Figure 8.24: Optical spectrum of the two spots, (bottom) first spot to appear and (top) second spot.

Looking at their optical spectrum (figure 8.24) we can confirm they are operating on different longitudinal resonances and the large shift between them can be attributed, in part, to the micro-cavity thickness inhomogeneity.

As with the two Gaussian pumps pumping scheme, we have a mostly on-axis emission for both spots. Figure 8.25 shows the FF intensity profile for the bottom spot (first one to appear) and the top spot (second one to appear). The centroid of both of those spots was measured with 13 mrad offset.

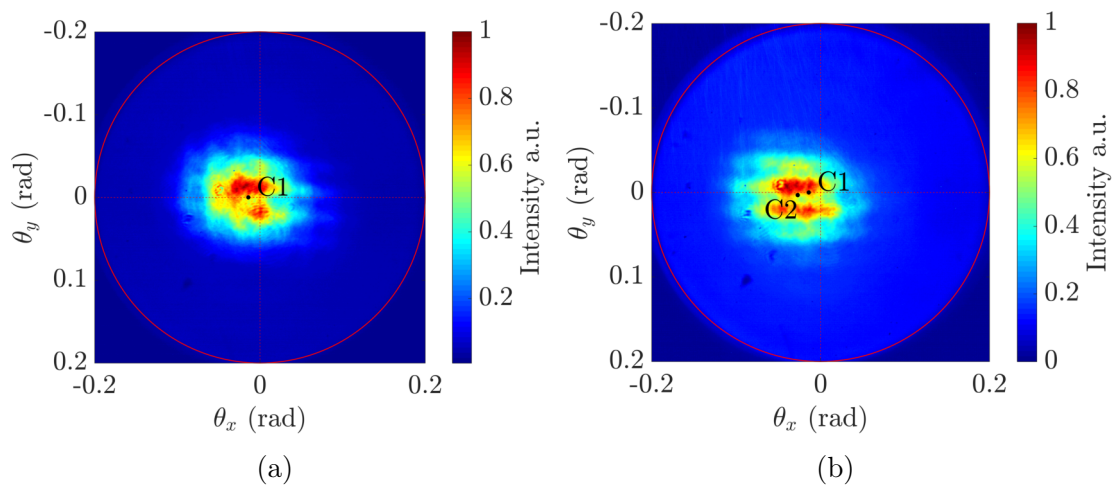


Figure 8.25: Far-field intensity for each multiplexed spot. (a) First spot (on the bottom of the NF), the center, is marked by the dot C1. (b) Second spot (on the top in the NF), the center, is marked by the dot C2. We observe an offset of 13 mrad

Conclusion and perspective

The goal of this project was to design a laser system capable of a high-level of 3D light structuration. This meant a highly spatially degenerated coherent optical system able to emit spatially localized states (SLS), together with a pulsed modelocked operation exhibiting temporally localized states (TLS). This work was carried out in collaboration with INPHYNI and C2N in the framework of the BLASON ANR project dedicated to the generation of 3D spatio-temporal localized state (i.e., Light bullet). The work on the temporal structuration and TLS was carried out mainly at INPHYNI, while at IES we focused on the degenerated cavity concept, and its spatial behavior together with semiconductor GaAs based heterostructure design and fabrication. The requirements were to design and build an extended system in both time and space exhibiting optical bistability. This meant a long round-trip time compared to matter response time and a high Fresnel number, together with saturable losses. To achieve this goal, we chose the semiconductor vertical external cavity surface emission laser technology coupled to a degenerate self-imaging cavity.

We choose semiconductor devices for their easy integration as end mirrors of the optical cavity, versatility in design wavelengths, modal gain, spatial and spectral bandwidth and spatial structuration of the susceptibility. We designed a high modal gain device while limiting the impact of inhomogeneous physical properties such as thermal lensing, all while keeping a large spatial and spectral bandwidth. We observed, together with a good crystal quality, a low laser threshold, a good differential efficiency and residual small-scale (few μm in-plane length scale) inhomogeneity from QW interfaces due to growth process. For weak transverse structuration (large transverse mode with Gaussian like profile) those inhomogeneities do not impact the laser field. However, in our highly degenerated case exhibiting small spatial structure in the bistability regime, they do moderately impact the structuration. We also designed a fast and slow semiconductor saturable absorber mirrors (SESAM) to generate the needed optical bistability. The design was matched to the gain properties to have the best modulation ratio. In this work,

we used a SESAM designed to exhibit a slow carrier lifetime to prevent any fast temporal dynamics or instability. This allowed us to focus on the spatial dynamics. Another design was developed for INPHYNI to have a fast response time, in order to study temporal structuration. Using our “slow” SESAM, we measured the carrier diffusion length to be $10\ \mu\text{m}$. This limits the size of the achievable narrow net gain window from the SESAM, and by implication the size of the non-linear localized structure.

Next we studied the cold cavity properties, first for classical system and then for 4-f self-imaging degenerate configuration. The self-imaging system allowed us to tune from normal to anomalous regime (-10 to $10\ \mu\text{m}^2$) the effective optical system second order diffraction by moving the end-mirror away from the perfect self-imaging position. Placing the end mirror further than SI position is equivalent to adding normal diffraction and inversely. To obtain the largest Fresnel number and the most complex spatial structuration, no effective diffraction is required. In this condition, we study non-local phase perturbative effects, such as optical aberrations. We showed, thanks to a ray tracing software and real lens wavefront error function, that optical aberrations have a strong impact on the effective on-axis numerical aperture. Spherical aberrations (4th order diffraction) are the main limiting factor, while higher-order terms induced wavefront error radial modulation.

To help us analyze the non-linear transverse laser emission, we combined all the important physical features: gain and loss space-time modulation, thermal lensing, spatial gain modulation, spherical aberrations, tunable second-order diffraction ($D_2 \propto -\delta z$), into a powerful model inspired from the Haus master equation used in time domain (or NL Schrödinger like equation). The novelty here was to include high order diffraction for non-local terms, like fourth order diffraction ($D_4 \propto -S_1$), together with local anharmonic complex potentials.

Finally, we have studied the emitted light states from a CW laser (without saturable absorber) and from a spatially non-linear laser cavity (with “slow” saturable absorber). We have observed three types of transverse emission depending on the cavity parameters. i) For large detuning from self-imaging (i.e., large second order diffraction) we observed classical mode basis such as HG or LG modes. They were stable with normal diffraction for a confining near-field (or local) potential, or stable with anomalous diffraction for a deconfining near-field potential. ii) Conical-wave emission (either Bessel-Gauss or tilted wave, depending on the azimuthal symmetry) close to self-imaging position; as well as guided Bessel beams near SI with a metallic guide (mask). This emission was stabilized thanks to spherical aberrations. The emission angle was shown to be strongly dependent on the optical cavity self-imaging detuning. The Tilted-Wave angle directly correlates with the second order diffraction. Using a powerful NL Schrödinger like model detailing the effects of non-local potential, it was shown that tuning the second order diffraction

with an opposite sign to the fourth order diffraction creates a local minima (normal 2nd order diffraction and anomalous 4th order diffraction) or maxima (anomalous 2nd order diffraction and normal 4th order diffraction) in the non-local phase diagram. The maxima will increase toward larger emission angle, the larger D_2 is. Around those points, a stable off-axis emission can be observed, depending on the local confining potential in near-field. In our case, by lens design, fourth order diffraction was always negative, $D_4 \sim -10 \mu\text{m}^4$ thus stable off axis emission occurred for anomalous diffraction with a confining near-field potential (positive thermal lens). The transverse field emission is characterized by an annular intensity ring in the far-field and an interference pattern in the near field. Depending on the local and non-local homogeneity (thermal lens astigmatism, optical cavity tilt, aberration modulation) the far-field pattern could be azimuthally homogeneous like a Bessel-Gauss beam or with a discrete azimuthal angle selection like a Gaussian beam circulating in a ring laser or Tilted-Wave. iii) Arbitrary degenerate transverse emission. By integrating a sub-lambda absorbing chromium metasurface on the gain mirror, we manage to shape the near-field laser emission into the letter “A” or to a non-uniform profile using artificial defects, demonstrating the high transverse degeneracy of our system.

Close to the self-imaging position with the SESAM, we have demonstrated non-linear spatial localization of the transverse laser field. As for temporal soliton, we balanced the positive SPM from QW gain saturation with normal diffraction. In the self-imaging position, the leading diffraction term is the fourth order diffraction from spherical aberrations, so non-linear localization was impossible for positive D_4 . The optical bi-stability allowed us to address (turn On) spatially the non-linear structure inside a reduce transverse area with step like absorptive boundary conditions (circular chromium mask metasurface). Some work remains to improve the control over a greater area and full addressability (On and Off). Switching from non-resonant to resonant seeding of the non-linear state is one possible future prospect. The need for a reduced transverse area may seem counterintuitive for the spatially extended system SLS condition, but is required to prevent transverse dynamics instabilities and deterministic motion of the localized structure during cavity build-up time ($\tau \sim 100 \text{ ns}$). Using a quantum-mechanical analogy, since the transverse dynamics are characterized by slow light behavior, we explain the need for step like potential (absorptive) barrier as a quantum reflector, preventing the transverse light particle from escaping the pumped area and dying out of the system. Phase and amplitude inhomogeneity, such as thermal lensing, small gain modulation, amplified spontaneous emission or optical system tilt, will induce motion (kinetic energy) of the light particle. The quantum reflection of the absorptive barrier will compensate for this spatial drift, leading to a stable non-linearly localized traveling wave laser emission. The same analysis can be made for the observed non-linear

laser multiplexing. Two uncorrelated light states were demonstrated to coexist within the same laser system (gain medium, cavity, pump). Each light state was stabilized by a step like absorptive potential from a periodic matrix of circular chromium mask.

Currently, we are limited in our ability to observe the transverse dynamics of the system with a characteristic time of few 10 ns. Only time integrated 2D intensity profile (using CCD camera) or space integrated relative intensity noise (using a photodiode) were available. Spatially resolved output power was too low (average power $P_{out} < 100 \mu\text{W}$) to use a time resolved Streak camera. Power limitation is due to both: below laser threshold operation and a design limiting unsaturable losses from the SESAM. For a more in-depth study, a higher transmission output coupler with a high-speed CMOS linear or 2D camera or Streak camera could be used to investigate dynamics in the sub-1 ps range. Increasing output power is also beneficial for concrete applications. More intra-cavity power would also help the light particle stability by reducing the amplified spontaneous emission.

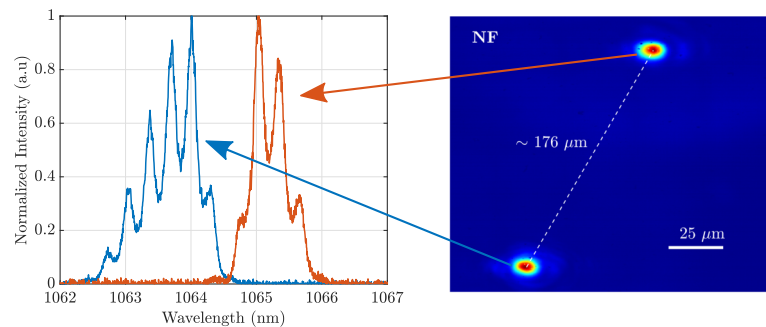


Figure 8.26: Optical spectrum of two Gaussian spot emission inside a self-imaging laser cavity with a fast SESAM. The two spots are shown on the right and are separated by $176 \mu\text{m}$

To improve this system, work is still needed to reduce local and non-local inhomogeneity. Thermal management of the semiconductor gain mirror could help to reduce the thermal lens induced local inhomogeneity. However, wafer bonding of transparent crystal heat sink onto the gain surface will have an impact on the homogeneity and optical performances (introduces loss, generates a coupled Fabry-Perot micro cavity, together with large chromatic dispersion for pulse operation). Another choice is substrate removal and wafer bonding of the resulting membrane, onto a high thermal conductivity host substrate. It usually leads to large defect density arising from mechanical strain. To tackle the non-local inhomogeneity (optical aberration), custom optical lenses could be designed with no radial phase modulation, flat wavefront error ($P-V < \lambda/10$) for more than 0.05 NA. However, manufacturing tolerances and cost could limit the achievable flatness. Another way

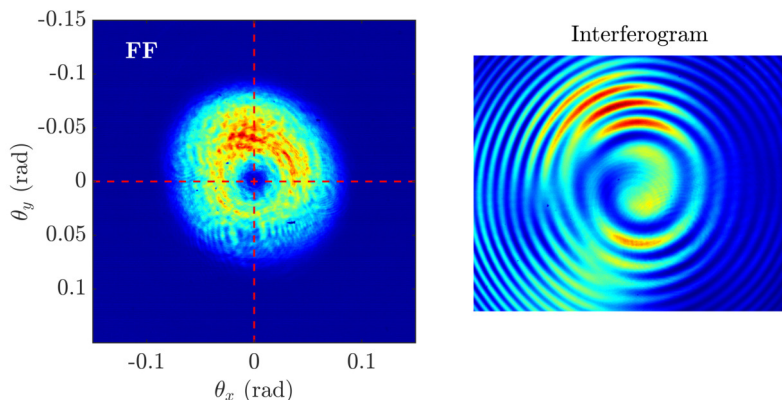


Figure 8.27: Far-field of the Vortex emission and the characteristic spiral phase interferometer for OAM carrying mode.

to circumvent custom lenses could be to use adaptive optics technics. Indeed, by replacing the folding dichroic mirror with a controllable deformable one, we could compensate for the optical system wavefront error. The carrier diffusion length in the SESAM could also be improved by slightly reducing (few nanoseconds) their carrier lifetime for CW operation. In the case of pulsed operation, carrier lifetime is already sufficiently fast for a short scale (about 10 nm) carrier diffusion length.

In its current state, the laser system was able to generate a variety of light states, from Bessel-Gauss beam to non-linear localized structure and laser multiplexing. With small adaptations, we could generate a dual comb mode-locked laser (see figure 8.26) for spectroscopy application, or an array of independent “vortex” modes carrying orbital angular momentum (see figure 8.27) for integration into optical tweezers. The dual-comb mode-locked laser was obtained by replacing the “slow” SESAM with a fast one and each frequency comb was generated by a transverse Gaussian mode at different transverse position using two optical pumps. The tuning of the comb offset can be done by tuning the distance between the two Gaussian modes, taking advantage of the semiconductor gain media large-scale inhomogeneity ($\Delta\lambda \sim -0.12\% \text{ mm}^{-1}$), or varying the pumps power to induce an emission wavelength red-shift ($\Delta\lambda = 8.8 \text{ nm/W}$). The Vortex laser emission shown in figure 8.27 was one of the solutions of the laser system operating with a near-field circular aperture (chromium mask). Using the spiral phase mask metasurface methods developed by Seghilani et al. [Seghilani 2016] to have a robust Vortex operation, and expanding it across a transverse array, we could generate a multiplexed emission of tunable in angular momentum Vortex beam. It is of great interest for applications in optical tweezers for the study of mechanical and dynamical processes in biological systems. At the same time, the phase metasurface could also be used for shaping the near-field phase potential and controlling the

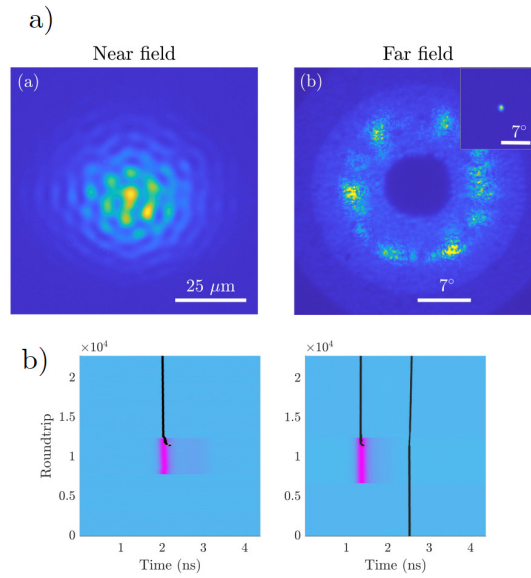


Figure 8.28: a) Average time profile of the near-field (left) and far field (right) intensity profile of the observed TLS Turing pattern. b) Spatio-temporal of the writing (left) and deleting (right) of a temporally localized pulse. The TLS pulse trajectory is marked by a black line.

mechanical dynamics of the light particle (adding drift, rotation, ...).

Lastly, advances towards optical 3D spatio-temporal localized state or Light bullet were made using the non-local and local phase and amplitude potential engineering developed in this work. Bartolo et al. [Bartolo 2022] have already demonstrated temporal localization of Turing patterns and optical addressability of individual pulses (see figure 8.28). This paves the way towards Light Bullets demonstration inside a laser cavity (dissipative system).

Bibliography

- [Abbes 2021] Abbes, A. (2021). *Photomixed Terahertz Emitters by Multipolar Photoconductive Terahertz Antennas*. PhD thesis, Université Montpellier.
- [Ackemann 1994] Ackemann, n. and Lange, n. (1994). Non- and nearly hexagonal patterns in sodium vapor generated by single-mirror feedback. *Physical Review A, Atomic, Molecular, and Optical Physics*, 50(6):R4468–R4471.
- [Arecchi 1995] Arecchi, F. T. (1995). Optical morphogenesis: Pattern formation and competition in nonlinear optics. *Physica D: Nonlinear Phenomena*, 86(1):297–322.
- [Arnaud 1969] Arnaud, J. A. (1969). Degenerate Optical Cavities. *Applied Optics*, 8(1):189–196.
- [Bagini 1996] Bagini, V., Frezza, F., Santarsiero, M., Schettini, G., and Spagnolo, G. S. (1996). Generalized Bessel-Gauss beams. *Journal of Modern Optics*, 43(6):1155–1166.
- [Baird 1965] Baird, K. M., Smith, D. S., Hanes, G. R., and Tsunekane, S. (1965). Characteristics of a Simple Single-Mode He–Ne Laser. *Applied Optics*, 4(5):569–571.
- [Balle 1998] Balle, S. (1998). Simple analytical approximations for the gain and refractive index spectra in quantum-well lasers. *Physical Review A*, 57(2):1304–1312.
- [Barland 2002] Barland, S., Tredicce, J. R., Brambilla, M., Lugiato, L. A., Balle, S., Giudici, M., Maggipinto, T., Spinelli, L., Tissoni, G., Knödl, T., Miller, M., and Jäger, R. (2002). Cavity solitons as pixels in semiconductor microcavities. *Nature*, 419(6908):699–702.
- [Bartolo 2022] Bartolo, A., Vigne, N., Marconi, M., Beaudoin, G., Pantzas, K., Sagnes, I., Huyet, G., Maucher, F., Gurevich, S., Javaloyes, J., Garnache, A., and Giudici,

- M. (2022). Temporal Localized Turing Patterns in Vertical External-Cavity Surface-Emitting Laser.
- [Bartolo González 2022] Bartolo González, A. A. (2022). *Structuration Spatiale Des Impulsions Localisées Dans Les Lasers à Émission Surfactive Avec Cavité Externe Auto-Imageante*. These de doctorat, Université Côte d'Azur.
- [Beijersbergen 1994] Beijersbergen, M. W., Coerwinkel, R. P. C., Kristensen, M., and Woerdman, J. P. (1994). Helical-wavefront laser beams produced with a spiral phaseplate. *Optics Communications*, 112(5):321–327.
- [Benisty 1999] Benisty, H. (1999). Physics of light extraction efficiency in planar microcavity light-emitting diodes. In *Confined Photon Systems*, pages 393–405. Springer.
- [Bernard 1961] Bernard, M. G. A. and Duraffourg, G. (1961). Laser Conditions in Semiconductors. *physica status solidi (b)*, 1(7):699–703.
- [Bieker 2015] Bieker, S., Stühler, R., Kiessling, T., Ossau, W., and Molenkamp, L. W. (2015). Dimensional crossover of free exciton diffusion in etched GaAs wire structures. *Applied Physics Letters*, 107(12):122106.
- [Bliedtner 2016] Bliedtner, J., Schindler, C., Seiler, M., Wächter, S., Friedrich, M., and Giesecke, J. (2016). Ultrashort Pulse Laser Material Processing. *Laser Technik Journal*, 13(5):46–50.
- [Booth 2004] Booth, H. J. (2004). Recent applications of pulsed lasers in advanced materials processing. *Thin Solid Films*, 453–454:450–457.
- [Born 2000] Born, M. and Wolf, E. (2000). *Principles of Optics: Electromagnetic Theory of Propagation, Interference and Diffraction of Light*. CUP Archive.
- [Bourdon 2002] Bourdon, G., Robert, I., Sagnes, I., and Abram, I. (2002). Spontaneous emission in highly excited semiconductors: Saturation of the radiative recombination rate. *Journal of Applied Physics*, 92(11):6595–6600.
- [Camelin 2017] Camelin, P., Javaloyes, J., Marconi, M., and Giudici, M. (2017). Electrical Addressing and Temporal Tweezing of Localized Pulses in Passively Mode-Locked Semiconductor Lasers. In *2017 European Conference on Lasers and Electro-Optics and European Quantum Electronics Conference (2017), Paper CB_8_6*, page CB_8_6. Optica Publishing Group.
- [Camelin 2018] Camelin, P., Schelte, C., Verschelde, A., Garnache, A., Beaudoin, G., Sagnes, I., Huyet, G., Javaloyes, J., Gurevich, S. V., and Giudici, M. (2018).

- Temporal localized structures in mode-locked vertical external-cavity surface-emitting lasers. *Optics Letters*, 43(21):5367–5370.
- [Cao 2019] Cao, H., Chriki, R., Bittner, S., Friesem, A. A., and Davidson, N. (2019). Complex lasers with controllable coherence. *Nature Reviews Physics*, 1(2):156–168.
- [Chang-Hasnain 1990] Chang-Hasnain, C. J., Orenstein, M., Von Lehmen, A., Florez, L. T., Harbison, J. P., and Stoffel, N. G. (1990). Transverse mode characteristics of vertical cavity surface-emitting lasers. *Applied Physics Letters*, 57(3):218–220.
- [Chomet 2019] Chomet, B. (2019). *Integration of High Coherence Tunable Semiconductor Laser. Non Linear Multimode Dynamics and Route to Single Frequency Operation*. These de doctorat, Montpellier.
- [Chriki 2018] Chriki, R., Barach, G., Tradosny, C., Smartsev, S., Pal, V., Friesem, A. A., and Davidson, N. (2018). Rapid and efficient formation of propagation invariant shaped laser beams. *Optics Express*, 26(4):4431–4439.
- [Čižmár 2011] Čižmár, T. and Dholakia, K. (2011). Shaping the light transmission through a multimode optical fibre: Complex transformation analysis and applications in biophotonics. *Optics Express*, 19(20):18871–18884.
- [Clemmow 1966] Clemmow, P. C. (1966). *The Plane Wave Spectrum Representation of Electromagnetic Fields*. Oxford.
- [Coldren 2012] Coldren, L. A., Corzine, S. W., and Mashanovitch, M. L. (2012). *Diode Lasers and Photonic Integrated Circuits*. John Wiley & Sons.
- [Collins 1963] Collins, S. A. and White, G. R. (1963). Interferometer laser mode selector. *Applied Optics*, 2(4):448_1–449.
- [Cortez 2000] Cortez, S., Krebs, O., and Voisin, P. (2000). In-plane optical anisotropy of quantum well structures: From fundamental considerations to interface characterization and optoelectronic engineering. *Journal of Vacuum Science & Technology B: Microelectronics and Nanometer Structures Processing, Measurement, and Phenomena*, 18(4):2232–2241.
- [Crank 1979] Crank, J. and Crank, E. P. J. (1979). *The Mathematics of Diffusion*. Clarendon Press.
- [De Silvestri 1984] De Silvestri, S., Laporta, P., and Svelto, O. (1984). The role of cavity dispersion in CW mode-locked dye lasers. *IEEE Journal of Quantum Electronics*, 20(5):533–539.

- [Einstein 1917] Einstein, A. (1917). Zur Quantentheorie der Strahlung. *Phys. Z.*, 18:121–128.
- [Fabry 1897] Fabry, C. and Pérot, A. (1897). Sur les franges des lames minces argentées et leur application à la mesure de petites épaisseurs d'air. *Ann. Chim. Phys.*, 12(459-501).
- [Fricke 2010] Fricke, J., Bugge, F., Ginolas, A., John, W., Klehr, A., Matalla, M., Ressel, P., Wenzel, H., and Erbert, G. (2010). High-Power 980-nm Broad-Area Lasers Spectrally Stabilized by Surface Bragg Gratings. *IEEE Photonics Technology Letters*, 22(5):284–286.
- [Garnache 2002] Garnache, A., Hoogland, S., Tropper, A. C., Sagnes, I., Saint-Girons, G., and Roberts, J. S. (2002). Sub-500-fs soliton-like pulse in a passively mode-locked broadband surface-emitting laser with 100 mW average power. *Applied Physics Letters*, 80(21):3892–3894.
- [Garnache 2003] Garnache, A., Sermage, B., Teissier, R., Saint-Giro, G., and Sagnes, I. (2003). A new kind of fast quantum-well semiconductor saturable-absorber mirror with low losses for ps pulse generation. In *International Conference on Indium Phosphide and Related Materials, 2003.*, pages 247–250.
- [Genevet 2008] Genevet, P., Barland, S., Giudici, M., and Tredicce, J. R. (2008). Cavity soliton laser based on mutually coupled semiconductor microresonators. *Physical Review Letters*, 101(12):123905.
- [Gibbs 2012] Gibbs, H. (2012). *Optical Bistability: Controlling Light with Light*. Elsevier.
- [Goodman 2005] Goodman, J. W. (2005). *Introduction to Fourier Optics*. Roberts and Company Publishers.
- [Gopinath 2001] Gopinath, J. T., Thoen, E. R., Koontz, E. M., Grein, M. E., Kolodziejcki, L. A., Ippen, E. P., and Donnelly, J. P. (2001). Recovery dynamics in proton-bombarded semiconductor saturable absorber mirrors. *Applied Physics Letters*, 78(22):3409–3411.
- [Grella 1982] Grella, R. (1982). Fresnel propagation and diffraction and paraxial wave equation. *Journal of Optics*, 13(6):367–374.
- [Grynberg 1988] Grynberg, G., Le Bihan, E., Verkerk, P., Simoneau, P., Leite, J. R. R., Bloch, D., Le Boiteux, S., and Ducloy, M. (1988). Observation of instabilities due to mirrorless four-wave mixing oscillation in sodium. *Optics Communications*, 67(5):363–366.

- [Gu 2000] Gu, M. (2000). *Advanced Optical Imaging Theory*. Springer Science & Business Media.
- [Gupta 1992] Gupta, S., Whitaker, J., and Mourou, G. (1992). Ultrafast carrier dynamics in III-V semiconductors grown by molecular-beam epitaxy at very low substrate temperatures. *IEEE Journal of Quantum Electronics*, 28(10):2464–2472.
- [Gurevich 2017] Gurevich, S. V. and Javaloyes, J. (2017). Spatial instabilities of light bullets in passively-mode-locked lasers. *Physical Review A*, 96(2):023821.
- [Gutiérrez-Vega 2003] Gutiérrez-Vega, J. C., Rodríguez-Masegosa, R., and Chávez-Cerda, S. (2003). Bessel–Gauss resonator with spherical output mirror: Geometrical- and wave-optics analysis. *JOSA A*, 20(11):2113–2122.
- [Hargrove 1964] Hargrove, L. E., Fork, R. L., and Pollack, M. A. (1964). LOCKING OF He–Ne LASER MODES INDUCED BY SYNCHRONOUS INTRACAVITY MODULATION. *Applied Physics Letters*, 5(1):4–5.
- [Haus 1975a] Haus, H. (1975a). Theory of mode locking with a slow saturable absorber. *IEEE Journal of Quantum Electronics*, 11(9):736–746.
- [Haus 2000] Haus, H. (2000). Mode-locking of lasers. *IEEE Journal of Selected Topics in Quantum Electronics*, 6(6):1173–1185.
- [Haus 1975b] Haus, H. A. (1975b). Theory of mode locking with a fast saturable absorber. *Journal of Applied Physics*, 46(7):3049–3058.
- [Haus 1975c] Haus, H. A. (1975c). Theory of mode locking with a fast saturable absorber. *Journal of Applied Physics*, 46(7):3049–3058.
- [Henry 1982] Henry, C. (1982). Theory of the linewidth of semiconductor lasers. *IEEE Journal of Quantum Electronics*, 18(2):259–264.
- [Heritage 1978] Heritage, J. P. and Jain, R. K. (1978). Subpicosecond pulses from a tunable cw mode-locked dye laser. *Applied Physics Letters*, 32(2):101–103.
- [Hoogland 2005] Hoogland, S., Garnache, A., Sagnes, I., Roberts, J., and Tropper, A. (2005). 10-GHz train of sub-500-fs optical soliton-like pulses from a surface-emitting semiconductor laser. *IEEE Photonics Technology Letters*, 17(2):267–269.
- [Iga 1988] Iga, K., Koyama, F., and Kinoshita, S. (1988). Surface emitting semiconductor lasers. *IEEE Journal of Quantum Electronics*, 24(9):1845–1855.
- [Ippen 1972] Ippen, E., Shank, C., and Dienes, A. (1972). Passive mode locking of the cw dye laser. *Applied Physics Letters*, 21(8):348–350.

- [Javaloyes 2016] Javaloyes, J. (2016). Cavity light bullets in passively mode-locked semiconductor lasers. *Physical review letters*, 116(4):043901.
- [Jeffries 2007] Jeffries, G. D. M., Edgar, J. S., Zhao, Y., Shelby, J. P., Fong, C., and Chiu, D. T. (2007). Using Polarization-Shaped Optical Vortex Traps for Single-Cell Nanosurgery. *Nano Letters*, 7(2):415–420.
- [Kane 1985] Kane, T. J. and Byer, R. L. (1985). Monolithic, unidirectional single-mode Nd:YAG ring laser. *Optics Letters*, 10(2):65–67.
- [Kärtner 1995] Kärtner, F. X. and Keller, U. (1995). Stabilization of solitonlike pulses with a slow saturable absorber. *Optics Letters*, 20(1):16–18.
- [Kastler 1962] Kastler, A. (1962). Atomes à l'Intérieur d'un Interféromètre Perot-Fabry. *Applied Optics*, 1(1):17–24.
- [Kawamura 2021] Kawamura, T., Shirakawa, A., and Saito, K. (2021). Phase-locked and mode-locked multicore photonic crystal fiber laser with a saturable absorber. *Optics Express*, 29(11):17023–17028.
- [Keller 2003] Keller, U. (2003). Recent developments in compact ultrafast lasers. *Nature*, 424(6950):831–838.
- [Keller 2021] Keller, U. (2021). *Ultrafast Lasers: A Comprehensive Introduction to Fundamental Principles with Practical Applications*. Graduate Texts in Physics. Springer International Publishing, Cham.
- [Khanin 2012] Khanin, Y. I. (2012). *Principles of Laser Dynamics*. Newnes.
- [Khilo 2001] Khilo, A. N., Katranji, E. G., and Ryzhevich, A. A. (2001). Axicon-based Bessel resonator: Analytical description and experiment. *JOSA A*, 18(8):1986–1992.
- [Khurgin 2010] Khurgin, J. B. (2010). Slow light in various media: A tutorial. *Advances in Optics and Photonics*, 2(3):287–318.
- [Kimura 1971] Kimura, T., Otsuka, K., and Saruwatari, M. (1971). Spatial hole-burning effects in a Nd³⁺:YAG laser. *IEEE Journal of Quantum Electronics*, 7(6):225–230.
- [Knitter 2016] Knitter, S., Liu, C., Redding, B., Khokha, M. K., Choma, M. A., and Cao, H. (2016). Coherence switching of a degenerate VECSEL for multimodality imaging. *Optica*, 3(4):403–406.

- [Kogelnik 1972] Kogelnik, H. and Shank, C. V. (1972). Coupled-Wave Theory of Distributed Feedback Lasers. *Journal of Applied Physics*, 43(5):2327–2335.
- [Koyama 1989] Koyama, F., Kinoshita, S., and Iga, K. (1989). Room-temperature continuous wave lasing characteristics of a GaAs vertical cavity surface-emitting laser. *Applied Physics Letters*, 55(3):221–222.
- [Krebs 1996] Krebs, O. and Voisin, P. (1996). Giant Optical Anisotropy of Semiconductor Heterostructures with No Common Atom and the Quantum-Confined Pockels Effect. *Physical Review Letters*, 77(9):1829–1832.
- [Lan 2004] Lan, Y.-P., Chen, C.-Y., Pan, R.-P., and Pan, C.-L. (2004). Fine-tuning of a diode laser wavelength with a liquid crystal intracavity element. *Optical Engineering*, 43(1):234–238.
- [Laurain 2010] Laurain, A. (2010). *Sources Laser à Semiconducteur à Émission Verticale de Haute Cohérence et de Forte Puissance Dans Le Proche et Le Moyen Infrarouge*. These de doctorat, Montpellier.
- [Liew 2017] Liew, S. F., Knitter, S., Weiler, S., Monjardin-Lopez, J. F., Ramme, M., Redding, B., Choma, M. A., and Cao, H. (2017). Intracavity frequency-doubled degenerate laser. *Optics Letters*, 42(3):411–414.
- [Lioubashevski 1999] Lioubashevski, O., Hamiel, Y., Agnon, A., Reches, Z., and Fineberg, J. (1999). Oscillons and Propagating Solitary Waves in a Vertically Vibrated Colloidal Suspension. *Physical Review Letters*, 83(16):3190–3193.
- [Mackenzie 2007] Mackenzie, J. I. (2007). Dielectric Solid-State Planar Waveguide Lasers: A Review. *IEEE Journal of Selected Topics in Quantum Electronics*, 13(3):626–637.
- [Mahajan 1983] Mahajan, V. N. (1983). Strehl ratio for primary aberrations in terms of their aberration variance. *JOSA*, 73(6):860–861.
- [Malacara 2001] Malacara, D. and Thompson, B. J. (2001). *Handbook of Optical Engineering*. Chap 26. Marcel Dekker New York.
- [Mandon 2009] Mandon, J., Guelachvili, G., and Picqué, N. (2009). Fourier transform spectroscopy with a laser frequency comb. *Nature Photonics*, 3(2):99–102.
- [Marconi 2014] Marconi, M., Javaloyes, J., Balle, S., and Giudici, M. (2014). How lasing localized structures evolve out of passive mode locking. *Physical review letters*, 112(22):223901.

- [Maréchal 1948] Maréchal, A. (1948). *Étude Des Effets Combinés de La Diffraction et Des Aberrations Géométriques Sur l'image d'un Point Lumineux...* Éditions de la Revue d'optique théorique et instrumentale.
- [Marée 1987] Marée, P. M. J., Barbour, J. C., van der Veen, J. F., Kavanagh, K. L., Bulle-Lieuwma, C. W. T., and Vieggers, M. P. A. (1987). Generation of misfit dislocations in semiconductors. *Journal of Applied Physics*, 62(11):4413–4420.
- [Minardi 2010] Minardi, S., Eilenberger, F., Kartashov, Y. V., Szameit, A., Röpke, U., Kobelke, J., Schuster, K., Bartelt, H., Nolte, S., Torner, L., Lederer, F., Tünnermann, A., and Pertsch, T. (2010). Three-Dimensional Light Bullets in Arrays of Waveguides. *Physical Review Letters*, 105(26):263901.
- [New 1974] New, G. (1974). Pulse evolution in mode-locked quasi-continuous lasers. *IEEE Journal of Quantum Electronics*, 10(2):115–124.
- [Palma 1997] Palma, C. and Bagini, V. (1997). Extension of the Fresnel transform to ABCD systems. *JOSA A*, 14(8):1774–1779.
- [Paquet 2016] Paquet, R. (2016). *Nouvelles sources lasers pour génération THz*. Thèse de doctorat, Université de Montpellier, 2015-...., France.
- [Pedaci 2005] Pedaci, F., Giudici, M., Tredicce, J. R., and Giacomelli, G. (2005). Experimental analysis of mode-hopping in bulk semiconductor lasers. *Applied Physics B*, 81(7):993–1000.
- [Piprek 2013] Piprek, J. (2013). *Semiconductor Optoelectronic Devices: Introduction to Physics and Simulation*. Elsevier.
- [Polzik 1991] Polzik, E. S. and Kimble, H. J. (1991). Frequency doubling with KNbO_3 in an external cavity. *Optics Letters*, 16(18):1400–1402.
- [Ramazza 2003] Ramazza, P. L., Boccaletti, S., Bortolozzo, U., and Arecchi, F. T. (2003). Control of localized structures in an optical feedback interferometer. *Chaos (Woodbury, N.Y.)*, 13(1):335–341.
- [Richter 2005] Richter, R. and Barashenkov, I. V. (2005). Two-Dimensional Solitons on the Surface of Magnetic Fluids. *Physical Review Letters*, 94(18).
- [Schawlow 1958] Schawlow, A. L. and Townes, C. H. (1958). Infrared and Optical Masers. *Physical Review*, 112(6):1940–1949.
- [Schimpf 2012] Schimpf, D. N., Schulte, J., Putnam, W. P., and Kärtner, F. X. (2012). Generalizing higher-order Bessel-Gauss beams: Analytical description and demonstration. *Optics Express*, 20(24):26852–26867.

- [Seghilani 2015] Seghilani, M. (2015). *Highly Coherent III-V Semiconductor Laser Emitting Phase-, Amplitude-, and Polarization Structured Light for Advanced Sensing Application: Vortex, SPIN, Feedback Dynamics*. PhD thesis, Montpellier II.
- [Seghilani 2016] Seghilani, M. S., Myara, M., Sellahi, M., Legratiet, L., Sagnes, I., Beaudoin, G., Lalanne, P., and Garnache, A. (2016). Vortex Laser based on III-V semiconductor metasurface: Direct generation of coherent Laguerre-Gauss modes carrying controlled orbital angular momentum. *Scientific Reports*, 6(1):38156.
- [Sellahi 2014] Sellahi, M. (2014). *Laser à semi-conducteur III-V à émission verticale de haute cohérence et de forte puissance : Etat vortex, continuum et bifréquence THz*. PhD thesis, Montpellier II.
- [Shimizu 1988] Shimizu, M., Koyama, F., and Iga, K. (1988). Polarization Characteristics of MOCVD Grown GaAs/GaAlAs CBH Surface Emitting Lasers. In *Integrated and Guided-Wave Optics (1988)*, Paper WA3, page WA3. Optica Publishing Group.
- [Siegman 1986] Siegman, A. E. (1986). *Lasers*. University Science Books.
- [Steinkogler 2003] Steinkogler, S., Schneider, H., Walther, M., and Koidl, P. (2003). Determination of the electron capture time in quantum-well infrared photodetectors using time-resolved photocurrent measurements. *Applied Physics Letters*, 82(22):3925–3927.
- [Stohs 2001] Stohs, J., Bossert, D., Gallant, D., and Brueck, S. (2001). Gain, refractive index change, and linewidth enhancement factor in broad-area GaAs and InGaAs quantum-well lasers. *IEEE Journal of Quantum Electronics*, 37(11):1449–1459.
- [Strehl 1895] Strehl, K. (1895). Aplanatische und fehlerhafte Abbildung im Fernrohr. *Zeitschrift für Instrumentenkunde*, 15(7):362–370.
- [Taranenko 1997] Taranenko, V. B., Staliunas, K., and Weiss, C. O. (1997). Spatial soliton laser: Localized structures in a laser with a saturable absorber in a self-imaging resonator. *Physical Review A*, 56(2):1582–1591.
- [Tian 2021] Tian, Y., Wang, L., Duan, G., and Yu, L. (2021). Multi-trap optical tweezers based on composite vortex beams. *Optics Communications*, 485:126712.
- [Turing 1952] Turing, A. M. (1952). The chemical basis of morphogenesis. *Philosophical Transaction of the Royal Society of London*, page 237.
- [Uehara 1989] Uehara, K. and Kikuchi, H. (1989). Generation of nearly diffraction-free laser beams. *Applied Physics B*, 48(2):125–129.

- [Vainio 2008] Vainio, M., Peltola, J., Persijn, S., Harren, F. J. M., and Halonen, L. (2008). Singly resonant cw OPO with simple wavelength tuning. *Optics Express*, 16(15):11141–11146.
- [Villares 2014] Villares, G., Hugi, A., Blaser, S., and Faist, J. (2014). Dual-comb spectroscopy based on quantum-cascade-laser frequency combs. *Nature Communications*, 5(1):5192.
- [Wang 2016] Wang, J. (2016). Advances in communications using optical vortices. *Photonics Research*, 4(5):B14–B28.
- [Wang 2011] Wang, Z., Zhang, N., and Yuan, X.-C. (2011). High-volume optical vortex multiplexing and de-multiplexing for free-space optical communication. *Optics Express*, 19(2):482–492.
- [Webb 2020] Webb, C. E. (2020). *Handbook of Laser Technology and Applications: Volume 1: Principles*. CRC Press.
- [Welford 1986] Welford, W. T. (1986). *Aberrations of Optical Systems*. CRC Press.
- [Yao 2011] Yao, A. M. and Padgett, M. J. (2011). Orbital angular momentum: Origins, behavior and applications. *Advances in Optics and Photonics*, 3:161.
- [Yariv 1991] Yariv, A. (1991). *Optical Electronics*. Saunders College Publishing, Philadelphia, PA.
- [Yoshida 1982] Yoshida, A. (1982). Spherical aberration in beam optical systems. *Applied Optics*, 21(10):1812–1816.
- [Yu 2011] Yu, J.-L., Chen, Y.-H., Tang, C.-G., Jiang, C., and Ye, X.-L. (2011). Observation of strong anisotropic forbidden transitions in (001) InGaAs/GaAs single-quantum well by reflectance-difference spectroscopy and its behavior under uniaxial strain. *Nanoscale Research Letters*, 6(1):210.
- [Zayhowski 1989] Zayhowski, J. J. and Mooradian, A. (1989). Single-frequency microchip Nd lasers. *Optics Letters*, 14(1):24–26.
- [Zory 1993] Zory (1993). *Quantum Well Lasers*. Academic Press.